On the genesis, evolution and characterization of veins, dykes and fracture networks: Unravelling the brittle tectonics in the rocks of the Chitradurga region, Western Dharwar Craton, India

Thesis submitted for the degree of

Doctor of Philosophy (Science)
of
Jadavpur University

By

SIRSHENDU KUMAR BISWAS

Geological Studies Unit

Indian Statistical Institute, Kolkata

Registered at:

Department of Geological Sciences

Jadavpur University

Kolkata 700032, India

Index Number: 118/22/Geol.Sc./28

Registration Number: SOGEO1111822; Date of Registration: 07.06.2022

Tridib Kumar Mondal, PhD
Assistant Professor
Geological Studies Unit
Physics and Earth Sciences Division
INDIAN STATISTICAL INSTITUTE

203 B. T. Road, Kolkata 700108, India
Email (1): tridibkumarmondal@isical.ac.in
Email (2): tridibkumarmondal@gmail.com
Phone: +91 033 2575 3152
https://gsu.isical.ac.in/tridib-kumar-mondal
https://sites.google.com/view/tridibkmondal/home

CERTIFICATE FROM THE SUPERVISOR

This is to certify that the thesis entitled "**On the genesis, evolution and characterization of veins, dykes and fracture networks: Unravelling the brittle tectonics in the rocks of the Chitradurga region, Western Dharwar Craton, India**" submitted by Sri **Sirshendu Kumar Biswas** who got his name registered on **07.06.2022** for the award of **Ph. D. (Science) degree** of **Jadavpur University**, is absolutely based upon his own work under the supervision of **Dr. Tridib Kumar Mondal** and that neither this thesis nor any part of it has been submitted for either any degree/diploma or any other academic award anywhere before.

Tridib K. Mondal
01.09.2025

(Signature of the Supervisor, date with official seal)

Dr. TRIDIB KUMAR MONDAL
Assistant Professor
Geological Studies Unit
Physics & Earth Sciences Division
Indian Statistical Institute
203, Barrackpore Trunk Road
Kolkata-700 108, INDIA

CONTENTS **Page No.**

Acknowledgements

As a student, I had never really thought of pursuing a Ph.D. Coming from humble beginnings, the immediate concern for someone like me was always to earn a modest living and support my family. Naturally, the obvious choice after completing my master’s degree was to take up a job. I worked briefly as an exploration geologist, but it did not take me long to realize that the field neither matched my interests nor gave me any sense of fulfilment. It was only while searching for an alternative path that I turned towards academia.

At that crucial turning point in my career, I was reminded of the words of my master’s dissertation guide, Prof. Gautam Ghosh of Presidency University, Kolkata. He was the only one who had ever encouraged me, right after graduation, to consider a Ph.D. At that time, I did not pay heed; rather, I could not. But when I finally chose this path, it was his early guidance and insight that made all the difference. For that, I shall remain forever indebted to him.

I consider myself immensely fortunate to have Dr. Tridib Kumar Mondal as my Ph.D. supervisor at the Geological Studies Unit of Indian Statistical Institute, Kolkata. Young, dynamic, and endlessly supportive, he stood by me as a friend, philosopher, and guide. His constant motivation and encouragement helped me navigate both academic challenges and personal struggles. Without his guidance and belief in me, I sincerely doubt I would have been able to complete this journey.

I also take this opportunity to sincerely acknowledge Indian Statistical Institute, Kolkata for funding this research throughout. I am also grateful to Jadavpur University, Kolkata for granting me the opportunity to register my Ph.D. My heartfelt regards go to Prof. Susanta Kumar Samanta, Head of the Department of Geological Sciences, Jadavpur University, as well as to my Research Advisory Committee members, Prof. Pulak Sengupta and Prof. Supriya Mondal, for their invaluable guidance and constructive feedback throughout the course of my work. I sincerely extend my gratitude to the Research Fellow Advisory Committee, as well as to all my teachers, friends, colleagues, and the staff of the Geological Studies Unit, Indian Statistical Institute, Kolkata, for their support and the pleasant time I have had here.

It would have been impossible for me to make it through the times before I began my Ph.D. and the initial phases of it, without the unwavering support of Sukanya Basu, who stood by me as a true pillar of strength when I had nothing to hold on to. Though life often takes its own course and certain things are not meant to be, I shall always remain profoundly grateful for her support and the memories that continue to inspire me.

Throughout the course of my work, I have greatly benefited from the kind, engaging and fruitful association with my lab mates. I am deeply grateful to my senior, Dr. Sreyashi Bhowmick, for her insightful discussions and timely assistance, and to my colleague, Gourav Das, whose dedicated assistance during our numerous field campaigns in the Dharwar Craton and back in the lab was invaluable. I also acknowledge my junior, Anubhab Dey, who, though joining later, extended his help with equal enthusiasm.

I am sincerely grateful to Prof. Md. Sakawat Hossain, Jahangirnagar University, Bangladesh, for his valuable help in the preparation of one of my manuscripts, which he also kindly co-authored. I also extend my thanks to Prof. Somnath Dasgupta and Dr. Shreya Karmakar for their insightful suggestions during the course of this work. I warmly acknowledge Kuntal Saha, Avijit Saha, Archisman Mukherjee, Alaap Kumar Mukhopadhyay and Brinta Banik, for their dedicated contributions and collaboration. Their support was instrumental in many of the works included in this thesis, several of which they co-authored with me.

I fondly remember the late Mr. H. N. Ravi Kumar, who not only served as our field vehicle driver but also as a trusted local guide during field campaigns, and I thank Mr. Manjunatha B. N., who later took on this role. I also gratefully acknowledge the Geological Survey of India, Bangalore, for providing logistical support during fieldworks in the Dharwar Craton.

With sincere regards and deep gratitude, I must also respectfully acknowledge the moral and academic foundations laid by all my teachers, right from school through college and university, upon which I continue to stand strong today.

Lastly, I realize that not everyone is fortunate enough to receive the kind of family support one hopes for and needs. However, it is my parents and my elder sister who have shaped me initially from my modest beginnings into the person that I am today. Whatever my needs may have been, they always did their utmost, and for that I shall remain forever indebted to them. Thank you.

Kolkata **Sirshendu Kumar Biswas**

Preface

Rocks, the sentinels of time immemorial, the omniscient, silent sage. From the fiery womb of mother earth to the trivial sand of the seven seas, they withstand, witness and chronicle. Annals of time fade away, yet, they remain. And in the process, they change. The indomitable granite bends, the magnificent marble dissolves, and the obstinate sandstone weathers away. Heat melts them, pressure moulds them, stress breaks them apart. Time transforms them. And it is in this endless cycle of transformation, that they persist.

And in my sojourn with geology, so far, somehow, I feel that we human beings are also a lot like rocks. The igneous ones; born with their grit, and no matter what, they preserve it all throughout their lifetime. Then comes the sedimentary ones; waves of life uproot them from where they belonged, break them apart, disintegrate them, transport them regardless of resistance and finally settle them down far away, where, after all these upheavals, they have the permission to rest and contemplate. And finally, the metamorphic ones; life transforms them; they become something new altogether, not even knowing that they still carry subtle traces of their true forms buried deep within. And throughout this journey of change, deformation is the inevitable companion. Just like rocks, we bend; we break, we shatter and we heal. Life happens. The cycle of deformation, recovery and recrystallization continues.

But what is this obsession with deformation? Something, that damages, something, that in essence, is destruction. Because, in this quest, it is not only the process of deformation that we seek to perceive, but we tend to undeform the deformed, to reconstruct the unhinged, to unfold the folded, to restore and balance. It is always the search for the one true core, the unaltered, unblemished story, the journey unto oneself, the introspection, of what we are, and what we were actually. But deformation is change, sometimes lingering and sometimes taking away parts, barely ever replaceable. Like rocks under stress, we also react differently to life. We bend, we stretch, we shatter and we break. We lose ourselves in the process, slowly or suddenly, but the struggle is to always keep that pristine core intact. We fail, but nevertheless, we try. We try to preserve our stories that time invariably etches. And we hope, that someone, someday will carefully find those stories out. Like rocks we persist. That is what life is. But life also heals. It takes time and patience. Fractures seal, veins form, the scars remain, but we learn to accept our flaws and live with our new forms. Life goes on. The wheel rotates. Our stories unfold.

I suppose, in the end, anything and everything, in retrospect, reflects life. Musings of the journey. The eternal cycle of formation and deformation, of rise and collapse, and rebirth; of change until oblivion. And structural geology, alike geology, the story of earth, is no exception.

Abstract

Deformation within the upper crustal regime is predominantly brittle in nature, manifested through rock fracturing, creating major pathways for fluid flow. The present research focuses on the structural investigation and characterization of brittle structures developed within the rocks of the Chitradurga Schist Belt, an Archean granite-greenstone sequence in the Western Dharwar Craton of southern India. The study aims to understand the varying controls on the formation, emplacement mechanisms, spatio-temporal evolution and inter-relationships of these brittle structures in order to reconstruct the brittle tectonic history of the terrain under ambient stress states.

Through this investigation, the research seeks to examine the tectonic evolution of cratons in general, during late stages of crustal deformation, focusing on how fracture systems evolve across successive tectonic episodes, the role of magma and fluids, the spatial link between brittle deformation and craton-scale architecture, and the broader implications for tectonic rejuvenation and long-term stabilization of cratonic blocks.

Field-based studies have been employed to identify the brittle structures within different lithologies of the schist belt. Three major suites of brittle structures have been recognized in the rocks of the study area: 1) Veins occurring in consistent orientations within both the metavolcanic rocks of the greenstone sequence and the younger granites that intrude them; 2) mafic dykes intruding the younger granites; 3) fracture networks developed through mutually interacting faults within the younger granites and the metavolcanic rock suite of the greenstone sequence.

Structural analyses coupled with statistical and mathematical methods involving field data collected from these brittle features have been employed to better constrain the conditions of their genesis. Observations on outcrop geometry and spatial relations of structures along with study of petrographic thin sections are utilized to determine the relative temporal evolution of brittle tectonic structures from the region.

The study demonstrates that pre-existing structural anisotropies played a key role in controlling vein emplacement, and further reveals at least three separate fluid pressure events that contributed to the development of the shallow-crustal quartz vein system in the metavolcanic rocks of the Chitradurga region, identified through statistical fuzzy-clustering of heterogeneous planar data.

Novel methodologies have been developed to calculate complete dyke dimensions from their partial exposures, enabling the estimation of magma overpressure and depth of origin for the mafic dykes of the region. Structural investigation of dyke outcrop patterns revealed sinistral shearing of the dykes induced by the effect of the adjacent Chitradurga Shear Zone and a geological model of their formation and subsequent emplacement under varying regional stress fields of the terrain has been proposed.

Fracture networks developed within the granites and metavolcanic rocks of the greenstone sequence have been characterized in terms of their geometrical, kinematic, topological and fractal attributes from 2D outcrop surfaces, indicating their development through a regional Riedel shear system activated by sinistral shearing along the Chitradurga Shear Zone during D_3 deformation of the terrain.

Spatial dispositions and relative temporal sequence of the brittle structures as established from all these studies collectively point towards a brittle tectonic event that the schist belt has undergone during the protracted D_3 deformation of the terrain. Accordingly, a comprehensive model has been developed to elucidate the brittle tectonic evolution of the region during late stages of deformation and craton stabilization.

Chapter 1: Introduction

CONTENTS **Page No.**

CHAPTER 1

Introduction

1.1 General

Cratonic regions represent the long-lived, stable nuclei of continents that preserve the earliest geological records of the Earth's lithosphere. Their evolution is typically characterized by protracted histories of magmatism, metamorphism, deformation, and surface processes that span billions of years (Windley, 1973; Meert et al., 2010). The tectonic evolution of cratons is fundamentally governed by the style and intensity of lithospheric deformation. A key pursuit of structural geology is to reconstruct such tectonic events from the ductile and brittle structures that are preserved in rocks as a product of deformation. These structures provide critical evidence for modelling the processes that shaped the present-day configuration of lithospheric plates and how they respond to stress. Ductile deformation structures develop at deeper crustal levels and are particularly valuable for distinguishing and correlating different phases of deformation that occur under elevated pressure-temperature conditions (Ramsay, 1986; Passchier and Trouw, 2005). In contrast, brittle structures typically form during the later stages of deformation within the upper crustal domain and are often associated with the stabilization of cratonic blocks (Twiss and Moores, 1992; Pollard and Fletcher, 2005; Davis et al., 2011; Fossen, 2016).

Despite their mechanical stability in the present-day tectonic framework, cratons preserve records of intense polyphase deformation in their interiors and also feature abundant evidence of brittle deformation that reflects multiple tectonic, magmatic, and fluid-driven events throughout their prolonged geological histories (Ball, 1980; Begg et al., 1987; Torvela and Ehlers, 2010; Ma et al., 2020). Polyphase deformation of terrains, dominated by ductile processes, has been the subject of extensive research and is well documented (Mukhopadhyay, 1986; Burg, 1999; Fossen et al., 2019; Warren and Hansen, 2023). The study of brittle deformation, that subsequently overprints the earlier ductile phase, is critical for reconstructing the stress regimes in cratonic blocks, their tectonic reactivations, and shallow crustal processes that have acted on these regions through time. Furthermore, such brittle structures often govern the localization of fluids, mineralization, and the emplacement of younger intrusives, thereby exerting direct control on the geodynamic evolution and economic potential of the cratons (Sibson, 1996; Brown and Bruhn, 1998; Lonergan, 1999).

Brittle deformation manifests in rocks in diverse ways, from discrete fractures and faults to their systematically developed regional scale interactions producing intense networks. These structures reflect the dynamic interplay between regional stress fields, pre-existing anisotropies, and evolving rheological conditions of the lithosphere (Pollard and Aydin, 1988; Caputo, 2005, Mandl, 2013). The recognition, analysis, and interpretation of such structures enable the reconstruction of paleostress fields, assessment of strain localization, and deciphering the temporal sequence of deformation events. In a cratonic context, where ductile deformation fabrics are commonly overprinted by late brittle features, the systematic study of brittle structures becomes an indispensable tool to unravel the tectonic rejuvenation history of the terrain. Consequently, investigating the origin and propagation of brittle structures such as fractures and faults through progressive deformation is fundamental for deciphering the brittle tectonic evolution of any region.

The Archean cratonic nuclei of the Indian subcontinent provide an excellent natural laboratory for such investigations, as they have undergone a protracted history of cratonization and multiple episodes of tectonic reactivation (Chadwick et al., 1981; Rogers, 1986; Jayananda et al., 2006). In contrast to the extensively studied polyphase ductile deformation of these cratons (Chadwick et al., 1978; Mukhopadhyay, 2001; Matin et al., 2012), the later brittle overprint has received comparatively limited attention in the Indian geological context (Srivastava and Pradhan, 1995; Mondal et al., 2020).

Cratons frequently host mineral deposits of significant economic importance (Condie, 1981; Naqvi and Rogers, 1987; Ramakrishnan and Vaidyanadhan, 2010). Notably, the greenstone sequences of the Archean Dharwar Craton, one of the largest cratonic blocks in peninsular India, are well-known for their gold and associated mineralization (Narayanaswami et al., 1960; Kolb et al., 2005; Sarma et al., 2008). Brittle structures exert a fundamental control on hydrothermal fluid migration and the localization of mineralization, thereby playing a key role in the formation of economically important deposits such as gold, base metals, and associated commodities. Their geometry, connectivity, and spatial association with major shear zones and pluton margins make them critical exploration targets for expanding the resource potential of the craton.

The present study area is located in the central part of the Chitradurga Schist Belt (CSB), adjoining the Chitradurga region, in the Western Dharwar Craton (WDC) of southern India. The CSB is an Archean granite-greenstone belt comprising distinctive volcano-sedimentary assemblages, metamorphosed from lower greenschist to amphibolite facies, which have been subsequently intruded by ~ 2.61 Ga younger granites. (Naqvi and Rogers, 1987; Ramakrishnan and Vaidyanadhan, 2010).

Previous investigations conducted with regard to the brittle deformation of the CSB, reveals the presence of abundant fractures, faults and veins of diverse orientations in the younger granites and metavolcanic rocks of the schist belt (Mondal and Mamtani, 2013; 2014; 2016; Mondal and Acharyya, 2018). These studies have primarily emphasized on fabric analysis and paleostress determination in the younger granites (Mondal, 2018; Mondal et al., 2020), while the same, along with vein emplacement mechanisms have been examined in the metavolcanic rocks of the region by Bhowmick and Mondal (2020; 2021). However, the episodicity of fluid ingression resulting in vein formation, the nature and emplacement mechanisms of igneous intrusions, the pervasive development of fracture networks, and the broader spectrum of brittle structures, together with their spatial and temporal development across the lithologies of the area remain insufficiently investigated, constituting a critical research lacuna in this context.

The present research focuses on the systematic study of these respective suites of brittle structures developed within various lithologies of the CSB, WDC, in and around the Chitradurga region, with the overarching aim of reconstructing the brittle tectonic evolution of the terrain. Integrating field based observations with analytical methods, the study seeks to unravel their genesis, connectivity, and spatio-temporal evolution within the regional tectonic framework of the CSB, WDC, India. Through this multi-pronged approach, the thesis seeks to address key questions regarding the brittle evolution of the studied cratonic block: How did fracture systems initiate and evolve through successive tectonic episodes? What role did fluids and magmas play in the development of brittle structures? How are the spatial patterns of brittle deformation linked to the larger-scale tectonic architecture of the craton? And ultimately, what does the brittle structural record reveal about the tectonic rejuvenation and long-term stabilization of cratonic blocks?

1.2 Objectives

The primary research objectives of the present thesis are briefly outlined as follows:

1. To systematically identify and document individual brittle deformation structures developed within the rocks of the study area.

2. To understand the genesis and evolution of respective suites of brittle structures observed in the study area within the context of the regional tectonic framework.

3. To characterize fracture networks in terms of their geometry, kinematics and connectivity and understand its implications for fluid flow and permeability.

4. To investigate the spatial interrelations and relative temporal evolution of brittle structures, in order to develop a comprehensive brittle tectonic evolution model of the study area.

1.3 Approach and scope of study

Among the wide array of brittle structures observed in the rocks of the study area, three suites of structures dominate the brittle geological record of the studied region: veins, dykes, and fracture networks developed through mutually interacting faults. These three categories of brittle structures, though distinct in origin and morphology, share a close genetic relationship through their dependence on fracture development, fluid activity, and stress reorganization in the crust. Their analysis, both individually and in concert, provides a powerful means of understanding the brittle tectonics of the craton.

Veins represent the precipitation of mineral matter from fluids that migrate through open fractures. They are indicators of fluid activity within the crust and mark transient episodes of fracture opening driven by changes in stress and fluid pressure conditions. The geometry, orientation, and cross-cutting relationships of veins encode information on the kinematics of brittle deformation, the directions of principal stresses, and the episodicity of fluid migration. The systematic analysis of vein systems thus offers insights into fracture-controlled fluid flow and the temporal evolution of paleostress fields (Ramsay, 1980; Cox, 1987; Sibson, 1992; Bons et al., 2012; Otsubo et al., 2016). Dykes, in contrast, record the interplay of crustal stresses and magmatic processes, facilitating the transfer of magma from deep to shallow levels of the crust. Their emplacement is intimately linked to regional stress regimes and the availability of magma at depth. Dykes preserve valuable information about extensional or transtensional tectonic episodes in relation to the state of stress during magmatic activity within a terrain (Delaney and Pollard, 1981; Delaney et al., 1986; Pollard, 1987; Burchardt, 2018; Gudmundsson, 2020; Pollard and Martel, 2020).

Fracture networks formed through mutually interacting faults, unlike isolated fractures, capture the connectivity, topology, and spatial organization of fracture systems at multiple scales. They reflect the cumulative effects of repeated fracturing, reactivation of faults, and linkage of fracture segments under evolving stress regimes. The analysis of fracture network geometry and connectivity, as deciphered from the topology of fracture intersections, along with scaling of fracture lengths, offers a robust approach to assess the mechanical state of the crust and its brittle tectonic evolution through time (Dershowitz and Einstein, 1988; Bonnet et al., 2001; Berkowitz, 2002; Sanderson and Nixon, 2015; Peacock and Sanderson, 2018; Forstner and Laubach, 2022).

The spatio-temporal evolution of these brittle features holds the key to deciphering the brittle tectonic development of the studied cratonic block. Field cross-cutting relationships between veins, dykes, and fractures allow the establishment of relative chronological frameworks, while isotopic or geochronological constraints on dykes or mineralized veins can provide absolute age markers. The regional distribution of these structures, when placed in a spatial context, reveals domains of strain localization, directions of stress propagation, as well as possible influence and interaction of lithospheric processes with inherent rock properties.

In addition to their tectonic significance, these brittle structures have important implications for crustal fluid pathways and mineralization. Veins mark the pathways of fluid migration and the sites of mineral precipitation, often hosting ore bodies of economic value. Fracture networks govern the permeability structure of the crust, dictating fluid flow regimes and the efficiency of fluid-rock interaction. Dykes, in turn, create effective pathways for magma transport to the crust thereby influencing the thermal regime and stress distribution of the crust. The interplay between these brittle structures therefore extends beyond tectonics to encompass tectono-magmatic and hydrothermal processes integral to craton evolution and stabilization.

This study is significant not only for reconstructing the brittle tectonic history of the studied terrain but also for contributing to the broader understanding of craton dynamics. By examining veins, dykes, and fracture networks as interconnected suites of brittle structures, the research underscores the importance of an integrated structural approach to brittle deformation. The findings are expected to provide insights into the processes governing the stabilization of cratonic blocks through brittle tectonic evolution during the late stages of deformation, as well as the interplay of stress, fluid activity, magmatism and rock rheology in shaping the upper crustal architecture.

1.4 Methodology

The present study employs a combined approach integrating detailed field observations with quantitative analytical techniques to investigate veins, dykes, and fracture networks within the study area. For veins, the methodology involves quantifying fluid pressure variations using heterogeneous vein data distributions, supported by statistical analyses of field-collected measurements. For dykes, in addition to the study of outcrop attributes for elucidating their emplacement mechanisms, novel mathematical methods involving field data, have been developed to estimate complete dyke dimensions from partial exposures, enabling the determination of well-constrained magmatic overpressure and depths of origin. For fracture networks, individual elements, such as faults, have been investigated through direct field observations and measurements of their morphology, attitude, apertures, and orientations. The networks as a whole have been analyzed using geometrical, topological, and fractal methods applied to 2D digitized outcrop photographs, providing insights into network connectivity and overall structural organization. The integrated methodology adopted in the present work ensures a comprehensive understanding of the genesis, geometry, and evolution of brittle structures in the context of the regional tectonic framework of the CSB. Following are details of the methods used in this study:

Fieldwork:

i. Study of outcrop lithologies and collection of structural data from different lithologies (younger granites, metavolcanic and metasedimentary rocks) of the study area. Both planar (foliation/fractures/faults/veins/dykes) and linear structural data (pitch/plunge of slickenside lineations) have been collected along with dimensional data (length/width etc.) from dyke and vein outcrops.

ii. Detailed mapping of targeted outcrops has been undertaken so as to understand the kinematics of the structures with respect to the regional tectonics and their mutual field cross-cutting relations.

iii. Scaled and oriented photographic recording of planar outcrop surfaces has been undertaken for different lithologies to capture the networking attributes of fractures within them as a whole.

iv. Collection of oriented block samples for preparation of petrographic thin sections and other laboratory investigations.

Laboratory studies:

i. Analysis of heterogeneous vein data distribution patterns through Bingham distribution using GArcmB, a MATLAB based code developed by Yamaji (2016) and scaled 3D Mohr circle analysis (Jolly and Sanderson, 1997), using FracTend code, developed by Healy (2017) for fluid pressure estimation.

ii. Developing novel methodologies for estimating complete dyke dimensions from partial exposures using mathematical and statistical approaches to calculate magma overpressure and depth estimates.

iii. Orthorectification and stitching of outcrop images to generate complete 2D outcrop orthomosaics using Agisoft Metashape Pro.

iv. Digitization of fracture traces from 2D outcrop photographs and orthomosaics using CorelDraw.

v. Characterization of fracture network attributes (geometry, topology, and abundance) using FracPaQ (version 2.8), a MATLAB based code developed by Healy et al. (2017) for the quantitative analysis of fracture networks.

vi. Study of fractal attributes of fracture networks through 2D box counting program in MATLAB (Moisy, 2008) and the software Benoit 1.3 (Steffens, 1999).

vii. Study of petrographic thin sections for mineralogical, textural and microstructural attributes of rocks.

1.5 Layout of the thesis

The present chapter introduces the research problem, outlines the objectives and scope of the study, and highlights its overall significance while providing the rationale behind the chosen approach. The structure of the thesis is further organized into six subsequent chapters, each addressing a specific aspect of the study. A brief overview of the chapters is provided below. Each chapter begins with a detailed outline of its contents, and all figures and tables referenced within the text are compiled sequentially at the end of the respective chapter.

Chapter 2. Regional geology and previous works

The geological background of the study area is presented here, with emphasis on the stratigraphy and tectonic framework of the Dharwar Craton. The chapter also summarizes previous structural studies that provide the context for the present work.

Chapter 3. Structural investigation

This chapter documents the field observations of brittle structures recorded across the various lithologies of the study area and the three principal suites of brittle structures: veins, dykes, and fracture networks are introduced here.

Chapter 4. Veins

The fourth chapter focuses on the characterization of quartz vein systems. It discusses their geometry, distribution, and structural attributes, and quantifies the number and magnitude of fluid pressure pulses that resulted in their formation in relation to the tectonic framework of the region.

Chapter 5. Dykes

This chapter develops novel methodologies to estimate complete dyke dimensions from partial exposures and applies them to infer magma overpressure and depths of origin. It also presents the structural analysis of dykes, examining their outcrop attributes and emplacement mechanisms in relation to regional stress regimes.

Chapter 6. Fracture networks

The sixth chapter provides a quantitative assessment of fracture networks, focusing on their geometry and topological attributes. It further interprets network connectivity, scaling relationships, and the structural controls that influenced their development.

Chapter 7. Discussion and Conclusions

The final chapter synthesizes the results of respective analyses into a comprehensive spatio-temporal model of brittle tectonic evolution in the study area, summarizes the key findings and implications, and concludes by outlining directions for future research.

Chapter 2: Regional geology and previous works

CONTENTS **Page No.**

CHAPTER 2

Regional geology and previous works

2.1 Introduction

The Chitradurga Schist Belt (CSB), located in the Western Dharwar Craton (WDC) of the southern Indian shield, constitutes one of the most significant Archean granite-greenstone terrains of the region. It is distinguished not only for its well-preserved record of Archean tectono-thermal evolution but also for its association with auriferous quartz veins that have long been recognized as prospective zones for gold mineralization. Lithologically, the CSB is composed of volcano-sedimentary assemblages of the Archean age, which rest upon and are spatially associated with the surrounding Tonalite-Trondhjemite-Granodiorite (TTG) gneisses. These TTGs represent some of the oldest fragments of preserved continental crust, thereby underscoring the geological importance of the region. Structurally, the schist belt preserves a complex array of deformation features that encompass both ductile and brittle regimes, reflecting a long-lived and polyphase tectonic history. Previous studies, however, have primarily concentrated on the ductile deformation patterns, utilizing them as the main framework for reconstructing the tectonic evolution of the craton. These efforts have been complemented by a substantial body of geochemical, petrological, and geochronological investigations, which collectively provide valuable insights into the magmatic and metamorphic history of the WDC. Despite this extensive body of work, the brittle deformation features of the CSB with regard to their genesis, characterization, kinematic relations, temporal evolution, and their collective contribution to the progressive modification of cratonic architecture, remain relatively underexplored. This lack in the systematic structural study of the region represents a critical gap in understanding, given that brittle structures often develop during the later stages of crustal stabilization and may exert a profound influence on fluid migration, mineralization processes, and the reactivation of pre-existing structural fabrics. The present study seeks to address this gap by documenting and analyzing the brittle deformation structures preserved across different lithological units of the CSB, which broadly includes the older metavolcanic and metasedimentary successions and the younger intrusive granitic plutons. By integrating field observations with structural analysis, the study aims to reconstruct the deformation history of the terrain associated with brittle tectonic processes and to evaluate their implications for the broader tectonic evolution of the Dharwar Craton.

2.2 Regional geology of the Dharwar craton

The Indian shield is composed of Precambrian cratons and Proterozoic mobile belts. It includes five major cratonic blocks; the Dharwar, Bastar, Singhbhum, Bundelkhand, and Aravalli cratons, and three prominent mobile belts, namely the Eastern Ghats, Pandyan, and Satpura belts **(Fig. 2.1)** (Ramakrishnan and Vaidyanadhan, 2010). The present study area constitutes a part of the Dharwar craton, one of the most extensively studied Archean provinces of the Indian shield. Together with the Southern Granulite Terrain (SGT), the Dharwar craton constitutes the two principal geological units of the southern Indian shield. These two are separated by the Palghat-Cauvery Shear Zone (PCSZ) (Naqvi and Rogers, 1987; Chakrabarti et al., 2006). Geographically, the

Dharwar craton is bounded in the north by the end-Cretaceous Deccan Traps and their underlying Proterozoic basins (Bhima and Kaladgi basins), in the north-east by the Godavari graben, in the east by the Neoproterozoic Eastern Ghats Mobile Belt (EGMB) and the Cuddapah basin (~ 1600 Ma), and in the west by the Arabian Sea (Ramakrishnan and Vaidyanadhan, 2010). The Dharwar craton preserves some of the most eminent evidences of Precambrian tectonics in peninsular India. It is subdivided into two tectonic blocks, originally termed the eastern and western blocks and later formalized as the Eastern Dharwar Craton (EDC) and the Western Dharwar Craton (WDC) (Rogers, 1986; **Fig. 2.2**). These blocks are thought to have amalgamated between ~ 2750 to 2510 Ma, forming a major zone of accretion. This suture is marked by a region of intense deformation, variously referred to as the Chitradurga Shear Zone (CSZ) or, alternatively, as an easterly dipping thrust fault, called the Chitradurga Boundary fault (Chadwick et al., 1999, 2000, 2003; Meert et al., 2010). According to Ramakrishnan and Vaidyanadhan (2010), the Closepet Granite, located east of the CSZ, defines the western margin of the EDC and has been interpreted as a ‘geo-suture’ along which the WDC and EDC were amalgamated. It has also been considered a ‘stitching pluton’ emplaced during the suturing of the two blocks (Meert et al., 2010; Meert and Pandit, 2015). However, this interpretation remains debated, as the boundary between the WDC and EDC appears to be transitional within the zone between the CSZ and the Closepet Granite. The general comprehensive stratigraphic framework of both the WDC and EDC is presented in **Table 2.1**.

The Dharwar craton broadly comprises of three major components: (i) Archean tonalite-trondhjemite-granodiorite (TTG) gneisses, collectively referred to as the Peninsular Gneissic Complex (PGC); (ii) two generations of Archean greenstone belts (also referred to as schist belts), represented by the Sargur Group, constituting the older supracrustals; and the Dharwar Supergroup, which collectively represents the younger supracrustals; and (iii) late Archean younger granitoids, with or without mantle affinity (Chakrabarti et al., 2006). These lithological units are discussed in detail in the subsequent sections. Geophysical investigations reveal that the WDC is characterized by a greater crustal thickness of ~ 42-51 km, in contrast to the thinner ~ 34-39 km crust of the EDC (Gupta et al., 2003; Mishra, 2011). The greenstone belts of the WDC are typically wider, and preserve older supracrustal successions. In contrast, the EDC is characterized by narrower, more linear greenstone sequences and schist belts that are largely confined to its western part and exhibit a younging trend from west to east. Consistent with the characteristics of other Archaean cratons worldwide, the Dharwar Craton (both WDC and EDC) is also intruded by extensive mafic dyke swarms in the uppermost stratigraphic levels, exhibiting multiple orientations, of which the broadly NNW-ESE trend dominate the WDC, while the ENE-WSW orientations are more prominent in the EDC. These dykes, predominantly doleritic in composition, intrude the younger granitoids across both terranes. Their overall distribution is interpreted as the product of thermal warping of the Archaean crust along a broadly E-W axis, with E-W trending dykes emplaced along the apical portions of domes and additional dyke sets intruding NE-SW and NW-SE conjugate fractures (Chakrabarti et al., 2006). Proterozoic mafic dykes of the Dharwar Craton record at least five distinct magmatic events: ~ 2.4 Ga, ~ 2.1 Ga, ~ 1.6 ± 0.3 Ga, ~ 1.0 ± 0.2 Ga, and ~ 0.7-0.6 Ga (Sarkar & Mallik, 1995), underscoring the long-lived and episodic nature of dyke magmatism associated with lithospheric extension and mantle plume activity in the region.

More recent studies have focused on the younger intrusives of the EDC, such as the Koppal syenite, to establish their emplacement history, evaluate their temporal relationship with the younger granites of the WDC, and constrain the relative timing of fabric development (Bhatt et al., 2017). Furthermore, pegmatite dykes cutting the Koppal pluton have been analyzed to reconstruct the stress regime active during pegmatite dyke emplacement (Bhatt et al., 2019). A comparative summary of the major differences between the WDC and EDC is provided in **Table. 2.2**.

Swami Nath and Ramakrishnan (1981) subdivided the Dharwar ‘System’ of the WDC into two distinct orogenic cycles: the older Sargur Group (~ 3300-3100 Ma) and the younger Dharwar Supergroup (~ 2800-2600 Ma). These successions are separated by deformed angular unconformities, but were subsequently folded into parallelism during the younger Dharwar orogeny. The Sargur rocks are extensively veined by granitic intrusions, whereas the adjoining Dharwar successions remain comparatively less affected, displaying relatively limited intrusive evidences. The Peninsular Gneiss forms the basement to the Dharwar Supergroup, and the contact is marked by a pronounced regional unconformity that reflects prolonged denudation following the cessation of the Sargur orogeny (Ramakrishnan et al., 1976). This unconformity is characterized by quartz-pebble conglomerates (QPC), which are locally uraniferous and contain minor occurrences of copper and gold mineralization. A concise account of these stratigraphic groups is provided below and the stratigraphic framework of the WDC is summarized in **Table 2.3**.

Gorur Gneiss

The Gorur Gneiss is considered the oldest trondhjemitic gneiss within the WDC and is commonly associated with tonalitic variants. Geochronological constraints based on Rb-Sr and Pb-Pb isochrons place its age between ~ 3500 and 3300 Ma. Petrologically, it is often described as a migmatitic TTG assemblage composed of oligoclase, microcline, quartz, biotite, and hornblende, and is further characterized as a silica-rich, low-alumina trondhjemite displaying a negative Eu anomaly (Rao et al., 1991;

Ramakrishnan and Vaidyanadhan, 2010). However, the Gorur Gneiss has not been delineated as a distinct mappable unit within the Peninsular Gneissic Complex, and consequently, its stratigraphic relationship with the Sargur Group remains uncertain.

Sargur Group

The Sargur Group, manifested either as linear mafic-ultramafic belts or as enclaves within the gneissic terrain, forms an integral component of the WDC and is thought to have developed through various geodynamic processes. Geochemical signatures suggest a calc-alkaline source for these rocks (Naqvi, 1981; Srikantia and Bose, 1985; Srikantia and Venkataramana, 1989; Srikantia and Rao, 1990; Venkatadasu et al., 1991; Paranthaman, 2005). The tectonic setting of the Sargur supracrustals has been interpreted variably. Their basal quartz-pelite-carbonate association has been linked to a continental margin environment, while the ultramafic-mafic-BIF association has been considered indicative of an oceanic setting. Meert et al. (2010) proposed that the Sargur sequence formed from partial melting of subducted oceanic slab material, thereby relating it to a subduction environment. In contrast, Jayananda et al. (2008) suggested that the sequence may have originated in plume-related events or as part of an oceanic plateau, which subsequently facilitated subduction-related processes. Geochronological constraints place the Sargur Group in the range of ~ 3100-3300 Ma. Detrital zircons yield Pb-Pb evaporation ages of ca. 3300 Ma, while SHRIMP U-Pb analyses suggest an age between ~ 3100 and 3300 Ma. Isotopic studies provide further support, with Sm-Nd model ages broadly consistent with Rb-Sr determinations of ~ 3100 Ma obtained from anorthosite (Ramakrishnan and Vaidyanadhan, 2010).

Peninsular Gneiss

Polyphase migmatites and granitoids are widespread within the Peninsular Gneisses of the WDC, reflecting a long and complex history of crustal growth. The region records three major crustal accretionary events: ca. 3300-3400 Ma, 3000-3200 Ma, and 2500-2600 Ma. Of these, the second event (3000-3200 Ma) was the most extensive and widespread, while the first and third events were relatively localized and sporadic in nature (Ramakrishnan and Vaidyanadhan, 2010). Whole-rock Rb-Sr dating indicates Archean gneiss formation around 3300-3400 Ma, and geochemical evidence suggests derivation from a Rb-depleted mantle source (Beckinsale et al., 1980). Syn-kinematic migmatization during at least three successive deformation phases affecting the Dharwar supracrustals transformed the Peninsular Gneisses into complex composite assemblages (Naha et al., 1991, 1993, 1995). These gneisses often preserve relicts of sedimentary precursors (Uday Raj and Naqvi, 1995), including subrounded quartz fragments. Petrologically, they have been classified into four main types: (i) quartz-orthoclase-microcline-plagioclase-biotite-chlorite gneiss; (ii) quartz-orthoclase-microcline-hornblende-epidote-calcite gneiss; (iii) quartz-orthoclase-microcline-epidote gneiss; and (iv) quartz-plagioclase-orthoclase-microcline-hornblende-actinolite gneiss (Chakrabarti et al., 2006). An alternative classification by Naqvi and Rogers (1983) groups them into (i) quartzo-feldspathic gneisses, (ii) banded migmatitic gneisses, (iii) paragneisses, and (iv) trondhjemite-granodiorite-granite (TTG) plutons. The TTG gneisses often occur as inliers within supracrustal belts and display concordant foliation at their contact zones with schist belt sequences. Geochemical investigations reveal a calc-alkaline differentiation trend in the migmatites, consistent with their origin through partial melting of a mafic source in the deep crust around 3000 Ma, accompanied by re-melting of older pre-existing crust.

Dharwar Supergroup

The Dharwar province is primarily a granite-greenstone terrain, characterized by NW-SE to NNW-SSE trending schistose belts. These schistose rocks represent the supracrustal sequences of the Dharwar Supergroup (~ 3000-2600 Ma). The Supergroup is stratigraphically subdivided into the lower Bababudan Group and the upper Chitradurga Group **(Table 2.4)**. Regionally, these successions are exposed in two major schist belts, commonly referred to as ‘superbelts’: (i) the Bababudan-Western Ghats-Shimoga belt, and (ii) the Chitradurga-Gadag belt (Ramakrishnan and Vaidyanadhan, 2010), with the present study primarily concerning the latter.

(i) Bababudan-Western Ghats-Shimoga Superbelt

The Bababudan Schist Belt extends over an area of nearly 30,000 sq. km, with the intervening regions largely occupied by the Peninsular Gneiss basement. The base of the Bababudan Group is distinguished by a thin but prominent horizon of quartz-pebble conglomerate, known as the Kartikere Conglomerate, which marks a distinct unconformity between the underlying TTG gneisses and the overlying Dharwar Supergroup. Stratigraphically, the Bababudan Group records three successive cycles of amygdaloidal metabasalts interbedded with cross-stratified quartzites, and each cycle is capped by a prominent Banded Iron Formation (BIF). The metabasalts are characterized as low-K tholeiites, displaying flat HREE patterns and moderate LREE enrichment, features that point to a mantle source enriched in lithophile elements. Geochronological constraints from Rb-Sr whole-rock and Sm-Nd isochrons indicate emplacement ages of ~ 2700-2800 Ma (Ramakrishnan and Vaidyanadhan, 2010). The stratigraphy of the Bababudan Group begins with the Kartikere Conglomerate (QPC) at its base, followed by the overlying Kalasapura, Allampur, Santaveri, and Mulaingiri Formations (Ramakrishnan and Vaidyanadhan, 2010).

The Bababudan Group begins with the Kartikere conglomerate, a discontinuous basal unit composed of subrounded to sub-angular pebbles of vein quartz and rare fuchsite quartzite derived from the underlying Sargur Group. The conglomerate, which is largely clast-supported with an arenaceous matrix containing detrital ilmenite, pyrite, and other sulphides, gradually grades upward into cross-bedded quartzite. Above this, the Kalaspura Formation is dominated by amygdaloidal metabasalts, with amygdules typically filled by quartz and chlorite. While some flows are massive, others are schistose and contain actinolite, epidote, plagioclase, carbonates, and opaque minerals. The overlying Allampur Formation is chiefly composed of metabasalts interlayered with thin units of phyllite, quartzite, and BIF. The arenaceous intercalations within this unit display a variety of soft-sediment deformation structures, including load casts, mud balls, dish and pillar structures, slump folds, and convolute bedding. Its basal member, the Lakya quartzite, is pebbly in nature and preserves herringbone and trough cross-bedding. Stratigraphically higher, the Santaveri Formation consists largely of metabasalts, interspersed with sills of gabbro, serpentinite, and ultramafic schists. These metabasalts are predominantly amygdaloidal but locally exhibit pillow structures and volcanic breccias, testifying to their volcanic origin. The succession culminates with the Mulaingiri Formation, which is initiated by chloritic phyllites that locally include graphitic varieties and are interbedded with quartzites and siltstones. A defining lithology of this formation is the Algoma-type BIF, which ranges from oxide to silicate facies and forms prominent horizons within the stratigraphy (Ramakrishnan and Vaidyanadhan, 2010). Structurally, the Bababudan Schist Belt is characterized by upright folds with curved hinges, with the westward-curving Bababudan syncline forming the dominant structure. Later N-S trending fabrics are superimposed on these earlier E-W oriented structures. Regionally, similar stratigraphic features of the Bababudan Group are recognized within the Western Ghats Belt, while the Shimoga Schist Belt, separated from both by intervening TTG gneisses, records comparable lithological and structural patterns. At the contacts between schists and gneisses, high-grade metamorphic assemblages such as garnet-bearing amphibolites are developed, and low-grade partial melting has produced quartzo-feldspathic veins along basement contacts. Younger intrusive granitoids occur in the northern Shimoga Schist Belt, where small schist enclaves are cusped between domal gneissic bodies, providing a structural linkage to the Chitradurga Schist Belt (Chadwick et al., 2007). The Dharwar schists also record southwest-verging folds and north-dipping reverse faults, consistent with the interpretation of sinistral transpression within an oblique-slip mobile zone as the primary mechanism in the structural development of the belt (Chadwick, 1994).

(ii) Chitradurga-Gadag Superbelt

The Chitradurga-Gadag Superbelt, also referred to commonly as the Chitradurga Schist Belt (CSB), is a linear, NNW-SSE trending belt, nearly 40 km wide at its center (Chitradurga region) and covering an area of about 6000 sq. km **(Fig. 2.3)**. It is composed of a thick volcano-sedimentary sequence representing a complete cratonic succession. Dominant lithologies include metabasalt and metagreywacke-argillite sequences, which are interspersed with bands of quartzite, polymictic conglomerate, and BIF (Sengupta and Roy, 2012). The contacts between the Chitradurga-Gadag superbelts and the older schist belts are frequently marked by conglomerates, often associated with quartz-sericite-chlorite schists.

Stratigraphically, the Chitradurga Group is broadly divided into the lower Vanivilas Subgroup and the upper Ranibennur Subgroup, with the latter conformably overlying the former. However, Seshadri et al. (1981) proposed a more detailed classification into three major formations. The Vanivilas Formation, which directly overlies the gneissic complex and the Bababudan Group, is composed of the Talya conglomerate, along with chloritic schist, quartzite, limestone, dolomite, Mn-Fe formations, and phyllite. This unit is succeeded by the Ingaldhal Formation, comprising a varied assemblage of basic to acidic lavas, pyroclastics, cherts, and fine-grained clastics. The overlying Hiriyur Formation is distinguished from the Ingaldhal Formation by the persistent K.M. Kere conglomerate at its base and is mainly constituted of greywacke sequences interbedded with chert, metavolcanics, and polymictic conglomerates (notably the Hiriyur conglomerate). The metavolcanic rocks of the Chitradurga Schist Belt are particularly notable for their well-preserved pillow structures, along with occurrences of agglomeratic and variolitic textures, which provide strong evidence of their volcanic origin.

Structurally, the belt is characterized by polyphase deformation with anticlinal cores flanked by synclinal closures on either side, especially well developed and documented in the Chitradurga region (Mukhopadhyay et al., 1981; Mukhopadhyay and Ghosh, 1983; Mukhopadhyay and Baral, 1985). The broad central antiform, interpreted as a second-generation (F_2) fold in this region, has refolded an earlier canoe-shaped syncline. As a result, the axial traces of the first-generation syncline now appear duplicated on either flank of the central antiform. Along the axial region of this F_2 antiform, the development of plunge culminations and depressions has been documented, reflecting variations in fold plunge along strike. In the southern sector of the belt, a major tectonic slide truncates the lower limb of the earlier syncline, indicating a phase of tectonic dislocation predating the F_2 folding event. Collectively, these structural relationships underscore a complex deformational history in which early stratigraphic architecture was substantially modified by superposed folding and localized tectonic slides, producing the present composite fold geometry of the Chitradurga-Gadag Schist Belt. The emplacement of younger granites along the outer margins of the belt, where they occur as steep sheets or wedge-like bodies, has been linked to southward overturning of folds and strike-slip displacements parallel to the orogenic trend. This tectonic activity not only controlled granite emplacement but also contributed to significant crustal thickening (Chadwick et al., 1989, 2007).

2.3 Tectonic evolution of the Dharwar craton

As evident from the preceding descriptions, the Dharwar Craton represents a major segment of the Indian shield that preserves a long and complex history of Archean crustal growth and stabilization. Its tectonic evolution is marked by repeated cycles of basin formation, volcanism, sedimentation, magmatism, and deformation, with contrasting models proposed to explain the amalgamation of its eastern and western domains.

During the late Archean time (~ 2.9-2.7 Ga), the Dharwar terrain experienced crustal extension and sagging, associated with extensive and episodic basic volcanic eruptions, leading to the formation of sedimentary basins which were subsequently filled with marine platformal deposits and volcanogenic detritals. While some researchers interpret this stage as the development of back-arc basins, others suggest a shallow marine depositional environment.

The cratonization history of the Dharwar craton has been extensively researched and variably interpreted from different geochronological and structural studies. According to Balakrishnan et al. (1999) and Manikyamba et al. (2005), the Eastern Dharwar Craton (EDC) evolved as an accreted island arc, amalgamated with the older and more stable Western Dharwar Craton (WDC) through sinistral transpression. During this process, linear schist belts were formed and metamorphosed in a back-arc basin setting, while the Eastern Ghats Mobile Belt (EGMB) marked the terminal collisional boundary of this accretion.

Chadwick et al. (1996, 1999, 2000) proposed a comparable model, though centered on the concept of the ‘Dharwar Batholith’. In this framework, pre-existing island arcs and granitic plutons are considered to have amalgamated into a single landmass, called the ‘Dharwar batholith’. The Dharwar Batholith subsequently underwent oblique convergence with the WDC, generating sinistral transpressive shear systems along its margins. The associated greenstone belts are interpreted as products of intra-arc basins linked to the batholith. The timing of this collisional history is constrained between 2750 and 2510 Ma, with these models further suggesting that the Closepet Granite was later accreted onto the WDC.

In contrast, another school of thought invokes a vertical tectonic model. Jayananda et al. (2000) and Chardon et al. (2002) proposed that a mantle plume located beneath the EDC-WDC boundary induced partial melting of the depleted lithospheric mantle, resulting in voluminous juvenile magmatism in the EDC. Within this framework, the greenstone belts are viewed as products of inverse diapirism and vertical crustal recycling, while the Closepet Granite is interpreted as a batholith rather than an accreted arc pluton.

An integrative perspective was outlined by Naqvi and Rogers (1983), who described the six-stage crustal evolution of the Dharwar Craton:

Stage 1 (> 3.4 Ga): Development of isolated continental nuclei within a mafic crust, with deposition of the oldest supracrustals (Sargur Group) in shallow basins.

Stage 2 (~ 3.4-3.0 Ga): Emergence of greenstone belts in island-arc environments, accompanied by emplacement of early granitoids, though large continental masses were not yet stabilized.

Stage 3 (~ 3.0 Ga): Intrusion of tonalitic material disrupted older supracrustals and greenstone belts (Kolar type), while high-grade regional metamorphism promoted the formation of extensive stable granitic crust.

Stage 4 (~ 3.0-2.5 Ga): Rifting of this stable continental crust led to ensialic basin formation, filled with mafic volcanics, banded iron formations, felsic volcanics, and greywacke sediment deposits, leading to the classic Dharwar-type younger greenstone sequences.

Stage 5 (~ 2.7-2.6 Ga): Assembly of extensive continental masses, accompanied by regional thermal rejuvenation that triggered granulite-facies metamorphism and the development of charnockitic nuclei.

Stage 6 (~ 2.6-2.5 Ga): Intrusion of younger granites coupled with continued granulite transformation, overprinted by widespread low-grade metamorphism.

The final stages of cratonization were punctuated by late brittle deformation, which has been reported from the Chitradurga Schist Belt (CSB). This phase produced prominent fractures, joints, and faults across diverse lithologies, including granites, metabasalts, conglomerates, and greywackes, and facilitated the emplacement of quartz and aplite veins within brittle structures.

2.4 Geology of the study area

The present study area is located in the central portion of the Chitradurga Schist Belt (CSB), adjoining the Chitradurga region, which is part of the Western Dharwar Craton (WDC) in the South Indian Shield **(Figs. 2.4a and b)**. The NW-SE trending CSB in the eastern portion of the WDC is an Archean-aged granite-greenstone belt that comprises volcano-sedimentary assemblages metamorphosed up to greenschist to lower amphibolite facies, interbedded with ferruginous chert and banded iron formations, and polymict conglomerates. Surrounding this belt are older Peninsular Gneisses (Ramakrishnan and Vaidyanadhan, 2010), which serves as the basement for the overlying suites of metavolcanic and metasedimentary successions of the greenstone sequence, which has been later intruded by the younger granitoids. The metavolcanic rocks in the study area belong to the Ingaldhal Formation and are predominantly metabasaltic in composition, with localized occurrences of acid volcanics while the metasedimentary rocks belong to the Hiriyur Formation and are mainly comprised of meta-argillites and greywackes.

The Chitradurga granite and J. N. Kote Granite, situated along the western and eastern margins of the belt respectively, are prominent granitoid bodies near the Chitradurga town **(Fig. 2.4b)** and form part of the younger granite suite of the WDC in the study area. These younger granites within the greenstone belt are syn-tectonic with the D_2 deformation phase (Chakrabarti et al., 2006; Sarma et al., 2011; Mondal and Mamtani, 2014) of the CSB. Radiometric studies of the Chitradurga granite indicate crystallization at 2614 ± 10 Ma (SIMS U-Pb zircon dating; Jayananda et al., 2006), consistent with whole rock Pb-Pb isochrons that provide an age of 2605 ± 18 Ma (Jayananda et al., 2006; Taylor et al., 1984). Structural and geochronological studies from the region indicate that the D_1/D_2 deformation in the CSB occurred between 2614 and 2555 Ma, with D_3 beginning around 2537 Ma (Sarma et al., 2011; Mondal and Mamtani, 2014; Bhatt et al., 2017), which aligns with the protracted cratonization process (~ 100 Ma) of the Dharwar Craton, as suggested by Jayananda et al. (2006).

The Chitradurga granite is a NNW-SSE oriented tadpole shaped body with a broader and well exposed southern part and a comparatively constricted linear northern part. The adjacent J.N. Kote granite, which lies to the south east of the Chitradurga granite, is broadly ovoidal in its outline. Both the granites are massive in nature and, in most outcrops, lack well-developed foliation, though it displays microgranitoid enclaves in certain areas, indicating reworking of early crustal rocks (Jayananda et al., 2006). Geophysical gravity studies suggest that the Chitradurga granite extends NW-SE and that the granites persist to a depth range of approximately 6 km (Rama Rao et al., 2015). The granites are mostly coarse-grained, with the exception of the central portion of the Chitradurga granite, which is comparatively finer grained, and are equigranular, relatively homogeneous, with compositions ranging from granite to granodiorite, and biotite as the primary mafic mineral (Mondal, 2018). While the granites lack mesoscopic fabric, some areas, particularly in the northern region of the Chitradurga granite and at the granite margins, show well-developed foliation. This foliation, characterized by the preferred planar orientation of quartz and feldspar grains, strikes ~ NW-SE and dips steeply to the NE (mean strike/dip: 316°/63°), in alignment with the foliation recorded in the adjacent meta-sedimentary and meta-volcanic rocks and the regional trend of the CSZ. However, it should be noted that the transitions in texture and grain size within the granites are not sharp but rather gradational in nature. As the younger granites do not ubiquitously exhibit mesoscopic foliation, Anisotropy of Magnetic Susceptibility (AMS) studies have been conducted on them to quantify the internal magnetic fabric orientation. Although the mean magnetic fabric is oriented NW-SE (related to D_1/D_2), it gradually shifts towards NNW-SSE near the CSZ (Mondal, 2018). The disposition of the granite bodies indicates that the northern part of the Chitradurga granite and J. N. Kote granite are proximal to the Chitradurga Shear Zone (CSZ), possibly causing them to be dominated by simple shear ($W_k = 0.8$), while the southern portion of the Chitradurga granite, further from the CSZ, is primarily influenced by pure shear ($W_k = 0.06$), as deciphered from fabric and vorticity analyses of the younger granites by Mondal (2018).

Geochemical studies of the dolerite dykes from the Chitradurga region indicate that these are derived from a common magmatic source, with compositions grading from alkaline olivine basalt to quartz-normative tholeiite. Their elevated Co, Ni, and V contents suggest derivation from a relatively deeper source. Age constraints based on K-Ar dating show that dyke emplacement occurred episodically between ~ 1850 and 1000 Ma, with particularly intense activity during ~ 1400-1100 Ma, reflecting repeated pulses of deep-seated magma and periodic crustal dilation linked to plume-induced upwarping beneath the southern Indian shield (Chakrabarti et al., 2006).

Structurally, the region has undergone three phases of deformation: D_1/D_2 co-axial deformation, on account of a NE-SW directed compression, followed by D_3 deformation with NW-SE to WNW-ESE directed compression (Chadwick et al., 1989; Jayananda et al., 2006; Mondal and Mamtani, 2013; Mondal, 2018). D_1/D_2 deformation resulted in tight to isoclinal asymmetric folds with NW-SE striking axial planes (Chakrabarti et al., 2006; Mondal and Mamtani, 2013), and an overall NW-SE oriented axial planar foliation is present in the meta-volcanic and meta-sedimentary sequences (Bhowmick and Mondal, 2020). The early D_3 deformation (NW-SE compression) superimposed the D_1/D_2 structures, creating a dome-basin geometry in the meta-sedimentary layers (Chadwick et al., 1981; Mukhopadhyay et al., 1981; Chakrabarti et al., 2006; Mondal and Mamtani, 2014) **(Fig. 2.4c)**. Quartz vein orientations from the Gadag region in the northern part of the CSB support this NW-SE shortening direction for D_3 (Mondal and Mamtani, 2014). Late-stage deformation in the Chitradurga region, however, is thought to result from broadly E-W shortening (Jayananda et al., 2006). The late D_3 deformation, characterized by WNW-ESE to E-W compression, has resulted in the development of a sinistral shear zone, namely the Chitradurga Shear Zone (CSZ) along the eastern margin of the schist belt (Chadwik et al., 2000) and generated brittle structures along the greenstone belt at shallow crustal depths (Mondal et al., 2020).

Fracturing and faulting throughout the greenstone belt (CSB) have been associated with late stages of D_3 deformation, which produced brittle structures in both granites and metavolcanic rocks at shallow crustal depths (< 4 km) (Mondal et al., 2020; Bhowmick and Mondal, 2020; 2021). Despite variations in lithology, the consistent disposition of faults and fractures in the region are suggestive of their tectonic origin. Paleostress analysis conducted from fault-slip data in the greenstone belt indicates a trans-tensional to pure-strike slip regime (regime index, $R' = 1.25$) in the Chitradurga area (Bhowmick and Mondal, 2020), attributed to sinistral shearing along the greenstone belt related to ~ WNW-ESE directed D_3 compression. The development of oblique-slip faults within the younger granites and metavolcanic rocks of the region is attributed to ~ NNE-SSW extension during this compressional phase, reflecting late-stage craton stabilization and residual stress adjustment through shear partitioning along the craton margin (Mondal et al., 2020).

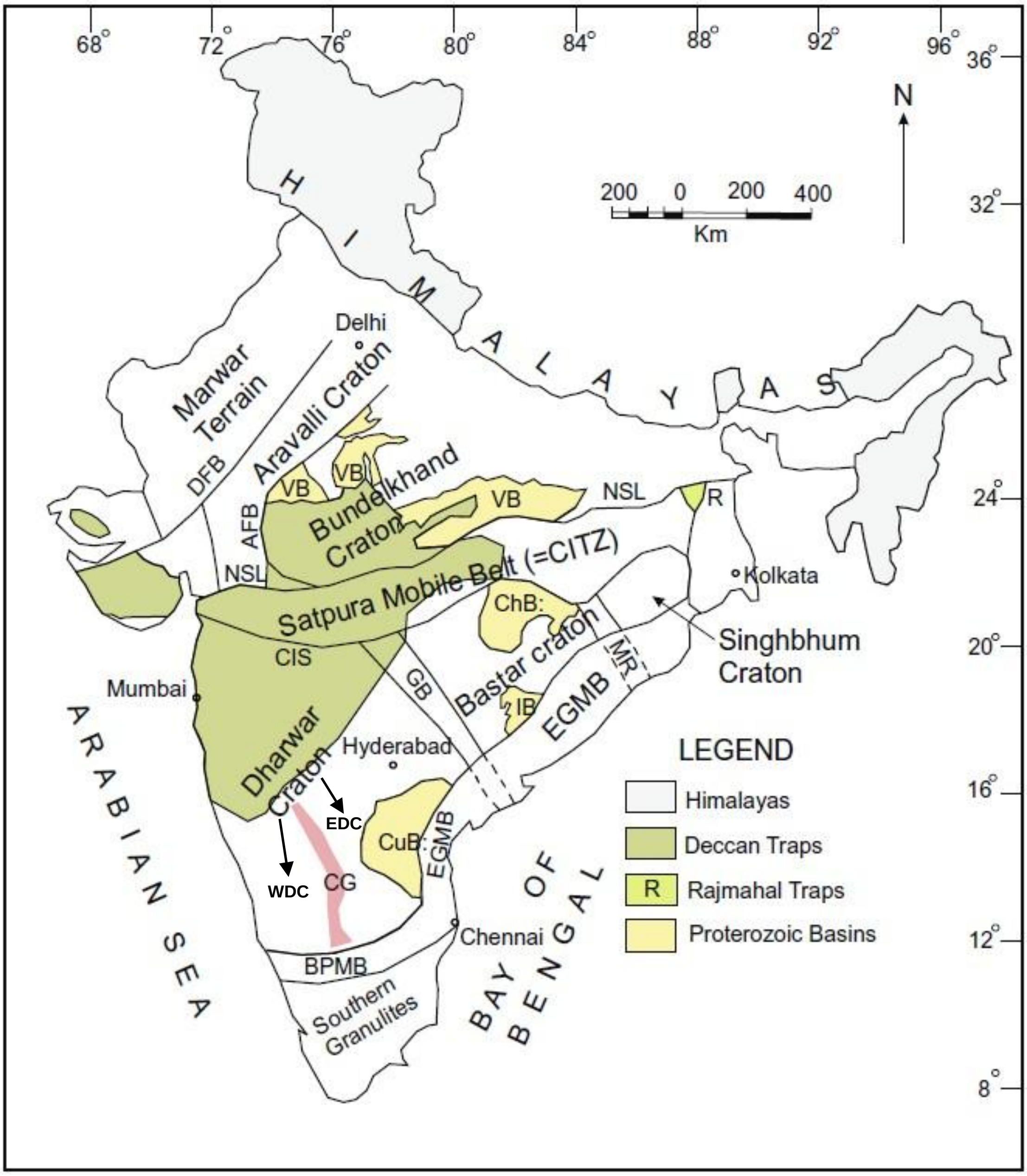

Fig. 2.1 Generalized tectonic map of the Indian subcontinent showing Precambrian cratons, mobile belts, and major lineaments. Abbreviations: AFB – Aravalli Fold Belt; DFB – Delhi Fold Belt; EGMB – Eastern Ghats Mobile Belt; SMB – Satpura Mobile Belt; NSL – Narmada-Son Lineament; CIS – Central Indian Suture; BPMP – Bhavani-Palghat Mobile Belt. Proterozoic rifts and basins: IB – Indravati Basin; ChB – Chhattisgarh Basin; GB – Godavari Basin; MR – Mahanadi Rift; CuB – Cuddapah Basin; VB – Vindhyan Basin. WDC – Western Dharwar Craton; EDC – Eastern Dharwar Craton; CG – Closepet Granite (after Meert et al., 2010).

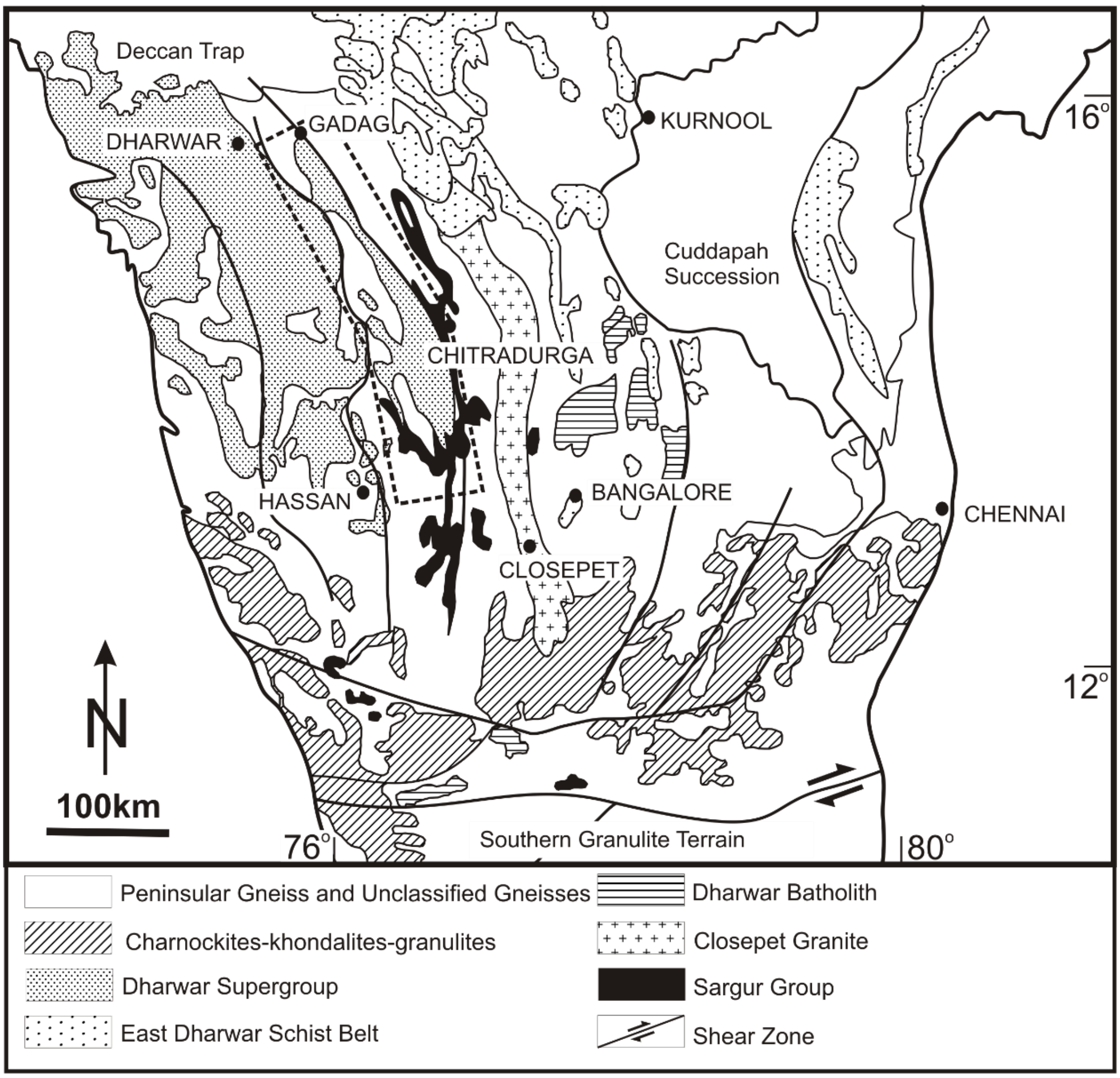

Fig. 2.2 Regional geological map of Dharwar craton (after Valdiya, 2010). Dashed box marks the Chitradurga-Gadag Schist Belt enlarged in Fig.2.3b.

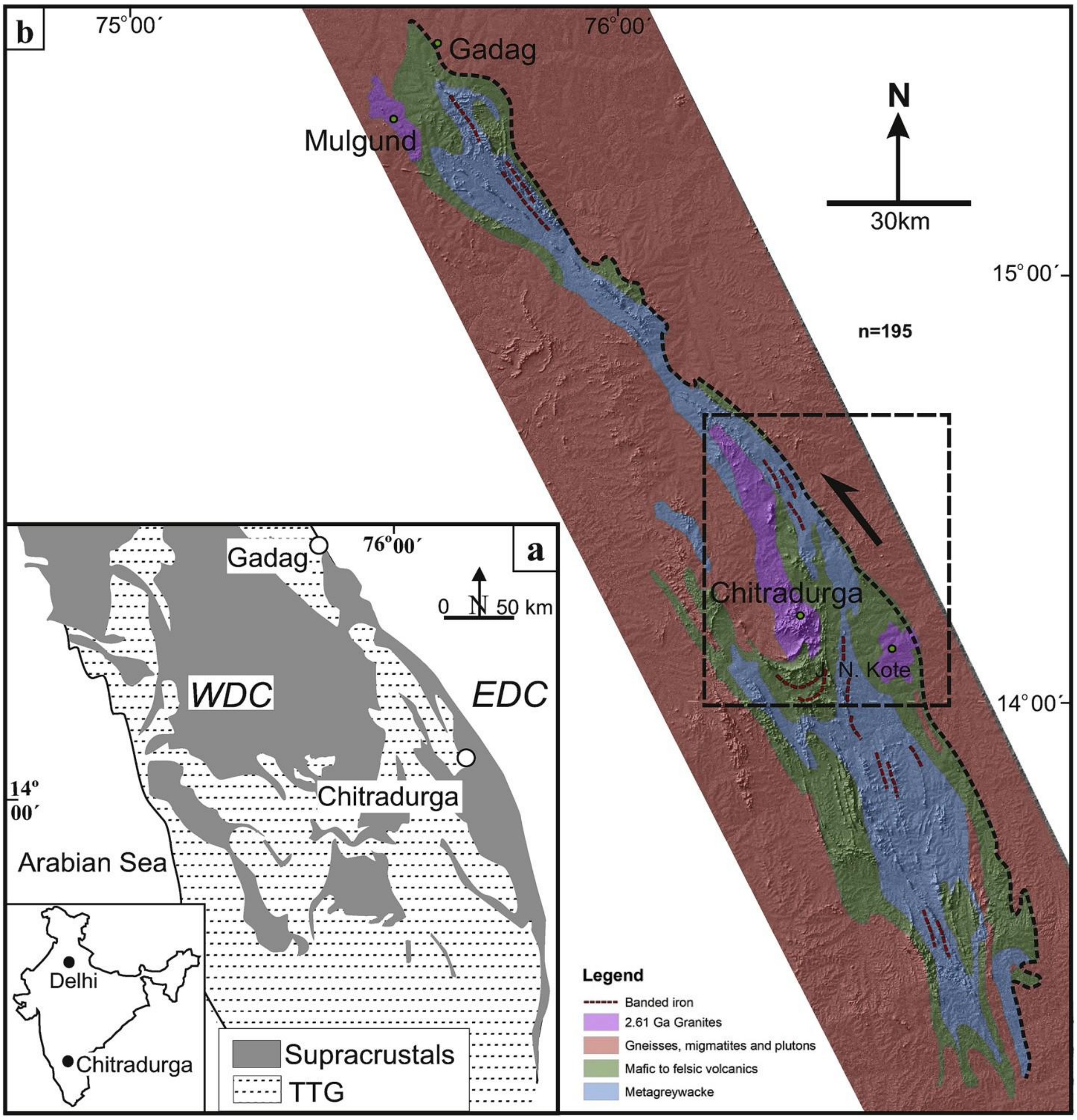

Fig. 2.3 (a) Regional map of western Dharwar craton, South Indian Shield (after Chadwick et al., 2003). Inset shows the map of India. **(b)** Regional geological map (DEM) of the Chitradurga-Gadag Schist Belt (after Bhowmick et al., 2020). Dotted line (in b) marks the eastern boundary of the Chitradurga Schist Belt, representing the Chitradurga Shear Zone (CSZ). Rectangular box near Chitradurga region demarcates the study area, which is enlarged in Fig. 2.4b.

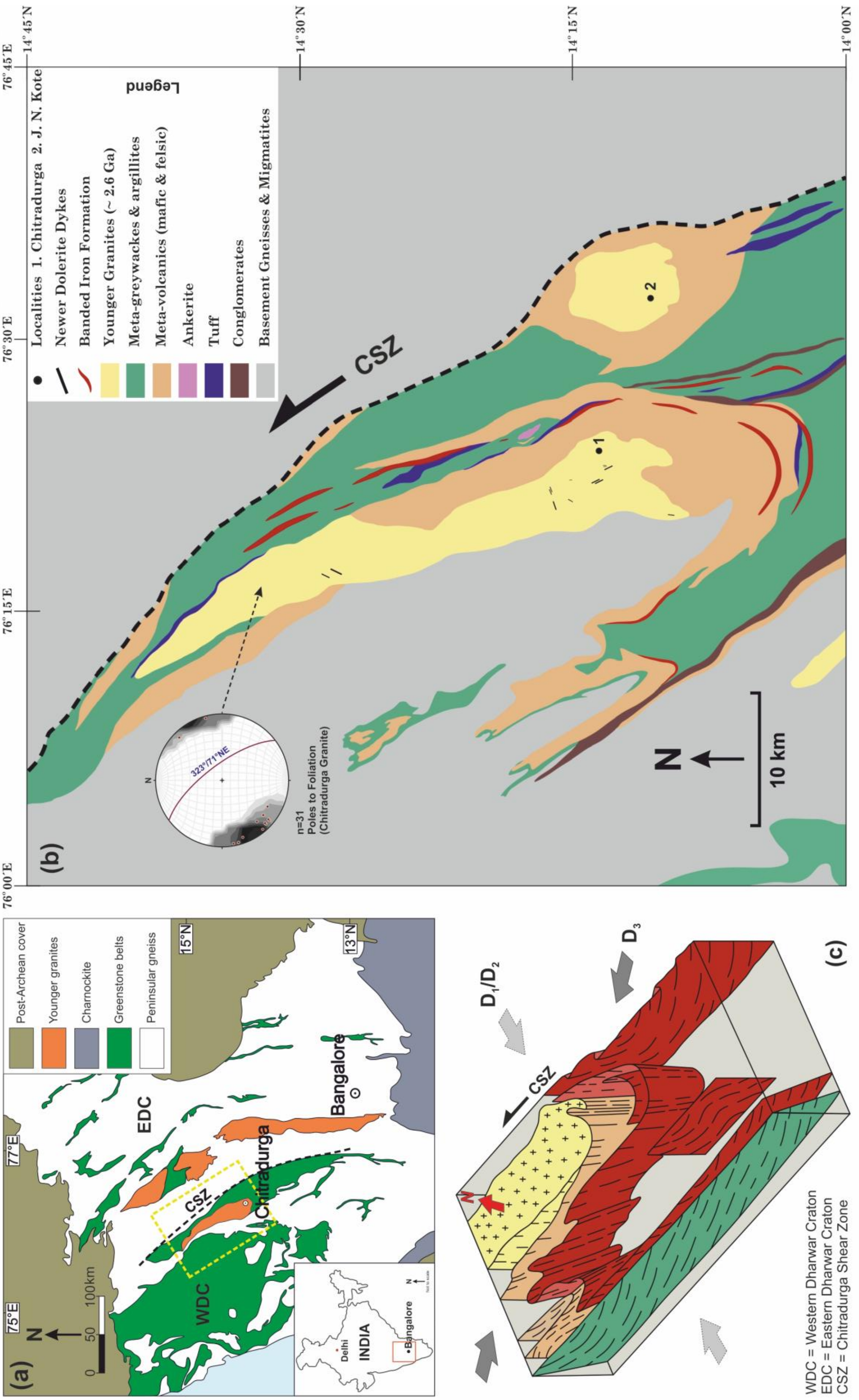
(a)
(b)
(c)
Localities 1. Chitradurga 2. J. N. Kote
Newer Dolerite Dykes
Banded Iron Formation
Younger Granites (~ 2.6 Ga)
Meta-greywackes & argillites
Meta-volcanics (mafic & felsic)
Ankerite
Tuff
Conglomerates
Basement Gneisses & Migmatites
Legend
CSZ
N
10 km
n=31
Poles to Foliation
(Chitradurga Granite)
323°/71°NE
76° 00'E
76° 15'E
76° 30'E
76° 45'E
14° 45'N
14° 30'N
14° 15'N
14° 00'N
Post-Archean cover
Younger granites
Charnockite
Greenstone belts
Peninsular gneiss
75°E
77°E
15°N
13°N
0 50 100km
EDC
WDC
Bangalore
Chitradurga
Delhi
INDIA
D1/D2
D3
WDC = Western Dharwar Craton
EDC = Eastern Dharwar Craton
CSZ = Chitradurga Shear Zone

Fig. 2.4 (a) Simplified geological map of the Dharwar Craton, India, modified after Dey et al. (2015) showing the location of the study area demarcated by yellow dashed box in the map. Chitradurga Shear Zone (CSZ) demarcates the boundary between Western Dharwar Craton (WDC) and Eastern Dharwar Craton (EDC). Inset shows the map of India and the location of the Dharwar Craton in it demarcated by red solid box. **(b)** Geological map of the study area, the central portion of the Chitradurga Schist Belt (CSB) around the Chitradurga town demarcated by 1 in the map; modified after Geological Survey of India Quadrangle map (57B) 1981-1982. The younger granites (~ 2.6 Ga) that intrude the schist belt in this region, namely, (1) Chitradurga granite and (2) J.N. Kote granite are shown in light yellow colour. The lower-hemisphere equal-area diagram in (b) shows poles to foliation (n = 31, mean ~ 323º/71º NE) in the northern exposures of the Chitradurga granite. **(c)** Schematic 3D block diagram depicting the structure of the study area resulting from the three tectonic deformation phases that the area has undergone; reproduced and modified after Chadwick et al. (1981).

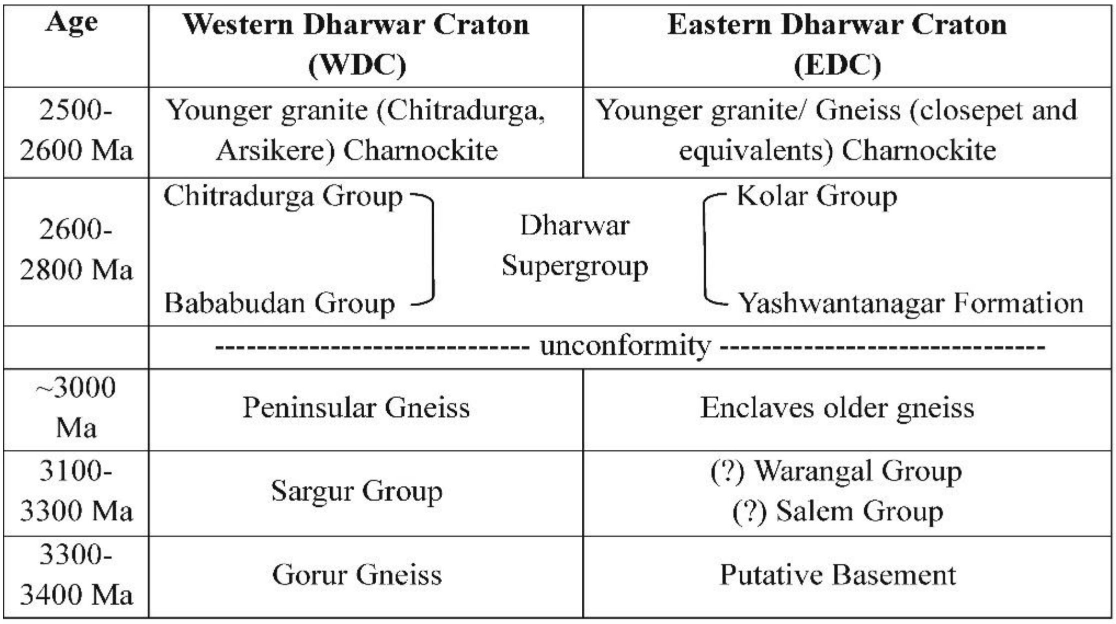

Age	Western Dharwar Craton (WDC)	Eastern Dharwar Craton (EDC)
2500-2600 Ma	Younger granite (Chitradurga, Arsikere) Charnockite	Younger granite/ Gneiss (closepet and equivalents) Charnockite
2600-2800 Ma	Chitradurga Group Bababudan Group Dharwar Supergroup	Kolar Group Yashwantanagar Formation
	----------------------------- unconformity ------------------------------	
~3000 Ma	Peninsular Gneiss	Enclaves older gneiss
3100-3300 Ma	Sargur Group	(?) Warangal Group (?) Salem Group
3300-3400 Ma	Gorur Gneiss	Putative Basement

Table. 2.1 Simplified stratigraphy of the Western Dharwar Craton (WDC) and Eastern Dharwar Craton (EDC) (after Swami Nath and Ramakrishnan, 1981).

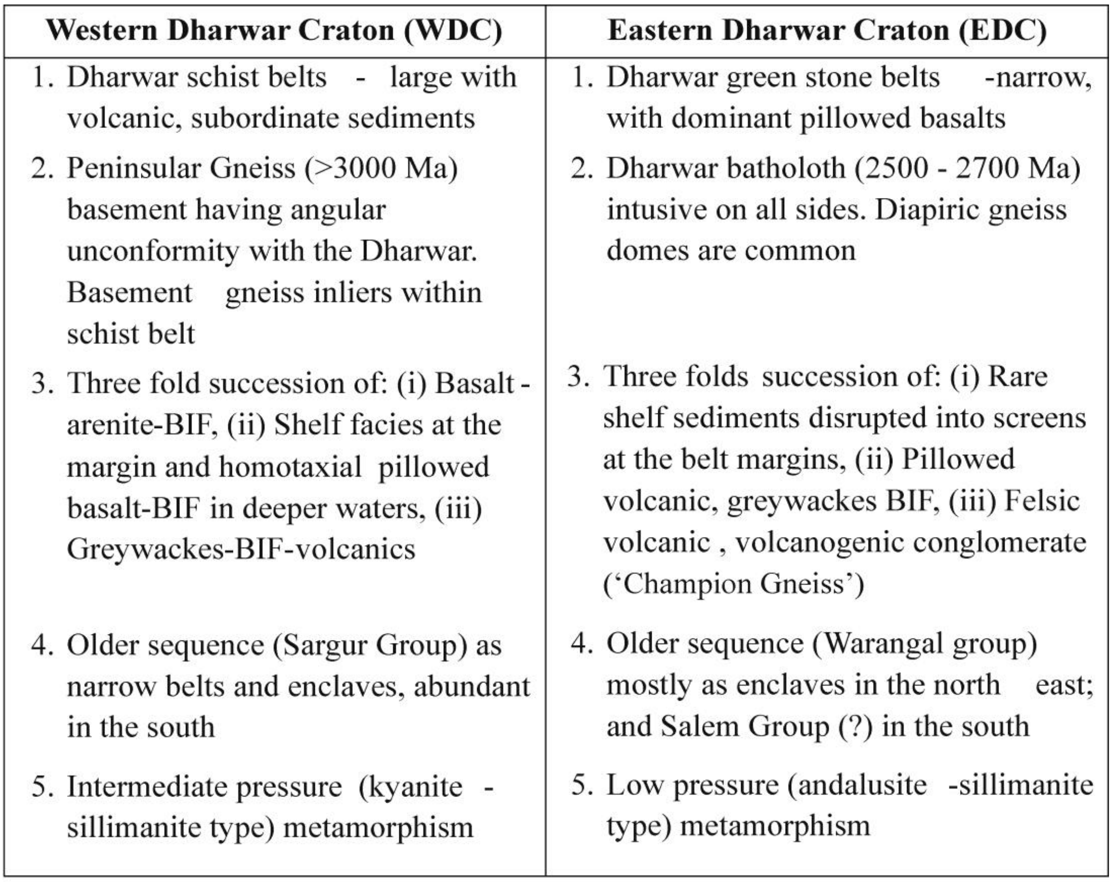

Western Dharwar Craton (WDC)	Eastern Dharwar Craton (EDC)
1. Dharwar schist belts - large with volcanic, subordinate sediments	1. Dharwar green stone belts -narrow, with dominant pillowed basalts
2. Peninsular Gneiss (>3000 Ma) basement having angular unconformity with the Dharwar. Basement gneiss inliers within schist belt	2. Dharwar batholoth (2500 - 2700 Ma) intusive on all sides. Diapiric gneiss domes are common
3. Three fold succession of: (i) Basalt - arenite-BIF, (ii) Shelf facies at the margin and homotaxial pillowed basalt-BIF in deeper waters, (iii) Greywackes-BIF-volcanics	3. Three folds succession of: (i) Rare shelf sediments disrupted into screens at the belt margins, (ii) Pillowed volcanic, greywackes BIF, (iii) Felsic volcanic , volcanogenic conglomerate (‘Champion Gneiss’)
4. Older sequence (Sargur Group) as narrow belts and enclaves, abundant in the south	4. Older sequence (Warangal group) mostly as enclaves in the north east; and Salem Group (?) in the south
5. Intermediate pressure (kyanite - sillimanite type) metamorphism	5. Low pressure (andalusite -sillimanite type) metamorphism

Table. 2.2 Differences between Western Dharwar Craton (WDC) and Eastern Dharwar Craton (EDC) (after Ramakrishnan, 1994; Ramakrishnan and Vaidyanadhan, 2010).

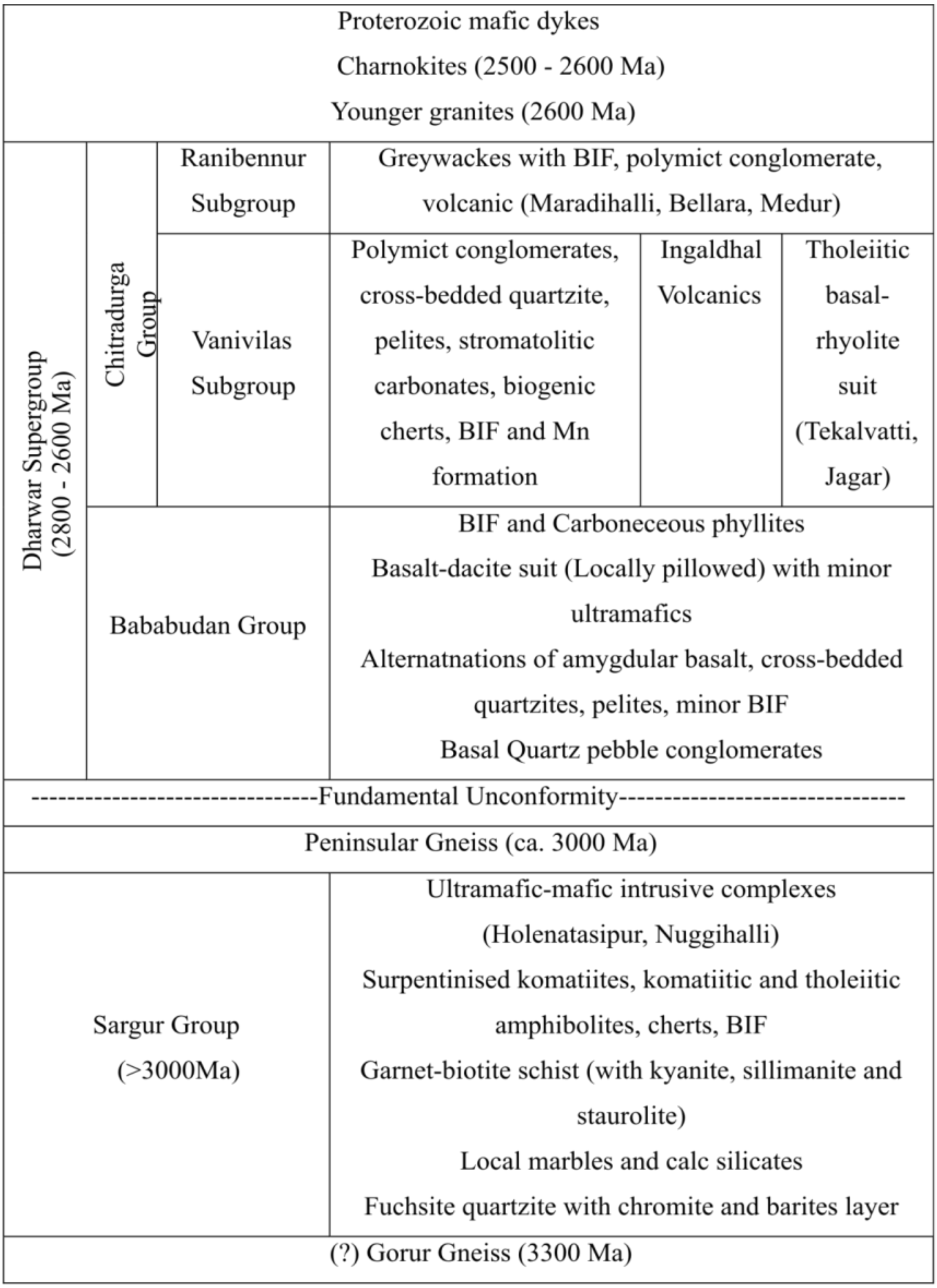

<table>
<tr><td colspan="6">Proterozoic mafic dykes
Charnokites (2500 - 2600 Ma)
Younger granites (2600 Ma)</td></tr>
<tr><td rowspan="3">Dharwar Supergroup (2800 - 2600 Ma)</td><td rowspan="2">Chitradurga Group</td><td>Ranibennur Subgroup</td><td colspan="3">Greywackes with BIF, polymict conglomerate, volcanic (Maradihalli, Bellara, Medur)</td></tr>
<tr><td>Vanivilas Subgroup</td><td>Polymict conglomerates, cross-bedded quartzite, pelites, stromatolitic carbonates, biogenic cherts, BIF and Mn formation</td><td>Ingaldhal Volcanics</td><td>Tholeiitic basal-rhyolite suit (Tekalvatti, Jagar)</td></tr>
<tr><td colspan="2">Bababudan Group</td><td colspan="3">BIF and Carboneceous phyllites
Basalt-dacite suit (Locally pillowed) with minor ultramafics
Alternatnations of amygdular basalt, cross-bedded quartzites, pelites, minor BIF
Basal Quartz pebble conglomerates</td></tr>
<tr><td colspan="6">-------------------------------Fundamental Unconformity--------------------------------</td></tr>
<tr><td colspan="6">Peninsular Gneiss (ca. 3000 Ma)</td></tr>
<tr><td colspan="3">Sargur Group (>3000Ma)</td><td colspan="3">Ultramafic-mafic intrusive complexes (Holenatasipur, Nuggihalli)
Surpentinised komatiites, komatiitic and tholeiitic amphibolites, cherts, BIF
Garnet-biotite schist (with kyanite, sillimanite and staurolite)
Local marbles and calc silicates
Fuchsite quartzite with chromite and barites layer</td></tr>
<tr><td colspan="6">(?) Gorur Gneiss (3300 Ma)</td></tr>
</table>

Table. 2.3 Regional stratigraphy of the WDC (after Swami Nath and Ramakrishnan, 1981; Ramakrishnan, 1994; Chakrabarti et al., 2006; Ramakrishnan and Vaidyanadhan, 2010).

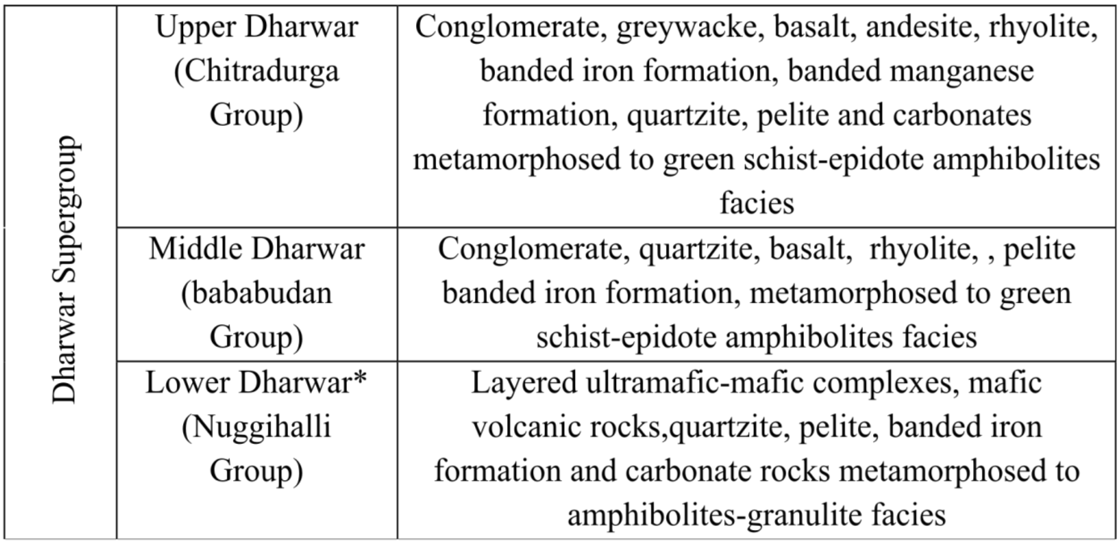

Dharwar Supergroup	Upper Dharwar (Chitradurga Group)	Conglomerate, greywacke, basalt, andesite, rhyolite, banded iron formation, banded manganese formation, quartzite, pelite and carbonates metamorphosed to green schist-epidote amphibolites facies
	Middle Dharwar (bababudan Group)	Conglomerate, quartzite, basalt, rhyolite, , pelite banded iron formation, metamorphosed to green schist-epidote amphibolites facies
	Lower Dharwar* (Nuggihalli Group)	Layered ultramafic-mafic complexes, mafic volcanic rocks,quartzite, pelite, banded iron formation and carbonate rocks metamorphosed to amphibolites-granulite facies

Table. 2.4 Stratigraphic succession of the supracrustal rocks of the Dharwar craton after (Chakrabarti et al., 2006). *Sargur group according to Swami Nath et al. (1976).

Chapter 3: Structural Investigation

CONTENTS **Page No.**

CHAPTER 3

Structural Investigation

3.1 Introduction

It is evident from previous studies that, while the regional structural architecture based on ductile deformation of the Chitradurga Schist Belt (CSB) and adjacent areas have been investigated extensively, the brittle structural framework of the area remains largely undocumented. Yet, field evidence strongly indicates that the varying lithologies of the schist belt, which for the sake of the present research objectives, can be broadly sub-divided into the younger granites, metavolcanic rocks, and, metasedimentary rocks, host a diverse array of brittle structural features preserving valuable records of the late-stage tectonic evolution of the terrain and their vital implications in upper crustal fluid-flow processes.

Structural investigation undertaken in the present study will therefore primarily focus on documenting the brittle deformation structures observed within the respective lithologies of the study area. Previous studies with regard to brittle deformation of the region have examined some aspects of fracturing and faulting within the younger granites of the Chitradurga Schist Belt (Mondal and Acharyya, 2018; Mondal et al., 2020), while, quartz veins emplaced within the metavolcanic rocks of the schist belt have been investigated by Bhowmick and Mondal (2020; 2021).

However, a detailed characterization of the various suites of brittle structures, and consequently a comprehensive understanding of the region's brittle tectonic evolution, remains to be achieved. This chapter, will therefore, take into account the previous observations on brittle structures reported from the study area while also providing a concise summary of the new field data collected on brittle structures observed within different lithologies during the present study. By systematically characterizing these brittle structures, in terms of their geometry, kinematics and networking attributes, this study will aim to fill a critical gap in the structural understanding of the region. The ultimate objective will be to integrate respective studies on the salient brittle deformation structures observed in the region into a comprehensive brittle tectonic evolution model, complementing existing knowledge of the ductile history and shedding light on the interplay between brittle deformation, pre-existing fabric, ambient stress states, and fluid pressure conditions during the late-stage tectonic evolution and stabilization of the craton.

3.2 Structures within the younger granites

The granites are replete with a plethora of brittle structures. Previous studies from the area report thermal fractures from the granites with varying orientations, but mostly occurring at a high angle to the pluton boundary **(Fig. 3.1a)** (Mondal and Acharyya, 2018). The micro-granitoid enclaves within the Chitradurga granite also show tensile fractures **(Figs. 3.1b and c)**, which have been linked to the later stages of D_3 deformation (Mondal and Acharyya, 2018). These studies estimate the upper limit for fracturing in the younger granites at ~ 2.4 km. Microstructural observations by Mondal (2018) revealed low-temperature solid-state deformation textures overprinting earlier high-temperature textures in the granites.

Presently, mafic dykes have been observed in the study area emplaced within the younger granites of the Chitradurga Schist Belt. Within the study area, these dykes do not form organized swarms; rather, they occur as isolated intrusions emplaced discretely within the younger granites. The observed dykes are all sub-vertical in attitude trending NNW and are meter scale in length and cm scale in thickness, maintaining a sharp contact with the host lithology **(Fig. 3.1d)**. The granites also host a diverse assemblage of veins. These include quartzo-feldspathic varieties **(Fig. 3.1e)** which are meter scale in length and cm scale in thickness, intruding predominantly along the pluton margins, consistently striking NW-SE to NNW-SSE and dipping steeply either towards NE or SW. Extensional (Mode I) quartz-filled veins **(Fig. 3.1f)** are also common, with orientations dominantly ranging from ENE-WSW to E-W. Additionally, at places, dilatational fractures infilled with a very fine-grained black coloured material **(Fig. 3.1g)** has been observed within the granites, displaying a uniform ESE-WNW orientation across the plutons. These extensional veins are typically cm scale in length and cm to mm scale in thickness and are identified by the presence of well-defined tips marking their terminations.

However, the most conspicuous brittle structure observed within the granites are small scale oblique-slip faults of varying orientations, abundant along the entire spatial extent of the plutons. These faults are mostly steeply dipping, cross-cutting all pre-existing brittle structures observed within the granites and are identified by the presence of slickenside lineations and congruous steps on exposed fault surfaces, which also help to identify the sense of movement along them (Petit, 1987; Mondal et al., 2020) **(Figs. 3.2a, b, c, and d)**. On planar outcrop surfaces of the granites, traces of these faults are often observed to occur in close proximity displaying strong spatial interaction through splaying, abutting, and cross-cutting mutual relations, resulting in the formation of extensive, interconnected fracture networks that are distributed throughout the granite plutons **(Figs. 3.2e and f)**.

3.3 Structures within the metavolcanic rocks

Metavolcanic rocks in the study area are extensively cut by fractures and faults of varying orientations. Some of these structures host quartz veins **(Fig. 3.3a)**, while others lack any vein material. Quartz crystal growth within the veins is often oriented perpendicular to the vein walls, indicating significant dilation during their formation **(Fig. 3.3b)**. The quartz veins reach maximum dimensions of ~ 1 m in width and ~ 130 m in length. In places, certain veins are displaced by others, producing a crisscross network across the area **(Fig. 3.3c)**. Wing cracks infilled with quartz are also observed **(Fig. 3.3d)**.

At a few localities, thicker quartz veins display successive fault planes with slickenside lineations **(Fig. 3.3e and inset)**. These veins often enclose angular metabasalt enclaves (host rock; **Fig. 3.3f**). Multiple median lines within some quartz veins provide evidence of a crack-seal mechanism, formed through cyclic fluid ingress **(Fig. 3.3g)**. Fault planes in the area exhibit slickenside lineations ranging from shallow to moderate and steep plunges. Both dextral and sinistral faults are recognized, identified by the relative motion of the hanging wall with respect to the footwall, with congruous steps aiding in their distinction **(Fig. 3.3h)**. Quartz veins observed in the study area vary in orientation and thickness, but the majority trend NNW-SSE **(Fig. 3.3i)**. Notably, the thickest quartz veins are also oriented along the NNW-SSE direction **(Fig. 3.3j)**.

Fractures and faults observed within the metavolcanic rocks also predominantly show a NNW-SSE oriented set (maxima), with subordinate WNW-ESE and NE-SW sets forming sub-maxima **(Figs. 3.4a and b)**. Additionally, WNW-ESE trending Mode I (tensile) cracks with well-defined tips are recorded, which are often quartz-filled. Throughout the study area, sub-vertical sections of exposed metavolcanic rocks exhibit fracture networks formed though the interaction of multiple cross-cutting fracture sets **(Fig. 3.4c)**. Strike data of these fracture planes show three dominant modes trending NNW, NNE and ENE respectively **(Fig. 3.4d)**. Traces of all these fracture sets appearing on the sub-vertical outcrop surfaces are rectilinear and are mostly steeply dipping to sub-vertical in attitude, although, few sub-horizontal fracture sets have also been recorded **(Fig. 3.4e)**.

3.4 Structures within the metasedimentary rocks

In contrast to the younger granites and metavolcanic rocks of the study area, which display abundant development of faults and fractures, the metasedimentary rocks are largely devoid of such brittle structures. As stated earlier, these rocks are highly foliated **(Fig. 3.5a)** with prominent field foliation striking NNW and dipping steeply (> 80°) towards E, and only few fracture sets, manifested as joint planes are observed sporadically in some outcrops lacking any extensive, interconnected network. Among these, two joint sets are most prominent; one sub-vertical, striking NE to ENE and another sub-horizontal, striking E to ENE **(Fig. 3.5c)**. Development of well-defined conjugate fracture sets have been observed in relatively massive, weakly foliated portions of the metasedimentary rocks **(Fig. 3.5b)**. These fracture sets are sub-vertical in attitude and strikes ~ 55° and ~ 125° respectively. The acute bisector of these conjugate fracture sets trends broadly E-W to ESE indicating the local compression direction. In some exposures relatively proximal to the adjacent CSZ, the metasedimentary rocks show development of kink folds **(Fig. 3.5d)** with conjugate kink bands. The well-developed, dominant kink band strikes 232°-242° and dips steeply (>

80°) towards NW while the less developed counterpart strikes 300°-310° and dips steeply (~ 80°) towards the NE. The acute bisector of these conjugate kink bands trends E-W to ESE-WNW, coinciding with the regional far-field compression direction prevalent during the D_3 deformation phase of the terrain **(Fig. 3.5e)**. This suggests that the kink folds likely formed in the late stages of deformation, under the same stress regime as is also recorded by the conjugate fractures developed within the metasedimentary rocks. However, it is plausible that the inherent rheological nature of the metasedimentary rocks, combined with the presence of well-developed pre-existing planar fabric (foliation), likely inhibited much of brittle deformation and instead promoted the formation of kink band geometries to accommodate strain during the late stages of deformation.

3.5 Summary

Structural investigations reveal that the brittle structures observed within the major lithologies of the study area, namely the younger granites, metavolcanic rocks, and metasedimentary rocks, can be broadly classified into three principal suites, viz. veins, dykes, and fracture networks. Each of these suites will be addressed in detail, sequentially, in the subsequent chapters.

Veins observed within the younger granites and metavolcanic rocks vary in their composition, dimensions, and orientations. However, the most pervasively developed ones are the quartz veins emplaced in the metavolcanic rocks of the region. Their emplacement has been previously attributed to *fault-valve action*, wherein pre-existing anisotropies within the host rocks are reactivated under fluctuating fluid pressure conditions during the D_3 deformation phase (Bhowmick and Mondal, 2020; 2021) of the terrain. The number and magnitudes of these fluid pressure pulses, however, remain undetermined, a gap the present study will seek to address.

Mafic dykes are prominent intrusive features observed within the younger granites. Given that dykes fundamentally originate as magma-driven extensional fractures, the present study will study them in detail, focusing on their composition, outcrop attributes, magma overpressure ranges, depths of origin, and emplacement mechanisms under the ambient stress states of the region.

Fracture networks are ubiquitously observed in both the younger granites and metavolcanic rocks of the area. These are formed by the interaction of numerous small scale faults within the granites and cross cutting fracture sets within the metavolcanic rocks. The present work will investigate their origin and characterize the subsequent networking of these late-stage brittle faults and fractures, both in terms of their geometry and connectivity, with particular emphasis on their controlling factors and evolution within the younger granites. The spatial interrelations and relative temporal development of the genetically distinct suites of brittle structures developed within the younger granites will also be examined based on field evidences.

Finally, the spatial relationships among different vein types, mafic dykes, and fracture networks, combined with observed mutual cross-cutting relationships in the field, will be utilized to reconstruct their relative temporal evolution, eventually culminating in the formulation of a comprehensive brittle tectonic evolution model for the study area.

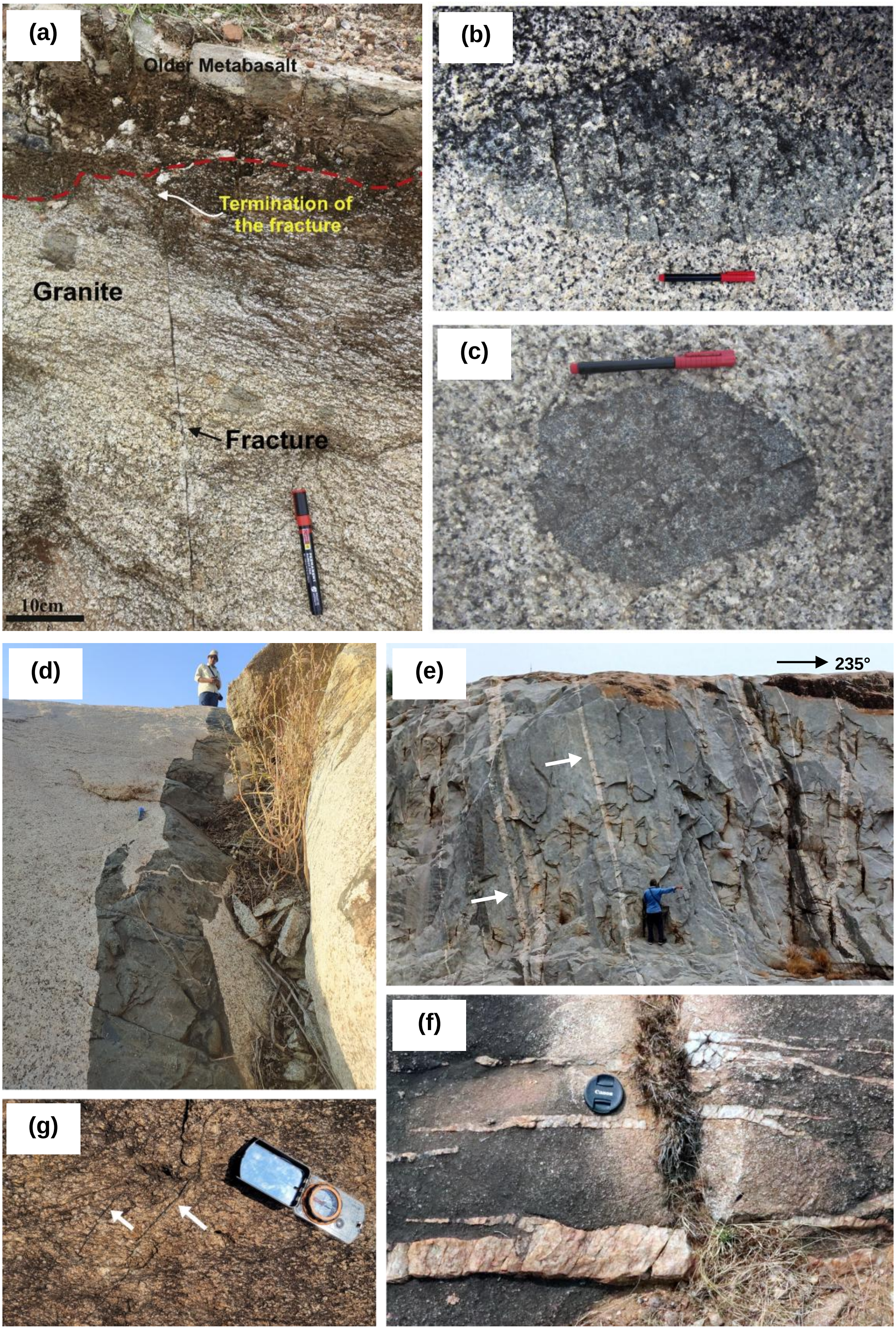
(a)
Older Metabasalt
Termination of the fracture
Granite
Fracture
10cm
(b)
(c)
(d)
(e)
235°
(f)
(g)

Fig. 3.1 (a) Field photograph showing thermal fracture developed within the younger granites at high angle to the pluton boundary (modified after Mondal and Acharyya, 2018). **(b)** and **(c)** Field photographs of micro-granitoid enclaves within the younger granites containing multiple parallel fractures. These enclave restricted fractures show a dominant E-W to ESE-WNW trend (modified after Mondal and Acharyya, 2018). **(d)** Field photograph of a sub-vertical mafic dyke outcrop observed intruded within the Chitradurga granite. The dyke trends NNW. **(e)** Outcrop photograph showing multiple parallel intruded quartzo-feldspathic veins within the Chitradurga granite (marked by white arrows). The veins are of variable thicknesses but are consistent in attitude, striking NW and dipping steeply towards SW. **(f)** Extensional (Mode I) quartz veins within the Chitradurga granite displaying prominent tips at both ends. **(g)** Thin dilatational fractures developed within the Chitradurga granite filled in by a very fine grained black coloured material (marked by white arrows).

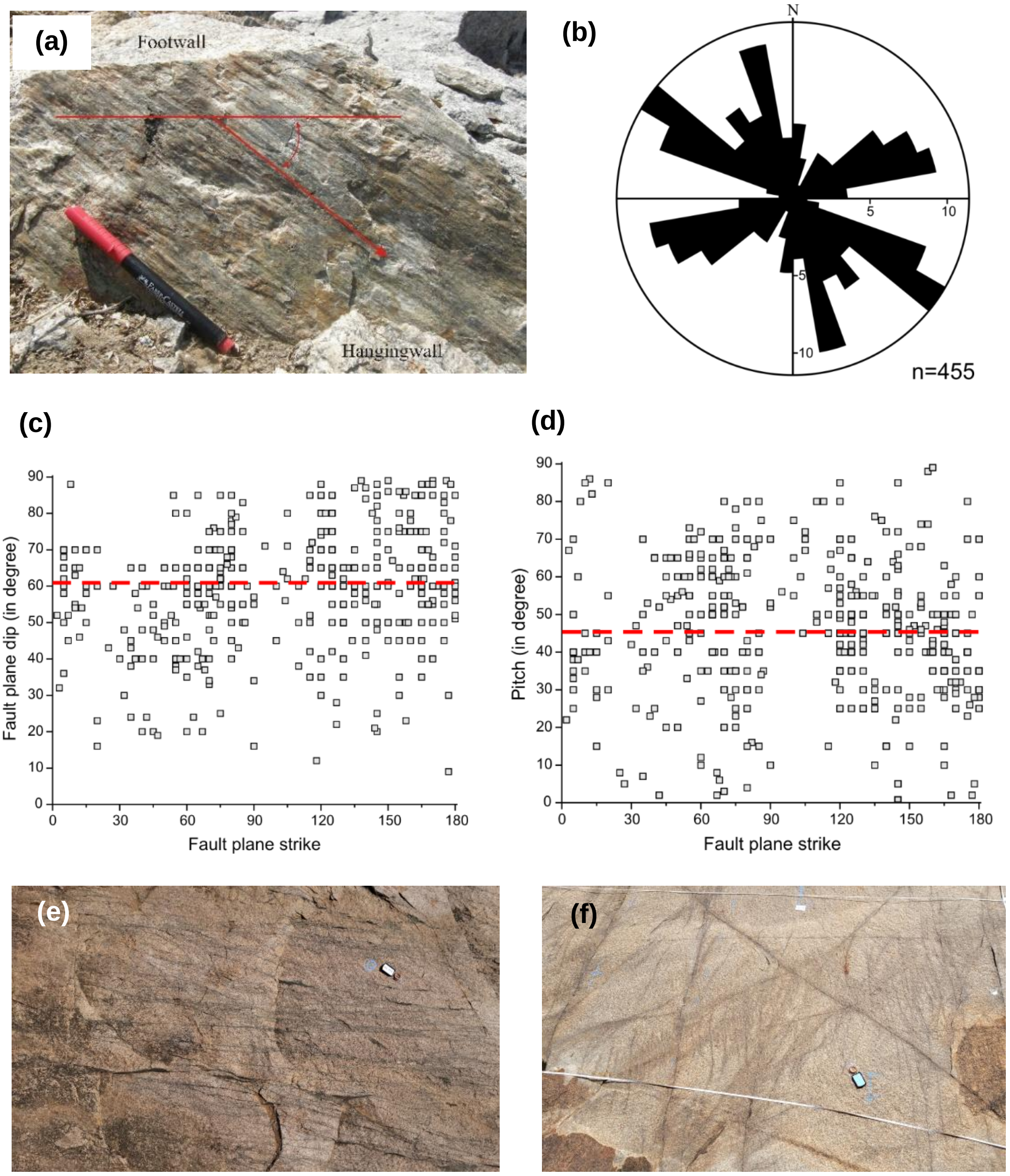

Fig. 3.2 (a) Field photograph showing obliquely oriented slickenfibres on fault planes observed within the younger granites. Red arrow shows the steps on fault plane which are used to determine the movement direction. **(b)** Rose diagram showing the variation in the orientations of brittle faults recorded within the younger granites. n = number of data. **(c)** Graph of fault plane strike vs. fault plane dip. The mean dip angle is ~ 60°. **(d)** Graph of fault plane strike vs. pitch of slickenfibres (lineations) measured on the fault plane. The mean pitch amount is ~ 46°, which implies that the faults in the younger granites are dominantly oblique slip faults. **(e)** and **(f)** show fracture networks developed through the interaction of the faults within the Chitradurga and J.N. Kote granites respectively. Figs. 3.2 (a), (b), (c) and (d) are modified after Mondal et al. (2020).

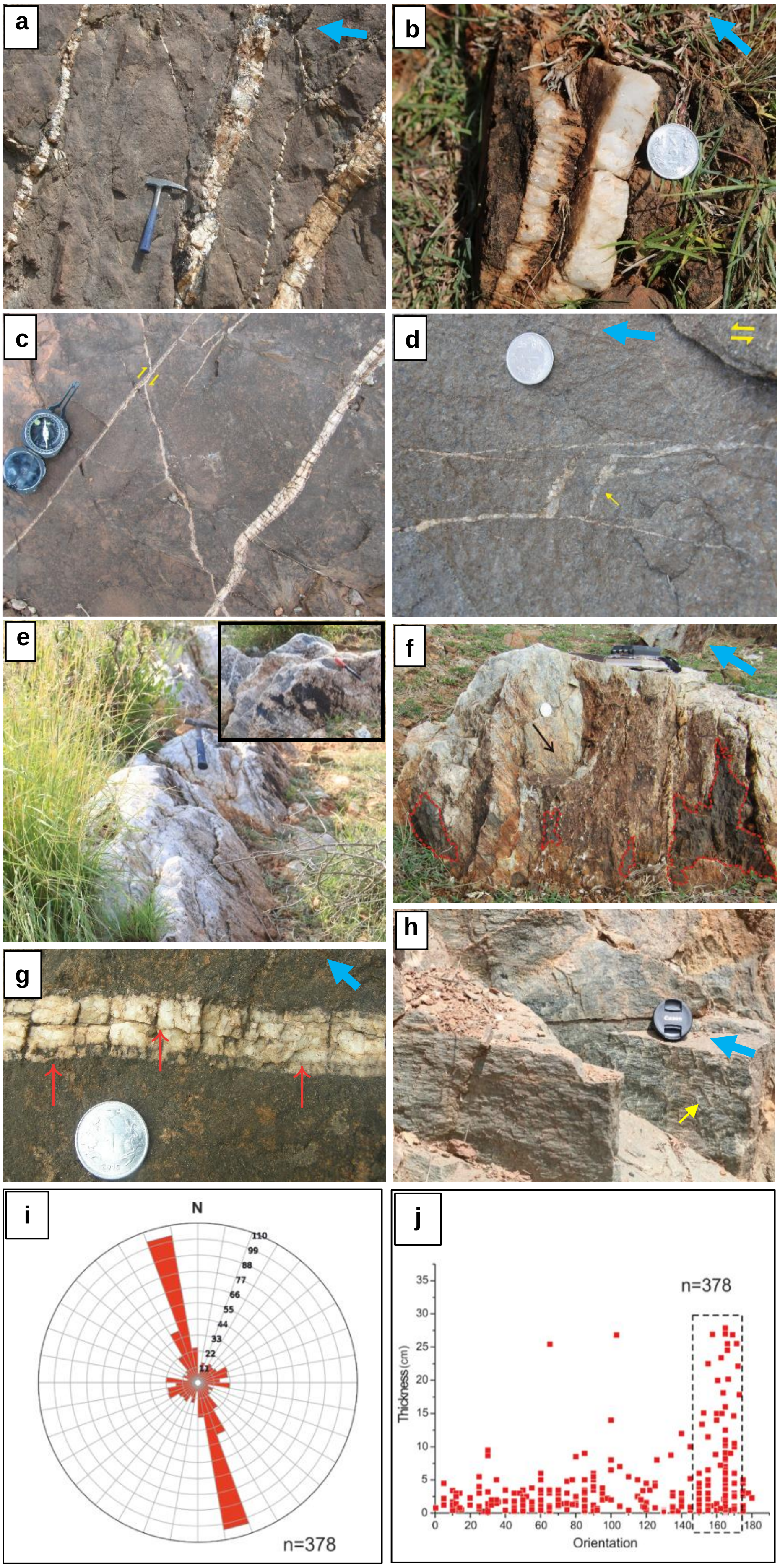
a
b
c
d
e
f
g
h
i
N
110
99
88
77
66
55
44
33
22
11
n=378
j
n=378
35
30
25
20
15
10
5
0
Thickness(cm)
0
20
40
60
80
100
120
140
160
180
Orientation

Fig. 3.3 Field photographs of quartz veins emplaced within the metavolcanic rocks of the study area. **(a)** Criss-cross orientation of quartz veins of variable thicknesses within metabasalt. **(b)** Close-up view of a quartz vein in metabasalt showing crystal growth perpendicular to the vein wall. **(c)** Cross-cutting quartz veins exhibiting dextral sense of displacement (marked by yellow half-arrows). **(d)** Wing cracks filled up with quartz veins associated with sinistral shearing (marked by yellow arrow). **(e)** NE dipping quartz vein showing slickenside lineations (maximum width recorded = 120 cm); inset showing close up view of the fault plane found in e. Marker pen is placed along the orientation of the slickenside lineations. **(f)** Angular chunks of metabasalt (enclaves) enclosed within faulted quartz vein. Dotted red line demarcates the enclave boundaries. Black arrow marks the slickenside lineation on the fault plane. **(g)** Field photograph of quartz vein (close view) showing multiple median lines (marked with red arrows) as an evidence of crack- seal mechanism. This clearly indicates cyclic fluid ingression and *fault valve action* that led to the formation of veins in the metabasalts of the Chitradurga region. **(h)** Fault planes in metabasalt showing congruous steps (marked by yellow arrow). Blue arrow in the respective figures point towards N. **(i)** Rose diagram of strike orientation of the quartz veins observed in the metavolcanic rocks, showing a dominant NNW-SSE trend. **(j)** Graph of quartz vein orientation vs. thickness, showing maximum vein thickness along NNW-SSE (marked with dotted black box). n = number of data. The figures are modified after Bhowmick and Mondal (2020).

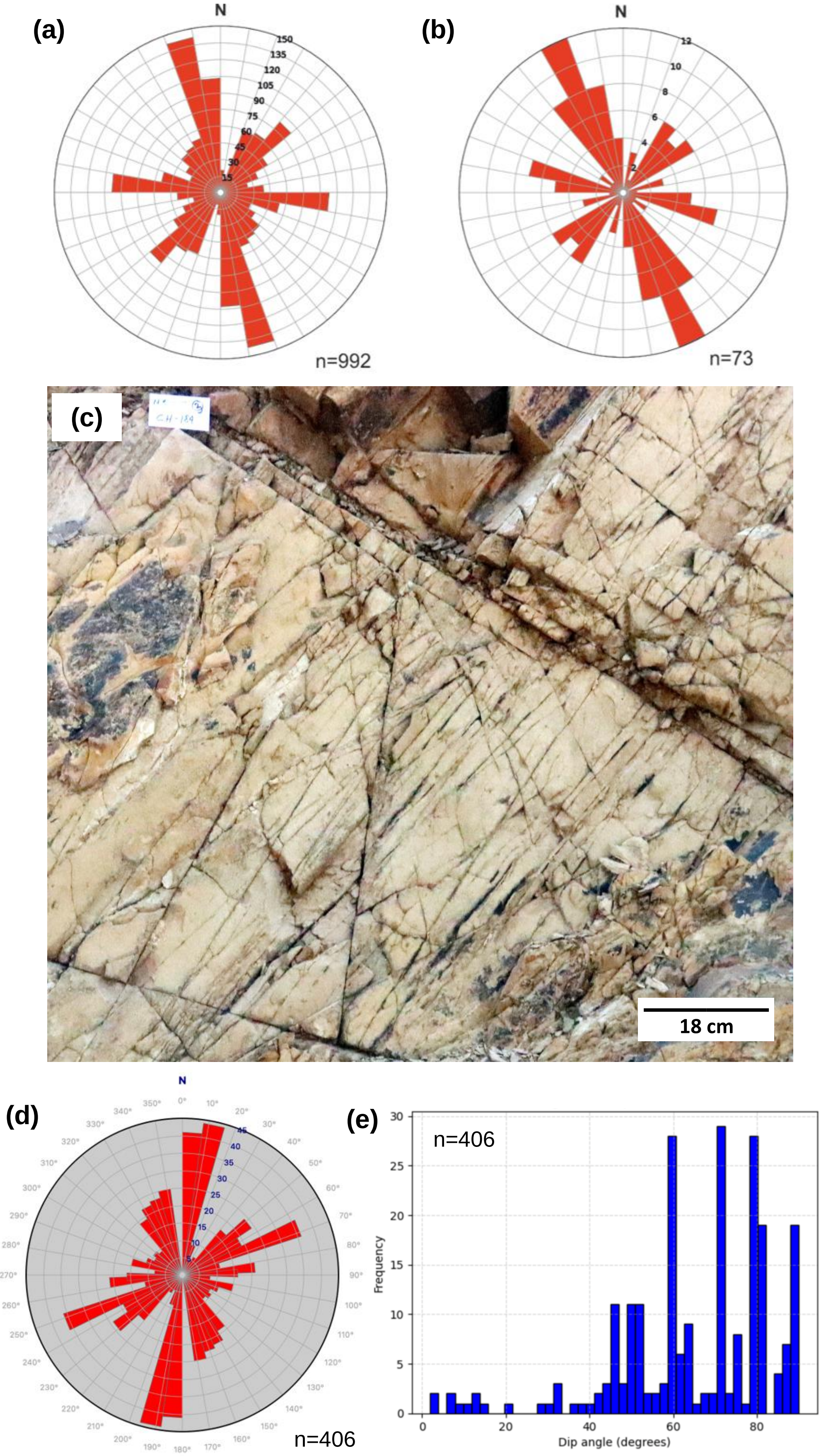
(a)
N
150
135
120
105
90
75
60
45
30
15
n=992
(b)
N
12
10
8
6
4
2
n=73
(c)
CH-184
18 cm
(d)
N
0°
10°
20°
30°
40°
50°
60°
70°
80°
90°
100°
110°
120°
130°
140°
150°
160°
170°
180°
190°
200°
210°
220°
230°
240°
250°
260°
270°
280°
290°
300°
310°
320°
330°
340°
350°
45
40
35
30
25
20
15
10
5
n=406
(e)
n=406
Frequency
0
5
10
15
20
25
30
0
20
40
60
80
Dip angle (degrees)

Fig. 3.4 (a) and **(b)** Rose diagrams illustrating the strike orientations of fractures and fault planes, respectively, recorded from the metavolcanic rocks of the study area. The data reveal a wide range of orientations, with a pronounced NNW-SSE trending maximum and subordinate WNW-ESE and NE-SW trending sub-maxima (modified after Bhowmick and Mondal, 2020). **(c)** Field photograph showing an interconnected fracture network formed by cross-cutting fracture planes exposed on a sub-vertical outcrop surface of metavolcanic rock. The white card placed as scale is 8.9 cm in length. **(d)** Rose diagram depicting the principal strike trends of fracture sets forming such networks within the metavolcanic rocks, highlighting three dominant orientations, viz. NNW, NNE, and NE–ENE. **(e)** Frequency distribution graph of fracture plane dip data, showing that the majority of fractures forming the networks are steeply dipping, with only a minor population of sub-horizontal planes. n = number of data.

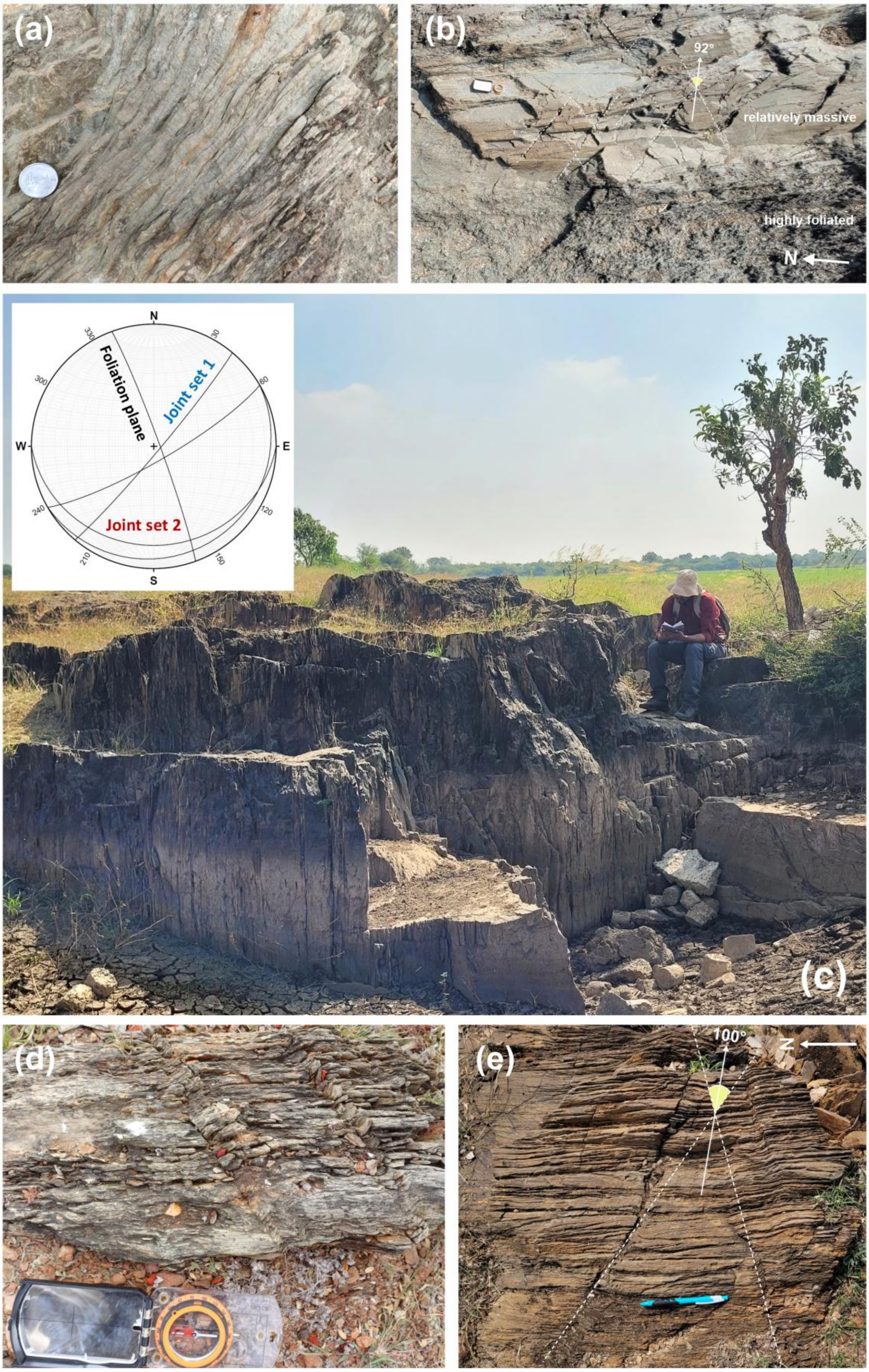
(a)
(b)
92°
relatively massive
highly foliated
N
N
30
60
E
120
150
S
210
240
W
300
330
Foliation plane
Joint set 1
Joint set 2
(c)
(d)
(e)
100°
N

Fig. 3.5 (a) Field photograph (close sectional view) showing the strongly foliated nature of the metasedimentary rocks in the study area. **(b)** Planar outcrop view showing conjugate fracture sets (indicated by faint white dotted lines) developed within relatively massive, competent domains of the metasedimentary rocks; the adjacent highly foliated, mechanically incompetent zones are devoid of fractures. The acute bisector of the conjugate fracture sets (solid white arrow) trends east. **(c)** Outcrop view of metasedimentary rock showing pervasive sub-vertical foliation planes intersected by two distinct joint sets; inset stereographic plot depicts the measured orientations of the foliation plane and both joint sets. **(d)** Kink folds developed within the strongly foliated domains of the metasedimentary rocks. **(e)** Outcrop (plan view) showing development of conjugate kink bands (marked by faint white dotted lines) within foliated metasedimentary rocks, with the acute bisector of the conjugate pair (solid white arrow) trending ESE.

Chapter 4: Veins

CONTENTS **Page No.**

CHAPTER 4

Veins

4.1 Introduction

Archean greenstone belts represent some of the cryptic records of crustal history and are globally acclaimed for hosting mineral deposits often found within shallow crustal veins. Such shallow crustal mineralized veins are the evidence of epithermal fluid ingression often emplaced along fracture networks (Sibson, 1992; 1996; 2000; Jolly and Sanderson, 1997; Simmons et al., 2005; Mondal and Mamtani, 2013; Faye et al., 2018; Mazzarini et al., 2019). Pre-existing structural anisotropies in the host rock form easy pathways for fluid migration (Mazzarini et al., 2019; Bhowmick and Mondal, 2020; Gudmundsson, 2022). The formation of fracture hosted vein networks requires substantially high fluid pressure (P_f) exceeding the strength of the host rock and the stresses acting on it. Understanding the formation of shallow crustal fracture systems is useful for mineral exploration, geotechnical engineering, paleostress field reconstruction, nuclear waste disposal and landslide mitigation (Pascal, 2021).

Parts of this chapter have been published in ***Bhowmick et al. (2023), International Journal of Earth Sciences****,* *https://doi.org/10.1007/s00531-023-02362-x.*

Dilational and shear fractures may develop under tectonic stresses and by fluid induced reactivation of pre-existing structural anisotropies/fractures or by the combination of both. Pre-existing structural anisotropies reduce the shear strength of the rock and allows fracturing at low differential stresses.

Veins and dykes are essentially Mode I (Gudmundsson, 2020) and sometimes mixed-mode fractures (Pascal, 2021; Pollard and Martel, 2020; Biswas et al., 2023). Previously, Jolly and Sanderson (1997) had successfully used dyke orientation data for inferring the principal stress fields and P_f magnitudes. Later, similar method has been extensively used for both vein and dyke orientation data to denote the relation between P_f and normal stresses acting on the fracture wall (Baer et al., 1994; André et al., 2001; Mazzarini and McKeagney et al., 2004; Mazzarini and Isola, 2007; Musumeci, 2008; Pascal, 2021). It is well depicted from these studies that such fracture data distribution patterns can be analyzed to determine the tectonic stresses and P_f conditions during vein emplacement. Further, spatial variations in P_f conditions and tectonic stress fields can be determined from such data distribution patterns.

Sometimes fluids are trapped within subsurface compartments by temporary pressure seals. Gradual rise in P_f within subsurface compartments compels fluid to breach the pressure seals and burp into pre-existing pathways, further sealing them until the next event of P_f rise (Faye et al., 2018). Such fluid induced reactivation of pre-existing pathways is often associated with seismogenic faulting (Cathles and Adams, 2005; Cox, 2005). Slickenlines and slickenfibres on the vein walls ascertain such slip movements. Thus, the fault itself acts as a valve promoting unidirectional fluid flow known as the *fault-valve action*, until the P_f drop leads to mineral precipitation and subsequent sealing of the pathway (Sibson, 1992; 1996; 2000).

However, the number of times such pressure seals are breached and subsequently sealed, depend on the P_f events. In this context, both high and low fluid pressure magnitudes can be expressed as P_f events. When P_f magnitude narrowly exceeds the minimum compressive stress (σ_3) it can be defined as a low P_f event, whereas, when P_f magnitude is substantially high and exceeds the intermediate principal stress (σ_2), it can be designated as a high P_f event. It is normally expected that fractures of similar orientations can be reactivated under a low P_f event, but a high P_f event can reactivate all possible fracture orientations.

Lode deposits and veins with multiple orientations, forming crisscross patterns (mesh-like structure) are attributed to such P_f variations (Jolly and Sanderson, 1997; Mondal and Mamtani, 2013). Usually, a high P_f event is always followed/preceded by multiple low P_f events that can reactivate small ranges of fractures (clusters) before the P_f is again high enough to reactivate a wider range of fractures forming a girdle pattern (Jolly and Sanderson, 1997; Sibson and Scott 1998; Yamaji et al., 2010). Such P_f fluctuations continue until the entire fluid source is drained. Hence, it is virtually impossible to have two successive high P_f events.

However, it is quite plausible that multiple low P_f events can follow/precede a high P_f event and in such a case, the girdle and clusters of vein orientation data might overlap. Quantifying the exact number of such high and low P_f events and estimating the accurate P_f magnitude for each event from such a vast episode is challenging (Yamaji, 2016; Yamaji and Sato, 2011; Yamaji et al., 2010; Faye et al., 2018).

As outlined in the previous chapter, the metavolcanic rocks of the Chitradurga Schist Belt (CSB) host an abundant network of quartz veins, representing the most widespread and consistently developed vein system in the study area. The occurrence of such abundant quartz veins has also been reported from the Gadag region, located at the northern fringe of the CSB (Mondal and Mamtani, 2013; 2014). These veins, often lode-type in nature, are well known for hosting auriferous deposits. Considering the shared regional tectonic framework of the Gadag and Chitradurga regions, a comparative study of their quartz veins is crucial for assessing spatial variations in fluid pressure conditions along the schist belt. This study, therefore, intends to statistically quantify the minimum number of such P_f events in these auriferous quartz veins of the Gadag and Chitradurga regions of the Chitradurga Schist Belt (CSB), a well-known Archean greenstone belt of the Indian sub-continent.

4.2 Mechanism of vein emplacement vis-à-vis state of stress

The NW-SE trending CSB in the eastern part of the Western Dharwar Craton (WDC) is an Archean age granite-greenstone belt hosting volcano-meta-sedimentary assemblages of the Chitradurga Group **(Figs. 4.1a and b)**. As stated earlier, metavolcanic rocks of the greenstone belt have developed a prominent ~ NW-SE oriented deformation fabric which has been delineated by the Anisotropy of Magnetic Susceptibility (AMS) studies and is attributed to the D_1/D_2 deformation of the terrain (Bhowmick and Mondal, 2020). The magnetic anisotropy/deformation fabric is parallel to the overall trend of the axial planar foliation of the adjoining metasedimentary sequences. The orientation of this magnetic fabric varies between ~ NW-SE in the Gadag region (Mondal and Mamtani, 2014) to ~ NNW-SSE in the Chitradurga region (Bhowmick and Mondal, 2020). Metavolcanic rocks observed in the present study areas, i.e., particularly in the Gadag and Chitradurga regions of the CSB, are replete with quartz veins of multiple orientations and thicknesses, often forming mesh like patterns **(Figs. 4.2a and b)**. It appears that the presence of magnetic fabric has played a significant role in the formation and propagation of brittle structures in the metavolcanic rocks. Gold-bearing quartz veins are abundant along this pre-existing fabric of the host metavolcanics showing a NW-SE to NNW-SSE prominence in the Gadag and Chitradurga regions respectively **(Fig. 4.1b)**. Lodes/veins with maximum thickness are also found along this magnetic fabric **(Fig. 4.1b)**, establishing a structural control on vein emplacement and mineralization. Some of the quartz veins exhibit crystal growth direction perpendicular to the vein wall, suggesting plane normal opening **(Fig. 4.2c)**. The veins are mostly syntaxial, however some antitaxial, blocky and stretching veins are also found in the study area. The quartz veins are planar and the entire length is not exposed in some cases. Few curved veins are also observed. Traces of these veins have been approximated by straight line segments whenever they are longer than 1 m and the orientation of each segment is recorded, following Yamaji et al. (2010). However, short segments and branches are neglected whenever they are less than 1 m. In this study, multiple events of fluid ingression are perceived from field evidence **(Fig. 4.2d)**. Maximum vein thickness recorded in Gadag (~ 47 cm) exceeds that of Chitradurga (~ 27 cm) (see thickness vs. orientation graph in **Fig. 4.1b**). Some of the thickest quartz veins **(Fig. 4.2e)** show evidence of *fault-valve action* with angular wall rock fragments incorporated within the quartz vein **(Fig. 4.2f)**.

Fractures within the metavolcanic rocks of the study areas, namely, Gadag and Chitradurga regions of the CSB, exhibit a wide range of orientations. It is evident from previous studies (Mondal and Mamtani, 2014; Bhowmick and Mondal, 2020) that irrespective of the spatial distance in between the two study areas, disposition of faults and fractures in both the region are overall similar, hinting towards their common tectonic origin and the coherent sets of fractures measured in the metavolcanic sequences of the CSB has been related to the later phase of D_3 deformation. Previous studies show that fracture formation/reactivation and faulting took place under the effect of this tectonic stress field with intermittent episodes of fluid flow and vein emplacement (Bhowmick and Mondal, 2020; 2021). Though the source of stress related to this later deformation (D_3) is not well understood, these fractures have been interpreted as the products of late phase craton stabilization processes reflecting residual stress adjustment (shear partitioning) along the craton boundary (Mondal et al., 2020). However, vein emplacement is most prominently developed along the NW-SE to NNW-SSE trends amongst other orientations. This predominance reflects significant structural control exerted by the pre-existing anisotropy present in the metavolcanic rocks, i.e., the (N)NW-(S)SE magnetic foliation inherited from earlier D_1/D_2 deformation of the schist belt. Vein emplacement within the metavolcanic sequences has been previously attributed to fault-valve mechanism, wherein pre-existing fractures were repeatedly reactivated under fluctuating fluid pressure conditions during the late D_3 phase of deformation (Bhowmick and Mondal, 2020). High fluid pressure conditions enabled dilation and reactivation of fractures across all orientations, while intervening lower-pressure events selectively reactivated only those orientations favourably aligned with respect to the regional NW-SE compressional stress field prevailing during D_3 deformation. Among these, the NNW-SSE fractures were most responsive, owing to their high dilation and slip tendencies (Bhowmick and Mondal, 2021). Although field data and structural evidence confirm cyclic fault-valve activity, the number of discrete fluid pressure pulses responsible for successive fracture reactivation and vein deposition could not be quantified. Taking the heterogeneous distribution of vein data recorded from the study areas, the present study seeks to clarify this unresolved aspect.

4.3 Quantifying fluid pressure events using vein orientation data

Vein/dyke orientation data distribution patterns are widely employed for stress inversion and for denoting relative P_f conditions (Jolly and Sanderson, 1997; Martínez-Poza et al., 2014; McKeagney et al., 2004; Mazzarini et al., 2019). In earlier methods, the orientations of the principal stress axes have been determined from the geometry of the distribution pattern of vein/dyke orientation data. For a girdle pattern denoting high P_f condition, σ_1 lies at the center of the domain devoid of any data points. Clustering of vein orientation data is a typical feature of fracture hosted vein networks. For an elliptical cluster defining a low P_f condition, the σ_3 forms the center of the data cluster. However, an overall girdle distribution of data is often encountered consisting of multiple clusters which can be hardly distinguished owing to the complexity of the data distribution pattern. Each of these clusters might represent separate P_f conditions or they might be related to a single high P_f condition, however, they are not univocally related to different phases of deformation. Such complex data distribution patterns can form when multiple P_f events have transpired with the later high P_f events overlapping the earlier ones (low P_f). In such cases, one can never be certain about the chronology and intermittent time lapse between these events. Most importantly, how to quantify the number of P_f events? This requires a statistical approach towards grouping data sets and approximating the minimum number of P_f events. Yamaji et al. (2010) used Bingham distribution for detecting the paleostress conditions in case of vein data distribution forming a nebulous pattern instead of a well-defined cluster margin. In their study, gradational density distribution of vein data attributes to P_f fluctuations.

4.3.1 Methodology

Each vein data cluster observed in the Gadag and Chitradurga regions represented in the equal area projections **(Figs. 4.1b and 4.3)** might represent a separate P_f condition or can be a part of a single high P_f event under the same state of tectonic stress. Both the situations are considered here, where each of the clusters is evaluated independently and also as a part of a high P_f event. However, grouping data from a complex data distribution pattern is a difficult and challenging process. Therefore, the statistical approach provided by Yamaji et al. (2010), Yamaji and Sato (2011) and Yamaji (2016) has been adopted to quantify the minimum number of vein data clusters.

a. Statistical parameters for grouping the dataset

Out of the many statistical methods that could be adopted for grouping data sets, the method that is largely developed for efficient fuzzy clustering of vein orientation data has been selected. Fuzzy approach is gaining popularity in various aspects of structural geology (e.g., Anand et al. 2021). The method of fitting a Bingham distribution to the vein orientation data by generating a genetic algorithm has been elaborated by Yamaji (2016), Yamaji and Sato (2011), Yamaji et al. (2010) and Faye et al. (2018). According to these studies, the Bingham distribution is a probability distribution function that can be well fitted to any uniform, circular, elliptical, nebulous or girdle distribution pattern of 3D orientation data. Bingham distribution is represented by the concentration axes (minimum, intermediate and maximum concentration axes coinciding with σ_1, σ_2 and σ_3 principal stress axes, respectively) and concentration parameters (κ_1 and κ_2) representing the shape and spread of the data cluster. Therefore, in case of more than one cluster within a data distribution, each of the data clusters can be represented as a Bingham component with three concentration axes. Each of these concentration axes coincides with the principal stress axes deduced from the vein cluster **(Fig. 4.3)**. Variation in the orientation of the principal stress axes for each data cluster is attributed to the perturbation in the local stress field. Such variations are inevitable during vein emplacement even under a consistent far field stress. For an elliptical cone of data distribution pattern (as observed in this case), σ_3 is the symmetry axis representing the maximum concentration of data points within the cluster. Therefore, any random data distribution consisting of multiple clusters can be fitted with a mixed Bingham distribution model represented as a linear combination of Bingham components with multiple sets of concentration axes **(Fig. 4.4)**.

In the present study, the GArcmB code (http://www.kueps.kyoto-u.ac.jp/~web-bs/tsg/software/GArcmB/), programmed by Atsushi Yamaji (Yamaji, 2016), has been used for analyzing vein data distribution. This code allows the partition of orientation data into *K* number of clusters, where *K* is selected by the user itself. Another statistical parameter called the Bayesian Information Criterion (BIC) is also calculated for model selection, based on which the feasible value of *K* is determined. BIC helps to select the best fit model by determining the least error in a distribution.

$$\text{BIC} = -2ln(L) + Kln(n) \text{ (Yamaji, 2016)} \qquad (4.1)$$

where, n = number of data points in the distribution

K = number of parameters estimated by the model (number of clusters)

L = log-likelihood function giving the goodness of fit of the data to a model.

The code can be run by gradually increasing the number of clusters, K=1, 2, 3….n. However, an increase in *K* elevates the complexity of the model. It also increases the probability of any data point to belong to more than one cluster. In case of a distribution consisting of more than one cluster, *L* also denotes the membership of a data point to a particular cluster. Therefore, if *L* i.e., the goodness of fit of a data point to a cluster increases, then the BIC value automatically decreases keeping the values of *K* and *n* fixed for a single run. Automatically it gives the least error for model selection. Therefore, the compatible K value is chosen based on the lowest BIC and optimum L values from all the iterations.

The code was run separately for the Gadag and the Chitradurga regions to select the best partition of the datasets denoting the minimum number of vein data clusters. Analysis revealed that for the Gadag region, it is $K = 2$ at which the BIC is lowest (= 561.3535, **Fig. 4.3**) and that for the Chitradurga region, it is $K = 3$, for the lowest BIC (= 1253.0302, **Fig. 4.3**).

b. States of stress and fluid pressure determination

Cluster selection using statistical parameters is useful for P_f determination. There can be multiple low P_f events following or preceding a high P_f event. Thus, a low P_f event might reactivate specific orientations several times forming clusters. However, all such clusters might be reactivated again under a high P_f event, if the fractures are well connected to a fluid source. Therefore, if a region has suffered consecutive high and low P_f events then the girdle and clusters might overlap. Moreover, statistically it is not possible to establish the chronological sequence and time lapse between such events. Data overlapping is therefore a hindrance towards cluster selection. In this study, the clusters have been analyzed discretely and conjointly to consider both high and low P_f conditions. However, magnitudes of P_f estimated in this study cannot be regarded as the absolute P_f values, rather, they are only instances of the high and low P_f conditions. A single cluster represents a particular state of the local stress field denoted by the orientations of the concentration axes of the Bingham distribution. Further, there can be multiple small, high/low-density clusters within a large cluster but they are relatively similar in terms of orientation formed under the same state of stress. Thus, all fracture orientations belonging to a similar state of stress can be collectively treated as a single cluster. In general, the vein data clusters identified through the statistical method have different orientations of principal stress axes attributing towards the perturbation in local stress field during vein emplacement under a consistent far field (tectonic) stress. The P_f determined in this study is the minimum P_f required to reactivate a particular set of fracture orientations or a single cluster. However, one can never be certain regarding the chronology of veining events based on such clusters. The clusters might have reactivated conjointly under a high P_f condition or successively under low P_f conditions. Thus, following Jolly and Sanderson (1997), it is considered that the derived P_f magnitudes for the entire data set and individual clusters are representatives of both high and low P_f conditions respectively.

As stated earlier, Gadag and Chitradurga regions are related in terms of the tectonic stress field (late D_3) generating fractures at a shallow crustal depth, with an overall similarity in fracture orientation and vein emplacement mechanism. Depth of fracturing and shallow crustal vein emplacement in the Chitradurga region was calculated to be ~ 2.4 km by Mondal and Acharyya (2018) and Acharyya and Mondal (2019). In this study, this shallow crustal depth (~ 2.4 km) of fracturing and vein emplacement is considered for both Gadag and Chitradurga regions to understand the P_f conditions at a similar depth. Therefore, magnitudes of the principal stresses have been evaluated considering the depth of fracturing/faulting at ~ 2.4 km. McGarr (1980) provided some empirical equations for determining changes in the shear stress (τ_m) gradient with depth (< 7 km) under both extensional and compressional stress fields. For extensional stress fields, it has been observed that the gradient of τ_m increases with depth for at least the upper 3-4 km in hard rocks. Based on these considerations, the equations,

$$\tau_m = 5.0 + 6.6z \tag{4.2}$$

and

$$(\Delta\sigma) = 2\tau_m \tag{4.3}$$

(McGarr, 1980), hold true for shallow crustal depths of ~ 1-4 km.

In a normal faulting regime, σ_v (vertical stress) = σ_1. Using $\sigma_1 = h\rho g$, where h = depth of fracturing in metabasalts (~ 2.4 km), ρ = approximate bulk density of crust (2700 kg/m^3), g = 9.8 m/sec^2; it is calculated that σ_1 = 63.5 MPa. An average density of the metabasalts has been considered for clarity and as the simplest way of P_f determination, however, studies related to the density variation can be taken into account as an alternative method (Mukherjee, 2018). Similarly, using the empirical approach by McGarr (1980) and Mazzarini et al. (2019), at a crustal depth < 7 km, the differential stress ($\Delta\sigma$) is twice the shear stress (τ_m) at depth z (in km) in equations (4.2 and 4.3). Therefore, at ~ 2.4 km, σ_3 = 21.82 MPa. As documented from field observations, median planes of the quartz veins acted as slip surfaces, which were reactivated under successive fluid ingression **(Fig. 4.2e)**. Thus, field evidence shows fluid induced faulting with veining. The calculated magnitude of the maximum principal stress is three times larger than the minimum principal stress which further justifies such field observations along the greenstone belt.

The states of stress and fluid pressures have been determined from the respective clusters and the overall girdle distribution pattern. The equations provided by Jolly and Sanderson (1997) and Baer et al. (1994) have been used for deriving parameters, i.e., stress ratio (Φ), driving pressure ratio (R') and P_f magnitudes. θ_1, θ_2 and θ_3 are the ranges of fracture orientation calculated along the $\sigma_2\sigma_3$, $\sigma_1\sigma_3$ and $\sigma_1\sigma_2$ planes constructed on the equal area projections of pole to vein data following the deterministic approach of Jolly and Sanderson (1997).

$$R' = \frac{P_f - \sigma_3}{\sigma_1 - \sigma_3} = \frac{1 + cos2\theta_2}{2}. \tag{4.4}$$

For $P_f > \sigma_2$,

$$\Phi = \frac{\sigma_2 - \sigma_3}{\sigma_1 - \sigma_3} = 1 - \frac{1 - cos2\theta_2}{1 - cos2\theta_3}. \tag{4.5}$$

For $P_f < \sigma_2$,

$$\Phi = \frac{\sigma_2 - \sigma_3}{\sigma_1 - \sigma_3} = \frac{1 + cos2\theta_2}{1 + cos2\theta_1}. \tag{4.6}$$

Parameters derived for quantifying P_f values representing the high and low P_f events of both, Chitradurga and Gadag regions, are given in **Tables 4.1** and **4.2** respectively. For Chitradurga region, the girdle distribution has been considered to imply high P_f condition ($P_f > \sigma_2$) and the three clusters ($K = 3$), implying low P_f conditions ($P_f < \sigma_2$); **Fig. 4.5a** and **Table 4.1**. Similarly, for the Gadag region, the girdle distribution represents a high P_f condition ($P_f > \sigma_2$) and the two clusters ($K = 2$), represents low P_f conditions ($P_f < \sigma_2$); **Fig. 4.5b** and **Table 4.2**.

4.4 Results and discussion

The CSB is known for its auriferous lode deposits in the metavolcanic hosts. Such gold bearing lodes are abundant in the Gadag region. Few lode deposits are also seen in Chitradurga, but here occurrence of pervasive networks of auriferous quartz veins is more common. In this study, the minimum number of P_f events responsible for vein emplacement in these two regions of the CSB has been estimated. The number of clusters obtained from fuzzy clustering of the heterogeneous vein orientation data represents the minimum number of recorded P_f events in the two regions. However, the precise number of such high and low P_f events cannot be asserted with absolute certainty. It can however be stated that the data clusters obtained from this statistical method each represent a low P_f event which must have contributed to the high P_f event. In this study, a shallow crustal depth range (~ 2.4 km) for vein emplacement has been considered in the region as estimated from the depth of fracturing (Mondal and Acharyya, 2018 and Acharyya and Mondal, 2019); however, the source of the silica enriched fluid is still debatable. It is suspected that residual fluids might have been channelized along the pre-existing fractures during the emplacement of granitic plutons in close vicinity. Emplacement of younger granites (~ 2.6 Ga) along the core of the schist belt and their time relationship to the regional tectonics is well established from previous studies, for example, the Mulgund granite close to the Gadag region, and the Chitradurga and J. N. Kote granites close to the Chitradurga region (Mondal and Mamtani, 2013; 2014 and Mondal et al., 2020). P_f needs to exceed the normal stress along the fracture walls. A variation in P_f with depth has been considered to understand the fluid pressure conditions prevailing at a depth of ~ 4 km, the lower bound for shallow crustal fracturing. Normally, it is found that P_f gradually increases with depth which also holds true for principal stresses. Presence of sub-surface pressure seals might suddenly elevate the P_f until the pressure seal is ruptured. However, such pressure compartments could not have sustained huge volumes of fluid for a very long time under a transtensional stress field. Besides, the pre-existing anisotropies were suitably oriented for channelizing the fluid. Spatial variation in fluid pressure calls for considering the lithostatic overburden at a shallow crustal level. To understand the variation in P_f with the overburden pressure, the pore fluid factor, $\lambda_v = P_f/\sigma_v$ (Sibson, 2020) has been considered. It has been found that the minimum and maximum recorded values of λ_v vary between 0.38 and 0.96, depending upon the minimum and maximum calculated P_f magnitudes in both the studied regions (see **Tables 4.1** & **4.2**). This indicates a sub-hydrostatic to near-lithostatic P_f condition in the two regions (Sibson, 2020; **Fig. 4.6**). In Chitradurga, the maximum P_f variation i.e., the difference between the highest and the lowest recorded P_f is ($\Delta P_f \sim 11.67$ MPa) and λ_v varies between 0.68 and 0.87 approximately, and, in Gadag, ($\Delta P_f \sim 36.25$ MPa) and λ_v varies between 0.38 and 0.96. At a similar depth, $\lambda_v \longrightarrow 1$ ($\lambda_v \approx 0.96$) in Gadag, hints towards a near-lithostatic P_f condition.

The fuzzy clustering of vein data enables us to identify the minimum number of P_f events in the Gadag and Chitradurga region **(Fig. 4.3)**. Comparing the two regions, the highest recorded P_f magnitude in Gadag exceeds that of Chitradurga. This indicates fluid overpressure in Gadag, justifying the formation of lode deposits. Signatures of fluid overpressure are also prominent in the veins showing clear evidence of *fault-valve action*, with fragments of wall rock incorporated in the quartz veins **(Fig. 4.2e)**. However, evidence of hydrofracturing with random fracture orientations within the host rock are not perceived. The fracture orientations are coherent and related to the tectonic stress field. It is also found that the highest estimated P_f magnitude is nearly close to the maximum principal stress (σ_1), justifying the abundance of lode deposits in Gadag. In the Chitradurga region a greater number of P_f events, statistically estimated from the vein data clusters (K = 3), generated an intense network of relatively thinner veins. The thickest vein recorded along the pre-existing anisotropy is ~ 27 cm in Chitradurga and therefore much less than the maximum vein thickness in Gadag (~ 47 cm); **Fig. 4.1b**. However, it is also observed that at the lowest normal stress (σ_n), veins are more abundant in Chitradurga than in Gadag, which justifies the intense vein network in the Chitradurga region **(Fig. 4.5)**.

Statistical models provide a unique opportunity to solve data clustering problems and in this study, for identifying the minimum number of low P_f events that contributed to the overall high P_f event. However, all statistical models have some limitations. With increasing randomness in the dataset, it is difficult to identify the smaller P_f events from a complex dataset representing a vast P_f event. There can be multiple small clusters within a large cluster belonging to the same state of stress. Sometimes, due to data overlapping the Bingham distribution function cannot distinguish the smaller clusters. Then the concentration axes represent the state of stress only for the larger cluster. Therefore, a clear idea regarding the maximum number of low P_f events cannot be perceived. Each of the clusters represent a range of vein orientations that were reactivated under a P_f condition. However, the statistical models do not help to understand the relative chronology of the events or the time interval between two such low or high P_f events, adding to the lacuna. Establishing the time relationship between the P_f events and segregating the smaller clusters from a large data cluster can be regarded as a challenge that needs to be addressed in the near future.

4.5 Summary

In the present study, statistical methods and deterministic approach have been combined for selecting the number of feasible vein data clusters representing the minimum number of P_f events and for evaluating the representative P_f magnitudes for each P_f event independently and collectively. In Gadag region, two distinct vein data clusters have been identified which corresponds to at least two P_f events. Maximum P_f variation i.e., the difference between the highest and the lowest recorded P_f is ($\Delta P_f \sim$ 36.25 MPa) for Gadag. In Chitradurga region, three data clusters have been separated from the bulk of vein orientation data distribution thereby indicating a minimum of three P_f events which might have eventually contributed or culminated in a high P_f condition. The difference between the highest and the lowest recorded P_f is ($\Delta P_f \sim 11.67$ MPa) in this region. Significantly high P_f magnitude (near-lithostatic P_f condition), close to the maximum principal stress and higher ΔP_f values justify the abundance of veins with greater thickness in the Gadag region with remarkable prospects for gold mineralization. Fuzzy clustering of vein data using a probability distribution function is extremely useful for approximating the minimum number of P_f events within a vast episode of fluid ingression. However, the chronology of P_f events, time interval between two successive events and considerable data overlapping adds to the limitation of this statistical method.

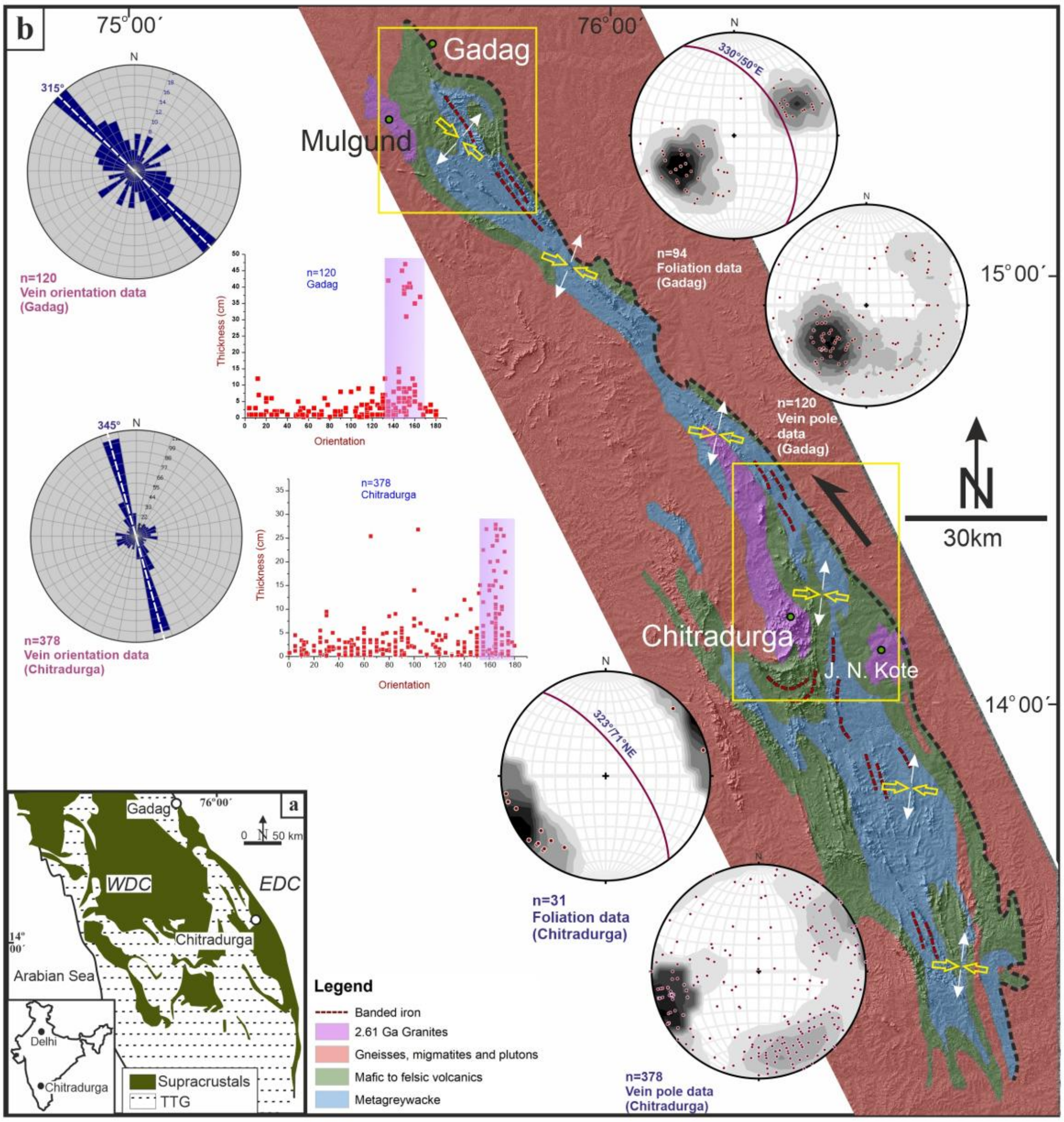

Fig. 4.1 (a) Regional map of WDC and EDC, South Indian Shield (modified after Chadwick et al., 2003), within the Indian subcontinent (inset). EDC=Eastern Dharwar Craton, WDC=Western Dharwar Craton, TTG=Tonalite-Trondhjemite-Granodiorite, Supracrustals=volcano-sedimentary assemblages. **(b)** Digital Elevation Model of the Chitradurga Schist Belt (CSB), modified after Jayananda et al., 2013. Eastern boundary of the CSB represents the Chitradurga Shear Zone (CSZ), marked with black dotted line. Stress history related to the late D_3 deformation along the greenstone belt. Stress axes orientations: White arrow marks the extension direction (σ_3) and yellow arrow marks the compression direction. Extension direction varies between NE-SW to NNE-SSW from Chitradurga to Gadag. Contd.

Fig. 4.1 Contd. Lower hemisphere equal area plots - Gadag foliation data (n=94, mean ~330/50° E), contoured vein pole data (n=120), Chitradurga foliation data (n=31, mean ~323/71° NE), contoured vein pole data (n=378), from top (right) to bottom (left). Rose diagrams for vein orientation data from Gadag and Chitradurga. Yellow boxes demarcate the study areas. Vein thickness vs. orientation graphs from Gadag and Chitradurga. Vein abundance and maximum vein thickness are recorded along the ~NW-SE orientations in Gadag and ~NNW-SSE orientations in Chitradurga.

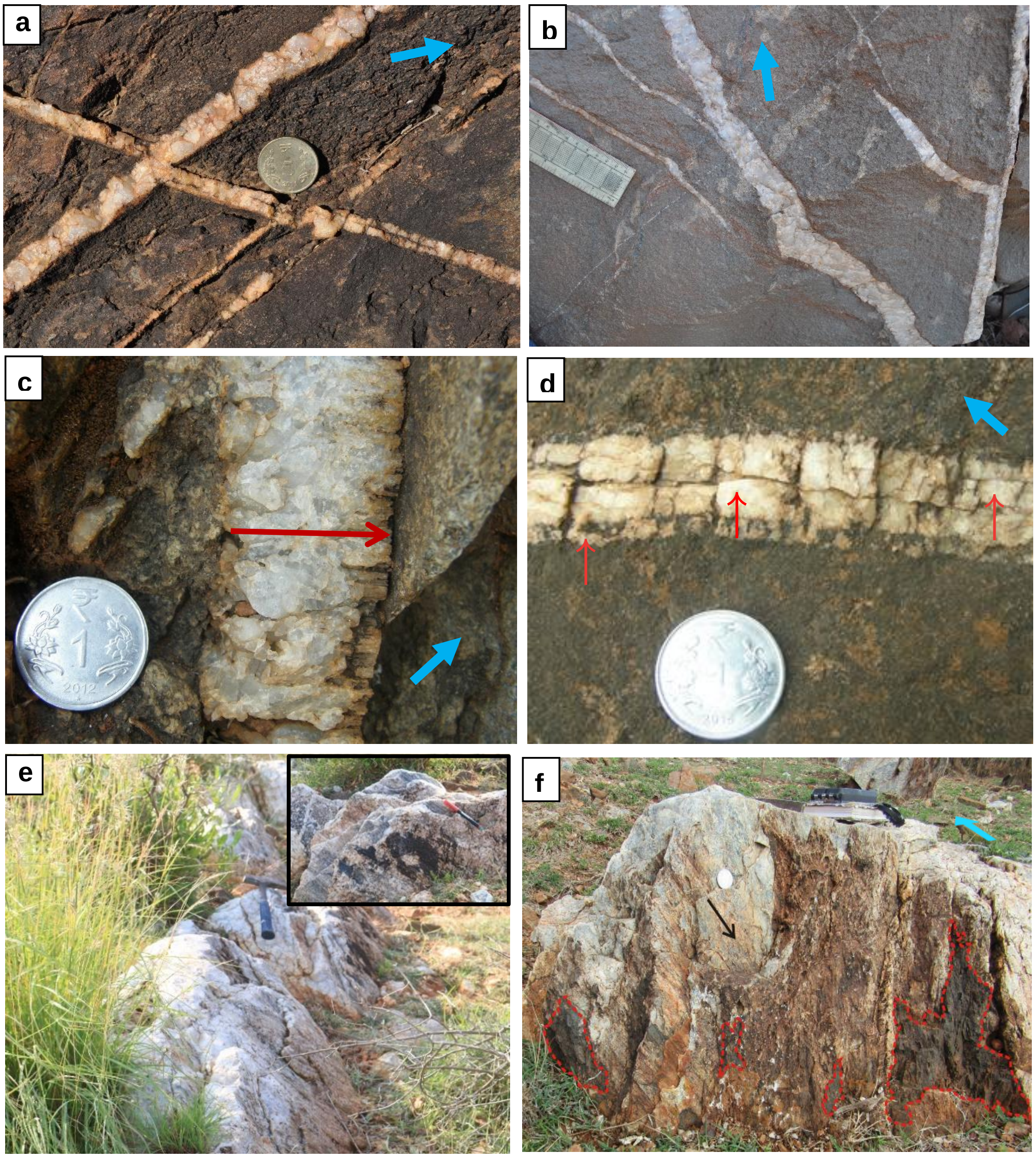

Fig. 4.2 Field photographs from the study area. **(a, b)** Criss-cross orientation of quartz veins, branching of veins in metabasalts (Gadag). **(c)** Close-up view of a quartz vein in metabasalt showing crystal growth direction (red arrow) perpendicular to the vein wall. **(d)** Multiple median lines (red arrows) preserved within a single quartz vein indicating cyclic fluid ingress. **(e)** NE dipping quartz vein showing slickenside lineations (maximum recorded width = 47 cm), inset showing close up of the fault plane found in e. Marker pen placed along the orientation of the slickenside lineations. **(f)** Angular chunks of metabasalt (enclaves) enclosed within a faulted quartz vein, denoting 'fault-valve' action. Dotted red line demarcates the enclave boundaries. Black arrow marks the slickenside lineations on the fault plane. Blue arrows mark the north direction.

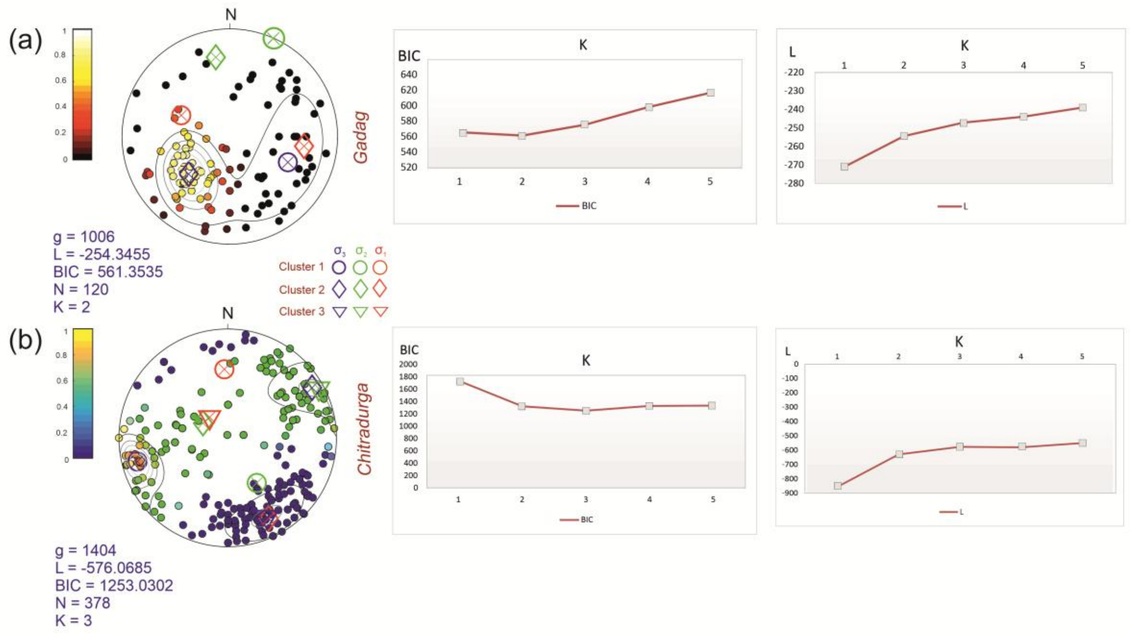

Fig. 4.3 Fuzzy clustering of vein pole data using GArcmB software. Results obtained from Gadag and Chitradurga regions, yellow boxes in Fig. 4.1b, demarcate the study areas from where vein orientation data has been collected. **(a)** For Gadag region (*K*=2) and **(b)** for Chitradurga region (*K*=3), at minimum BIC and optimum *L* values which means the data can be partitioned into two and three clusters respectively. The colored symbols represent the stress axes orientations for each cluster (resembling the concentration axes for a Bingham distribution).

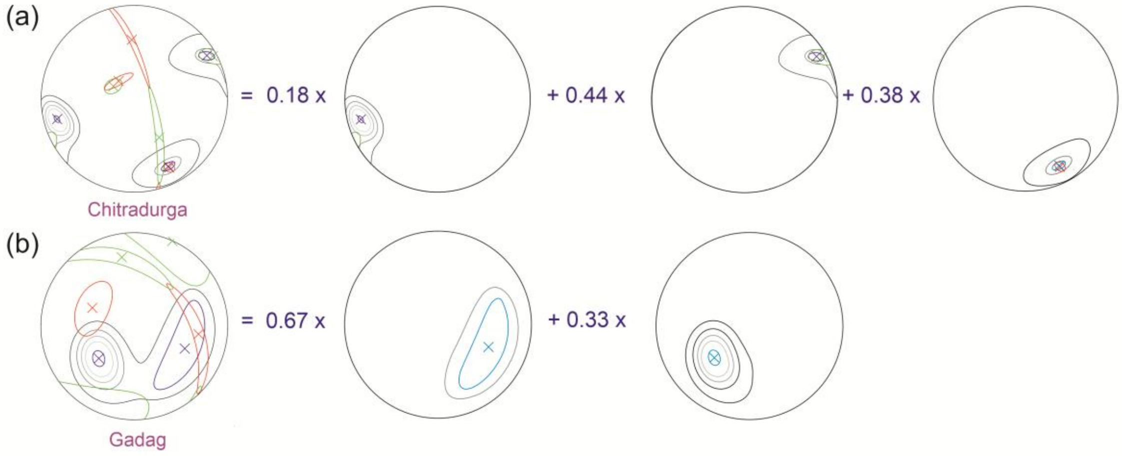

Fig. 4.4 Equal area projections of contoured vein data denoting the probability densities (mixing coefficients) of the clusters. **(a)** for Chitradurga region and **(b)** for Gadag region. Yellow boxes in Fig. 4.1b, demarcate the study areas from where vein orientation data has been collected for the respective equal area projections. The clusters represent the Bingham components of a mixed Bingham distribution. Concentration axes (cross symbols) within the contours are provided with 95% confidence regions (red, green and blue ellipse) for each cluster. Mixing coefficients for Chitradurga vein data, 0.18 (WSW cluster), 0.44 (NE cluster), 0.38 (SE cluster). Mixing coefficients for Gadag vein data, 0.67 (SE cluster), 0.33 (SW cluster).

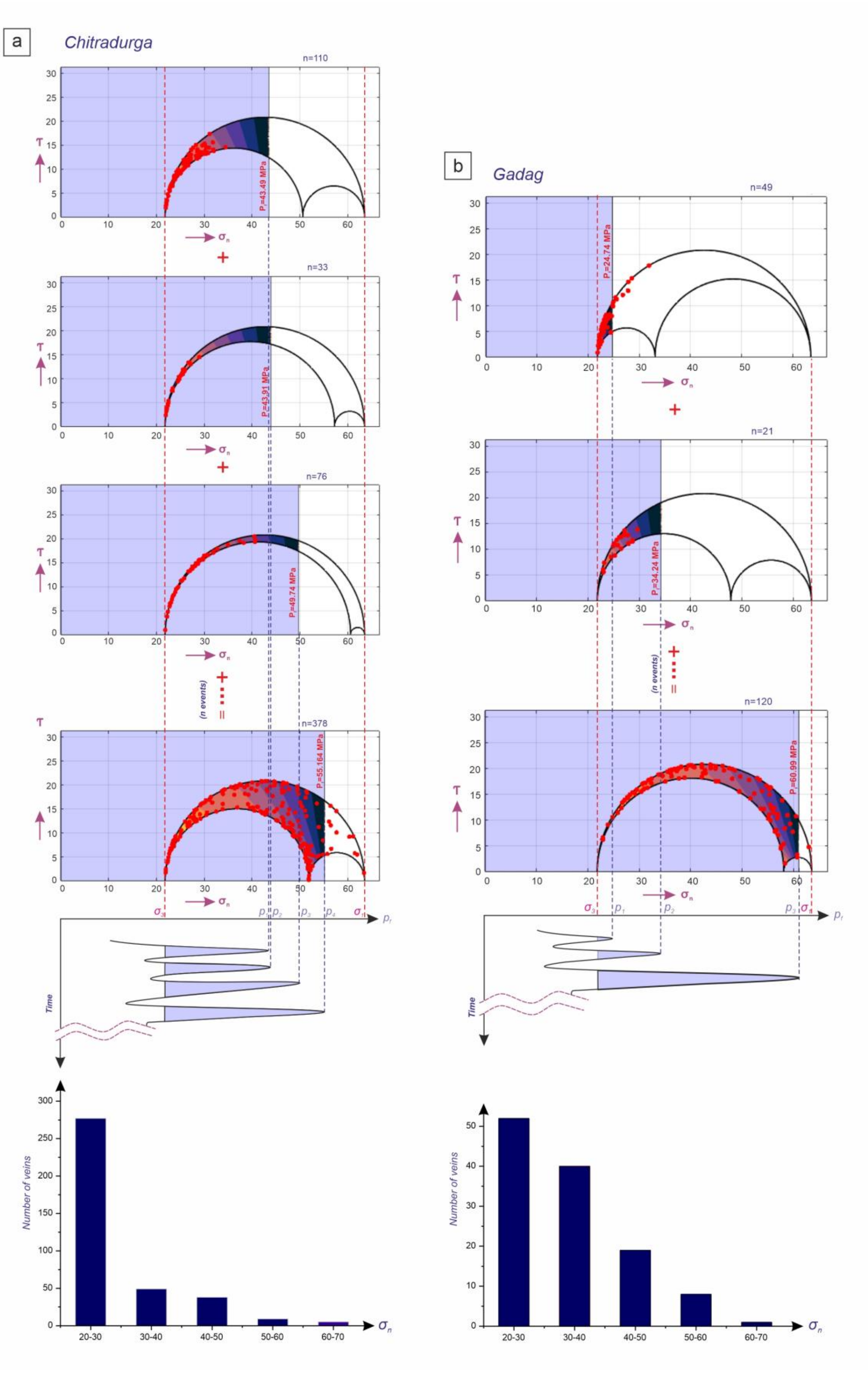
a
Chitradurga
n=110
P=43.49 MPa
n=33
P=43.91 MPa
n=76
P=49.74 MPa
(n events)
n=378
P=55.164 MPa
τ
σn
σ3
p1
p2
p3
p4
σ1
pf
Time
Number of veins
20-30
30-40
40-50
50-60
60-70
b
Gadag
n=49
P=24.74 MPa
n=21
P=34.24 MPa
(n events)
n=120
P=60.99 MPa
σ3
p1
p2
p3
σ1
pf
Time
Number of veins
20-30
30-40
40-50
50-60
60-70

Fig. 4.5 Schematic model showing the estimated P_f events along the CSB in **(a)** Chitradurga and **(b)** Gadag regions. P_f magnitudes determined and graphically represented in 3D Mohr circles (FracTend code available via Healy, 2017). The dotted line at the right end of the blue rectangular space denotes the P_f. Under high P_f condition, the P_f line crosses the σ_2 along the normal stress axis. The conceptual graph shows multiple high and low P_f events *(n times)* until the fluid source is exhausted. Each of the peaks stand for the P_f magnitude represented in the Mohr circle. It is to be noted that the P_f exceeds σ_3 but even the highest recorded P_f does not exceed σ_1. In the case of Gadag, the highest recorded P_f is close to σ_1. Red dotted lines represent the principal stresses and the blue dotted lines mark the peak of each P_f cycle. Red circular dots within the Mohr circles represent the vein pole data. In the bar diagrams, the number of veins considerably decreases with increasing normal stress along the fracture surface. Highest P_f magnitude is recorded in Gadag, whereas vein frequency of Chitradurga exceeds Gadag supporting the field evidence of intense vein network. 'Thermal' colour scheme from Thyng et al. (2016).

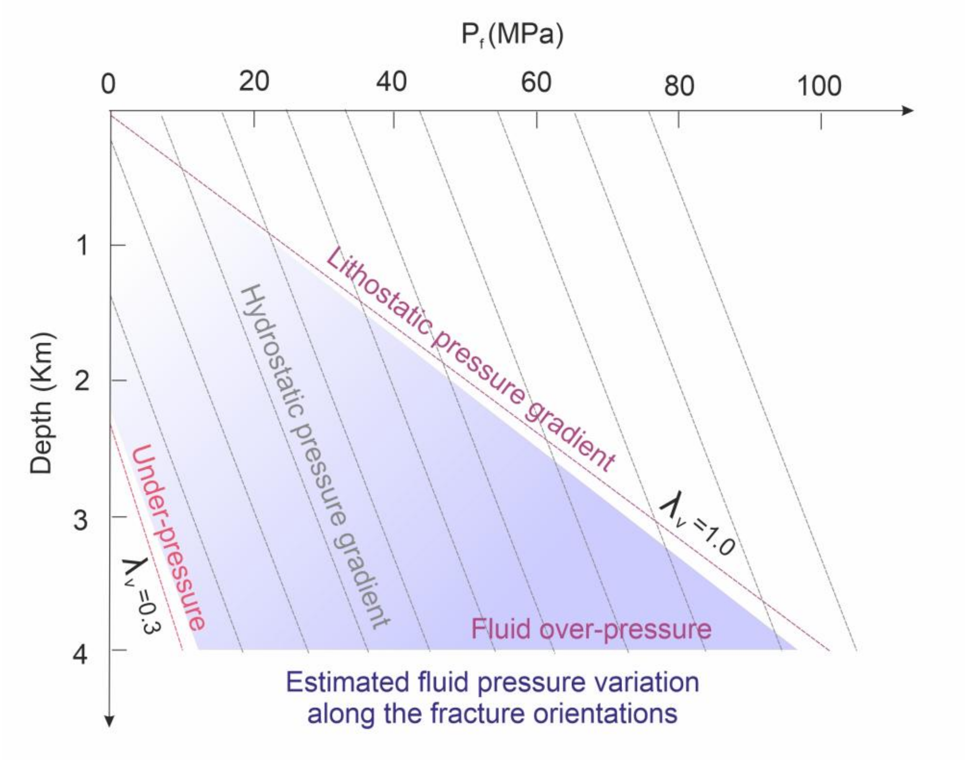

Fig. 4.6 Conceptual diagram on depth dependence of fluid pressure. Vein emplacement under sub-hydrostatic to near-lithostatic P_f condition as evident from pore fluid factor (λ_v). λ_v broadly varies between 0.38 to 0.96 in the region, indicating a sub-hydrostatic to near-lithostatic P_f condition.

Chitradurga region				
Parameters	$P_f > \sigma_2$	$P_f < \sigma_2$		
	Entire Girdle	WSW cluster	NE cluster	SE cluster
Φ	0.72	0.85	0.93	0.69
R´	0.8	0.53	0.67	0.52
P_f (MPa)	55.164	43.91	49.74	43.49

Table. 4.1 Parameters derived for quantifying P_f values in Chitradurga region.

Gadag region			
Parameters	$P_f > \sigma_2$	$P_f < \sigma_2$	
	Entire Girdle	SW cluster	SE cluster
Φ	0.87	0.27	0.62
R´	0.94	0.07	0.29
P_f (MPa)	60.99	24.74	34.24

Table. 4.2 Parameters derived for quantifying P_f values in the Gadag region.

Chapter 5: Dykes

CONTENTS **Page No.**

CHAPTER 5

Dykes

5.1 Introduction

Dykes are ubiquitous intrusive igneous bodies which are integral components of the earth’s crust. They act as major pathways for magma transport from depth to the surface of the earth and also carry crucial information about geodynamic processes (Gudmundsson, 2020). Their widespread occurrence at every scale in almost all of the cratons around the world indicates their relation to craton evolution and stabilization (Evans and Halls, 2010; Söderlund et al., 2019). Extensive research has been conducted to infer probable mechanisms of dyke emplacement (Currie and Ferguson, 1970; Pollard, 1973; Pollard, 1987; Townsend et al., 2017; Pollard and Martel, 2020; Gudmundsson, 2020; 2022a). While dyke geometry in 2D has been utilized to understand far-field stress, their orientations have been widely used to infer relative stress state using 3D Mohr circle (Jolly and Sanderson, 1997; Yamaji and Sato, 2011; Martinez-Poza et al., 2014; Martinez-Poza and Druguet, 2016; Pascal, 2021).

Parts of this chapter have been published in ***Biswas et al. (2023), Journal of Structural Geology****, https://doi.org/10.1016/j.jsg.2023.104822;* ***Biswas and Mondal (2024), Journal of Asian Earth Sciences****, https://doi.org/10.1016/j.jseaes.2024.106359; and* ***Biswas et al. (2025), Journal of Structural Geology****, https://doi.org/10.1016/j.jsg.2025.105350 .*

Mechanically, dykes form as extension fractures in the sense that magma pressure inside them surpasses the least principal compressive stress acting normal to their walls effectively making the principal stress tensile. The magnitude of this ‘overpressure’ has long been estimated utilizing length/width (thickness) ratios of the dykes assuming a linear elastic fracture model (Sneddon and Lowengrub, 1969; Parker, 1981; Gudmundsson, 1983b; Pollard and Martel, 2020) based on a set of idealizations, viz. 1) The host rock is assumed to be infinite, homogenous and isotropic with respect to linear elastic material properties. 2) The crack/fracture is straight and infinitely long in the coordinate direction perpendicular to the plane of view. 3) The fracture is loaded by a uniform internal pressure and by a homogenous remote stress with the least compressive principal stress oriented perpendicular to the fracture plane. Subject to fulfilment of the above-stated conditions, the fracture will ideally open in an elliptical shape. This method of estimating magma overpressure from dykes therefore requires determining the center of this ellipse or knowing its complete length and maximum thickness or the maximum opening displacement (measured either along the strike dimension or the dip dimension of dykes). Complete dyke dimensions and thereby their aspect ratios are also crucial for the estimation of a plethora of other important parameters like depth of origin of the dykes, fracture toughness of the host lithology and assessing potential explosivity of fissure eruptions when they occur in the vicinity of volcanoes (Gudmundsson, 1983a; Kusumoto et al., 2013; Becerril et al., 2013; Geshi et al., 2020). However, most dyke outcrops observable at any scale are only partial, due to weathering, fault related obliteration or due to the nature of the outcrop in itself, which creates difficulty in deducing their true dimensions and therefore, the aspect ratios. Such limited outcrops often result in erroneous estimates of magma overpressure, since the length dimension of dykes mostly remain underestimated.

Therefore, in the present study, mathematical methods have been pioneered to estimate complete dyke dimensions from their partial exposures consisting either a single tip at one end as well as from those which are devoid of any tips. Since dykes form as dominantly opening mode fractures, the methods are built upon its idealized canonical model and utilizes the predicted elliptical shape of fracture opening in the model, to estimate their full length, maximum opening displacement/width and aspect ratio (width/length) from limited outcrop measurements. The validity of the methods has been tested against ground data and published data. Although developed for dykes, the methods have potential for wider application, since they can be used fundamentally to predict complete dimensions of any elliptical shaped natural features from their partial exposures.

Although the current research focuses on the Chitradurga region of the CSB, WDC, where partially exposed mafic dykes intruding the ~ 2.61 Ga younger granites have been analyzed, applying the presently developed methods, to estimate magma overpressures and depths of origin, the consistent occurrence of mafic dykes at the uppermost stratigraphic levels of both the WDC and EDC necessitates a comparative analysis. To this end, mafic dykes intruding the Closepet granite, an equivalent pluton in the EDC, have also been incorporated within the scope of the study allowing direct comparison of magma overpressure and emplacement depth estimates of mafic dykes between the two parts of the craton.

Dykes also retain key information to decipher the tectono-magmatic evolution of the rocks through which they intrude, which leads to the reconstruction of local variations in paleostress states ambient at the time of their ascent, utilizing their outcrop shapes and geometry (Martinez-Poza et al., 2014).

Mafic dykes encountered within the younger granites of the Dharwar Craton (both in the WDC and EDC), India often exhibit outcrop attributes which differ from the ideal elliptical opening and are characteristic of emplacement under conditions of mixed mode loading. Comparative structural analysis of such dyke outcrops from the Chitradurga and Closepet granites of the WDC and EDC respectively, has been conducted to assess whether similar emplacement mechanisms operated uniformly across the Dharwar Craton during its late-stage stabilization or if regional variations in stress regimes played a role in dyke emplacement processes.

In this regard, different discrete modes of fracture formation and their possible combinations have been discussed to understand the generation and eventual emplacement of dykes under mixed mode loading. This leads to the development of a comprehensive sequence of progressive dyke evolution under mixed mode I-III loading and thereby distinguishing incremental orders of dyke horn formation.

These concepts along with collected field evidence on dyke body geometries have been applied in unison to propose an evolutionary model of dyke formation and emplacement within the Chitradurga granite under varying regional stress fields of the Chitradurga Schist Belt, Western Dharwar Craton, India. It has been inferred, that the dykes initiated as extensional fractures within an earlier NE-SW directed compressive stress field and were subsequently sheared sinistrally by the effect of the adjacent Chitradurga Shear Zone on account of a later E-W to ESE-WNW directed compression.

5.2 Magma overpressure estimation from partially exposed dykes with single tip

A mathematical method for calculating total length and maximum thickness of dykes from their partial outcrops having at least one exposed tip has been proposed, considering them to have formed as dominantly opening mode fractures. The method has been validated through observations made on felsic dykes found within porphyritic granitoids of Chotanagpur Granite Gneiss Complex (CGGC), India, which are either completely exposed or have an exposed tip and confirmed middle part. The method has also been tested against published data and results available on the dykes exposed on the caldera walls of the Miyake-jima volcano, Japan (Geshi et al., 2010; Kusumoto et al., 2013). It is found, that calculated results agree well to those published. Finally, the method has been applied to partially exposed mafic dykes emplaced within younger granite (Chitradurga granite) of the Chitradurga Schist Belt located in Western Dharwar Craton, Karnataka, India and the calculated results are used to estimate the range of their magma overpressures and depths of origin, as well as, the fracture toughness of the host granite.

5.2.1 Methodology

For dykes which are dominantly magma-driven Mode I cracks or extension fractures, the total internal magma pressure exceeds the minimum principal compressive stress acting normal to their walls, effectively opening the fracture in the direction perpendicular to the maximum principal compressive stress (Gudmundsson, 2020). For pure opening mode fractures, the fracture plane is perpendicular to the least principal compressive stress and opens parallel to it. The difference between the total magma pressure and the least principal compressive stress is termed as ‘magma overpressure’. The magnitude of this overpressure has long been estimated by several researchers (Gudmundsson, 1983b; Becerril et al., 2013; Kusumoto et al., 2013) using the following equation (Sneddon and Lowengrub, 1969, Parker, 1981):

$$u_y = \frac{\mathbf{2(1-\upsilon^2)P_o}}{\boldsymbol{E}}\sqrt{\boldsymbol{a^2 - x^2}} \tag{5.1}$$

where, P$_0$ is the magma overpressure; E and υ are the Young's modulus and Poisson's ratio of the host rock, and a is the half-length of the extension fracture or the dyke, respectively. Here, u$_y$ gives the opening displacement of the dyke measured along the ordinate at a distance x from the center of the dyke. Rearranging equation (5.1) as:

$$\boldsymbol{\frac{x^2}{a^2} + \frac{u_y^2}{\left[\frac{2(1-\upsilon^2)P_O}{E}\right]^2 a^2} = 1} \tag{5.2}$$

shows that the dyke shall open in the shape of an ellipse (plane strain condition) where its semi minor axis (half of the opening displacement), b is represented by the following relation:

$$\boldsymbol{b = \frac{2(1-\upsilon^2)P_0 a}{E}} \qquad (5.3).$$

Although natural extension fractures, in the present context, dykes, often show curvy or irregular boundaries, their overall irregular shape tends to closely approximate that of an ellipse, if they originate as dominantly opening mode fractures (Gudmundsson, 2022b). This ellipse is herein referred to as the 'mean ellipse'. Ideally, every point on the margin of an extension fracture/dyke should lie on the perimeter of this 'mean ellipse' but naturally they may occur at some deviation from it which may be caused due to intrinsic heterogeneities of the host rock and magma or as a result of the thermal effects of the ascending magma and its subsequent cooling at later stage (Bruce and Huppert, 1989; Becerril et al., 2013). Positioning the origin of the coordinate system at one of the vertices of this 'mean ellipse' (which corresponds to the respective tip of the extension fracture/dyke) and the abscissa along its length, the equation of the ellipse becomes:

$$\frac{(x-a)^2}{a^2}+\frac{y^2}{b^2}=1 \tag{5.4}$$

where, a and b are the half-length and half maximum thickness of the 'mean ellipse' respectively and (x, y) denotes the coordinates of any point lying on the perimeter of the 'mean ellipse' **(Fig. 5.1)**. The equation can be solved for the values of a and b if any two points lying on the perimeter of the 'mean ellipse' are known. Measured intervals along the abscissa and their corresponding half thicknesses give the co-ordinates of points which lie on the margin of the fracture/dyke. Since all observed points on the margin of the fracture/dyke do not coincide with the perimeter of the 'mean ellipse', the equation has been solved with every possible combination of two such measured points to obtain the total length (2a=A) and maximum thickness (2b=B) of the ellipse. The solutions produce several ellipses of varying lengths and thicknesses and some error values. The errors arise from the combination of any two such points which, subject to the same origin, do not permit an ellipse to be drawn through them. Excluding the errors, the mean values of all calculated lengths and thicknesses are considered to obtain the aspect ratio of the extension fracture or the dyke **(Fig. 5.2)**.

5.2.2 Testing of proposed methodology

a. Testing of method against ground data

In order to test the validity of the proposed method completely exposed (tip to tip visible) dyke outcrops have been searched for in vicinity and some were located within the intrusive granitoid bodies of Chotanagpur Granite Gneiss Complex (CGGC), eastern India. The CGGC is a sub-arcuate shaped, E-W trending Proterozoic belt located in the eastern part of India within the states of West Bengal, Jharkhand and parts of Bihar. In the south, its extent is marked by a E-W to ENE-WSW trending crustal-scale shear zone known as the South Purulia Shear Zone (SPSZ) (Mazumdar, 1988; Sanyal and Sengupta, 2012). Three distinct lithostratigraphic units are recognized here viz. the oldest crystalline basement, older metasediments and later intrusives (Ghose, 1983; Banerji, 1991). The regional gneissic foliation trends E-W to ENE-WSW. The targeted area, namely Bero-Saltora sector, located in Purulia and Bankura districts of West Bengal, India consists of migmatitic quartzo-feldspathic gneiss with enclaves of metapelitic gneisses which is further intruded by massif type anorthosite and porphyritic granitoids (Sanyal and Sengupta, 2012).

To validate the present method, data has been collected from seven ESE-WNW trending felsic dykes found within the porphyritic granitoids close to Bero hills, Purulia. (See **Supplementary sheet – 5.1** for location, geological map and field photographs of the dyke outcrops). Four of these dykes are completely exposed showing nearly symmetric tips at both ends, while three of them have a confirmed exposed middle part with at least one visible tip. The dykes are meter scale in length and centimeter scale in thickness and propagate linearly maintaining a distinctly sharp contact with the host rock. These dykes do not show curvature near their tips and are not arranged in systematic arrays of en echelon segments. Based on these observations, these dykes are considered to have formed as dominantly opening mode fractures. It may be noted that the present method has also been tested for one entirely exposed (tip to tip) dominantly opening mode mafic dyke observed within Chitradurga granite of Chitradurga Schist Belt, Western Dharwar Craton, India **(Fig. 5.4)**, thereby summing up the test dataset to a total of eight dykes. On application of the present method to the data collected from these eight dykes (See **Supplementary sheet – 5.2** for details of the collected data), it is found that the calculated dyke dimensions match closely with the actual measured data.

Average error for calculated full dyke lengths stands at 2.4% with a standard deviation of 1.7 (coefficient of variation=0.7) while that for calculated maximum thicknesses is 5.6% with a corresponding standard deviation of 5.3 (coefficient of variation=0.9) (See **Supplementary sheet – 5.2** for details of calculations and comparison). **Figure 5.3a** represents the graphical comparison of actual dyke dimensions and the calculated results.

b. Testing of method against published data

The method has also been tested for fifteen dykes reported in Geshi et al. (2010). These are arrested non-feeder dykes exposed in the caldera walls of Miyake-jima, Japan, where the upper tips of the dykes are known, but the lower tips are concealed. The required length intervals and corresponding half thicknesses measured from the known tip of the dykes are collected from the supplementary sheet of Geshi et al. (2010) and the present method has been applied to calculate total lengths and maximum thicknesses for these dykes. Calculated results are congruent to those published in Kusumoto et al. (2013), where full lengths and maximum thicknesses of these fifteen partially exposed dykes (collected from Geshi et al., 2010) have been estimated using a non-linear (Gauss-Newton) least squares analysis. **Figures 5.3b and 5.3c** represent the graphical comparison of the calculated and published results. See **Supplementary sheet – 5.3** for details of comparison.

Calculated dimensions of all other dykes match well to those estimated by Kusumoto et al., 2013 (coefficient of variation equals to 0.609 and 0.694 for total dyke lengths and maximum dyke thicknesses, respectively) except for one dyke showing stark contrast in estimated lengths. According to Kusumoto et al. (2013), estimated length of dyke no. 90-03 is 114.2m while our length estimate for the same dyke stands at 215.7m. For this dyke, data has been collected up to about 97 m with a corresponding thickness of 0.86 m. The abrupt termination of the dyke length at 114.2 m as estimated by the non-linear least squares model used by Kusumoto et al. (2013), results from the optimization converging at a local minimum instead of the global minimum. This happened due to a considerable difference between the actual dyke length and the random starting value for the same which has been used to begin the optimization, eventually resulting in an underestimation of dyke length.

5.2.3 Application

The present method has been applied to partially exposed mafic dykes emplaced within younger granite (2.61 Ga; Jayananda et al., 2006) of Chitradurga Schist Belt (CSB), which is an Archean granite-greenstone belt located in the Western Dharwar Craton (WDC) of India (**Figs. 5.4a, 5.4b**; Chakrabarti et al.,2006; Ramakrishnan and Vaidyanadhan, 2010). **Figure 5.4b** shows the location and regional geological map of the study area. **Figure 5.4c** exhibits the disposition of some mafic dykes encountered in one of the study areas. The dykes are mostly meter scale in length and centimeter scale in thickness, their mean orientation varying from NW-SE to N-S. Mostly, the dykes propagate linearly maintaining a sharp boundary with the host granite **(Fig. 5.5a)**. They do not exhibit markedly curved tips or systematic array of en echelon segments. A set of fractures are observed to have developed within the dyke bodies with orientations varying from E-W to ESE-WNW **(Fig. 5.5b)**. One dyke encountered in the field preserve prominent pointed tips at both ends which are mostly symmetric. However, most of the dykes observed within the study area are partly exposed and are either devoid of exposed tips or show only one exposed tip **(Fig. 5.5c)**. Based on these observations we infer them as dominantly opening mode dykes.

However, at places, few dykes show curved segments and are sometimes offset both dextrally and sinistrally by small scale shear zones. It has been observed that some of these dykes feature protuberances called 'horns' (Delaney and Pollard, 1981; Weinberger et al., 2000; Gudmundsson, 2020; 2022a) which branch out from the margin of the main dyke body and propagate for some distance before ending up in a tip **(Fig. 5.6)**.

Calculated full lengths (A) and maximum thicknesses (B) of the dominantly opening mode dykes are used to obtain their aspect ratio which we define as B/A. The aspect ratio is used to calculate magma overpressure (P_o) for each dyke by re-arranging equation (5.3) as:

$$P_o = \frac{E}{2(1-\upsilon^2)}\frac{b}{a} \qquad (5.5).$$

P-wave velocity of the host granite has been measured from NX size drill core samples using the Portable Ultrasonic Non-destructive Digital Indicating Tester (PUNDIT) following ISRM (2007) standards.

Average P-wave velocity for the host Chitradurga granite is found to be around 5500m/s. Density and Poisson's ratio of Chitradurga granite are considered to be 2700kg/m^3 and 0.3 respectively (Mondal and Acharyya, 2018). The dynamic Young's modulus is calculated applying these values in the equation:

$$E_d = \frac{V^2(1+\upsilon)(1-2\upsilon)\rho}{(1-\upsilon)} \qquad (5.6)$$

where E_d is the dynamic Young's modulus, V is the P-wave velocity and ρ is the density of the host rock material (Jaeger & Cook, 1969). According to Jaeger and Cook (1969) and Jaeger (1979), for most rocks, the E_d/E_s ratio ranges from about 1.4 to 2.8, where E_s is the static Young's modulus. The static value of Young's modulus ($E=E_s$) is utilized assuming $E_d/E_s=2.8$ (Gudmundsson, 1983b; 1988). Considering the density of the intruding mafic magma (ρ_m) to be ~ 3000 kg/m^3 (Bajgain et al., 2015; Paulatto et al., 2019), the depth of origin for the dykes are calculated using the equation:

$$P_o = |(\rho_r - \rho_m)| gz \tag{5.7}$$

where, ρ_r is the density of the host granite (2700 kg/m^3), g is acceleration due to gravity (9.8 m/s^2) and z is the depth at which the dykes originate (Gudmundsson, 1983a).

According to Becerril et al. (2013), the excess pressure (P_e) built within the magma chamber before eruption adds up to the total overpressure of magma. Considering an additional excess pressure (P_e) (perhaps 2-3 MPa) would reduce the depth estimates, but only slightly.

Stress intensity factors associated with each dyke are also calculated from the equation:

$$K_I = P_o\sqrt{\pi a} \tag{5.8}$$

where, K_I is the stress intensity factor for Mode I fractures (Sneddon and Lowengrub, 1969; Anderson, 2005). All the calculated results are summarized in **Supplementary sheet – 5.4**.

As stated earlier, **Figure 5. 6** shows a sketch map of two dykes encountered in the study area which feature horns. Field photographs of two such horns are shown in its insets. When the distance between the horn tip and dyke tip at its opposite end (A´, referred to as the ‘horn length’) is known, the horn thickness (B´) can be calculated by recording the co-ordinates of any one point on the horn margin positioning the origin of the co-ordinate system at its tip. In practice, several points on the horn perimeter can be measured and the average of their respective solutions for B´ can be considered as the mean horn thickness. Thicknesses of horns encountered in field are calculated in this method where possible and it is found that aspect ratio of horns (B´/A´) are always similar to that of the main dyke from which it protrudes **(Fig. 5. 7a)**. This connotes a possibility of using dyke horns as proxies for estimating magma overpressure where complete dyke lengths are not exposed but total horn lengths are known. We applied the method to three horns branching out from dyke number CH-161a whose full length (tip to tip) and maximum thickness were measured in the field. **Table. 5.1** compiles the results calculated from dyke horns and **Figure 5.7b** shows a graphical comparison of magma overpressures calculated from aspect ratios of complete dykes and from that of their respective horns.

5.2.4 Results and discussion

a. Estimation of magma overpressure from partially exposed dykes

The proposed method has been validated against ground data (felsic dykes emplaced within intrusive porphyritic granitoids of CGGC, Purulia, India) and has been applied to estimate magma overpressure from dykes emplaced in two very different geological settings; one for the arrested non-feeder dykes exposed in the caldera walls of the Miyake-jima volcano in Japan (collected from Geshi et al., 2010) and the other for the centimeter to meter scale dykes emplaced within the ~ 2.61 Ga old granites found within CSB, WDC, India. For Miyake-jima, the calculated total lengths and maximum thicknesses agree well to those estimated by Kusumoto et al. (2013) through non-linear least squares analysis. While in Kusumoto et al. (2013) the average aspect ratio (B/A) estimated for the dykes in Miyake-jima is 0.009 yielding an average magma overpressure of 4.8 MPa, the present calculated result stands at 0.01 and 5.4 MPa respectively for the same. Although both results lie within a close range it may be noted that the small increment in the present results arise out of the fact that it considers every possible combination of any two such points on the boundary of the dyke through which an ellipse can be drawn subjected to a common origin while the non-linear least squares fitting used in Kusumoto et al. (2013) might have excluded some outlier points which stands out from the common trend of the population in the data collected for each dyke.

For the dykes intruded within the granites of CSB, WDC, the length varies from 2.15 meters to 61.9 meters with corresponding maximum thicknesses of 1.3 centimeters to 36.3 centimeters. The average aspect ratio (B/A) is 0.004 which yields an average magma overpressure of 48.29 MPa for a limit varying from 27.01 MPa to 71.99 MPa. The depth of origin for these dykes corresponding to the calculated magma overpressure ranges lie within 9 to 24.5 kilometers. While laboratory values of tensile strength for granites range at around 16-20 MPa (Basu et al., 2013), the calculated high magma overpressure values might result from the enhanced tensile strength of the host rock attained at higher confining pressures with increasing depth. Calculated Mode I stress intensity factors (K_I) for these dykes range from 132.30 MPa/m^2 to 688.44 MPa/m^2 indicating high fracture toughness of the host granite. Similar magnitudes of K_I have been estimated in Gudmundsson (2009) for typical dykes found in volcanic edifices. Such high values of K_I may indicate that the dykes attained their maximum thicknesses in a single event of magma injection while the lower values of K_I hold true for dykes where episodic magma injection resulted in their final thickness over a period of time (Gudmundsson, 2009). High values of overpressure and stress intensity factors may also result from plastic deformation associated with the propagating dyke tip. When a crack tip propagates, experiments have shown that a plastic damage zone develops at the propagating tip (Irwin, 1968). This plastic zone provides a shielding effect to tip propagation which results in the increase of ‘effective fracture toughness’ by more than an order of magnitude (Papanastasiou, 1997). This can also widen the opening displacement of fractures, effectively increasing their thickness/length ratio. Also, the presence of a plastic damage zone in front of the tips increases the effective length of fractures (Irwin, 1960; 1968) which amplifies the magnitude of associated stress intensity factors.

b. Estimation of magma overpressure using dyke horn

Apophyses branching out from the main dyke body are common features associated with dyke emplacement (Currie and Ferguson, 1970, Jolly and Sanderson, 1995; Weinberger et al., 2000; Gudmundsson, 2020). These protuberances named 'horns' shooting out of the main dyke body have been described as 'failed magma paths' by Gudmundsson (2020). This implies that the main dyke had once tried to propagate along the path now terminated at a tip and abandoned as horn in favour of another pathway which might have been 'easier' for it to propagate further. 'Easier' in this sense may imply requiring less energy of propagation (Mériaux et al., 1999; Maccaferri et al., 2010). Horns have also been stated to develop under conditions of mixed mode I-III loading (Delaney and Pollard, 1981). Weinberger et al. (2000) explains this phenomenon using a damage rheology model (Agnon and Lyakhovsky, 1995; Lyakhovsky et al., 1997a, b) which is based on non-linear elastic fracture mechanics. Their simulations show that under mixed mode I-III loading, when two dyke segments propagate towards each other, a damage zone of high intensity develops around them, leading magma to invade those zones, thereby resulting in the development of horns which marks the asymmetric ends of the dyke segments.

The horns observed in dyke no. CH-161a emplaced within the Chitradurga granite **(Fig.5.6)** are similar to those illustrated in Fig.2a(F) of Weinberger et al. (2000), in the sense that they typically branch out near the bridge zones of continuous dyke segments and terminate at a tip after propagating more or less linearly for some distance in a fashion much similar to that of the main dyke. The aspect ratios of these horns are calculated following the method mentioned earlier and it is found that they are similar to that of the parent dyke **(Fig.5.7b)**.

However, it is important to note that the ambit of utilizing horns in calculating parent dyke's aspect ratio is limited due to the complexity of the local stress distribution around the horn and the mechanical interaction of the horns with the parent dyke body; factors, which eventually control its final shape (ellipticity) (Delaney and Pollard, 1981; Weinberger et al., 2000). Therefore, the scope of using horns as effective proxies for magma overpressure estimation demands caution and further investigation.

c. Constraints of the present method

The present method successfully calculates complete dyke dimensions from partial outcrops of dominantly opening mode dykes where at least one tip can be observed and has produced validated results for such dykes exposed in three different geological settings.

Where the dyke margin tends to be more irregular, the errors arising out of the combinations of points lying on the dyke margin increase in number. The error can be minimized by collecting as many dyke thicknesses as possible with corresponding small increments in dyke length measured from the tip. Data collected in the prescribed format for at least one third of the total dyke length have produced valid results for some dykes but it is advisable to collect data from the entire exposed length of the dykes for better approximation.

However, it should be noted that the present method is based on the idealized canonical model for dikes which shows it to open up in an elliptical shape. Although pure to dominantly opening mode fractures may tend to comply with some of the conditions assumed for the canonical model, under natural circumstances, it is very likely that these idealized conditions will considerably deviate. Under such circumstances, the shape of the fracture will digress from that of an ideal ellipse. For example, mixed mode I-II loading will bend the fracture plane resulting in curvature near dyke tips. Mixed mode I-III loading will produce continuous or discontinuous en echelon arrangement of dyke segments which may underlap or overlap thereby distorting the ellipticity of individual segments whenever their mutual mechanical interaction increases (Delaney and Pollard, 1981; Weinberger et al., 2000; Pollard and Martel, 2020). It should also be noted that, the assumptions of the canonical model will not be valid for dykes intruding through heterogeneous crustal layers. In such a scenario, although, the strike-dimension of the dyke might be exposed along layers of similar mechanical properties, the dip-dimension of the dyke will not. The basic premise of the model will also undergo modification if the dip-dimension of the dyke is smaller than that of its strike-dimension, as may happen in case of a ‘part-through’ Mode I crack (Gudmundsson, 2011). The basic assumptions of the canonical model hold true in the context of the present work, since, the observed dykes are all meter scale in their strike-dimension, far less compared to their dip-dimensions and are emplaced within a granitic pluton.

Within a uniform host rock, dykes may initially open in an elliptical shape which is gradually altered to some degree owing to spatial and temporal changes in the regional stress field leading to mixed mode loading as they ascend towards the surface from greater depth (Pollard and Martel, 2020). Thus, to some extent, dykes may retain their original ellipticity. It might be possible to utilize this relict ellipticity in the context of the present method, however its applicability and effectively requires further investigation which is beyond the scope of the present work that particularly addresses dominantly opening mode fractures/dykes.

In the field, dykes which do not markedly show curved ends or offset segments arranged systematically in en echelon patterns have been considered to have formed as dominantly opening mode fractures. These dykes permit the use of the canonical model in order to estimate their complete dimensions from partial exposures as is evident from the results of the present study. However, since the premise of the idealized canonical model is purely elastic, it fails to incorporate the effects of any plastic deformation associated with late phases of dyke evolution, particularly at its tips where maximum concentration of stress occurs (Irwin, 1968), posing a level of uncertainty to interpretations made on the basis of linear dyke dimensions or aspect ratios estimated through the present method.

5.3 Magma overpressure estimation from partially exposed dykes without tips

Considering the canonical model of Mode I fracture **(Fig. 5.8a)**, Kusumoto et al. (2013) and Biswas et al. (2023) devised two different methods for estimating complete dyke dimensions from partial exposures. But both these methods are limited owing to the fact that their applicability is restricted to partial outcrops which have at least one visible tip **(Fig. 5.8b)**. Very often, if not most, finding a dyke exposure with only one visible tip is also a matter of pure chance. To overcome this persistent problem, a mathematical method has been conceived to estimate complete dyke dimensions even from their partial exposures devoid of any tip **(Fig. 5.8c)**. Considering the elliptical shape of dyke opening in 2D (as formulated by the canonical model, which mostly holds true for dominantly opening mode dykes), its discrete derivative representatives are used in the differential equations of an ellipse to evaluate the parameter estimates, namely: total length (A), maximum width (B) and aspect ratio (B/A) of the dykes. The method has been validated against ground data collected from completely exposed felsic dykes emplaced within porphyritic granitoid bodies of Chotanagpur Granite Gneissic Complex (CGGC), India and also against published data reported from the caldera walls of Miyake-jima volcano in Japan. The method has also been applied on two partially exposed mafic dykes, one from the Western Dharwar Craton (WDC) and the other from the Eastern Dharwar Craton (EDC) of India and the estimated results have been utilized to calculate their magma overpressures and depths of origin. Estimates made from partial exposure of dykes are often flawed generally due to an under-estimation of their linear dimension. The present method is important in this regard since it can potentially infer close parameter estimates for dykes where limited exposures have been used to date. Although the present method has been developed dedicatedly for dominantly opening mode dykes and can be applied at every scale, its usage is not limited to dykes alone but suffices any natural feature which resembles an ellipse in its shape.

5.3.1 Methodology

a. Theory

Considering deformation to be purely elastic in nature, the idealized canonical model for dyke shows it to open up in an elliptical shape under a set of assumptions. The crux of the idea here is to use the differential equation (DE) of the ellipse. Since, in the general position, 5 points (and hence 5 parameters) are required to uniquely identify an ellipse on the Cartesian plane, the general differential equation of an ellipse is expected to be of 5th order.

However, in practice, higher order discrete derivatives are worse approximations of the actual derivatives. Therefore, it is prudent to minimize the order of the DE. Here, the ellipse already has two degrees of freedom constrained, since both of its foci and hence the major axis must lie on the x-axis. Additionally, to estimate the aspect ratio of the ellipse using the equation, the completely unparametrized DE is not required. Thus, a second order equation suffices. The following paragraph explains in more detail.

Here, it is assumed that the points lie on an ellipse whose center lies on the x-axis, with semi-major axis a, and semi-minor axis b. So, it's center is of the form (k, 0) **(Fig. 5.8c)** and thus the equation of the ellipse is:

$$\frac{(x-k)^2}{a^2} + \frac{y^2}{b^2} = 1 \qquad (5.9)$$

Differentiating equation (5.9) once with respect to x:

$$\frac{2(x-k)}{a^2} + \frac{2yy'}{b^2} = 0 \qquad (5.10)$$

Any parameter apart from a and b is not solicited to appear in the final differential equation. However, at this point, k, the parameter for the x-coordinate of the center of the ellipse still appears. To remove this term, the equation (5.10) is differentiated once again with respect to x, to get:

$$\frac{2}{a^2} + \frac{2}{b^2}(y' \cdot y' + y \cdot y'') = 0 \Longrightarrow (y')^2 + yy'' = -\frac{b^2}{a^2} \qquad (5.11)$$

where, y' and y'' are the first and second order derivatives of y respectively. Note that as far as the aspect ratio is concerned, the final equation alone suffices. In order to estimate k, a, and b individually, the original and the 1st order equations will also be required.

b. Estimation

First, the discrete (single and double) derivative representatives of the points labelled as 3, 4, 5 … n-3, n-2 are required. Now, considering data points

$(x_{i-1}, y_{i-1}), (x_i, y_i)$ and (x_{i+1}, y_{i+1}) in increasing order of x-coordinate, the slope (y') and rate of change in slope (y'') at point (x_i, y_i) can be calculated respectively as:

$$y_i' = y'|_{(x_i, y_i)} = \frac{y_{i+1} - y_{i-1}}{x_{i+1} - x_{i-1}} \tag{5.12}$$

$$y_i'' = y''|_{(x_i, y_i)} = \frac{y_{i+1}' - y_{i-1}'}{x_{i+1} - x_{i-1}} \tag{5.13}$$

Figure 5.8d schematically portrays the discrete single derivatives (y') of the points lying on the margin of an ellipse. Note the decreasing slope (y') in increasing order of the x coordinate **(Fig. 5.8e)** and therefore, the rate of change of slope (y'') is always negative **(Fig. 5.8f)**.

If the data points $(x_1, y_1), (x_2, y_2) \ldots (x_n, y_n)$ are taken in increasing order of x-coordinate then y'' for $(x_3, y_3), (x_4, y_4) \ldots (x_{n-2}, y_{n-2})$ can be calculated **(Fig. 5.8f)**. So, using Equation (5.11), the aspect ratio $\frac{b}{a}$ can be estimated in the following way:

$$\frac{\hat{b}}{a} = \sqrt{-\mathrm{mean}\left(y_i y_i'' + y_i'^2\right)|_{i=3}^{n-2}} \tag{5.14}$$

Using Equation (5.10) we have:

$$\hat{k} = \left[\frac{\mathrm{median}\left(y_i y_i'\right)|_{i=2}^{n-1}}{\left(\frac{\hat{b}}{a}\right)^2}\right] + \mathrm{median}(x_i)|_{i=1}^{n} \tag{5.15}$$

Now using Equation (5.9) we have:

$$\hat{b} = \sqrt{\mathrm{median}\left[\left(\frac{\hat{b}}{a}\right)^2 \left(x_i - \hat{k}\right)^2 + y_i^2\right]|_{i=1}^{n}} \text{ and hence } \hat{a} = \frac{\hat{b}}{\left(\frac{\hat{b}}{a}\right)} \tag{5.16}$$

It is to be noted that Equations (5.15) and (5.16) uses median while mean is used in Equation (5.14). In Equation (5.15) and Equation (5.16), there is no restriction, so median can be taken over all data points. In the expression for $\hat{b}$, the part under the square root is always positive by definition, no matter how non-ideal our situation is. However, in Equation (5.14), the part inside the square root, is only theoretically positive for concave down data. Although an ideal Mode I dyke will conform to an overall concave downward shape (in either of the upper quadrants), in practice, it is observed that the distribution of values is skewed, with considerable number of negative values. Mean performs better than median in this case due to the skewness, and occasionally, the median may turn out to be positive itself, making the expression inside the square root negative. That is why even though median is a more robust measure of central tendency, mean is used in this one specific formula.

c. Smoothing and Goodness of Dyke

Natural dykes forming as dominantly opening mode fractures approximate an overall elliptical shape as formulated by the canonical model, but in practice, data points measured on the dyke margin can often be irregular, deviating from the ideal ellipse to a considerable extent. Since the present method relies on the rate of change of curvature of the exposed dyke margin, it is necessary to smooth the dataset. Standard moving average techniques have been tried to smooth the data. However, this causes a problem as some of the more extravagant outliers change their neighbours' values as well and affect the final outcome. If the outliers are removed however, the gap between points increases and thus the accuracy of the estimated derivatives may drop further. That is why, an additional condition is imposed:

Suppose a total of n points are there, (x_i, y_i) with i = 1, 2, 3 … n. Then, the new y values are considered as:

$$\text{New } y_i = \begin{cases} y_i & \text{if } i \leq 2 \text{ or } i \geq n-1 \text{ or } \min\limits_{i-2 \leq j \leq i+2} y_j < y_i < \max\limits_{i-2 \leq j \leq i+2} y_j \\ \dfrac{y_{i-1}(x_{i+1}-x_i)+y_{i+1}(x_i-x_{i-1})}{(x_{i+1}-x_{i-1})} & \text{otherwise} \end{cases} \tag{5.17}$$

The reasoning behind this constraint is that now, only the outlier point itself (characterised by a local maxima or minima) is smoothed into the line connecting its neighbours. Assuming that the neighbours of the outlier are not themselves so, this means those points will remain unchanged during smoothing. In case of an ideal ellipse, the only non-outlier to be considered an outlier would be the end of the minor axis. But in this case too, the effect will not be much as the points become practically collinear close to that point. In practice, two cycles of smoothing may solve this problem much better.

Since the ideal ellipse is concave down and the present method depends on the double derivative, a metric of the "goodness" of the dyke data can be defined based on the extent to which it is locally concave up **(Fig. 5.8g)**. Goodness of dyke $\mathrm{G_D}$ is defined as:

$$\mathrm{G_D} = \frac{1}{n-4}\sum_{i=3}^{n-2} \mathbb{I}(y_i'' < 0) \tag{5.18}$$

The y''_i here is defined in the earlier section. $\mathrm{G_D}$ is not guaranteed to increase uniformly with cycles of smoothing, however in general we can say that a dataset with $\mathrm{G_D} < 0.5$ i.e., where greater than 50% of the measured data points show a concave upward attitude, requires at least up to two cycles of smoothing to give good results. Nevertheless, the Python code developed for the method (see **Supplementary sheet – 5.5**) solves the equations first with the collected raw data and then successively up to three cycles of smoothing, respectively denoted in the output result sheets as 0, 1, 2 and 3 respectively.

5.3.2 Validation

A test set of 23 dykes were used to validate the proposed method. Out of these 23 dykes, 7 are felsic dykes (dyke nos. D1, D3, D5, D7, D8, D9, D10) emplaced within intrusive porphyritic granitoid bodies of Chotanagpur Granite Gneiss Complex (CGGC), which is an E-W trending, sub-arcuate shaped, Proterozoic belt located in the eastern part of India. The ESE-WNW trending felsic dykes are found within the porphyritic granitoids located near Bero hills, Purulia, India. Four of these felsic dykes are entirely exposed displaying nearly symmetric tips at both ends, while three of them are exposed beyond the middle part starting at one visible tip. One mafic dyke (dyke no. Ch-162b), recorded, is NNE trending, and is completely exposed (tip to tip), emplaced within the Chitradurga granite of Chitradurga Schist Belt, Western Dharwar Craton, India, the detailed geological setting of which is discussed in Section. 4. In outcrop dimensions, all these dykes are meter scale in length while being centimeter scale in thickness and propagate linearly maintaining a sharp contact with the host rock bodies. Details of location and measurements of all these dykes can be found in **Supplementary sheets – 5.1** & **5.2**. The dykes are sub-vertical to near vertical in attitude and do not display systematic arrays of en echelon segments, nor do they exhibit curvature near their tips. These observations are indicative of their formation as dominantly opening mode fractures as shown in field photographs forming **Supplementary sheet – 5.6**. The rest 15 are arrested, partially exposed (upper tip observed, lower tip concealed), non-feeder dykes in the caldera walls of Miyake-jima volcano, Japan, reported by Geshi et al. (2010), whose complete dimensions have been estimated through two different methods; first by Kusumoto et al. (2013) and subsequently by Biswas et al. (2023), both of which show congruent results. A portion of the measured parts of these dykes have been selected for the present analysis such that they do not include any or either of the tips. This selected part of the dykes is referred to as 'used data portion' in **Figure 5.9a**. On an average 40.91% of the entire lengths of the dykes have been selected for use (see **Supplementary sheet – 5. 7**). Length/width ratios of full dykes and of the parts of the dykes used in the analysis are shown graphically in **Figure 5.9b**. Average raw $G_D$value for all the selected dyke portions corresponds to 0.52 within a range varying from 0.29 to 0.71. See **Figure 5.9c** for graphical comparison of $G_D$values in raw data and in 1st and 2nd cycles of smoothing. When run on raw data, the method failed to produce results for six dykes (90-02, 90-03, 90-04, 88B, 88D and 94-05). Average error for estimated aspect ratio (B/A), maximum width (B) and total length (A) for the remaining 17 dykes are considerably high, standing at 37.65% with a standard deviation of 38.76 (coefficient of variation = 1.03) for aspect ratio (B/A); 12.69% with a standard deviation of 14.11 (coefficient of variation = 1.11) for maximum width (B) and 31.53% with a standard deviation of 42.63 (coefficient of variation = 1.35) for total length (A). 1st cycle of smoothing increased average $G_D$value to 0.53 and considerably improved the estimated results but failed to produce results for one dyke (D10), whose dimensions are closely estimated in the 2nd cycle of smoothing.

It is to be noted that for D10, raw $G_D$was 0.5 (corresponding results deviated widely from the actual) which decreased to 0.37 in the 1st cycle but again increased to 0.5 in the 2nd cycle of smoothing. For the rest 22 dykes, average error stands at 7.85% with standard deviation of 8.72 (coefficient of variation = 1.11) for aspect ratio (B/A); 8.97% with standard deviation of 7.69 (coefficient of variation = 0.86) for maximum width (B) and 11.06% with standard deviation of 7.75 (coefficient of variation = 0.70) for total length (A). Although average $G_D$value further increases to 0.54 in 2nd cycle of smoothing, average error for all estimated parameters also increases when compared to those estimated in the 1st cycle. Also, parameter estimates of one dyke (88B) was unavailable in this cycle which was closely estimated in the 1st cycle of smoothing. Raw G_D for 88B was 0.5 but results were not obtained for raw data too. 1st cycle of smoothing increased G_D to 0.75 which again decreased to 0.62 in the 2nd cycle. Here, average error stands at 13.67% with standard deviation of 15.95 (coefficient of variation = 1.17) for aspect ratio (B/A); 9.81% with standard deviation of 8.23 (coefficient of variation = 0.84) for maximum width (B) and 11.75% with standard deviation of 7.79 (coefficient of variation = 0.66) for total length (A). See **Supplementary sheet – 5.8** for details of error analysis. Graphical comparisons of actual and estimated dyke dimensions are represented in **Figures 5.9 d, e, and f** which correspond to estimated full lengths (A), maximum widths (B) and aspect ratios (B/A) respectively. Keep note that for the dykes of Miyake-jima, Japan, the estimates of Kusumoto et al. (2013) are considered as standard. The method also generates similar results when applied to different selected portions of the same dyke. Results of this analysis are shown for dyke nos. D1 and D5 from Purulia, India and dyke nos. 94-01 and 270-2 from Miyake-jima, Japan in **Figure 5.10**. Note in **Figure 5.10a**, when full data for a dyke (from visible tip to last measured point) is used, the estimates of Biswas et al. (2023) fall closer to the actual measurements than those estimated by the present method. It is therefore prudent to use the earlier method when the observed dyke outcrops consist of a visible tip.

It is evident that the parameter estimates generated in the 1st cycle best approximate the measured and earlier estimated complete dyke dimensions in most of the cases with exceptions only where the G_D value drops below 0.5, whereupon close estimates are yielded in the 2nd cycle, although, an increase in G_D to 0.5 or more in successive smoothing cycles cannot be assured. Therefore, the inferred convention to be followed is to accept the results of 1st cycle as the best estimates when the corresponding G_D value reaches 0.5 or more. If $G_D<0.5$ in the 1st cycle, only then the results of 2nd cycle should be accepted, provided that the G_D value increases or remains at least the same as that of the 1st cycle. Since repetitive smoothing cycles does not guarantee increase in G_D values, rather it may alter the nature of raw data, therefore, further smoothing of the data is not advisable. As it can also be observed in the present test dataset, that results for all the dykes have been successfully acquired within the first two cycles of smoothing thereby limiting the use of a further 3rd cycle of smoothing for any of the dykes.

5.3.3 Application

The method has been applied on two partially exposed dykes, one each from the Western and Eastern Dharwar Cratons of southern India. As discussed earlier, these two cratons amalgamated along the Chitradurga Shear Zone (CSZ) and share similar characteristics in terms of basement tonalite–trondhjemite–granodiorite (TTG) gneisses (3.3-2.7 Ga; Taylor et al., 1984), metamorphosed volcano-sedimentary assemblages forming greenstone belt sequences (3.3-2.7 Ga; Peucat et al., 1995) and younger granitic intrusions (2.6-2.5 Ga; Jayananda et al., 2006). However, the Western Dharwar Craton has a greater crustal thickness (42-51 km) compared to that of the Eastern Dharwar Craton (34-39 km), also known as the Dharwar batholith (Gupta et al., 2003). The dyke from the Western Dharwar Craton (WDC), located near Chitradurga town (CH), is emplaced within the Chitradurga granite (2.61Ga; Jayananda et al., 2006) which has intruded along the core of the Chitradurga Schist Belt (CSB). The dyke from the Eastern Dharwar Craton (EDC), located near Pavagada town (PV), is emplaced within the Closepet granite (2.51-2.56 Ga; Jayananda et al., 1995), which is one the largest granitic plutons of the Dharwar batholith. **Figure 5.11a** shows a simplified geological map of the Dharwar Craton and **Figure 5.11b** is a Google Earth image which shows the location of Chitradurga and Pavagada regions.

Both the dykes are mafic in composition. In their outcrop dimensions, both are meter scale in length and centimeter scale in thickness. While both dykes are near vertical in attitude, the one from Chitradurga trends NNW while the one from Pavagada trends

ENE. Almost all along their linear dimension both dykes retain sharp contacts with the host granite bodies. Field photographs of the dykes in Pavagada and Chitradurga are shown in **Figures 5.11c** and **5.11d** respectively. In Chitradurga, the dyke does not display any tip and the outcrop is exposed almost continuously for a length of 67.5 m only with a vegetation cover of ~ 8.5 m in between. Whole of the observed length has been recorded. For the dyke near Pavagada, a visible and accessible length of 75 m, has been utilized beyond which the dyke could still be inferred to be exposed for at least another 50 m devoid of any tip. To record the ground points, thickness of the dykes or their aperture width is measured at fixed increments along the abscissa starting from the left visible starting point of the exposure **(Fig. 5.8c)**. Offsets related to secondary faulting or shearing are retro-deformed so as to produce a continuous outcrop length. The dykes are near vertical in attitude and the faults which have been observed to offset them into segments are also sub-vertical trending perpendicular to the linear dimension of the dykes. Although the exact amount and sense of movement cannot always be discerned along these faults, they do have a major strike-slip component. Therefore, the retro-deformation has been done by shifting dyke contacts laterally. The fixed intervals along the abscissa and their corresponding half thicknesses provide the co-ordinates of the measured points which lie on the upper margin of the dyke. See **Supplementary sheet – 5.9** for details of data recorded on these two dykes.

On application of the method, the dyke in Chitradurga yielded results on the raw data as well as in every cycle of smoothing. Following the inferred convention, the results of the 2nd cycle of smoothing (G_D=0.49) are accepted, since G_D in the 1st cycle of smoothing was 0.48. For the dyke in Pavagada, parameter estimates were not generated for raw data. G_D value remained the same (0.49) in the 1st and 2nd cycles but then decreased to 0.43 in the 3rd cycle. Following the convention, the results generated in the

2^{nd} cycle of smoothing are accepted. The observed and estimated dyke lengths along with their corresponding length/width ratios are shown in **Figs. 5.11 b(i)** & **b(iii)**, respectively corresponding to Chitradurga and Pavagada. Results for each cycle of smoothing for the dykes in Chitradurga and Pavagada are shown in **Figs. 5.11 b(ii)** & **b(iv)** respectively.

Estimated total lengths (A) and maximum widths (B) of the dykes are employed to obtain their aspect ratio which has been defined as B/A. Using the aspect ratios, magma overpressure (P_o) and depth of origin (z) for each dyke has been calculated using equation nos. (5.5), (5.6), and (5.7), considering the same elastic moduli and density values as are mentioned in section no. 5.2 for partially exposed dykes with a single exposed tip. All results thus obtained are summarized in **Supplementary sheet – 5.10**.

5.3.4 Results

For both the dykes, G_D values for raw data corresponds to 0.53. However, results are obtained for the Chitradurga dyke but not for the Pavagada dyke when the method was run on raw data.

Note, that raw data also failed to produce results for six dykes within the test dataset. This results from the inherent irregularity of the collected raw data which is often outlier prone. In Chitradurga, estimated full length from the raw data is five times the observed length. This is not in agreement with the overall trend of the collected data which shows a distinct decreasing trend on both sides of the central part of the dyke. Estimated full length in the 1^{st} cycle of smoothing (G_D=0.48) is 64 m which is marginally less than the observed length. In the 2^{nd} cycle (G_D=0.49), estimated length of 86.42 m with a corresponding maximum width of 0.44 m appears logical which also agrees with the adopted convention. In the 3^{rd} cycle G_D value drops to 0.48 again with a length and width estimate of 76.83 m and 0.49 m respectively. All results are graphically represented in **Figure 5.11 b(ii)**. In Pavagada, estimated length and width are respectively 194 m and 0.89 m in the 1st cycle (G_D=0.49) and 278 m and 0.88 m in the 2nd cycle (G_D=0.49). In the 3rd cycle G_D value dropped to 0.43 but parameter estimates are very nearly the same as those in the 2nd cycle. All results are graphically shown in **Figure 5.11 b(iv)**. Considering the results generated in the 2nd cycle, magma overpressure (P_o) and depth of origin (z) calculated for the Chitradurga dyke stands at 60.7 MPa and 20.6 km respectively. The results lie within the range of estimates made by Biswas et al. (2023) on some mafic dykes recorded with one observed tip from the same area. For the dyke in Pavagada, EDC, calculated magma overpressure (P_o) and depth of origin (z) stands at 37.7 MPa and 12.84 km respectively.

5.3.5 Discussion

In the test dataset of 23 dykes, it has been observed that, for an average full length/maximum width ratio of about 160 (within a range of 61 to 500), the dyke portions selected for the present method has an average visible length/maximum visible width ratio of about 53 (within a range of 20 to 118) **(Fig. 5.9b)**. Average raw G_D value for all the selected dyke portions stands at 0.52 **(Fig. 5.9c)**. Therefore, as a lower bound, it can be generally stated, that rational estimates of full length and maximum width can be anticipated for any tipless dyke outcrop which has a visible length/maximum visible width ratio of at least 50 (nevertheless, the more the better) and a G_D value close to 0.5 or more.

The present method relies heavily on the rate of change of curvature of the elliptical margin of a dyke which under normal circumstances should be overall concave downward in either of its upper quadrants. However, any phenomenon leading to a significant concave upward shape of the dyke margin will make the proposed method ineffective. Such a concave upward shape can result from permanent wedging of dyke tips by chilled magma which produces a comparatively thinner middle part than the thicker tips (Daniels et al., 2012). In such scenarios, G_D values will approach zero rather than unity. Layer heterogeneity (Gudmundsson, 2020) and mixed mode loading conditions (Pollard and Martel, 2020) can result in significant alteration of a dyke's final shape thereby limiting the scope of the present method which focusses particularly on dominantly opening mode dykes. Applicability of the present method on data collected from segmented dyke outcrops (Ruz et al., 2020; Drymoni et al., 2021) requires further investigation since their final emplacement might not always be governed within the premise of the canonical model for pure opening mode fractures, therefore, leaving scope for potential future studies. Since the theoretical premise of the present method concerns a penny-shaped fracture formed within a purely elastic medium, it cannot account for other modelling approaches which predict different dyke shapes in 3D formed under varying conditions of emplacement and incorporates effects of plastic deformation involved with the formation of dykes (Rivalta et al., 2015; Townsend et al., 2017). Apart from the mechanical considerations, the final shape of a dyke might also be constrained to a considerable extent by variations in the composition and thereby viscosity of the intruding magma, changes in its volatile content as solidification progressively concentrates volatile content in the magma and associated factors like magma replenishment, mingling, duration of intrusion, effects of thermo-mechanical erosion etc. Such varying thermodynamic properties cannot be resolved within the theoretical considerations of the canonical model for dyke formation.

It is to be noted that an outcrop/erosional surface will not necessarily cut a penny shaped dyke at its middle where its length and width are the maximum. Parameter estimates from any 2D section other than this one will therefore underrate the values of A and B, however, the aspect ratio (B/A) in all parallel transverse sections perpendicular to the height of the dyke remains the same. This aspect ratio is crucial to determining the overpressure of the magma (P_o) which is primarily responsible for the formation of a dyke. The magnitude of this overpressure was used to independently estimate the depth of origin (z), which, within the premise of the canonical model, gives the height of the dyke above the magma chamber. Therefore, estimates of these three parameters in unison (A, B and z) enables us to perceive the complete 3D theoretical shape of a dyke. For partially exposed dykes, even devoid of any visible tip, application of the present method allows for prediction of the 3D dyke geometry based on their limited 2D outcrops. Although not necessarily exact, this estimation provides a first order approximation of complete dyke dimensions considering them as ideal Mode I fracture, which has been hitherto impossible to determine given their partial exposures.

The magma overpressure values of 37.7 MPa and 60.7 MPa estimated for the dykes emplaced within the younger granites of the Eastern and Western Dharwar cratons are in a good agreement with the calculated magma overpressure ranges of Geshi et al. (2020) corresponding to dykes of different aspect ratios intruding host rocks of different Young’s modulus. The depths of origin estimated at 12.84 km and 20.6 km for the dykes in Pavagada and Chitradurga respectively also accords to the greater crustal thickness of the Western Dharwar Craton compared to that of the Eastern Dharwar Craton.

5.4 Mechanisms of dyke emplacement

As magma continues to accumulate within a magma chamber, fractures can be formed when pressure of the intruding magma exceeds the magnitude of the least principal compressive stress (σ_3) acting normal to the fracture walls, functionally making this principal stress component tensile. Therefore, when loaded by a uniform internal pressure, dykes will supposedly open as Mode I (opening mode) fractures **(Fig. 5.12a)** within an isotropic, elastic host rock body as long as σ_3 acts perpendicular to their margin in a uniform stress field. In this case, theoretically, the fracture/dyke will have a highly eccentric elliptical shape of opening (Parker, 1981; Gudmundsson, 1983a, 1983b) and the displacement component (Δu) will be perpendicular to its walls across the fracture plane.

Often, intrusion of magma is also governed by preferably oriented pre-existing anisotropies such as fractures and foliations present within the host rock (Xu et al., 2013). Contrary to the mechanism of extensional fractures, ring dykes and cone sheets are formed as shear fractures. The former initiates when subsidence of magma results in the formation of shear fractures in the overlying rocks in a situation of low magma pressure and relatively higher deviatoric stress, while the latter forms by occupying shear fractures created by dynamic stresses produced by a rapidly expanding magma undergoing retrograde boiling (Anderson, 1937; Phillips, 1974).

Although field observations of dyke shapes and cross-cutting relationships suggest that a statistically significant number of dykes originate as dominantly opening mode fractures (Gudmundsson, 2020; Gudmundsson et al., 2022) and their overall irregular boundary as observed on a planar outcrop tends to approximate that of a highly eccentric ellipse (Biswas et al., 2023, 2025), several studies also record dyke shapes and geometries which differ considerably from the ideal linear elliptical shape (Jolly and Sanderson, 1995; Correa-Gomes et al., 2001; Misra and Mukherjee, 2017; Babar et al., 2017; Ghodke et al., 2018). It is obvious that all the assumptions of the idealized elastic theory cannot be sustained under diverse natural conditions, and the final shape of a dyke, besides the material properties of the host rock and the dispositions of near and far-field stresses will largely be a function of the composition and viscosity of the intruding magma along with changes in its rheology due to gas exsolution or varying volatile content with progressive crystallization (Halls and Fahrig, 1987; Ernst et al., 1995), rate of intrusion, effects of thermal erosion (Fialko and Rubin, 1999) and several other associated factors.

However, a consistent observation recorded in such studies is a systematic segmented nature of dykes in outcrops; characteristic curvature of dykes or their segments towards their tips and often apophyses shooting out from the main dyke body (Currie and Fergusson, 1970; Delaney and Pollard, 1981; Kattenhorn and Watkeys, 1995; Weinberger et al., 2000; Poland et al., 2004; Clemente et al., 2007). Such segmented outcrops were initially thought to be faulted offsets of an originally continuous body (Watterson, 1968) but later studies demonstrated that they can be the result of progressive evolution of dykes under conditions of mixed mode loading as they propagate upward from greater depths (Pollard et al., 1982; Nicholson and Pollard, 1985; Bussell, 1989). Understanding the mechanisms which cause such changes to occur is important since it enables us to envision the propagation path and thereby the ambient stress states through which such dykes have evolved.

Provided that the magma creates its own path, dykes will always have the primary opening displacement component but the sense of this displacement might not always remain perpendicular to its margins owing to changes in the orientations of the principal stress axes, which might result from local heterogeneities in the wall rocks (Foley, 1989) or varying stress states during its gradual ascent (Pollard and Martel, 2020). Based on the displacement fields, two other end member modes of fracturing can also exist (II and III), in both of which, unlike Mode I, the displacement component (Δu)

lies on the fracture plane itself (Lawn and Wilshaw, 1975). Both of these modes initiate when the maximum and minimum compressive stress axes are oriented at an angle oblique to the fracture plane, thereby inducing shear on it. In Mode II or shearing mode, the displacement (Δu) is along the line of fracture propagation but it is perpendicular to the edges of fracture walls **(Fig. 5.12b)** and in Mode III or tearing mode, the displacement (Δu) is perpendicular to the line of fracture propagation but parallel to the edges of its walls **(Fig. 5.12c)**. Note, that in case of Mode II fractures, the line of fracture propagation lies on the plane on which the principal stress axes rotate but in Mode III fractures, the line of fracture propagation is normal to the plane on which the rotation of principal stress axes occurs. These modes may exist in juxtaposition with the initial opening mode (hybrid fracturing/mixed mode loading) due to a change in the initial orientation of the principal stress axes as the dyke propagates and this will result in characteristic curved or segmented dyke shapes/geometries (Delaney and Pollard, 1981; Pollard and Martel, 2020) contrasting to the ideal elliptical shape. Other than hybrid fracturing resulting from changes in loading conditions during the dyke's emplacement, several other factors including differential cooling rates of the ascending magma (Daniels et al., 2012), layer heterogeneity within the host rock (Gudmundsson, 2020) or presence of an elastic free surface at the upper ascending end of the dyke (Rivalta and Dahm, 2006) can also affect the final shape and geometry of the dyke. Different mechanical models of dyke formation and propagation have been compiled in the review works of Rivalta et al. (2015) and Townsend et al. (2017) which elucidate factors playing key roles behind the origin and propagation of dykes.

As mentioned earlier in the chapter (Section 5.1), mafic dykes emplaced within granitic host rocks from the Archean Dharwar Craton of peninsular India often exhibit outcrop shapes and geometries that differ considerably from the outcome predicted by the canonical model. Dykes displaying such outcrop attributes are observed within the Chitradurga granite of the CSB, WDC, as well as in the Closepet granite, an equivalent granitic pluton that forms a substantial part of the Dharwar batholith in the EDC. Accordingly, dykes intruding the Closepet granite in the Pavagada region of the EDC have also been examined, as they display mixed-loading emplacement features comparable to those in the Chitradurga region of WDC. These dykes are segmented and their systematic offset pattern displaying either a continuous or discontinuous en echelon geometry suggest emplacement under mixed loading condition.

Within the basic premise of the elastic theory and in light of previous literature, the distinctive features that these dykes display, have been enumerated and discussed, followed by the explanation of how these features relate to their genesis and evolution under conditions of mixed mode loading. The study provides critical insights into the ambient stress regimes that governed the ascent and emplacement of mafic dykes during the late-stage stabilization of the Dharwar Craton. Finally, a mechanical model of dyke emplacement and subsequent evolution within the younger granites of the CSB has been proposed, under varying regional stress fields of the terrain.

5.4.1 Modes of fracturing vis-à-vis mixed mode emplacement of dykes

When magma intrudes pre-existing anisotropies, the pathway of the magma, which in effect will become the final shape of the dyke will largely be a function of the disposition and architecture of those pre-existing anisotropies (Currie and Ferguson, 1970; Delaney et al., 1986). But if the magma intrudes a homogenous host rock, then, other than the material properties of the host rock and the intruding magma, the resulting dyke shape will largely be a function of the ambient state of stress

(Gudmundsson, 1983b). The mechanisms through which a dyke forms and evolves up to its final emplacement may occur in the following ways:

a. Pure Mode I dykes

This is the primary scenario where the dyke will initially open along the least compressive principal stress (σ_3), and will propagate towards the maximum compressive principal stress (σ_1). If this stress state remains unchanged during the course of its ascent and final emplacement, the dyke will be a purely opening mode (Mode I) fracture **(Fig. 5.13a)**. Under theoretical considerations of the canonical model of dyke formation, the three dimensional shape of this opening mode fracture will resemble that of a flattened disc or a penny or an *idli* (Kavanagh et al., 2018; Pollard and Martel, 2020). Therefore, the tip line of the fracture (the curved line along which two opposing surfaces of an opening mode fracture join) will be circular and any observation plane (e.g. the Earth's surface) cutting this circular tip line will result in an elliptical outcrop shape having two tips **(Fig. 5.13a inset)**.

As the dyke continues to ascend after its formation, any change in the orientation of the ambient stress field will be reflected by its distortion. Rotation of the principal compressive stress axes will result in their obliquity to the initial plane of dyke propagation thereby imparting shear along the dyke body. The end members of this rotation (two principal stress axes rotate about the remaining axis, the latter remains fixed) can occur on two planes, both perpendicular to the dyke/fracture plane, but one is parallel to the line of dyke/fracture propagation while the other is normal to it.

b. Mixed Mode I-II dykes

In 3D space, if σ_2 remains in its initial position (as in the commencing Mode I opening) but σ_1 and σ_3 rotate about it, then, the line of initial dyke propagation direction (parallel to earlier orientation of σ_1) lies on the plane on which σ_1 and σ_3 have rotated. In such a situation, the initial advancing dyke tip will try to turn towards the changed orientation of σ_1 such that its opening component aligns parallel to the new σ_3 orientation. Therefore, imposition of Mode II loading on initial Mode I will result in "turning" of the dyke plane in accordance with the changed orientation of the principal stress axes, resulting in curvature of the dyke body towards its tips (Pollard, 1987). If the dyke is ascending upward in the z coordinate direction, then this turned/curved geometry will be manifested in the x-z section (plane on which the principal stress axes rotate), x-y being the horizontal or planar section, on which the manifestations of a pure Mode I and mixed Mode I-II dyke will be similar **(Fig. 5.13b)**.

c. Mixed Mode I-III dykes

As the dyke ascends, two principal stress axes rotate in a plane oriented normal to the dyke propagation direction. Therefore, σ_2 and σ_3 rotate from their initial position about the σ_1 axis **(Fig. 5.13c)**. Since the line of dyke propagation direction is now normal to the plane on which rotation of the principal stress axes occur, the advancing dyke plane will undergo "twisting" in response to the changed orientation of the principal stress axes. This results in continuous or discontinuous en echelon geometry of the dyke body (Delaney and Pollard, 1981; Pollard, 1987). In case of discontinuous en echelon segments, each twisted segment will be oriented parallel to the rotated direction of σ_2, which is the maximum principal stress component acting on that plane. If σ_2 has rotated dextrally, then the en echelon segments of the dyke will be arranged in a right stepping sequence. In case of continuous en echelon arrangement of the dyke body, the portion of it which connects two adjacent twisted parts will carry vestiges of the dyke's initial orientation. The acute angle between the initial orientation and final twisted orientation of the dyke body is termed as the “twist angle” (Pollard et al., 1982; Nicholson and Pollard, 1985) which implies the degree of rotation of the principal stress axes on that plane **(Fig. 5.13c)**. For a dyke propagating upward/along the z-direction, this twisted geometry will be manifested in the x-y section (plane on which the principal stress axes rotate), x-z being the vertical section, on which the manifestations of a pure Mode I and mixed Mode I-III dyke will be similar **(Fig. 5.13c)**.

d. Mixed Mode I-II-III dykes

If all three mutually perpendicular principal stress axes rotate together from their initial orientation, then ‘twisting’ and ‘turning’ may commence simultaneously. Such hybrid fracturing is thus a result of the imposition of both Mode II and III loading together on the initial Mode I opening of the dyke in response to the changed orientation of the principal stress axes **(Fig. 5.14)**. This might happen if an initially twisted (mixed Mode I-III) dyke body turns in response to the imposition of Mode II loading. On the contrary, an initial mixed Mode I-II dyke might not get twisted efficiently on imposition of Mode III loading. This is because, the advancing turned portion of the dyke might get so curved that it gets near parallel or at a very low angle to the horizontal plane on which shearing is induced. **Figure 5.14** demonstrates with the help of a ternary diagram, all possible combinations of the three end member loading conditions (Mode I, II, and III) on a dyke body.

5.4.2 Morphological features of the observed dykes

Four mafic dykes, all doleritic in composition, from the Archean Dharwar Craton of peninsular India has been investigated. These are representative dykes from the studied areas which display maximum exposed lengths and also preserve their body geometries along the entirety of their exposed lengths making them suitable for examination. Three among them are from the Chitradurga granite of the Chitradurga Schist Belt (CSB), Western Dharwar Craton (WDC) and one is from the Closepet granite of the Eastern Dharwar Craton (EDC), found near Pavagada town in Tumkur district of Karnataka. The EDC and WDC are separated by the Chitradurga Shear Zone (CSZ) (Drury et al., 1984; Chardon et al., 1998), however, both the cratons are characterized by the presence of the Peninsular basement gneiss (3.3-2.7 Ga) (Beckinsale et al., 1980; Taylor et al., 1984), metamorphosed volcano-sedimentary assemblages forming distinct linear greenstone belt sequences (3.3-2.7 Ga) (Peucat et al, 1995; Jayananda et al., 2008; Nutman et al., 1996; Jayananda et al., 2013) and younger granitic intrusions (2.6-2.5 Ga) (Jayananda et al., 2006; Ramakrishnan and Vaidyanadhan, 2010; Meert et al., 2010). **Figure 5.15a** shows a simplified geological map of the Dharwar Craton and **Figure 5.15b** is a Google Earth image which shows the location of the study areas. The geological setting of these regions along with the details of the dykes found in them are discussed separately in the following sections.

a. Chitradurga granite, Chitradurga Schist Belt, Western Dharwar Craton

Three dykes with outcrop attributes suggestive of emplacement under mixed mode conditions have been encountered within the southern part of the Chitradurga granite. Dyke 1, which has a continuous exposed length of ~ 70 m and an average thickness of 30-35 cm, trends broadly NW-SE and is sub-vertical **(Fig. 5.16a)**. Throughout its exposed length, the dyke maintains a sharp contact with the host granite body and shows systematic curvature representing a sinistral (left stepping) continuous en echelon geometry. Only at its NW distal end, two discontinuous segments are observed, both of which feature horns **(Figs. 5.16b, c, d)**. The longer segments have a mean orientation of ~ 320° and the shorter arms in between two adjacent segments trend ~ 10°. Therefore, the twist angle is ~ 50°. All of the shorter arms are fractured and these fractures trend diagonally from the inner margin towards the outer margin of the dyke body **(Figs. 5.16e, f, g)**. Where such fractures are relatively wider in their aperture, they consist of broken fragments of the dyke body, which are characteristically angular. Veins intruding such fractured areas have propagated within the dyke body and they also show a sinistral en echelon geometry at places **(Figs. 5.16h, i)**. The mafic dyke reveals microscopically the presence of plagioclase laths which have been altered along their boundaries and relict pyroxenes which are now mostly converted to actinolite and chlorite, suggesting the dyke to be originally of a doleritic composition. The relict igneous texture is preserved at the interior portions of the dyke **(Fig. 5.17b)**, however towards its margins, the dyke shows development of strong fabric defined by preferred alignment of its mineral grains **(Fig. 5.17c)**. The fracture filling minerals are mostly tremolite, calcite, epidote and minor talc **(Fig. 5.17d)**, which might be the products of a metamorphic fluid. The altered mineral assemblage is indicative of lower greenschist facies metamorphism within a temperature range of 300-400°C.

Closely occurring dykes 2 and 3 are smaller in dimensions and have an exposed length of ~ 17 m and ~ 21 m respectively, while both have an average thickness of ~ 10 cm. These two dykes are nearly vertical, trend NNW-SSE and are arranged in a discontinuous sinistral en echelon geometry **(Figs. 5.18 and 5.19)**. Some of the segments project small horns from their outer margins. Average twist angles for these two dykes are ~ 30°. Microscopic observation shows the presence of undeformed, euhedral igneous crystals of olivine, plagioclase and augite and the development of distinct variolitic texture at places **(Figs. 5.17e and f)**. The undeformed and un-metamorphosed pristine olivine dolerite mineralogy of these dykes suggests a relatively younger age than that of Dyke 1. Evidence of episodic dyke injection during different stages of crystallization of host plutons has been presented from the Late Archean granitoids of the Eastern Dharwar Craton by Jayananda et al. (2009) who also record mafic magma injections predating the 2.5 Ga metamorphic event which affected the whole of Archean crust.

b. Closepet granite, Pavagada region, Eastern Dharwar Craton

The Closepet granite (2.56-2.51 Ga; Jayananda et al., 1995) is a part of the younger granites in the Eastern Dharwar Craton and constitutes a significant part of the Dharwar batholith (Chadwick et al., 2000). It is a syn-tectonic body (Moyen et al., 2003) emplaced along a crustal-scale shear zone (Jayananda and Mahabaleshwar, 1991; Bouhallier, 1995). The pluton is ~ 400 km long and 30 km wide (Moyen et al., 2003), and is divided into two main parts by a magmatic gap zone. The southern part, a deeper crustal section, is known as the main mass, whereas the shallower northern part is known as the northern intrusions. The main mass is made up of porphyritic monzogranites, pink and grey anatectic granites, clinopyroxene-bearing monzonite bodies, and feldspar accumulations (Moyen et al., 2003) and is subdivided into the root zone in the south and the transfer zone in the north. The region adjoining Pavagada town, where the dyke has been located, falls within this transfer zone. Well-defined N-S trending macroscopic foliation, marked by preferred alignment of K-feldspar porphyroclasts represents the major fabric in the granitic country rocks. Recent study conducted in Pavagada, Madhugiri and adjoining regions within the transfer zone reveals that an E-W directed compression attributed to the late-stage deformation in this portion of the Closepet granite (Das et al., 2024).

The mafic dyke observed near Pavagada town is ~ 80-85 m in its continuous exposed length with an average thickness of ~ 80-90 cm. The dyke trends nearly E-W and dips steeply (>75°) towards south and shows two overlapping right stepping en echelon segments **(Fig. 5.20)**. The tips of these segments are curved towards each other in the overlap zone and one of the curved tips feature multiple branching out horns, which together form a serrated flame-like structure (**Fig. 5.20e**). One segment has a significantly greater exposed length than the other and it also displays systematic curvature representing a continuous dextral en echelon geometry. Each curved portion feature development of horns from the outer margins of the dyke body **(Fig. 5.21)**.

5.4.3 Discussion

All the observed dykes are (sub)vertical and are segmented when exposed on planar outcrops. These segments are systematically oriented in a continuous and/or discontinuous right or left stepping en echelon manner. Although vertical sections (x-z sections) are seldom exposed in the field, no characteristic curvature of the dyke bodies, suggestive of Mode I-II loading, has been observed in such sections. Therefore, the systematic, segmented en echelon geometry of the dykes, is indicative of dyke emplacement under mixed mode I-III loading condition, as discussed in section 2.3. The progressive stages of a dyke's spatio-temporal evolution under mixed mode I-III loading are elaborated in the following section.

a. Progressive spatio-temporal evolution of dykes under mixed Mode I-III loading

As magma tries to ascend, preferably, the rupture will occur at the roof of the magma chamber. As the dyke ascends, perturbations in the orientation of principal stress axes arising from wall rock inhomogeneity or variations in the regional stress field will cause it to respond accordingly, such that its opening component always remains parallel to the minimum compression direction. Assume, as the dyke approaches shallower depths, the orientation of the ambient regional stress field changes, such that, the new maximum compressive stress axis acting on the horizontal plane (σ_{max}') is oriented at a clock-wise positive acute angle to the existing maximum stress axis acting on the horizontal plane (σ_{max}). In this situation, the dyke will undergo twisting since its propagation direction (vertical) becomes normal to the plane on which the principal stress axes have rotated (horizontal) **(Figs. 5.22 and 5.27)**. If rheological conditions are ductile at this depth, the body will deform aligning itself with the changed orientation of principal stress axes by developing a continuous curved geometry. Since, the maximum compressive stress axis has rotated dextrally, the dyke body will also twist in a similar fashion such that, its longer segments align parallel to the new maximum compressive principal stress and the shorter curved portion in between two adjacent longer segments remain more or less in its original position. The angle in between the longer segments and the shorter connecting arms will therefore give the "twist angle" **(Fig. 5.22c)**. As twisting continues, stresses will continue to accumulate at the outward curved margins of the longer segments which are preferably aligned with the stress field. This continued stress built-up will result in the propagation of narrow linear fringes from the outward margins of the dyke segments which are also known as "horns". Although horns have been described as failed magma paths (Gudmundsson, 2020), it has also been reported earlier that development of horns in dykes occurs under conditions of mixed mode I–III loading (Delaney and Pollard, 1981). This behaviour is explained by Weinberger et al. (2000) with a damage rheology model (Agnon et al., 1995; Lyakhovsky et al., 1997a, 1997b) that utilizes non-linear elastic fracturing mechanisms. According to their simulations considering discontinuous en echelon segments, under mixed mode I–III loading, as two dike segments move in the direction of one another, a high-intensity damage zone forms around them, causing magma to invade those areas, which results in the growth of horns at the asymmetric ends of the dike segments. It has been observed in presently reported dykes of Dharwar Craton that their terminal portions undergo more discontinuous segmentation relative to their central portions which are comparatively thicker and show a continuous curved geometry. Therefore, depending on the ambient rheology and dimension of the dyke body, twisting may produce both continuous and discontinuous segments. The type of horns which protrude from the outward curvature/margin of initially continuous or discontinuous en echelon segments can be termed as first order horns. In a progressively deforming sequence, as the dyke ascends to shallower depths, continued twisting in a comparatively brittle regime will eventually result in detachment of dyke segments. This progressive sequence of deformation that the dyke body undergoes as it propagates upwards is shown in **Figure 5.22**. The parent dyke body can even produce sharply truncated segments without the development of an initial continuous curvature if the rate of twisting is relatively faster within a comparatively more mechanically rigid host rock. As the detached segments grow and overlap, their proximal tips advancing towards each other will show distortion characterized by greater curvature at their inner margins compared to the relatively linear outward margins **(Fig. 5.23)**. This phenomenon has been explained using elastic solution for pressurized en echelon cracks by Delaney and Pollard (1981). As overlapping increases, the segments will tend to turn towards one another due to strong mutual mechanical interaction. Occurrence of such curved en echelon segments has been clearly depicted from field exposures of felsic veins observed in the Pavagada region, adjacent to the reported dyke **(Fig. 5.24)** and also from the Chotanagpur Granite Gneissic Complex (CGGC) **(Fig. 5.25)** (see Supplementary sheet – 1 of Biswas et al. 2023 for location and geological map of the region). If supply of magma is still unhindered, two adjacent segments approaching one another may even try to bridge. Such bridging is also evident in the field exposures of the above mentioned felsic veins

(Fig. 5.26). In field exposures, two bridged segments can appear apparently similar to a continuously curved dyke body featuring horns at its both outer margins. However, bridges share a discontinuous boundary with the two segments they connect unlike a continuously curved parent dyke body and are often irregular. They may even preserve portions of the host rock material within them **(Fig. 5.26)**. Now, second order horns may similarly develop from the outward margins of the curved en echelon segments since they are still favourably aligned to the ambient stress field. Such horns are distinctly developed in the felsic veins of CGGC **(Figs. 5.25b & c)**. The curved tip of the dyke segment in Pavagada also feature multiple horns branching out from the outer margin of the segment **(Fig. 5.21i)**. In essence, all these horns are of second order although each horn might have developed at discrete time intervals as the dyke segment expanded and propagated. Initial curvature caused the first horn to protrude from the outward margin of the curved segment tip but strong mechanical interaction caused it to curve in a similar fashion which prompted the initiation of the next horn from its outward margin. Repetition of this process eventually resulted in the formation of a flame like branching structure at the dyke tip, which as a whole is itself curved towards its adjacent segment with the exception of the last horn. A comprehensive sequence of progressive dyke evolution under condition of mixed mode I-III loading is depicted in **Figure 5.27**.

b. Dyke emplacement in the Chitradurga granite, Chitradurga Schist Belt, Western Dharwar Craton

All three mafic dykes encountered within the Chitradurga Schist Belt belong to the Proterozoic mafic dyke swarm that intrude the younger granites (~ 2.61 Ga) of the schist belt (Ramakrishnan and Vaidyanadhan, 2010) but show some contrasting characteristics in terms of their outcrop shapes, sizes and geometries and mineralogy as mentioned in section 3.1. Firstly, dyke 1 is considerably larger in dimension than dykes 2 and 3. Since its aspect ratio (maximum thickness/total length) is higher compared to the other two, it will have a higher magma overpressure and therefore a greater depth of origin. The constituent mineralogy of dyke 1 also shows evidence in support of metamorphism at least up to lower greenschist facies within a temperature range of 300 to 400°C. The outcrop pattern is characterized by curvature of the whole dyke body to form a continuous en echelon geometry. Also, microscopic study reveals the development of strong fabric adjacent to its margins. These observations are suggestive of deformation in a ductile manner. The presence of blunt-ended tips of the dyke segments **(Figs. 5.16d and j)**, suggesting forcible intrusion of magma by ductile deformation of the host rock (Kattenhorn and Watkeys, 1995) along with spatially restricted development of preferably aligned fabric within the host granite adjacent to the curved portions of the dyke **(Fig. 5.16e)** also attests to this fact. Evidence of later brittle behaviour in this dyke is present in the form of fractures and veins intruded therein at the curved portions of the dykes. By the time the dyke has ascended to shallower depths, the granite has solidified more. Further twisting of dyke segments in response to change in the orientation of the principal stress axes at this shallower depth has resulted in the initiation of fractures at the connecting arms in between two adjacent segments as they try to pry away from each other. Dykes 2 and 3 however show no evidence of metamorphism as they retain original euhedral igneous crystals which are unaltered and undeformed. In field exposures also, they display sharply truncated segments. Their overall character is indicative of deformation strictly within a more brittle domain. Since their aspect ratios (maximum thickness/total length) are smaller compared to dyke 1 they will have a lower magnitude of magma overpressure corresponding to a shallower depth of origin. It is plausible that these two dykes probably originated from a shallower magma chamber at a relatively later period as compared to the dyke 1. By this time, the Chitradurga granite has solidified to a greater extent and therefore in response to changing stress field, the dykes have deformed in a purely brittle manner. In order to conveniently visualize their emplacement histories, it is therefore crucial to constrain the timings of the deformation episodes that these bodies along with the host granite has suffered. Radiometric studies conducted on Chitradurga granite indicate that the granite crystallized at 2614 ± 10 Ma (SIMS U–Pb dating zircons; Jayananda et al., 2006). This is also in line with the whole rock Pb–Pb isochrons, which yield an age of 2605 ± 18 Ma (Taylor et al., 1984). Studies conducted by Mondal and Mamtani (2014) show that the Mulgund granite (2555 ± 6 Ma; Sarma et al., 2011), another younger granite of the CSB equivalent to the Chitradurga granite, emplaced syn-tectonically with the CSZ. It has also been demonstrated recently by Bhatt et al. (2017) that D_3 deformation of the Mulgund granite can be constrained to ≤2537 Ma. It is to be noted that both the plutons (Mulgund and Chitradurga) have experienced D_1/D_2 deformation on account of a regional NE-SW directed compression, which has resulted in the development of a NW-SE oriented magnetic fabric (foliation) in these regions. Therefore, the D_1/D_2 deformation in the CSB occurred between 2614 and 2555 Ma, followed by the onset of a D_3 event at ~2537 Ma, which is consistent with the protracted cratonization process (~ 100 Ma) of the Dharwar Craton as suggested by Jayananda et al. (2006). In light of these geochronological constraints coupled with the well documented regional deformation history, a possible picture of the relative sequence of dyke evolution within the CSB can be perceived. Emplacement of the Chitradurga granite took place within a NE-SW directed compressive stress field. All three observed dykes which have intruded the granite are vertical to steeply dipping and are segmented in a systematic sinistral en echelon pattern with an overall NW-SE to NNW-SSE trend. However, the shorter connecting arms in between two adjacent twisted segments of the continuously curved dyke (Dyke 1) trend NNE and the twist angles vary from 30 to 50°. This indicates that the initial orientation of the dykes was NNE-SSW to NE-SW. It is possible that the dykes initiated along NNE-SSW to NE-SW oriented extension fractures which were generated under the NE-SW directed D_1/D_2 compressive stress field and propagated for a period of time thereafter. As the regional stress field changed to a E-W to ESE-WNW directed compression (D_3), sinistral shear was induced along the NNW-SSE oriented schist belt boundary. In response to this shearing, the dykes emplaced within the Chitradurga granite, which had still not solidified completely, initially experienced rigid body rotation (sinistral) to some extent. As soon as the angle between the dykes and the regional compression axis exceeded 90°, shear was induced along the dyke bodies which resulted in their present sinistral en echelon segmented geometry. Dyke 1 being older and larger, possibly emplaced at a greater depth in the earlier phases of D_2 deformation. As D_3 initiated, the rheology of the dyke body as also of the host granite at greater depths allowed an initial ductile behaviour as is evinced by its greater twist angle and continuous curved geometry along with the presence of plastic deformation characters. As cooling continued, both the bodies became more rigid, which resulted in the initiation of fractures along the connected portions of the twisting segments. While dykes 2 and 3, being younger and shorter in dimension, intruded a much more solidified granite from a shallower depth at a later stage, possibly by the closure of the D_2 event, which is also supported by its pristine mineralogy and thereby got sharply truncated into en echelon segments, unlike dyke 1, on the advent of D_3. Their smaller twist angles (~ 30°) and absence of any preferred fabric within the host granite body lying in proximity to the detached dyke segments also supports a more brittle behaviour of these dykes. The evolutionary sequence of the dyking event within the Chitradurga granite as described here is portrayed schematically in **Figure 5.28**. The suggested model is a plausible explanation culminating from observed field evidences and the deformation history of the terrain but is by no means exhaustive. Although mineralogical and textural observations evince the relative ages of the dykes, their absolute geochronological constraints are a requisite to substantiate the model and that leaves scope for future work. However, it can be apprehended that consistent patterns of dyke segmentation within a considerable spatial extent, as in swarms, may act as potential indicators of shear sense at regional scales.

c. Dyke emplacement in the Closepet granite, Pavagada region, Eastern Dharwar Craton

The dyke encountered in Pavagada region, emplaced within the Closepet granite belongs to the Proterozoic mafic dyke swarm that has intruded the Dharwar batholith (Ramakrishnan and Vaidyanadhan, 2010). It has an overall E-W trend but is segmented, arranged in a right-stepping sequence. The dominantly exposed segment in itself shows continuous curvature in a consistent right-stepping en echelon pattern along with the development of horns from the outward margins of each curvature. This is indicative of dextral shearing initiated along the dyke body as it ascended. Considering a twist angle of ~ 30°, the initial trend of the undistorted dyke body should have been ENE-WSW. The deformation history of the Closepet pluton is not still well constrained. However, structural investigations from the adjacent Sandur Schist Belt, located at the core of the northern intrusion part of the Closepet pluton ~ 120 km north-west of Pavagada, indicates an initial ENE-WSW directed compression which has resulted in the formation of NNW-SSE axial plane of the D_1 folds, while the D_2 folds, generated due to later E–W compression, are oblique to the earlier fold axis, inducing sinistral shearing along the D1 axial plane (Mukhopadhyay and Matin, 1993). It has been inferred that the Closepet granite also experienced a similar compression direction (Moyen et al., 2003). Recent studies conducted on fractured feldspar porphyroclasts within the transfer zone of the Closepet granite also corroborate a late E-W paleostress direction (Das et al., 2024). In light of these studies, it might be inferred that the formation of the dyke commenced as a Mode I fracture within the Closepet granite under an initial ENE-WSW directed compressive stress regime. As the regional stress field rotated dextrally to an E-W directed compression, Mode III loading was imposed on the ascending dyke body (Mode I) which twisted in response (Mode I-III), resulting in a series of continuous/discontinuous right-stepping en echelon segments.

5.5 Summary

This study presents two new mathematical approaches for estimating the complete dimensions, i.e., total length and maximum thickness of dykes formed predominantly as opening mode (Mode I) fractures, from their partial exposures, and validate them against ground data as well as against published data. The first method is applicable to partial dyke outcrops where at least one dyke tip is exposed. Considering the canonical model of Mode I fractures; complete dyke dimensions are estimated by solving the equation of the ellipse which the dyke approximates using all possible combinations of two points lying on the dyke margin measured from the observed tip. Using this method, magma overpressure ranges for mafic dykes emplaced within Chitradurga granite, Western Dharwar Craton, India are estimated. Calculated results range from 27 MPa to about 72 MPa, which corresponds to a depth range of 9 to 25 kilometers. Calculated Mode I stress intensity factors for the host granite range from 132 MPa/m^2 to 689 MPa/m^2 indicating high fracture toughness of Chitradurga granite.

The second method extends this approach to partial dyke outcrops with no exposed tips. In this pioneering mathematical method differential equations for an ellipse are employed, which is the predicted shape of an opening mode dyke in the idealized canonical model (Mode I dykes). Complete dyke dimensions estimated through this method are used in calculating magma overpressure (P_o) and depth of origin (z) of two partially exposed mafic dykes emplaced within the younger granites of the Dharwar craton, one near Chitradurga town in the WDC and the other near Pavagada town in the EDC. P_o and z are calculated to be 60.7 MPa and 20.6 km and 37.7 MPa and 12.84 km for the dykes in Chitradurga and Pavagada regions respectively. The potential of the method lies in the fact that it can provide near true parameter estimates for dykes where limited outcrop has previously restricted the ability to estimate their true dimensions. Magma overpressure and depth of origin values, calculated from complete dyke dimensions estimated for all observed partially exposed dykes, both with one exposed tip and without exposed tips, emplaced within the younger granites of the Dharwar Craton, India, using the two proposed methods (Biswas et al., 2023; 2025), are represented graphically in **Figure 5.29**.

In addition to these methodological advances, the present study provides a comprehensive compilation of the different modes of fracture formation and their mutual interactions giving rise to hybrid modes of fracturing. The phenomenon of hybrid fractures has been extensively used to explain different attributes that dykes display in their outcrop patterns, which cannot be conveniently explained by pure opening mode of fractures. A progressive spatio-temporal sequence of dyke evolution under mixed Mode I–III loading is outlined, distinguishing incremental orders of dyke horn formation, and continuous curved dyke geometries from bridged dyke segments. It has been found that mafic dykes emplaced within the younger granites of the Dharwar Craton exhibit outcrop attributes consistent with such mixed-mode I-III emplacement. The study identifies two generations of dyking within the Chitradurga granite of the Chitradurga Schist Belt, Western Dharwar Craton, India. Dykes of both these generations belong to the newer dolerite dyke swarm which have intruded the younger granites (~ 2.61 Ga) at the uppermost stratigraphic levels of the schist belt and therefore indicate episodic dyking events within this stratigraphic horizon. Structural investigation of their outcrop patterns reveals that the dykes are sinistral sheared induced by the effect of the adjacent Chitradurga Shear Zone and a geological model of their formation and subsequent emplacement under varying regional stress fields of the region has been proposed. Further, outcrop attributes of the dyke intruding the Closepet granite in the Pavagada region of Eastern Dharwar Craton, India suggest initiation under an ENE-WSW directed compression and subsequent dextral shearing on account of a later E-W directed compression.

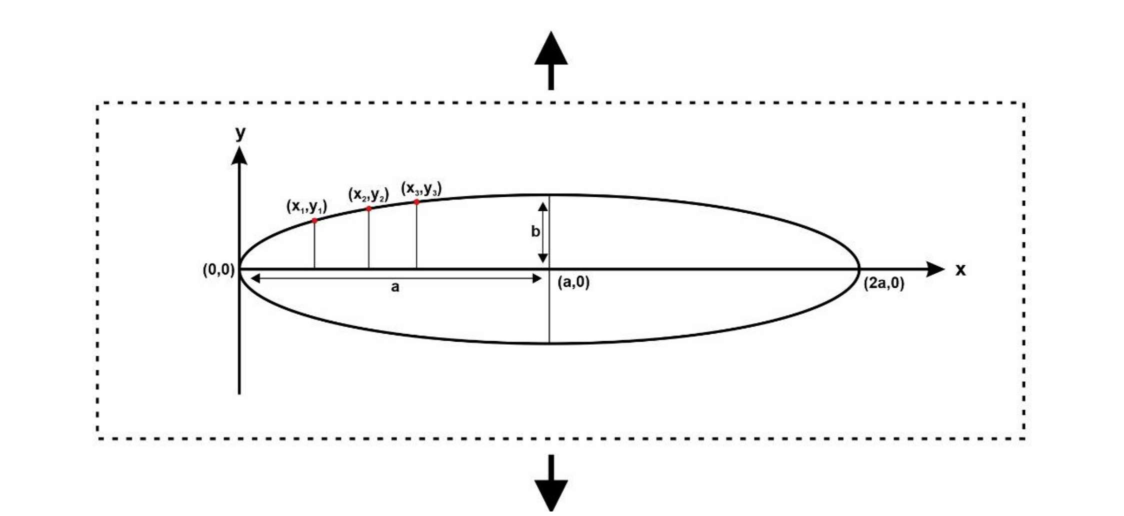

Fig. 5.1 A hypothetical Mode I crack developed within an infinite, homogenous, isotropic, elastic material under remote stress. The crack length is along the x-axis and its opening displacement is along the y-axis. Measurements for all observed points on the crack perimeter are made from the tip of the crack. Half-length and half maximum thickness of the crack are indicated by a and b respectively.

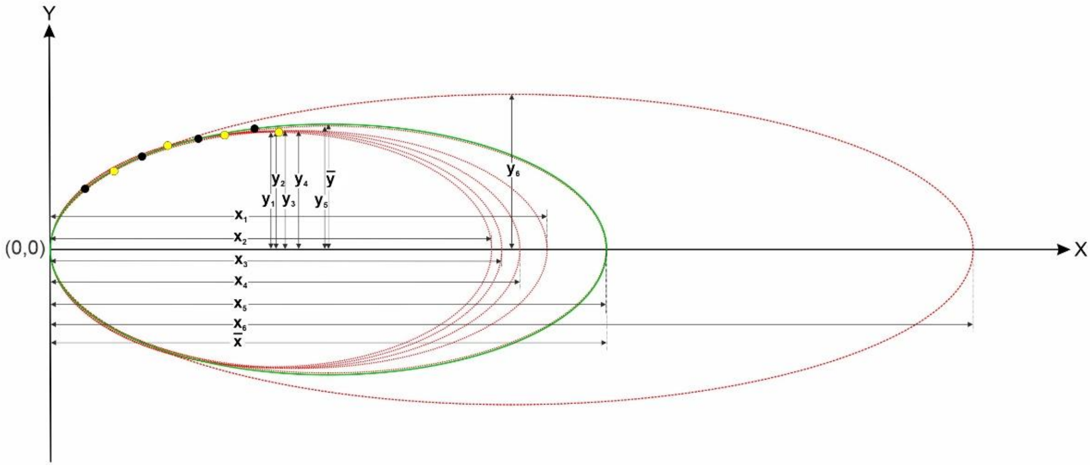

Fig. 5.2 Conceptual model used for the calculation of full length and maximum thickness of an ellipse by combination of points which lie at some deviation from its perimeter. Origin of the co-ordinate system is positioned at the vertex. We consider an ellipse (solid green) and mark four different points on its perimeter (black dots). A total of six ellipses can be drawn taking a combination of any two points (black dots) (${}^{4}C_{2}=6$) which will produce the same ellipse (solid green). Now, four points (yellow dots) are considered which lie at some deviation from the perimeter of the solid green ellipse. The mean length ($\bar{x} = \frac{1}{6}\sum_{i=1}^{6} x_i$)and the mean thickness ($\bar{y} = \frac{1}{6}\sum_{i=1}^{6} y_i$)of the six different ellipses (dashed red) which can be drawn through the combination of any two yellow dots corroborates exactly to the length and thickness of the solid green ellipse.

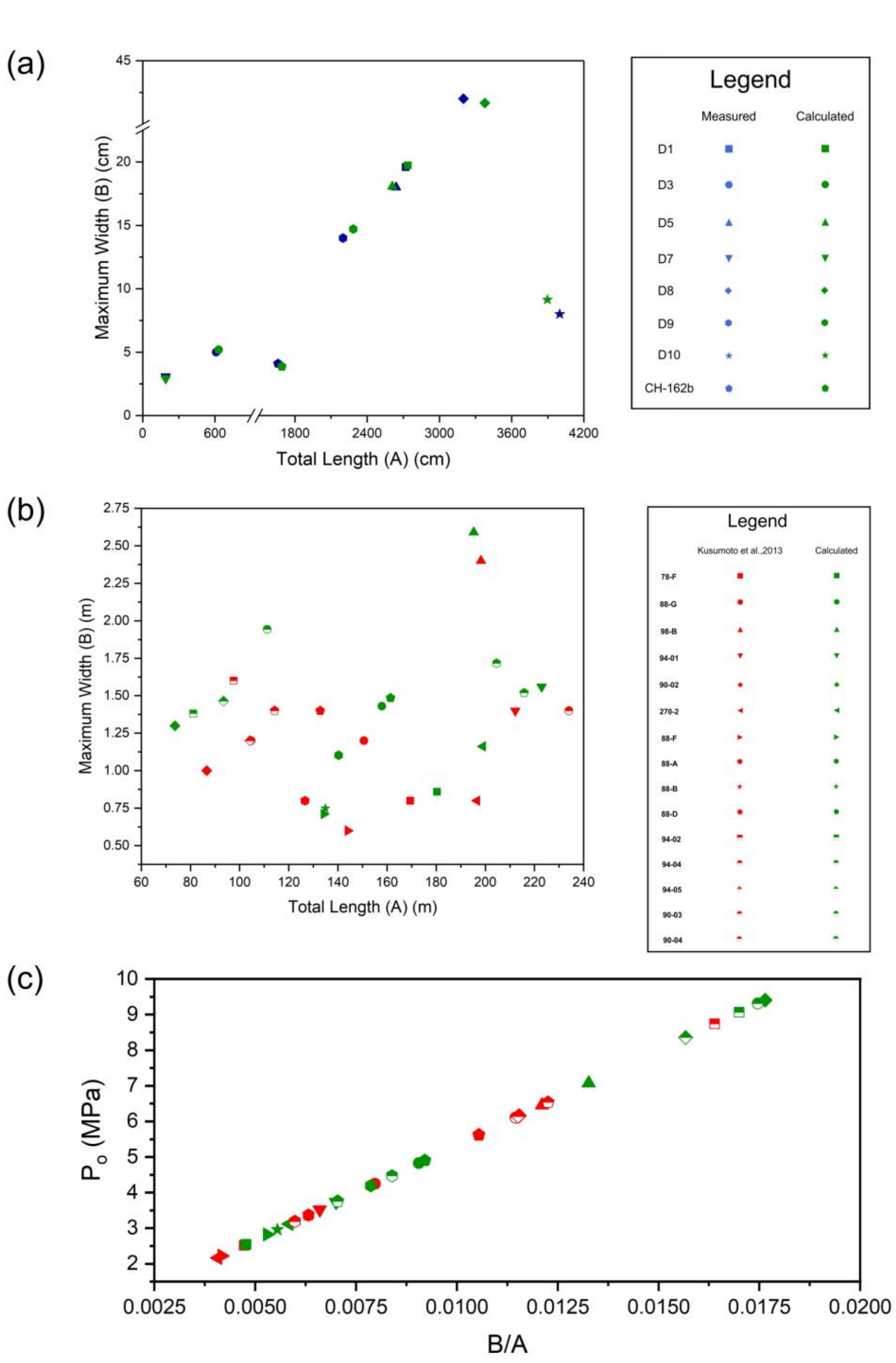

Fig. 5.3 (a) Graphical comparison of actual dyke dimensions measured in the field (Purulia & Chitradurga, India) and calculated results using the proposed method. **(b)** Comparison of calculated total lengths and maximum opening displacements (or maximum thicknesses) of fifteen dykes reported in Geshi et al., 2010 to those estimated by Kusumoto et al. (2013). **(c)** Estimated magma overpressure values (P_o) using the calculated lengths and maximum thicknesses for the same fifteen dykes corroborate to those published in Kusumoto et al. (2013). It may be noted that all dyke numbers have been kept unchanged.

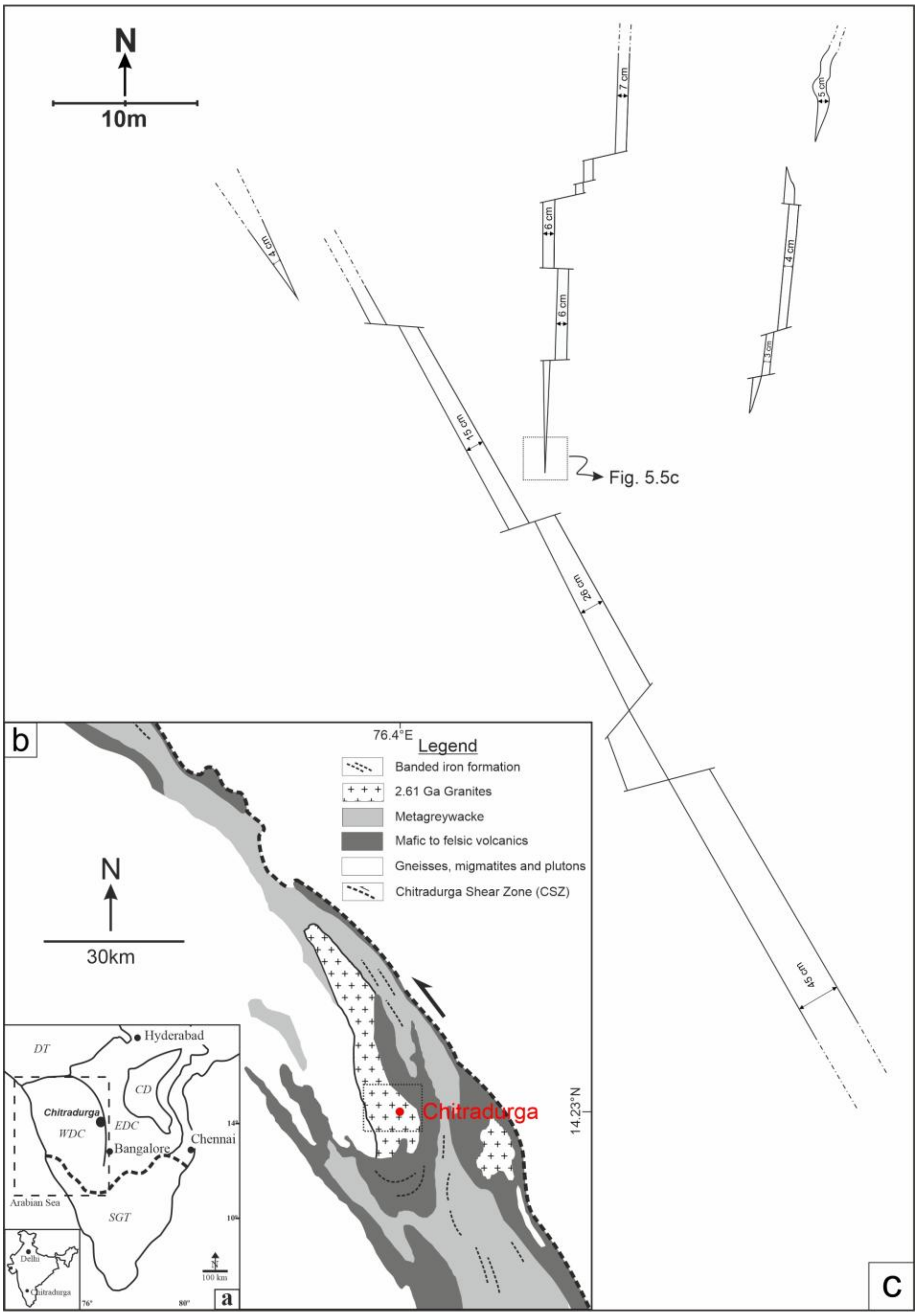

Fig. 5.4 (a) Map showing location of Chitradurga region in the southern Indian shield (after Sarma et al., 2012); SGT= Southern Granulite Terrain; EDC = Eastern Dharwar Craton; WDC = Western Dharwar Craton; CD = Cuddapah Basin rocks; DT = Deccan Trap basalts. Dashed line represents the Moyar Bhavani Shear Zone. Inset shows the map of India. **(b)** Regional geological map of the Chitradurga schist belt (after Jayananda et al., 2013). Dashed box near Chitradurga demarcates the region of study. **(c)** Detailed map showing disposition of dolerite dykes within Chitradurga Granite from location CH-162 (near Chitradurga fort). Thicknesses of dyke segments are indicated. Field photograph of the dyke tip marked by dashed box is shown in Fig.5.5c.

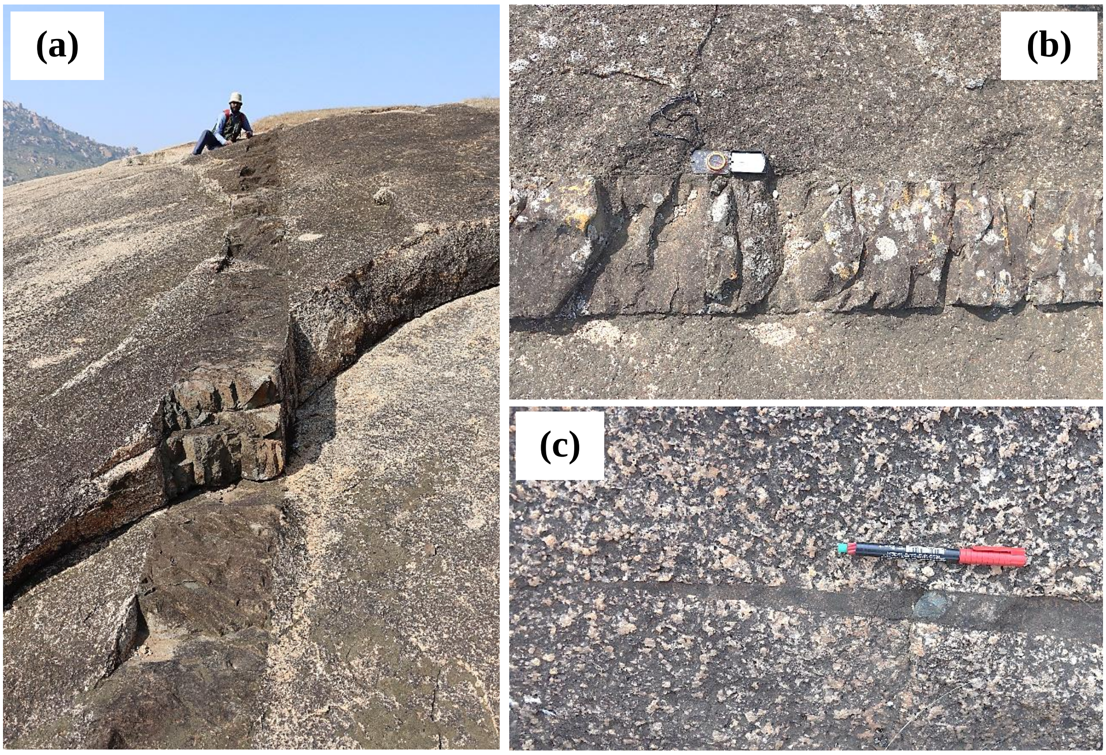

Fig. 5.5 (a) Field photograph showing an exposure of dolerite dyke which intrudes the host granite. **(b)** Close view of the dyke showing fractures developed within it. **(c)** Field photograph of the tip of dyke marked in Fig.4c. Length of the marker pen is 14cm.

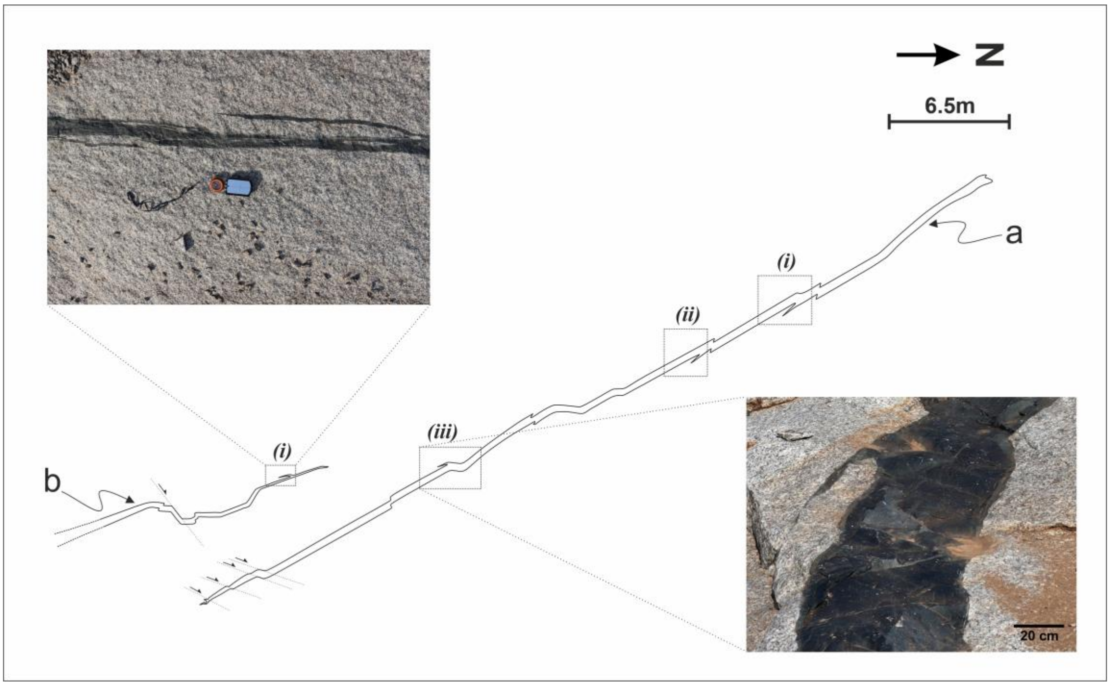

Fig. 5.6 Sketch map of dolerite dykes from location CH-161 showing curved segments and development of apophyses also called dyke ‘horns’ which are demarcated by dashed boxes. Inset figures show field photographs of two such dyke horns.

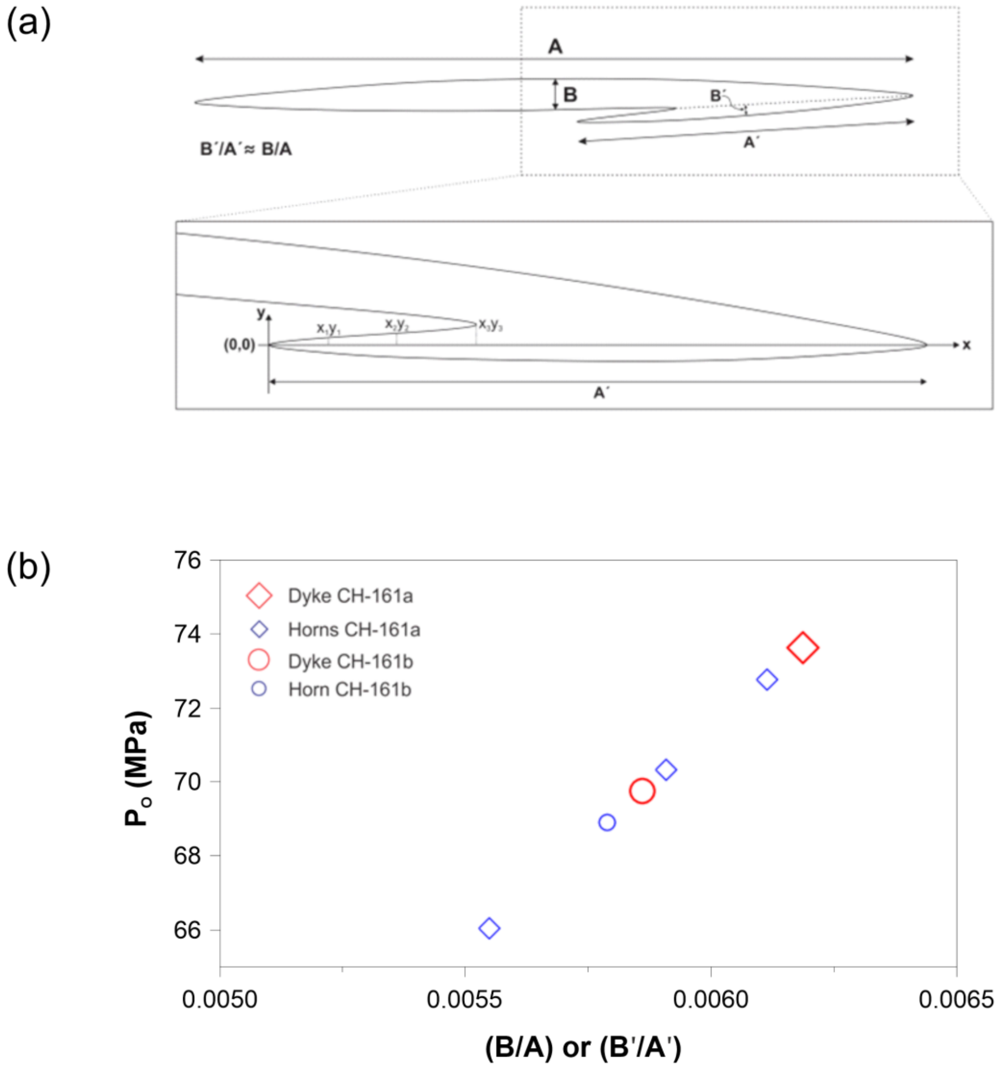

Fig. 5.7 (a) Schematic diagram indicating dyke horns maintain similar aspect ratios to that of the whole dyke. Total length and maximum thickness for whole dyke are represented by A and B respectively while A´ and B´ respectively represent the same for the dyke horn. **(b)** Comparison of calculated magma overpressures using aspect ratios of whole dyke and dyke horns.

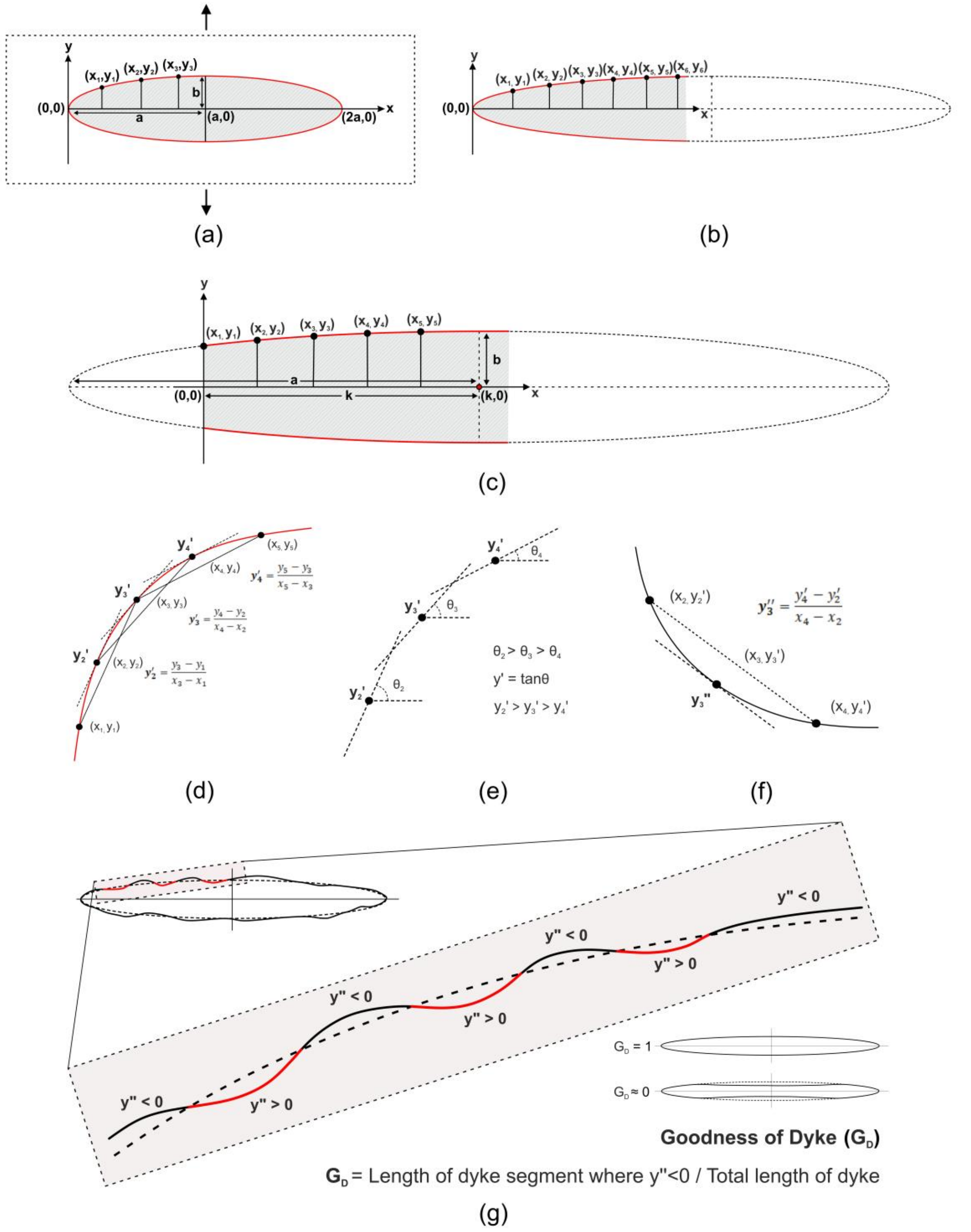

Fig. 5.8 (a) Development of a hypothetical Mode I crack under remote stress, within an infinite, homogenous, isotropic, elastic material. The x-axis represents the crack length, and the y-axis represents the opening displacement. All observed sites along the crack's perimeter are measured starting at its tip. The crack's half-length and half-maximum thickness are represented by a and b respectively. **(b)** A partially exposed opening mode dyke with a visible tip at one end (shaded part bounded by red lines). Contd.

Fig. 5.8 Contd. All measurements on the dyke boundary are made from the tip. Complete dyke dimensions in this scenario have been estimated by Kusumoto et al. (2013) and Biswas et al. (2023). **(c)** A partial dyke exposure devoid of any tip (shaded part bounded by red lines). The complete dyke is of an elliptical shape (demarcated by dashed line) with a semi-major axis a and semi-minor axis b, whose center (k, 0) lies on the x-axis. Measurements are made on the dyke margin placing the origin at the left starting point of the outcrop. **(d)** Slope at a point on the dyke margin (y') calculated using discrete derivative at that point. The curvature of the dyke margin (red bounding line) is exaggerated for illustrative clarity. **(e)** Gradual change in the slope of the curve. Note that in an ideal concave down dyke margin, slope gradually decreases with increasing x coordinate. **(f)** Rate of change of slope of the curve (y''). Note that for an ideal concave down dyke margin, rate of change of slope is always negative. **(g)** Goodness of dyke (G_D) is a metric of regularity for a naturally irregular dyke based on the extent to which its margin is locally concave up where the rate of change of slope will also be locally positive. In an ideal elliptical shaped dyke, G_D tends to be unity, whereas, in an overall concave upward shape G_D value will move towards zero.

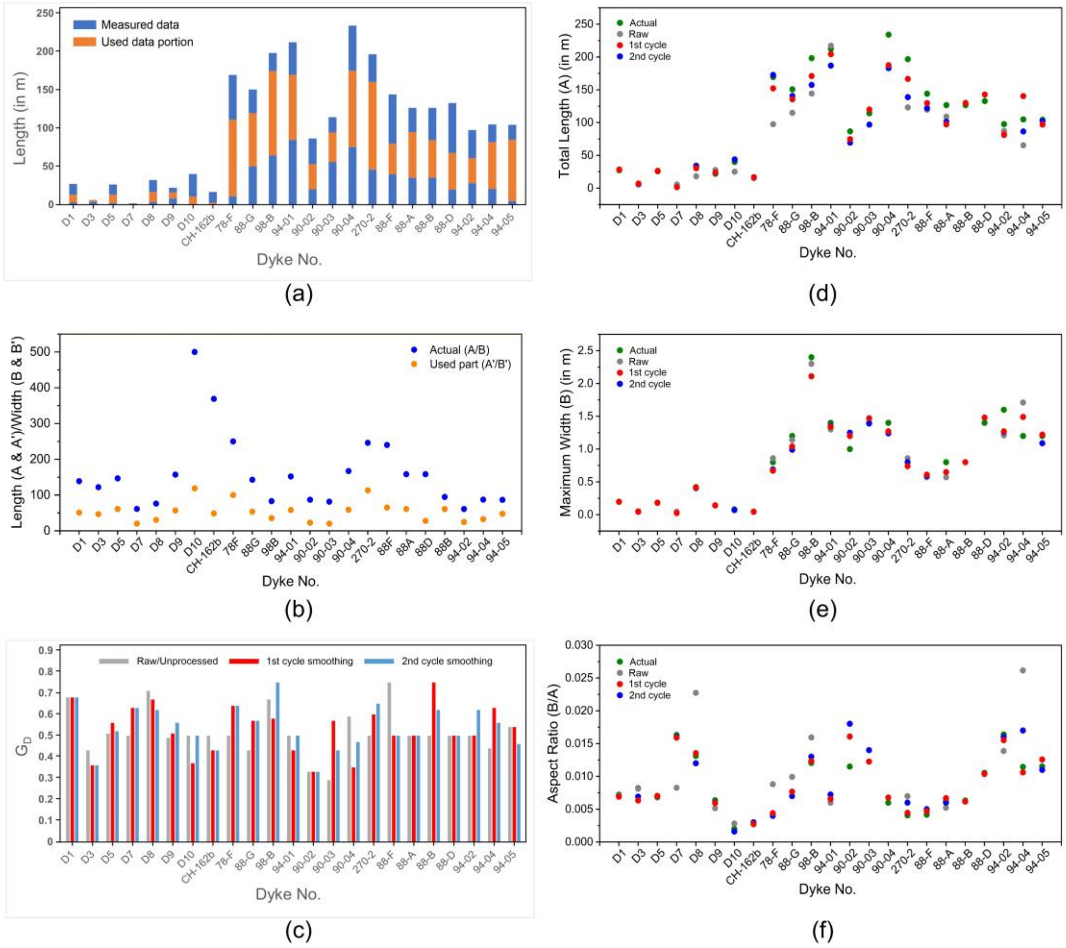

(a) (d)

(b) (e)

(c) (f)

Fig. 5.9 Graphical comparisons of **(a)** measured data and used (selected) part of the measured data for all dykes in the test dataset; **(b)** actual length/maximum width ratios of the dykes to visible length/maximum visible width ratios of the selected parts of the dykes; **(c)** G_D values of raw data and in the 1st and 2nd cycles of smoothing for all selected dyke portions; **(d)** actual full length (A) and estimated full length for raw data followed by two successive cycles of smoothing; **(e)** actual maximum width (B) and estimated maximum width for raw data followed by two successive cycles of smoothing; **(f)** actual aspect ratio (B/A) and estimated aspect ratio for raw data followed by two successive cycles of smoothing. Note, for the dykes of Miyake-jima, Japan, the estimates of Kusumoto et al. (2013) have been taken as standard. All dyke nos. from Kusumoto et al. (2013) and Biswas et al. (2023) have been kept unchanged. Please refer to Supplementary sheet-4 for details of error calculations among the actual results and raw, 1st cycle and 2nd cycle results for all parameter estimates.

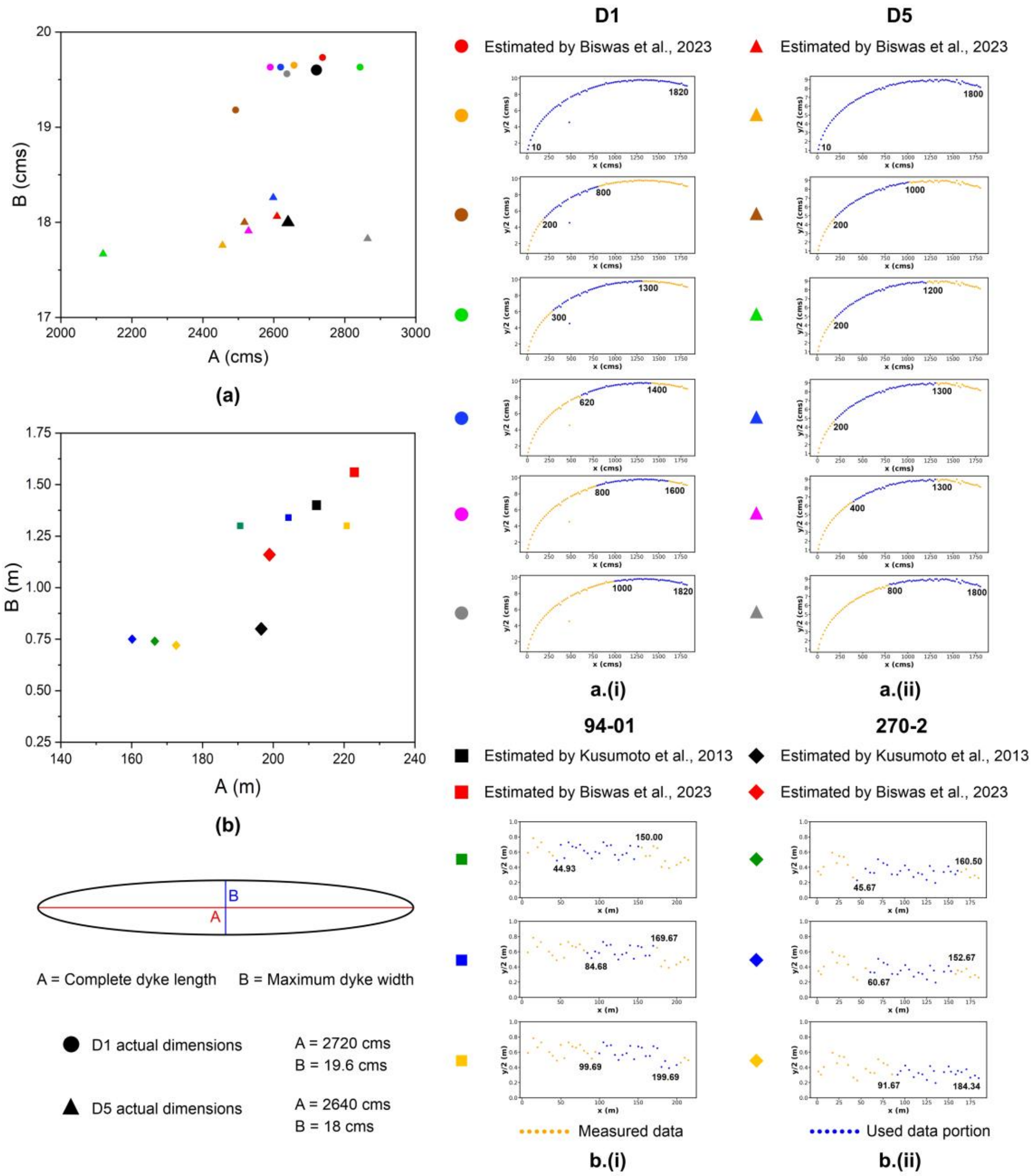

Fig. 5.10 (a) Application of the present method to different selected portions of the same dyke. The analysis shown is conducted on four dykes: **(a)** D1 and D5 from Purulia, India; **a(i)** and **a(ii)** shows the six different portions selected each from dyke nos. D1 and D5 respectively. **(b)** 94-01 and 270-2 from Miyake-jima, Japan; **b(i)** and **b(ii)** shows the three different portions selected each from dyke nos. 94-01 and 270-2 respectively.

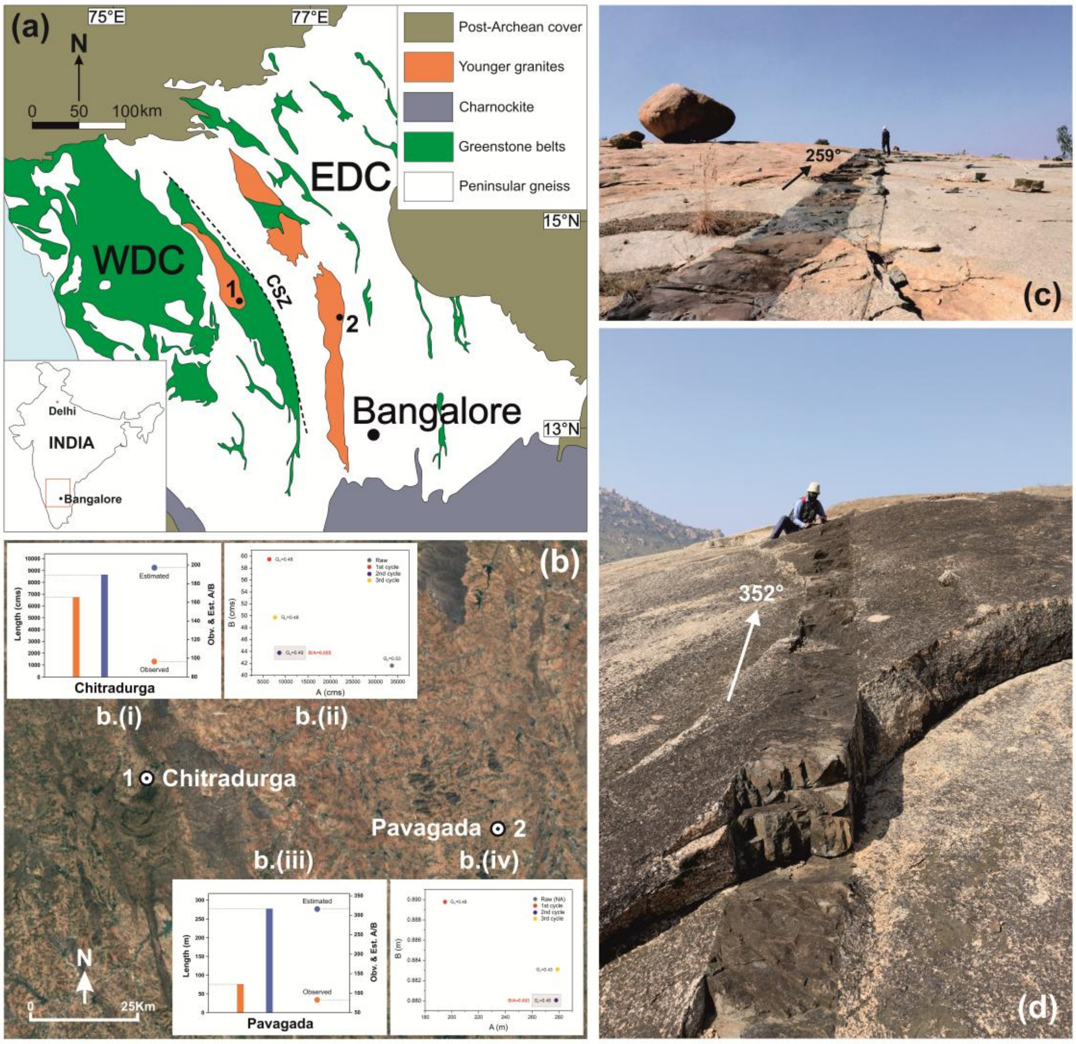

Fig. 5.11 (a) Simplified geological map of the Dharwar Craton modified after Dey et al. (2015) showing the location of Chitradurga and Pavagada towns demarcated by 1 and 2 in the map respectively. Chitradurga Shear Zone (CSZ) demarcates the boundary between Western Dharwar Craton (WDC) and Eastern Dharwar Craton (EDC). Inset shows the map of India. **(b)** Google earth image showing a close-up view of Chitradurga and Pavagada towns, surrounded by exposures of Chitradurga granite and Closepet granite respectively. Figures **b.(i)** and **(ii)** shows the observed vs. estimated lengths and full length (A) & maximum width (B) estimated for raw data and in 1st and 2nd cycles of smoothing for the dyke in Chitradurga. Figures **b.(iii)** and **(iv)** show the observed vs. estimated lengths and full length (A) & maximum width (B) estimated for raw data and in 1st and 2nd cycles of smoothing for the dyke in Pavagada. **(c)** and **(d)** show field photographs of the dykes observed in Pavagada and Chitradurga respectively.

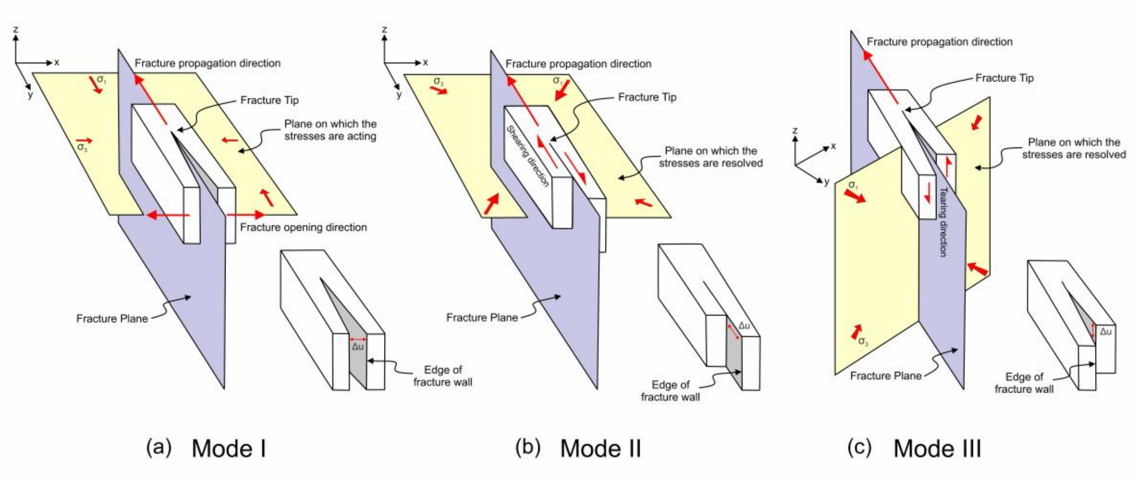

(a) Mode I (b) Mode II (c) Mode III

Fig. 5.12 (a) Mode I or pure opening mode fracture. Within a compressive stress regime where the intermediate stress axis (σ_2) is vertical, the fracture opens in the direction of the minimum compressive principal stress (σ_3), albeit, in the opposite sense, when the magnitude of the tensile stresses acting across the fracture plane exceeds that of σ_3. The tips of the fracture propagate along the trend of the maximum compressive principal stress (σ_1). Note that the opening displacement (Δu) across the fracture plane (y-z plane) is perpendicular to the direction of fracture propagation as also to the edges of the fracture walls. **(b)** Mode II or shearing mode fracture. Note that σ_1 and σ_3 still lie on the horizontal plane but have rotated (clock-wise) becoming oblique to the fracture plane (y-z plane) thereby inducing shear (dextral) along it. This causes the blocks lying on either side of the fracture plane to slide past each other. The line of fracture propagation direction lies on the plane on which the principal stress axes rotate (x-y plane) and the displacement component (Δu) is parallel to it but is perpendicular to the edges of the fracture walls. **(c)** Mode III or tearing mode fracture. ‘Tearing’ refers to the effect where one block lying on any side of the fracture plane moves up or down with respect to the block lying on the other side of the fracture plane. This happens when both σ_1 and σ_3 lie on a vertical plane but are individually oriented obliquely to the fracture plane (y-z plane) thereby inducing shear along it. Note, that here the line of fracture propagation direction does not lie on the plane on which rotation of the principal stress axes occurs (x-z plane) and the displacement component (Δu) is perpendicular to it but is parallel to the edges of the fracture walls. (Modified after Fossen, 2016 and Pollard and Martel, 2020).

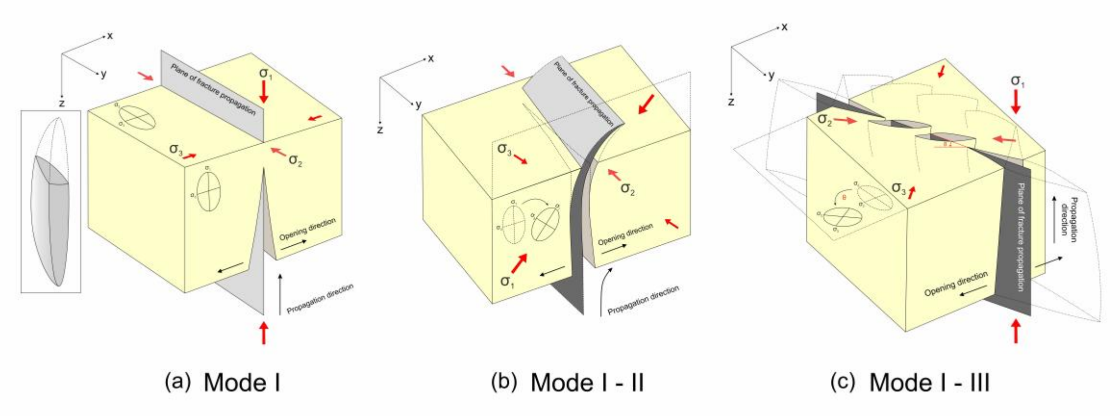

(a) Mode I (b) Mode I - II (c) Mode I - III

Fig. 5.13 (a) A pure Mode I dyke formed within a compressive stress regime where the maximum compressive principal stress axis (σ_1) is vertical. Inset shows the idealized 3D shape (flat ellipsoid) of the dyke as formulated in its canonical model. **(b)** Mixed mode I-II dyke. Here, the advancing dyke tip turns towards the rotated orientation of σ_1 such that, its progressive opening displacement aligns parallel to the trend of ambient σ_3. Note, in the figure, σ_1 and σ_3 rotates dextrally from their initial orientation on the vertical x-z plane which contains the line of dyke propagation direction (along the z axis). **(c)** Mixed mode I-III dyke. Here, σ_1 remains vertical, however, σ_2 and σ_3 rotates on the horizontal x-y plane. As a result, the advancing dyke body twists so as to orient its progressive opening displacement parallel to the changed orientation of σ_3. Such twisting is manifested by the development of en echelon dyke segments where the twist angle (θ) denotes the angle between the initial trend of the dyke body and the new trend of the dyke segments produced due to twisting of the parent dyke body. Note that the direction of dyke propagation (along the z axis) is normal to the plane on which σ_2 and σ_3 rotate (x-y plane). (Modified after Pollard and Martel, 2020).

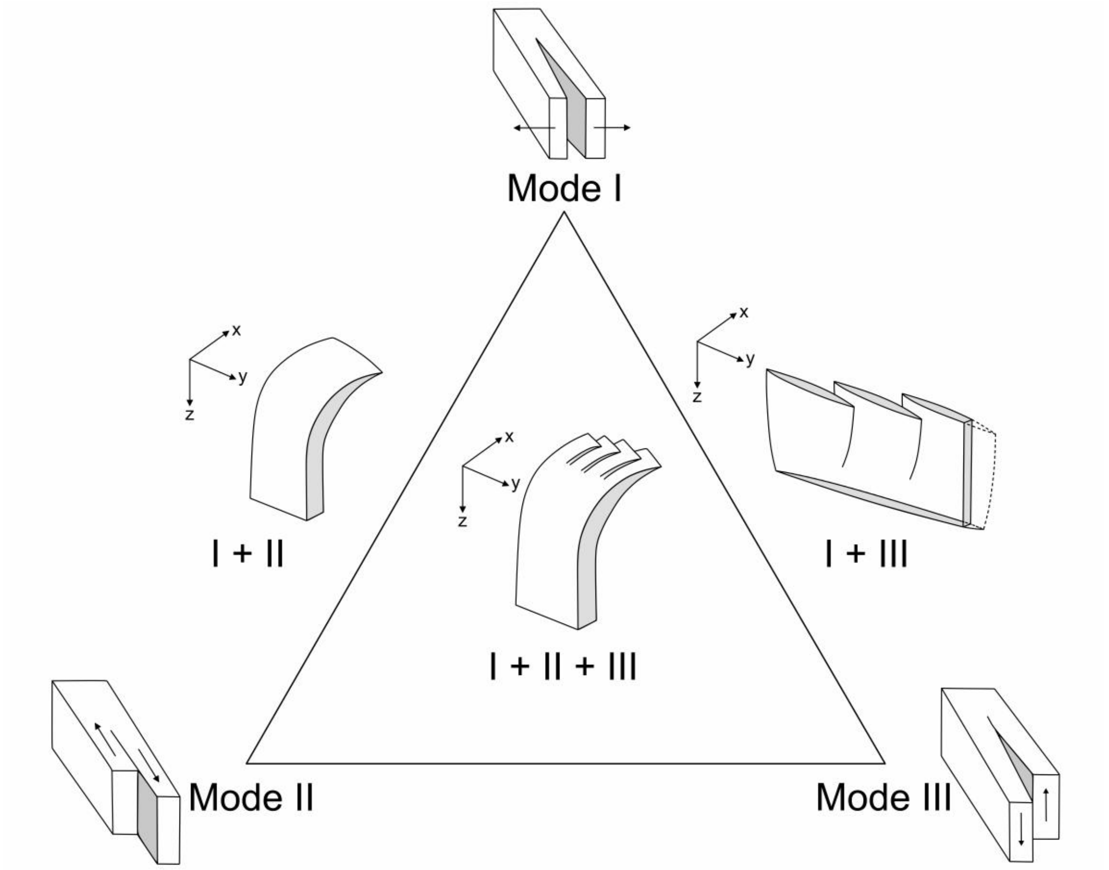

Fig. 5.14 A schematic ternary diagram showing all possible combinations of the three discrete end-member fracture modes (Modes I, II and III) giving rise to various mixed mode (mixed mode I-II; I-III and I-II-III) dyke geometries. Combination of only Mode II and III is not feasible since, all dykes should primarily have an opening displacement component.

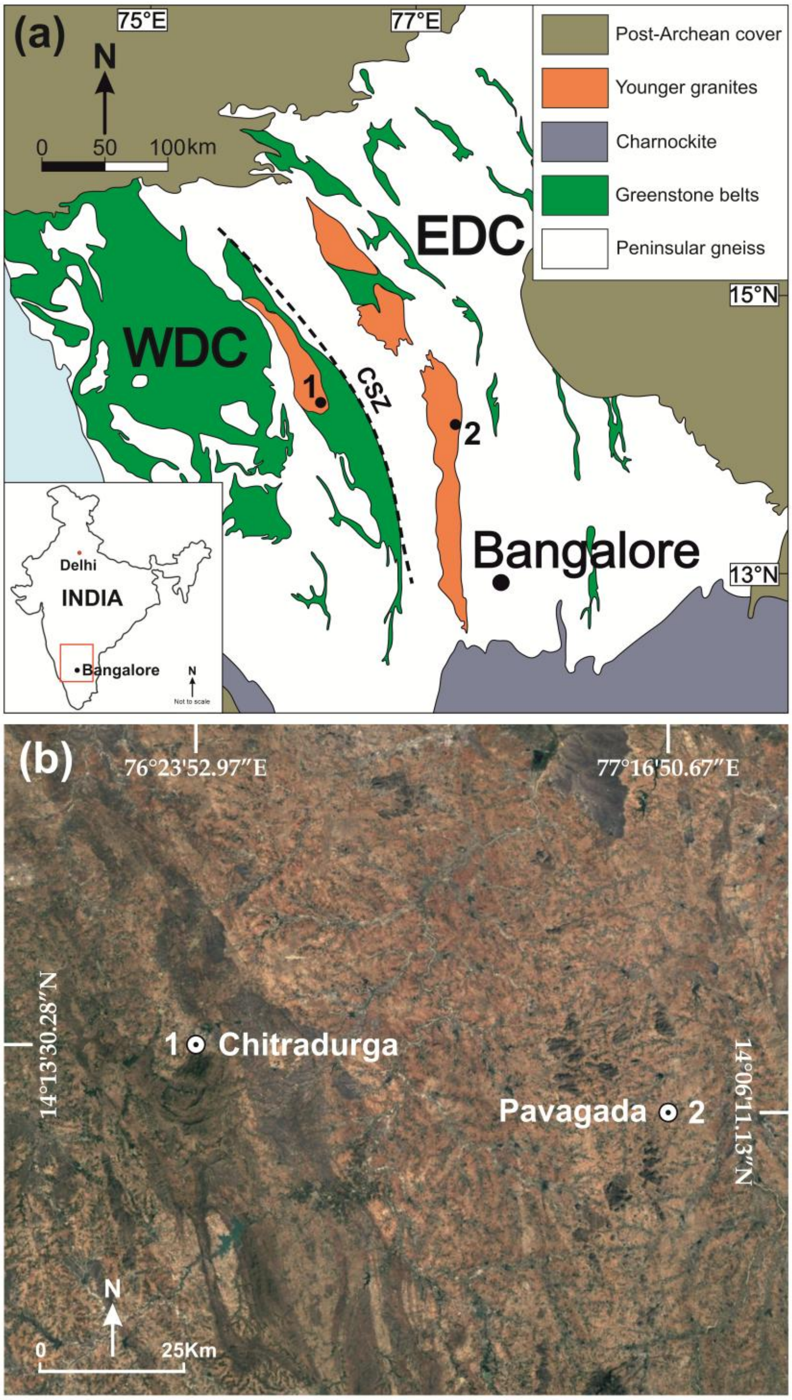

Fig. 5.15 (a) Simplified geological map of the Dharwar Craton, peninsular India (modified after Dey et al. 2015). EDC = Eastern Dharwar Craton; WDC = Western Dharwar Craton; CSZ = Chitradurga Schist Belt. Points 1 and 2 demarcates the two study areas; namely Chitradurga and Pavagada in the WDC and EDC respectively. Inset shows the location of the Dharwar Craton in the map of India. **(b)** Google Earth image showing the aerial disposition of the two study locations: Chitradurga and Pavagada, which fall within the Survey of India toposheet nos. 57B/8 and 57F/8 respectively.

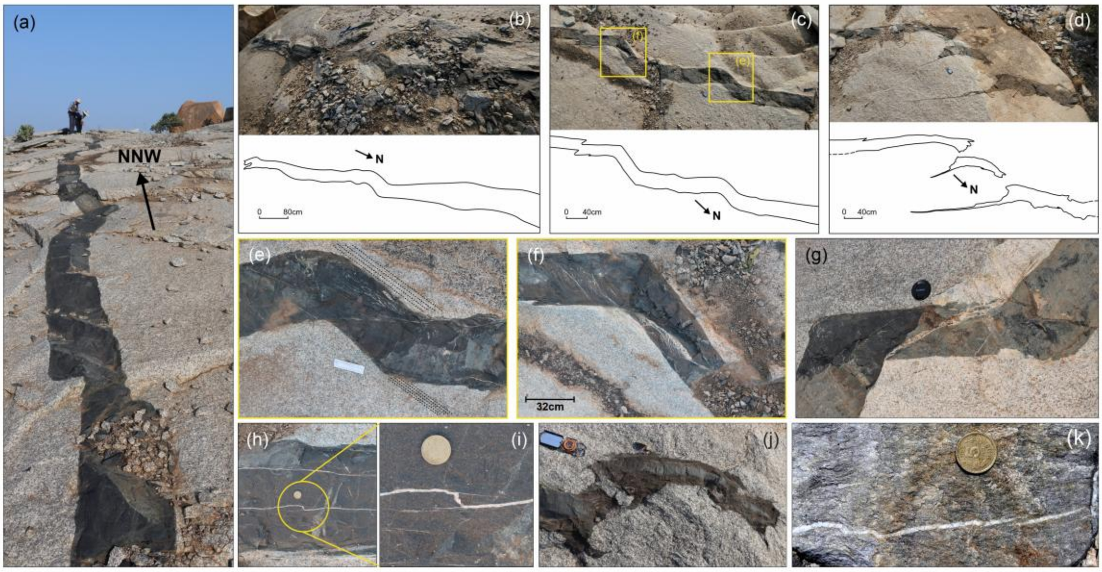

Fig. 5.16 (a) Field photograph showing the general trend of the Dyke 1 encountered within the Chitradurga granite, WDC, India. Note the curvy nature of the dyke body. **(b)** Portion of the dyke body consisting of its visible SSE end; **(c)** central portion of the dyke body; **(d)** segmented nature of the dyke at its NNW visible end and their traced counterparts. The two discontinuous en echelon segments feature long narrow horns protruding from their outward margins. Note the consistent left-stepping sequence of the dyke body which is continuous along the majority of its exposed length and becomes discontinuous towards its distal parts. **(e)** and **(f)** show blown-up views of the two curved portions of the dyke body visible in Fig. 5(c). **(g)** shows a similar curvature in another portion of the dyke body. Note the development of fractures across the shorter connecting arms in between two adjacent en echelon segments which consists of highly angular fragments of the dyke and has been intruded by veins. Also note the development of a preferred fabric within the host granite in the vicinity of the curved portions of the dyke body (marked by black dashed lines in Fig. 5e). **(h)** and **(i)** Veins intruded parallel to the dyke body show a similar sinistral (left-stepping) en echelon geometry along with the development of horns. **(j)** Blunt-ended tip of a dyke segment possibly suggesting forcible intrusion of magma by ductile deformation of the host granite. Such blunt tips are also visible in Fig. 5d. **(k)** A thin quartz vein within a Lesser Himalayan mica-schist shows development of exactly similar sinistral en echelon geometry within a much limited scale. Note the continuous nature of the vein in its comparatively thicker middle portion compared to the discontinuous segments developed at its distal end.

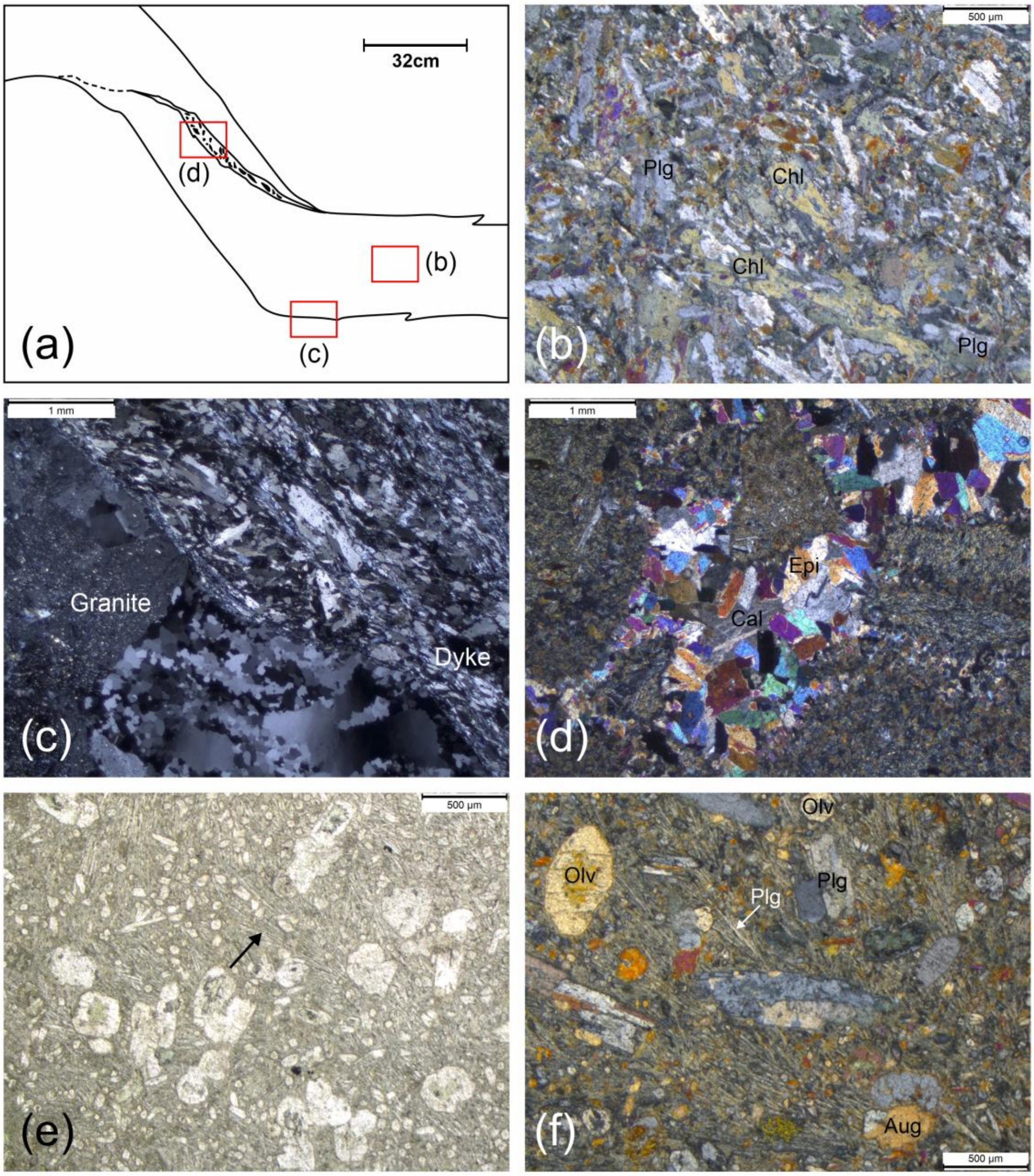

Fig. 5.17 (a) Traced reference image of a curved portion of Dyke 1, WDC. Red boxes mark portions of the dyke from where samples have been collected for microscopic study. **(b)** Relict igneous texture in the interior portion of the dyke defined by altered laths of plagioclase feldspar (Plg) and pyroxenes now almost entirely converted to mostly chlorite (Chl) and actinolite, suggesting an original doleritic composition. **(c)** Dyke margins show development of fabric defined by preferred alignment of elongated constituent mineral grains. Contd.

Fig. 5.17 Contd. **(d)** The fractured zones within the dyke filled by calcite and epidote crystals. Note the angular fragments of the dyke body present within the fracture zones and the reaction halo formed around them. **(e)** and **(f)** shows respectively PPL and XPL images of thin sections prepared from Dykes 2 and 3. These dykes preserve their pristine variolitic igneous texture defined by euhedral crystals of olivine (Olv), augite (Aug) and plagioclase (Plg) set in a groundmass of fine radiating needles of plagioclase which diverge out in a consistent direction; marked by black arrow in (e), suggestive of rapid cooling rates.

Fig. 5.18 (a) Stitched image of the full outcrop of Dyke 2 emplaced within the Chitradurga granite, WDC. The dyke has a continuous visible length and terminates at a tip at one end. **(b)** shows its traced counterpart. **(c)** Blown-up view of the portion demarcated within the white rectangular box in (a). Note the consistent development of discontinuous en echelon segments and curvature of the segments tips towards each other.

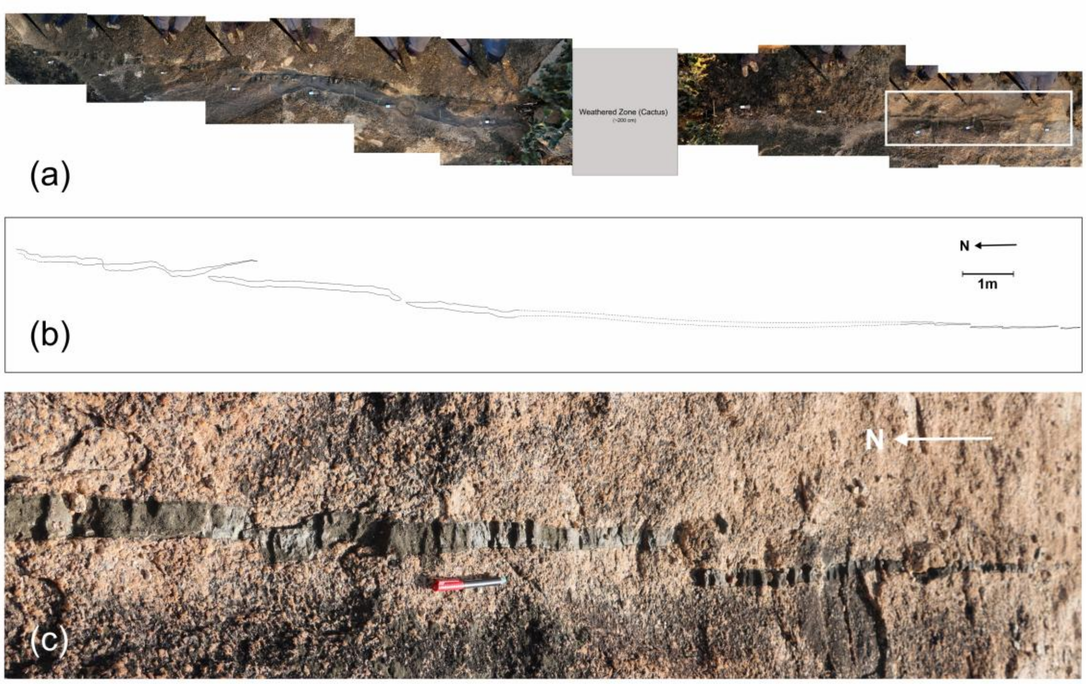

Fig. 5.19 (a) Stitched image of the complete exposed length of Dyke 3 intruded within the Chitradurga granite, WDC. Portion of the dyke is obliterated by weathering/vegetation cover. **(b)** Traced image of Dyke 2. **(c)** Close-up view of the portion marked within the white rectangular box in (a). Note the consistent left-stepping discontinuous en echelon segmentation pattern. Outward margins of some segments feature small horns.

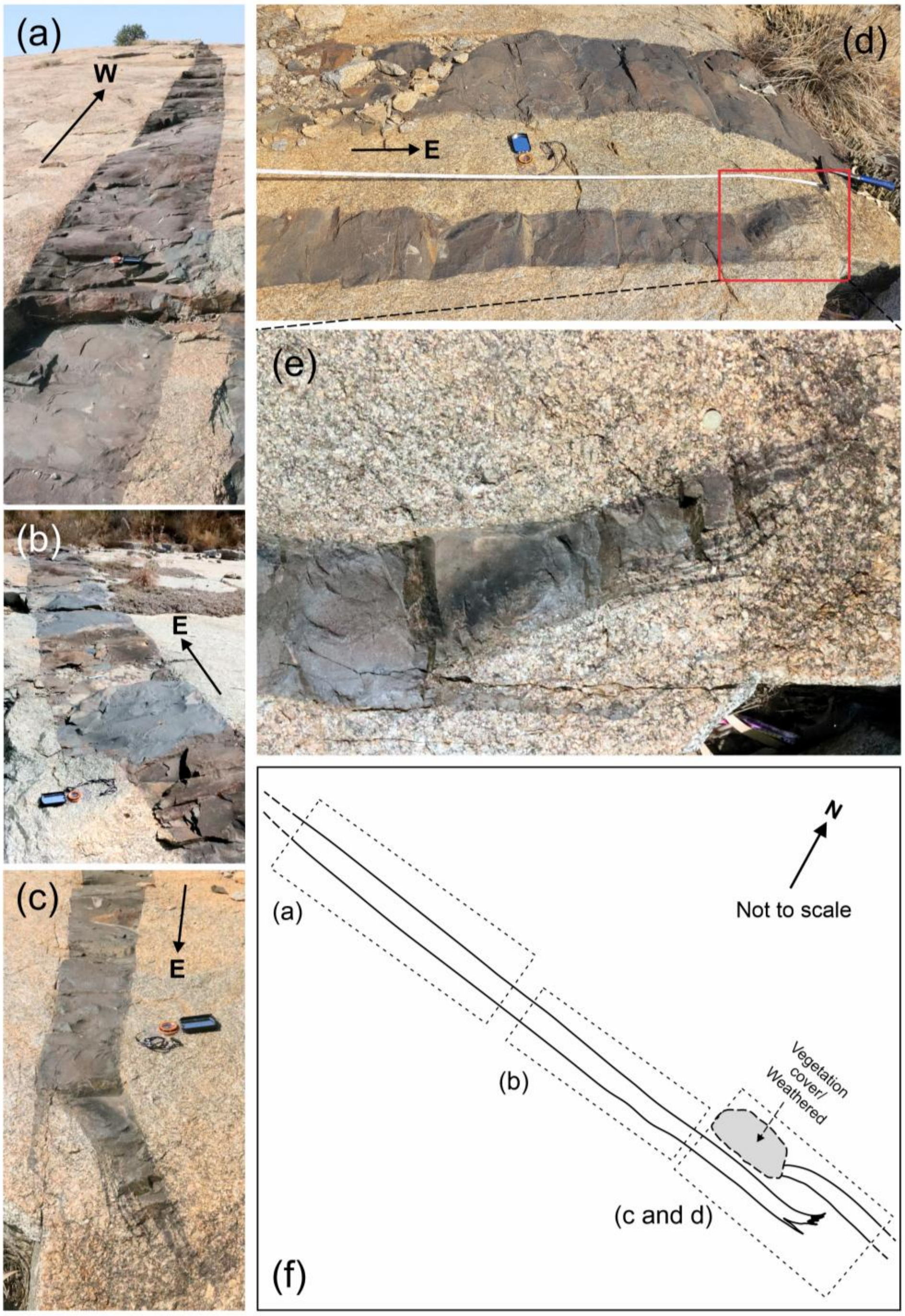

Fig. 5.20 (a) and **(b)** show field photographs of the E-W trending mafic dyke emplaced within Closepet granite near Pavagada, EDC. **(c)** shows the eastern tip of one dyke segment. **(d)** shows the segmented nature of the dyke. The two segments are arranged in a right-stepping sequence. Note the branched pattern of one of the segment tips marked within the red rectangular box which is curved towards its adjacent segment. **(e)** shows the zoomed in view of the flame-like branched segment tip demarcated within the red box in (d). **(f)** Schematic map of the entire dyke exposure showing the spatial dispositions of (a), (b), (c) and (d).

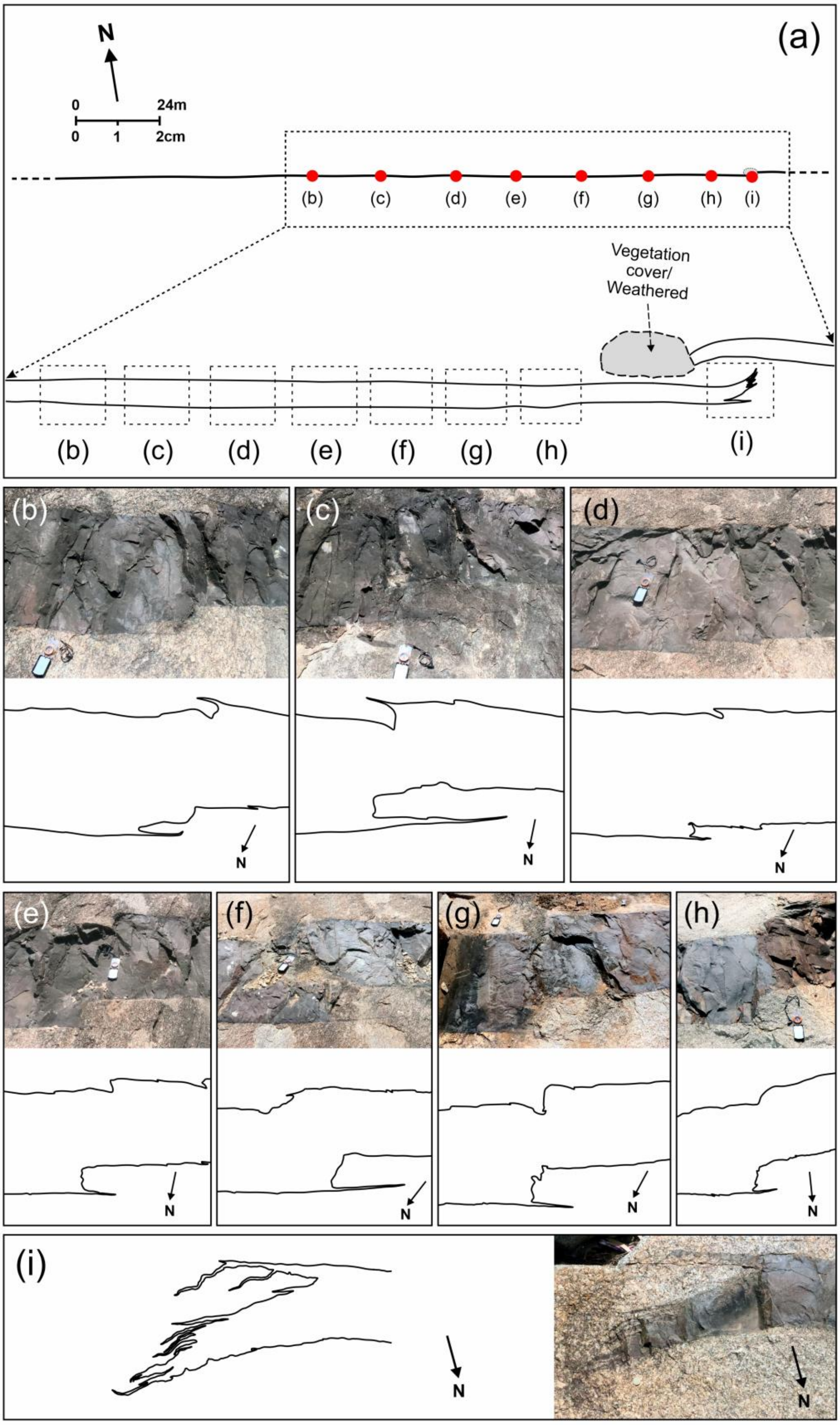

Fig. 5.21 (a) Outcrop map of the dyke observed in Pavagada region showing spatial disposition of the horns developed in it marked by red dots. The portion demarcated within the dashed box is schematically enlarged for clarity. Contd.

Fig. 5.21 (a) Contd. Two dyke segments are exposed arranged in dextral en echelon sequence and the segment of greater exposure length shows consistent right-stepping continuous curvature. Horns emerging out from the outer margins of each curvature are shown in figures **(b)**, **(c)**, **(d)**, **(e)**, **(f)**, **(g)** and **(h)** along with their traced counterparts. **(i)** shows the branched segment tip and its traced image. Note the curved nature of the segment tip and development of multiple horns from the outward margin of the curvature. Horns were generated in increments from the outer margin as the advancing segment tips gradually overlapped and got curved towards each other under strong mutual mechanical interaction.

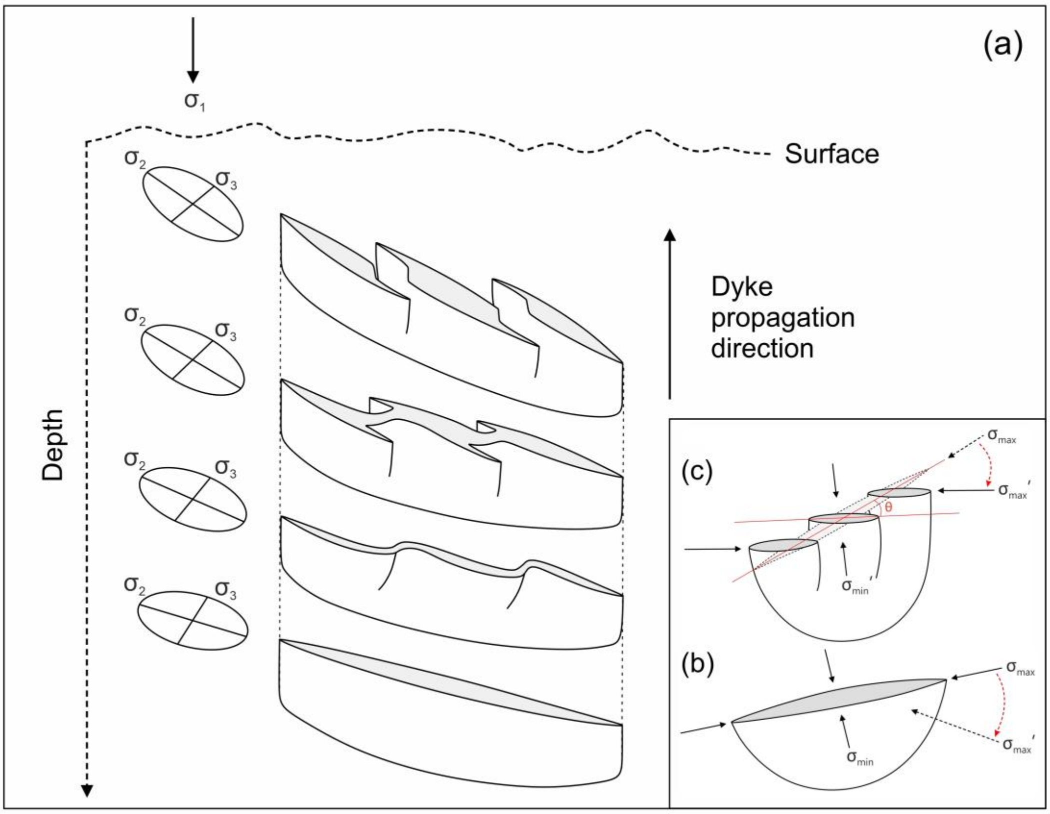

Fig. 5.22 (a) Schematic vertical section showing progressive stages of dyke evolution under mixed mode I-III loading as it ascends upwards from greater depths. The dyke body twists in response to the changed orientation of the principal stress axes acting on the horizontal plane. Ductility at greater depth may favour development of continuous en echelon geometry however as the dyke approaches shallower levels it is likely to get detached into segments which will be connected at depth (after Foley, 1989). **(b)** and **(c)** shows the twist angle (θ) which demarcates the angular change between the initial orientation of the dyke and the new trend at which the segments get oriented (after Pollard and Martel, 2020).

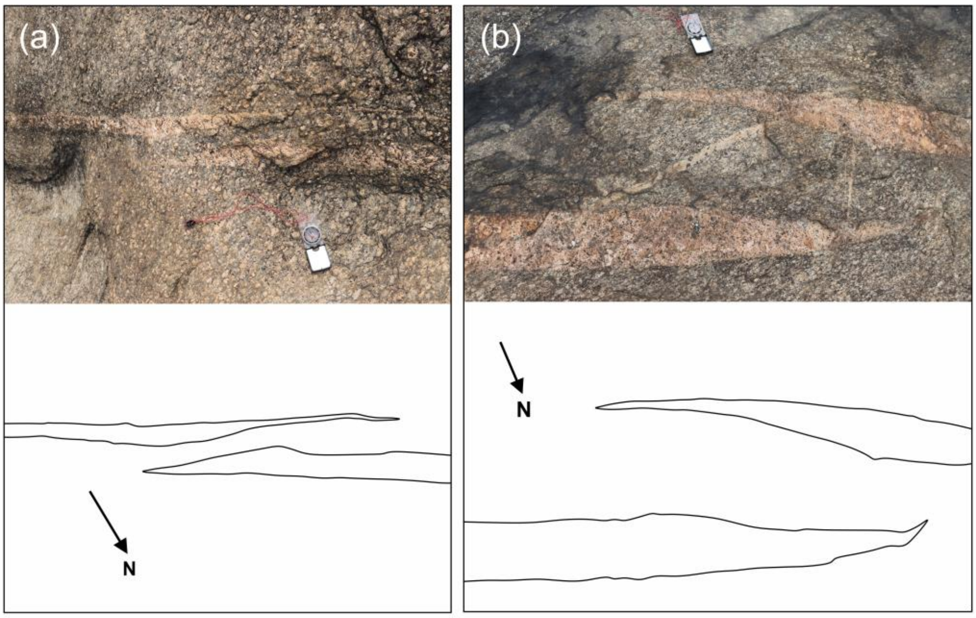

Fig. 5.23 (a) and **(b)** Overlapping en echelon felsic dyke segments observed within the Chotanagpur Granite Gneiss Complex (CGGC) near Bero Hills, Purulia, India. Note the distorted ellipticity of the segments defined by greater inner curvature compare to that of the outer margin.

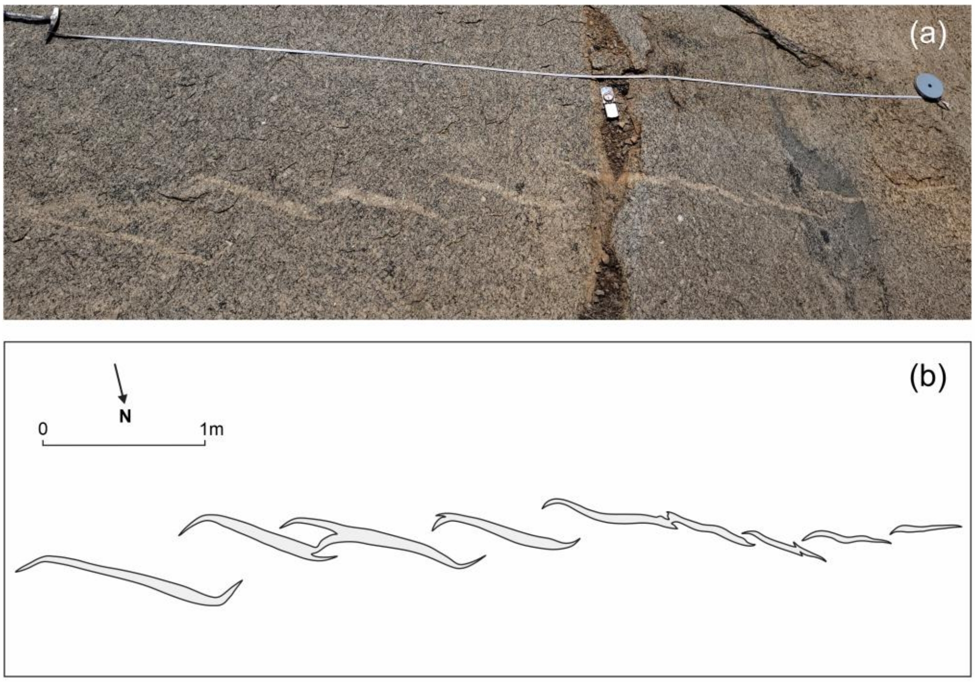

Fig. 5.24 (a) Series of discontinuous right-stepping en echelon felsic vein segments intruded within Closepet granite observed in the vicinity of the mafic dyke encountered near Pavagada, EDC. Note the distinct curvatures of the overlapping segment tips caused by mutual mechanical interaction. Also note the emergence of horns from the outer margins of the curved segment tips. **(b)** shows traced image of the same.

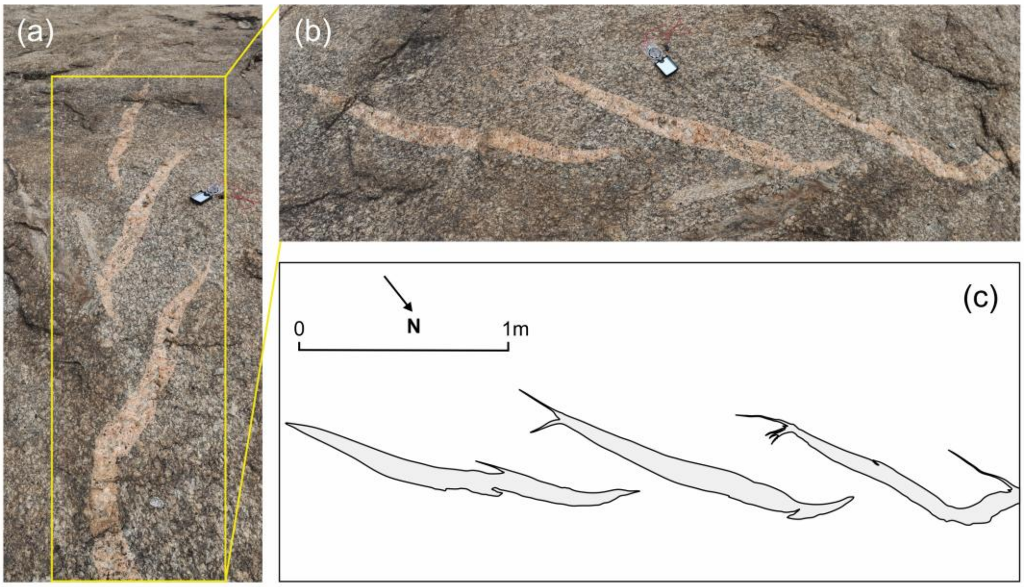

Fig. 5.25 (a) Series of five visible discontinuous right-stepping en echelon felsic dyke segments observed within the Chotanagpur Granite Gneiss Complex (CGGC) near Bero Hills, Purulia, India. **(b)** shows undistorted close view of three of those segments. **(c)** Traced counterpart of (b). The segment on the left shows minor rightward continuous curvature and horns emerge from the outer margin of the curved segment. The advancing tips of the segments gets curved towards each other as they overlap. Note the horn protruding out from the outer margin of the curved tip of the middle segment. Also note the branched nature of the curved tip of the right segment similar to the one observed in Pavagada, EDC.

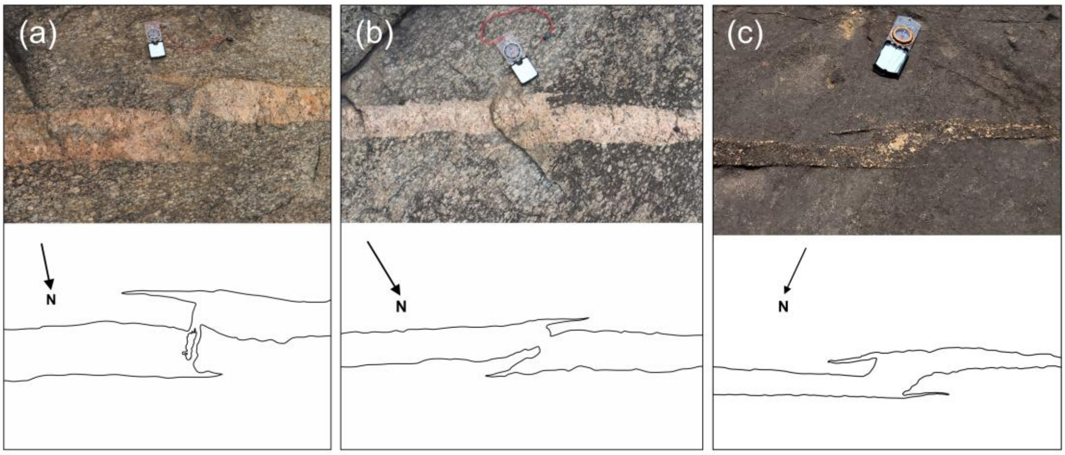

Fig. 5.26 (a) and **(b)** Bridged felsic dyke segments observed within the Chotanagpur Granite Gneiss Complex (CGGC) near Bero Hills, Purulia, India. Such bridging may occur in between two overlapping dyke segments when magma intrudes the critically stressed host rock lying in between the two segments. Contd.

Fig. 5.26 Contd. Note the irregular nature of the bridge which contains islands of host rocks within it (a). **(c)** A continuous curved felsic dyke body within Peninsular gneiss, WDC. Note that unlike bridged segments, the whole dyke body is curved and thin horns develop from its outer boundaries.

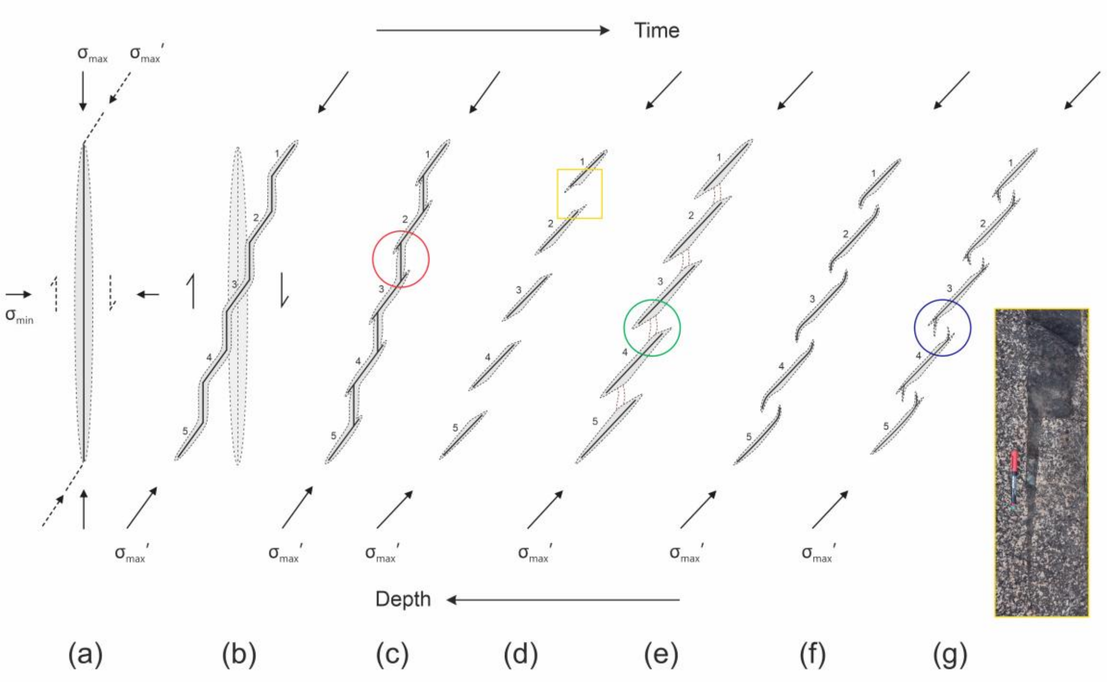

Fig. 5.27 Schematic sequence of a progressively evolving dyke under mixed mode I-III loading. **(a)** Initial formation of the dyke as a pure opening mode fracture. σ_{max} and σ_{min} respectively represent the maximum and minimum principal compressive stress components. σ_{max}' represents the rotated position of the maximum principal compressive stress axis. **(b)** The dyke body develops a continuous right stepping en echelon geometry as it responds to shearing induced along it in a dextral sense due to clock-wise rotation of the maximum principal compressive stress axis. Comparatively competent rheology of the dyke body at greater depths may favour such ductile behaviour. **(c)** Horns emerge from the outer margins of the favourably aligned dyke portions. For a continuous curved dyke geometry formed under dextral shear, two horns protruding from the outer margins of two adjacent segments along with the intermittent shorter connecting arm will together form a Z shape (red circle). Horns developed in this manner are termed first order horns. Contd.

Fig. 5.27 Contd. **(d)** As the dyke ascends, the continuous curvature will get detached into segments. En echelon segments may also initially form if a dyke undergoes rapid twisting while intruding a more rigid host rock. Such segments will display sharp truncations. The inset figure demarcated by yellow box shows field photograph of such a dyke segment. **(e)** As the segments continue to grow since they are connected at depth below, they might overlap. Overlapping segments gets distorted in shape and bridges connecting two adjacent segments may develop if magma supply is unhindered (green circle). **(f)** Tips of overlapping segments tend to get curved towards each other owing to mutual mechanical interaction. **(g)** Horns of second order emerge from the outer margin of the curved segment tips if supply of magma is extant (blue circle).

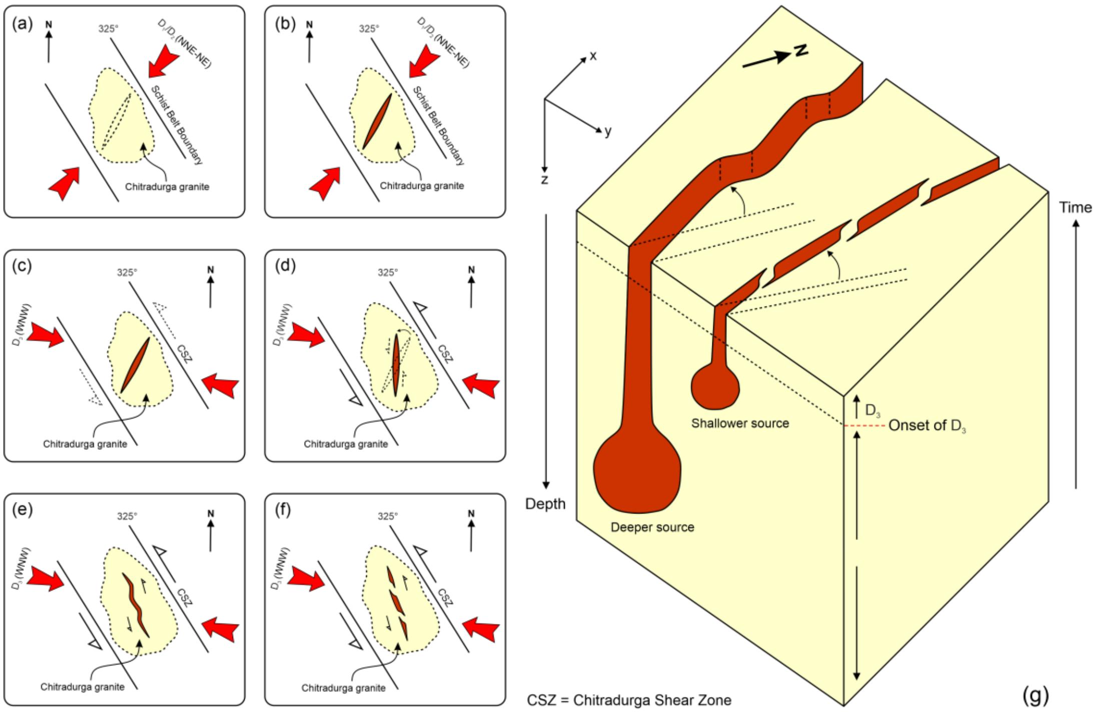

Fig. 5.28 Schematic evolutionary model of the mafic dykes emplaced within the Chitradurga granite, CSB, WDC. **(a)** Emplacement of the Chitradurga granite at ~ 2.61 Ga within the Chitradurga Schist Belt (CSB) under a NNE/NE directed compressive regional stress field (D_1/D_2). Initiation of NNE-NE trending extensional fractures within the granite favoured by the pressure imparted by the intruding mafic magma. **(b)** Formation and propagation of mafic dykes with an initial NNE/NE trend within the granite under the same stress field. Contd.

Fig. 5.28 Contd. **(c)** Commencement of ESE-WNW directed D_3 deformation event resulting in sinistral shearing along the NW trending schist belt boundary (initiation of the CSZ). **(d)** As the solidifying granite undergoes sinistral shearing, the dykes emplaced in it experiences initial rigid body rotation in an anti-clockwise sense up to some extent. Eventually, as the angle between the ESE directed D_3 compression and the dykes exceeds 90°, the dykes are also subjected to sinistral shearing. **(e)** Under favourable rheological conditions at depth, the relatively older dykes respond by developing a continuous sinistral en echelon geometry however, **(f)** at shallower depths within a much more rigid granite (owing to greater degree of solidification with time) younger dykes form discontinuous en echelon segments arranged in a left-stepping sequence. **(g)** Block diagram portraying the relative depths and timings of dyke emplacement within the varying regional stress fields that the granite is subjected to.

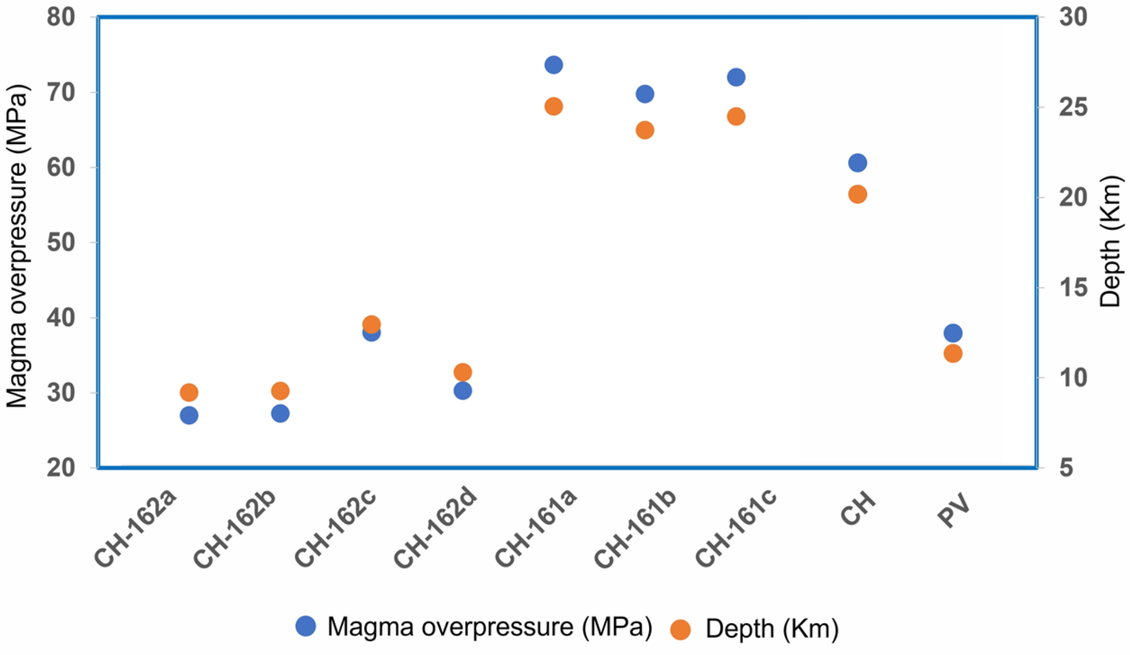

Fig. 5.29 Graphical representation of magma overpressure and depth of origin values calculated using complete dyke dimensions estimated from all the observed partially exposed dykes (with one exposed tip and without exposed tips) emplaced within the younger granites of the Dharwar Craton, India, using both the proposed methods (Biswas et al., 2023 and 2025).

Dyke no.	**Horn No.**	**B´/A´**	**P_o (MPa)**	**K_I (MPa $m^{1/2}$)**
CH-161a	*a(i)*	0.006113	72.78	332.16
	a(ii)	0.005549	66.06	362.60
	a(iii)	0.005908	70.35	510.29
CH-161b	*b(i)*	0.005788	68.91	139.00

Table. 1 Aspect ratio (B/A), magma overpressure (Po), and stress intensity factor (K_I) calculated from observed horns of two dykes of location CH-161, Chitradurga granite, Chitradurga Schist Belt, Western Dharwar Craton, India.

Chapter 6: Fracture Networks

CONTENTS **Page No.**

CHAPTER 6

Fracture Networks

6.1 Introduction

Fractures are the manifestation of brittle deformation encompassing all forms of secondary discontinuities within rocks, viz. faults, joints, veins, dykes, deformation bands and stylolites (Twiss and Moores, 1992; Davis et al., 2011; Fossen, 2016). Fractures impart significant secondary porosity to geological formations and play a critical role as conduits for fluid flow in upper crustal rocks. Under natural conditions, the origin and propagation of fractures in brittle rocks are mainly controlled by the state of stress, presence of pre-existing weak planes in the rock mass, and rock matrix heterogeneity. Quantification of fractures is therefore important to investigate the state of stress that acted on the rock during fracture formation and how the rock responded to stress during subsequent geological events (Zhao et al., 2009; Quinta et al., 2012; Kruhl, 2013; Hossain et al., 2015; Deb and Bhattacharyya, 2022; Lan et al., 2024).

Parts of this chapter have been submitted to the ***Journal of Structural Geology*** *as* ***Biswas et al.*** *and is currently under review, as of 29.08.2025.*

Fractures have been extensively investigated from a genetic perspective to elucidate the physical processes and mechanisms that govern their formation (Pollard and Aydin, 1988; Mandl, 2005; Pollard and Martel, 2020). However, in nature, fractures rarely occur discretely within a rock mass and very often exist as an interconnected mesh of various sets **(Fig. 6.1a)**. Within the same rock volume, multiple fractures with similar orientations can form fracture sets **(Fig. 6.1b)**, and the combination of two or more sets creates a fracture network (Segall, 1984; Sanderson and Nixon, 2015). Fracture networks generally evolve over geologic time and involve the systematic development of a number of distinct fracture sets, of similar or varying genetic affinities, which may or may not intersect. In time, a growing system of fractures may interact with each other and with the rock matrix, to control the physics of the rock (Bonnet et al., 2001; Berkowitz, 2002; Neuman, 2005). Therefore, in practice, it is not only the individual fracture type or its geometry, but also the mutual interactions between fractures and fracture sets of the network that control the bulk rock properties (Sanderson and Nixon, 2015; 2018).

The presence of fracture networks within a rock mass significantly influences rock strength, porosity, and permeability, and thereby fluid flow, storage capacity, and containment integrity. The study of fracture networks and their characterization are therefore crucial in various geological applications, including mineral resources (Abdullahi et al., 2022) and hydrocarbon exploration (Spence et al., 2014; Xu et al., 2021; Węglińska et al., 2024), engineering constructions (Li et al., 2017; Zhang et al., 2023), nuclear waste disposal (Liu et al., 2009; Seetharam et al., 2014), and carbon sequestration (Tsang et al., 2015) and a holistic grasp of fracture characteristics is essential for optimizing exploration, construction, recovery, disposal, and storage processes, contributing significantly to economic viability and environmental sustainability.

Individual fractures within a network can be typically characterized by their geometric properties, including orientation, size, morphology, length, and angular relationships. Fracture sets are analyzed through the statistical distribution of these characteristics, often expressed as average values or observed ranges (Terzaghi, 1965; Dershowitz and Einstein, 1988; Priest, 1993; Odling et al., 1999). Spatial arrangement and distribution of fracture sizes have also been quantitatively studied using statistical and stochastic models to reveal random or clustered, scale-dependent patterns within networks (Marrett et al., 2018; Laubach et al., 2018a, 2018b; Shakiba et al., 2023; 2024). Geometric data are obtained through direct field measurements, which involve determining the spatial orientation of the fracture surface, sense of displacement or slip along the fracture surface or trace, along with physical dimensions such as trace length, aperture, surface area, volume, and number of fracture traces observed within a defined areal extent. Fractures may also be classified based on other attributes such as fracture type or the presence of mineral infill. Fluid flow models based on fracture network characterization fundamentally rely on a detailed geological description of the fracture types that constitute the network (Peacock and Sanderson, 2018). When a fracture network comprises fractures of diverse genetic origins, it becomes increasingly important to understand the underlying physical processes responsible for the formation of each fracture type **(Fig. 6.1c)**.

Geometrical attributes, such as orientation, spacing, and size, are metric properties of a network. These can be measured using specific units (e.g., degrees, meters) and may change under certain conditions, like during a deformation process. In contrast, fracture connectivity, resulting from inter-relations between individual elements of a network, is a property that cannot be measured with unit dimensions and remains unchanged during continuous deformation processes. For instance, two fractures that are connected will stay connected unless the block of rock containing them is completely separated, which, however, involves a discontinuous deformation process. In topology, a branch of mathematics that focuses on the abstraction and generalization of spatial relationships like connectivity and continuity, such properties that remain unaffected by continuous transformations are called topological properties. These transformations alter geometric properties (like lengths and angles) but do not affect the topology. Connectivity, being a topological property of a network, cannot be directly measured but can only be represented in a combinatorial way, meaning, it can be counted (Jing and Stephansson, 1997; Manzocchi, 2002; Sanderson and Nixon, 2015).

Sanderson and Nixon (2015) pioneered the wide usage of network topology to describe geological fracture patterns and their network characterization, wherein fracture networks are modelled as graphs, where nodes represent fracture intersections and terminations, while edges represent fracture traces. On a 2D observational plane (say, an outcrop surface), a fracture trace may remain isolated or unconnected to any other fracture trace, thereby bounded by two isolated nodes or I nodes on its two ends. A fracture trace may abut against another, forming an abutting node or Y node, or two fracture sets might intersect or cross-cut, forming an X node **(Fig. 6.1d)**. This abstraction allows for the quantitative evaluation of fracture connectivity, using the concepts of node and branch topology, thereby enhancing the comprehension of pathway efficiency and flow potential. Also, topology, being invariant to scale changes and continuous transformation, helps in the assessment of network attributes, even with limited access to the fracture network as a whole (Sanderson and Nixon, 2015). It is important to note that fracture networks that appear similar in geometry can exhibit significantly different connectivity. Since connectivity is governed by the interactions among individual fractures within the network, this difference cannot be captured by only recording the network geometry, but can be quantified by analyzing its topology **(Figs. 6.1e, f and g)**. Over the last decade, the application of network topology has emerged as a powerful tool for analyzing the structure and connectivity of fracture networks. These methods offer a quantitative framework to assess fracture connectivity and how it influences flow, transport, and mechanical properties in various geologic media (Mendes et al., 2022; Osagiede et al., 2023; Panara et al., 2023; Nordback et al., 2023; Honorio et al., 2025; Lucca et al., 2025).

Within a fracture network, multiple orientations of fractures, together with their spacing and interconnectedness, form a complicated network pattern. Such complex fracture patterns, which are statistically self-similar (i.e., fractal) over a range of scales, can be best quantified by fractal-geometry techniques such as 2D box-counting (Mandelbrot, 1982; Kaye, 1993; Park et al., 2010; Kruhl, 2013). Interestingly, the fractal quantification of fracture patterns shows variations in fractal dimensions, which can be interpreted as resulting from different fracturing processes, the number of deformation events, and subsequent geological evolution (Blenkinsop, 1991; Dimri, 2005; Das et al., 2019). Fractal analysis therefore helps identify underlying patterns across different scales and contributes to predictive modelling of fracture distribution in areas with limited data. Topological analysis has been integrated with fractal geometry in recent studies to assess multiscale connectivity in fracture systems, especially in reservoirs and geothermal fields. For example, Luo et al. (2024) presented a fractal permeability model for fracture networks based on graph theory, improving predictions of gas seepage in stress-dependent conditions.

A comprehensive understanding of fracture networks, encompassing their origin, development, structural attributes, and network characteristics, demands a multidisciplinary and integrated approach. This includes detailed field investigations that provide direct evidence of fracture formation and progression under the ambient stress state, as well as quantitative approaches involving the geometrical, topological, and fractal attributes of natural fracture networks that offer deeper insight into the structure of a network as a whole.

Since, granite-greenstone belts are major constituents of early continental crust, and are often replete with fractures formed under varying tectonic stress conditions (Velde et al., 1991; Janoušek et al., 2020; Mondal et al., 2020), in the present study, this integrated approach has been undertaken with an aim to decipher the origin and characterize the subsequent networking of fractures developed within the younger granites (~ 2.6 Ga), namely, Chitradurga and J.N. Kote granites and the adjoining metavolcanic rocks of the Chitradurga Schist Belt, an Archean age granite-greenstone sequence from the Western Dharwar Craton of southern India known for its gold potential (Sarangi et al., 2013; Swain et al., 2018). Previous studies conducted on the rocks of this region have primarily relied on traditional fabric analysis and paleostress determination, drawing conclusions through conventional interpretative methods (Mondal, 2018; Mondal et al., 2020; Bhowmick and Mondal, 2020). However, the pervasive development of fracture networks observed ubiquitously within these rock bodies has yet to receive any attention. In this context, the present work introduces a novel approach by examining fractures and their networks across varying outcrop scales through a coherent lens of geometrical, topological, and fractal analyses coupled with direct field observations, offering a fresh perspective on how fractures initiate, evolve, and interconnect to form networks in a regional scale under ambient stress conditions.

The study has implications in understanding late-stage Precambrian brittle tectonics associated with craton stabilization and demonstrates an integrated methodology that can be applied to varying lithologies to develop a mechanical or fracture stratigraphy, enhancing both theoretical insights and potential practical applications in the fields of hydrogeology, carbon sequestration, mineral exploration, geotechnical engineering, waste management, and hazard assessment.

6.2 Characterizing fracture networks – attributes and methods

The aim of the present work is to record fractures and their network attributes so as to assess their connectivity, spatial variations, if any, and as such understanding the controls on their genesis and evolution under the ambient state of stress. For this, a holistic methodology integrating field-based observations with geometrical, topological, and fractal analyses of the fracture networks has been undertaken. Fracture networks were primarily observed within the younger granites and metavolcanic rocks of the study area. Therefore, reconnaissance fieldwork was conducted lithology-wise throughout the study area to identity target areas based on the accessibility and availability of suitable exposures.

6.2.1 Data acquisition

After all target exposures are located, data acquisition commences with direct field measurement of structural data involving faults, fractures, and foliation planes (attitudes, fault-slip data, etc.), wherever feasible. In order to capture the fracture networks as a whole, which is the primary focus of the present work, photographic recording of outcrop surfaces has been undertaken. Fracture networks in granites are mostly visible on 2D horizontal outcrop surfaces, whereas, fracture networks within the metavolcanic rocks were primarily exposed on sub-vertical to vertical 2D outcrop surfaces of hill slopes or road cut sections. Due to the nature of the outcrops themselves, the observed networks vary widely in their exposed areal dimensions, particularly so, in case of the granites. Therefore, choosing one specific areal dimension for outcrop photography was not feasible, as a standard analysis window of fixed dimension may not be applicable to all outcrops, potentially resulting in the loss of crucial information regarding network attributes that vary across scales. Thus, as a consensus, it was resorted to capturing fracture networks visible on planar horizontal and vertical outcrop surfaces across macroscopic scales of observation. It is observed that manually photographing a flat horizontal or vertical outcrop surface from a height or distance of ~ 2 meters yields a single photograph covering approximately ~ 4 sq. m with distinct clarity, corresponding to a ground sampling distance of 0.58 mm/pixel. To record fracture networks exposed over greater areal extents, larger areas were photographed from a fixed height of 2 meters in an overlapping grid pattern (overlap > 70%) and were ortho-rectified and stitched to produce a complete 2D outcrop orthomosaic using Agisoft Metashape Pro. All outcrop photographs were scaled and oriented with respect to the geographic north.

6.2.2 Digitization and processing

To extract and process the data captured through outcrop photography, digitization of fracture networks from the acquired field photographs was done by manual tracing using Corel Graphics academic perpetual Suite 2021. Subsequently, the binary traced image files are processed in FracPaQ version 2.8 for geometrical and topological analyses and also for 2D box counting in Benoit version 1.3 for fractal analysis.

6.2.3 Dimensional and orientation attributes - Geometrical analysis

Geometrical analysis of any feature primarily entails evaluating two key aspects: orientations and dimensions. Most fractures constituting the networks within the granites or the metavolcanic rocks have negligible apertures that are beyond the resolution of field measurements. Therefore, within the scope of the present study, assessment of fracture dimensions will be limited to fracture lengths only. For planar horizontal outcrop surfaces, FracPaQ quantifies the lengths and orientations of individual fracture elements present within the fracture network from a scaled and oriented binary input image file of the network employing coordinate geometry. It is important to note that for a natural fracture, resembling a curvilinear path on a 2D horizontal outcrop surface, FracPaQ identifies the continuous line as a 'fracture trace', and the multiple straight lines of which the curvilinear path is composed of are each designated as a 'fracture segment'. For each analyzed image, FracPaQ counts the total number of fracture traces and segments present within the analyzed outcrop area and utilizes the average of segment lengths to represent the characteristic length (L_C) (Sanderson and Nixon, 2015) of the fracture network. Segment lengths are also used to generate different orientation and length statistics, including frequency measurements of segment angles and lengths. An equal area, length-weighted rose diagram based on fracture segment data is generated to visualize fracture orientation patterns within the network. Based on the number of distinct fracture orientations, the number of dominant fracture sets can be determined from the rose plot. However, in case of planar (sub)vertical outcrop surfaces, orientation data of individual fracture planes cannot be extracted independently through FracPaQ. Therefore, for the metavolcanic rocks, fracture attitude data has been collected manually from the field to assess the distribution of their orientation and sets.

An attempt has also been made to analyze fracture spacing where fracture orientation patterns show a strongly unimodal distribution. In such outcrop photographs, a linear scanline has been placed across the dominant fracture trend, and the interspacing between individual fractures is assessed along this scanline.

It is also important to ascertain the statistical distribution that fracture lengths follow within a fracture network in order to understand the underlying scaling behavior of fracture lengths. This is determined through Maximum Likelihood Estimation (MLE) analysis in FracPaQ, which provides statistically calculated probabilities for fracture lengths to follow log-normal, exponential, or power-law distributions within the designated sample area. Since natural fractures occurring at any scale can be formed through the interaction and coalescence of smaller fractures, the results of MLE analysis are represented both in terms of fracture trace lengths and segment lengths. The details of all geometrical and statistical analyses performed in FracPaQ are provided in Healy et al. (2017) and are therefore not elaborated here.

6.2.4 Connectivity attributes - Topological analysis

Topological analysis of a fracture network is crucial to address the connectivity of the system arising from the interrelations between individual fractures comprising the network. In the present work, fracture network topology is analyzed using the node and branch classification framework outlined by Sanderson and Nixon (2015). This method involves mapping and quantifying fracture traces within a defined 2D sample area. Fracture traces need to be digitized and classified based on their intersections and termination types, which are then used to define nodes and branches.

When a 2D plane of observation (e.g., a flat horizontal outcrop surface) intersects variably oriented fracture planes, fracture traces of corresponding orientations are produced on it. Such fracture traces may terminate at a point or may intersect or abut against other adjacent fracture traces. The points of such terminations and intersections are designated as nodes, which delimits a part or the entirety of a fracture trace. Based on these relations, nodes can be categorized into three types: I-nodes (isolated tips), representing fracture terminations that do not connect with other fractures; Y-nodes (splays or abutments), where one fracture terminates or abuts against another one; and X-nodes (crossing intersections), where two or more fractures intersect through one another **(Fig. 6.1d)**. However, the concept of C-nodes or 'Contingent nodes' which has been introduced in recent studies to account for the effects of scale, diagenetic processes and thereby fracture aperture evolution, particularly within porous geological media (Forstner and Laubach, 2022), has not been incorporated within the scope of the present study.

Therefore, a 2D fracture network always consists of multiple lines, nodes, and branches, wherein each line may comprise of multiple branches, each having a node at either end. Branches are thus defined as part of fracture traces delimited between two nodes and can be classified based on the node types at their end-points into three categories: I–I, I–C, and C–C, where C represents a connected node (either Y or X). This classification aids in the quantitative estimation of network connectivity.

The number of each node type (N_I, N_Y, N_X) and the characteristic length (L_C) of fractures within a network of designated sample area (A), given by the arithmetic mean of all fracture lengths, can be used to derive a number of quantitative topological parameters, including node proportions, number of lines and branches, branch type distributions, and measures of fracture connectivity, density, and intensity, as follows (Sanderson and Nixon, 2015):

Number of Lines (N_L) = $\frac{1}{2}(N_I + N_Y)$ (6.1)

$$\text{Number of Branches } (N_B) = ½ (N_I + 3N_Y + 4N_X) \qquad (6.2)$$

$$\text{Probability of a branch end to be isolated } (P_I) = N_I / (N_I + 3N_Y + 4N_X) \qquad (6.3)$$

$$\text{Probability of a branch end being connected } (P_C) = (3N_Y + 4N_X) / (N_I + 3N_Y + 4N_X) \qquad (6.4)$$

$$\text{Probability of completely isolated branch type } (P_{II}) = P_I^2 \qquad (6.5)$$

$$\text{Probability of partially connected branch type } (P_{IC}) = P_I . P_C \qquad (6.6)$$

$$\text{Probability of completely connected branch type } (P_{CC}) = P_C^2 \qquad (6.7)$$

$$\text{Connections per Line } (C_L) = 2 (N_Y + N_X) / N_L \qquad (6.8)$$

$$\text{Connections per Branch } (C_B) = (3N_Y + 4N_X) / N_B \qquad (6.9)$$

$$\text{2D Fracture Density/Frequency } (P_{20}) = N_L / A \qquad (6.10)$$

$$\text{2D Fracture Intensity } (P_{21}) = N_L.L_C / A \qquad (6.11)$$

$$\text{Dimensionless Intensity } (P_{22}) = N_L.L_C^2 / A \qquad (6.12)$$

FracPaQ identifies and counts the connectivity node types from a binary input image file and estimates network connectivity using the relative proportions of different node types via an I-Y-X ternary diagram. For any given 2D sample area, analyses on fracture density (P_{20}) and intensity (P_{21}) are conducted in FracPaQ within standardized scan windows following Mauldon et al. (2001) to ensure consistency and comparability across datasets.

6.2.5 Self-similar attributes - Fractal analysis

Fractures that occur in any rock masses often form complex patterns characterized by the arrangement of smaller components of the structure. Such patterns can be fractal if they are statistically self-similar over a certain range of scales (Mandelbrot, 1982; Kruhl, 2013). Quantification of such patterns is not possible using conventional methods, as traditional techniques cannot fully account for the geometric arrangements of fractures. Only fractal-geometry techniques (Mandelbrot, 1982) are capable of considering the geometric aspects of the structure (i.e., pattern), and therefore, able to decipher structure-forming processes (Kaye, 1993; Kruhl, 2013). The basic concept of all fractal-geometry methods is that a structural pattern will be repeated in the same manner across different scales (Velde et al., 1990). Although self-similar fracture patterns may be observed across several orders of scale, due to variations in rock fabrics and deformation behaviour at different scales, self-similarity may change from one range of scale to the next (Kruhl, 2013). The relationship in fractal-geometry method can be expressed as:

$$N = d^{-D} \tag{6.13}$$

where, N, d, and D represent the number of events, the measurement dimension (e.g., 1D, 2D, 3D), and the fractal dimension, respectively (Hossain et al., 2015).

Among all the fractal-geometry methods, the box-counting technique (Mandelbrot, 1977; Kaye, 1989) is one of the most powerful tools to quantify the degree of complexity in fracture distribution patterns in various rock masses, ranging from micro- to mega-scale (Castaing et al., 1996; Park et al., 2010; Kruhl, 2013). In the box-counting method, the fractal dimension of the pattern is calculated using the formula:

$$N = r^{-D_{box}} \tag{6.14}$$

where, N, r, and D_{box} are the number of boxes containing the pattern, the scaling factor, and box-counting fractal dimension, respectively (Perugini et al., 2003). In simple terms, the number of occupied boxes containing fracture lines is plotted against the box side length on a double logarithmic scale. If the resulting plot is linear, it suggests a power-law relationship, in which the exponent is considered the fractal dimension or *D*-value (Turcotte, 1989; Roy et al., 2007). In this study, the 2D box-counting dimension of the fracture patterns is calculated from the digitized binary image files of fracture networks using an open source 2D box-counting program in MATLAB (Moisy, 2008) and the software Benoit 1.3 (Seffens, 1999). As the box-counting method is sensitive to both the total area of analysis (i.e., upper limit) and the lower limit of fracture pattern resolution, box sizes ranging from of 0.3–500 cm were chosen for this study. A detailed flowchart summarizing the integrated methodology adopted in this work is illustrated step-wise in **Figure 6.2**.

6.3 Fracture network characterization in the younger granites

The ~ 2.61 Ga younger granites of the study area, namely, the Chitradurga and J.N. Kote granites, together span a linear dimension of about 65 km from north to south and cover an area of ~ 400 sq. km. Along the entirety of their exposed portions the granites are replete with faults and fractures of varying orientations which exhibit mutual interaction forming fracture networks. The entirety of these two granite plutons has been sub-divided into four sectors based on the texture and field appearance of the granites viz. the foliated northern part (CHn), the relatively finer grained central part (CHc), the very coarse-grained southern part (CHs) of the Chitradurga granite and the medium grained J.N. Kote granite (JN), a separate pluton, whose grain size ranges in between that of CHc and CHs **(Fig. 6.3a)**. This sub-division also allows for better segregation and analysis of bulk data collected in a more convenient way. Field photographs showing the general appearance, texture, and grain size, observed at mesoscopic scale in the different sectors of the granites are provided in **Figure 6.4**. A total of 48 outcrop photographs capturing fracture networks within the granites were collected from these sectors, covering surface areas ranging from approximately 1 sq. m to ~ 50 sq. m. Each granite sector in the study area contributed at least 10 outcrop photographs, with areal dimensions broadly representing this range of scales with average incremental steps of ~ 5-10 sq. m, ~ 15-20 sq. m, ~ 25-30 sq. m and so, depending upon the nature and size of the outcrops available (see **Fig. 6.3a** for location of data points). Corresponding details for each data point are provided in **Supplementary File_6.1, Sheet-1**.

Field photographs of representative fracture networks encountered in each sector of the granites, along with their traced counterparts, are shown in **Figures 6.3b to i**. Individual faults comprising the networks are mostly steeply dipping and cross-cut all pre-existing brittle structures observed within the granites. These are identified by the presence of slickenside lineations and congruous steps on exposed fault surfaces, which also help in identifying the sense of movement along them (Petit, 1987) **(Fig. 6.3j)**. Microscopic observation reveals that minimal apertures along these faults, mostly too small to be detected through field measurements, are also filled in by chlorite **(Fig. 6.3k)**. When the planes are not exposed and only traces of the faults appear on an outcrop surface, their sense of movement can be discerned utilizing the offsets of earlier quartzo-feldspathic veins along them **(Fig. 6.3l)**. It is observed that individual fracture traces in the central (CHc) part of the Chitradurga granite appear sharp and relatively linear, propagating longer distances, characterized by regular and smoother outlines. Fracture traces from the northern part (CHn) also share this appearance in terms of relatively regular outlines, while in its southern part (CHs), fracture traces propagate over comparatively shorter distances and are much irregular in their outline. Fracture traces observed within different locations of the J.N. Kote granite (JN) display both of the above mentioned features, with the former at places having a comparatively finer grain size, while the latter is observed at outcrops characterized by a coarser grain size.

Fault-slip data collected from these granite bodies have been used to reconstruct the paleostress condition of the region related to late D_3 deformation (Mondal et al., 2020), however, the huge variation of fault data along the spatial extent of the plutons and their ubiquitous networking attributes have not been addressed to date. Notably, no evidence of deformation post-D_3 has been recorded in the study area, either in previous studies or from present field observations. The aim of the present study will be to examine the origin and to characterize subsequent networking of these late-stage brittle faults developed within the younger granites of the region in particular. Temporal evolution of all the genetically differing suites of brittle structures developed within the granites and their spatial inter-relations will be discussed in a subsequent chapter.

6.3.1 Geometrical characters

a. Fracture trace lengths and segment lengths

Analyzing the geometric properties of any system fundamentally involves two key aspects: the dimensions and orientations of its individual elements. In this study, fracture networks are characterized using digitized images of 2D outcrop surfaces, on which traces of fracture planes are visible. Therefore, in the present context, ‘dimension’ refers specifically to the length or linear extent of the fractures. Fracture width (aperture) is not considered, as most fractures observed in the granites are oblique-slip faults with negligible apertures that are beyond the resolution of field measurements.

In terms of fracture traces, it is observed that the average number of traces constituting the fracture networks is highest within the CHc sector, followed by the CHn, JN, and

CHs sectors in decreasing order of abundance. Average trace length is also highest in the CHc sector (0.37 m), followed by the JN sector (0.26 m), and then the CHn and CHs sectors (~ 0.23 m). The JN sector is characterized by a widespread distribution of trace lengths, as it contains both the average maximum and minimum trace lengths amongst all sectors at 3.29 m and 0.02 m respectively. The average total trace length recorded across all the granite sectors is also highest for the CHc sector (222.34 m), followed by CHn (176.67 m), JN (142.87 m), and CHs (93.68 m) **(Fig. 6.5a)**.

For fracture segments, on average, the CHn sector shows the highest number of segments, followed by the CHc, JN, and CHs in decreasing order. However, the average segment length is the highest in the CHc sector (0.12 m), followed by JN (0.09 m), CHn (0.07 m), and CHs (0.06 m), with CHc also showing the highest average maximum segment length (1.09 m). The average total segment length across all the granite sectors is again highest in CHc sector (220.70 m), followed by CHn (181.40 m), JN (143.81 m), and CHs (91.38 m) **(Fig. 6.5b)**. Detailed data on fracture trace and segment counts and lengths for all sample locations are provided in **Supplementary File_6.1, Sheet-1** and sector-wise averages are provided in **Sheet-3** of the same.

b. Fracture orientations and sets

Fracture strike orientation patterns vary distinctly across the different sectors of the two younger granite bodies within the CSB. In the CHn sector, fracture orientations consistently display a strong NW to NNW trend, with a minor NNE to NE trending mode recorded across all observational scales. Strong mutual interaction amongst multiple closely spaced, parallel to sub-parallel oriented fracture sets defines the 2D fracture network architecture here. The pronounced NW to NNW trending unimodal distribution aligns closely with the orientation of distinct field foliation observed in the granite in this sector. In the CHc sector, fractures exhibit mostly a bimodal distribution of orientation. The dominant mode is ENE to ESE trending, with an additional NW to NNW mode present at some locations. These two primary fracture sets, which propagate linearly across the granite body, often cross-cut or abut one another, giving rise to the typical fracture network pattern of this sector. The CHs sector shows a strong NE trending mode, with remnants of ENE to ESE trending fractures at some locations. At the extreme southern end of the Chitradurga granite, a broadly bimodal distribution is observed, comprising ESE trending and NNW trending fractures. Fracture orientations within the JN sector show a wide variation, giving rise to a more multimodal distribution. However, the NE trend as observed in the CHs sector, is persistent here too. **Figure 6.6a** shows the outline map of the two younger granite bodies, sub-divided into four sectors. Dominant fracture orientations in each sector are depicted in six representative equal-area length-weighted rose diagrams in **Figure 6.6b**, generated using FracPaQ from the 2D digitized outcrop images of fracture networks spanning a range of areal dimensions from each sector.

c. Fracture spacing

Fracture orientation data reveal that while the CHn sector displays a strongly unimodal pattern, several locations in the other sectors also exhibit noticeable unimodal trends to varying degrees. This allows for a convenient assessment of fracture spacing patterns by placing linear scanlines perpendicular to the dominant fracture trend observed on these outcrop surfaces. The spacing between adjacent fractures intersecting the scanline is recorded. This analysis was conducted on eight outcrop photographs, two from each sector of the granites viz. CH 266 and CH 267 from the CHn sector, having a dominant NNW trend of fractures within outcrop areas of 25.57 sq. m and 18.50 sq. m respectively; CH 215 D and CH 312 B from the CHc sector which show a dominant ESE fracture trend along with a smaller NE trending mode within outcrop areas of 23.96 sq. m and 32.16 sq. m respectively; CH 272 C and CH 272 from the CHs sector with a dominant NE trend of fractures within outcrop areas of 15.45 sq. m and 18.03 sq. m respectively, and, CH 187 A, showing a dominant NE trend of fractures and CH 273 A, which, within a wider range of fracture orientations shows a considerable NE trend from the JN sector within outcrop areas of 15.65 sq. m and 20.15 sq. m respectively.

In the CHn sector, scanlines intersect 129 and 60 fractures in outcrops CH 266 and CH 267, respectively. Fracture spacing ranges from a minimum of 0.23 cm to a maximum of 27.48 cm, with an overall average of 5.08 cm. Most spacing values are below 10 cm, averaging 3.53 cm, while those exceeding 10 cm are few and have an average of 15.08 cm.

In the CHc sector, 95 and 61 fracture traces intersect the scanlines placed in outcrops CH 215 D and CH 312 B, respectively. Fracture spacing span a much wider range here from a minimum of 0.12 cm to a maximum of 86.67 cm, with an overall average of 8.62 cm, signifying higher frequency of smaller spacing values which fall below 10 cm, averaging 3.28 cm, while those exceeding 10 cm are less in frequency having an average of 31.10 cm.

In the CHs sector, the scanlines intersect 77 and 75 fracture traces in outcrops CH 272 C and CH 272, respectively and here fracture spacing ranges are similar to that of the CHn sector with a minimum of 0.23 cm and a maximum of 23.20 cm. The overall average is 4.94 cm which is closer to the average of spacing values falling below 10 cm, at 3.43 cm. Spacing values exceeding 10 cm have an average of 12.13 cm.

In the JN sector, the scanlines placed in outcrops CH 187 A and CH 273 A, intersect 47 and 88 fracture traces respectively. Here again, the range of fracture spacing becomes considerably wider, from a minimum of 0.26 cm to a maximum of 51.36 cm, with an overall average of 5.98 cm. Here, spacing values falling below 10 cm, average 3.30 cm, while those exceeding 10 cm have an average of 19.98 cm. The detailed data on fracture spacing analysis as discussed is provided in **Supplementary File_6.2**.

Figures 6.7a, **b**, **c** and **d** respectively show traced images of the fracture networks within four granite outcrops viz. CH 266, CH 215 D, CH 272 C, and CH 187 A, from the CHn, CHc, CHs, and JN sectors, respectively, and the orientation of the scanlines placed along them. The graphical representations of corresponding spacing data are shown in **Figures 6.7e**, **f**, **g** and **h**. The measurements clearly indicate that fracture spacing is not uniform. Instead, fracture spacing pattern in each sector of the granites, exhibit two distinct phases which can be distinguished considering the 10 cm spacing mark as a threshold value. Although the average spacing below 10 cm remains consistent across all sectors and closely aligns with the overall average spacing, the average spacing above 10 cm shows significant variation throughout the spatial extent of the granites. The disparity between the average spacing values below and above the 10 cm threshold is notably greater in the CHc and JN sectors (27.82 cm and 16.68 cm, respectively) compared to that of the CHn and CHs sectors (11.55 cm and 8.70 cm, respectively). These differences may reflect underlying variations in the characteristic space-filling fracture patterns across different sectors of the granites which are further discussed in section 6.3.4.

6.3.2 Statistical distribution of fracture lengths

Maximum Likelihood Estimation (MLE) analyses, as conducted by FracPaQ on all 48 outcrop images of fracture networks captured across the entire spatial extent of the granites, reveal that the statistical distribution of fracture lengths, both in terms of trace lengths and segment lengths, predominantly follows a power law scaling relationship, irrespective of sampling dimension, in every sector. In the CHn sector, the probability that both fracture trace lengths and segment lengths conform to a power law distribution is highest, at 95.67% and 97.28%, respectively. In the CHc sector, fracture trace lengths show the greatest likelihood of an exponential distribution at 98.03%, closely followed by the power law distribution at 97.97%. For fracture segment lengths in this sector, the power law distribution has the highest likelihood estimate at 97.57%, while the exponential and lognormal distributions have significantly lower probabilities, at 79.16% and 60.71%, respectively. In the CHs sector, fracture trace lengths are most likely to follow a power law distribution at 98.94%, compared to 98.11% for the exponential and 97.08% for the lognormal distributions. For fracture segment lengths, the exponential distribution holds the highest likelihood at 99.39%, with the power law distribution closely behind at 98.07%, and the lognormal distribution trailing at 53.80%. Similar to the CHn sector, in the JN sector, the probability that both fracture trace and segment lengths follow a power law distribution is the highest, at 98.32% and 98.91%, respectively. When considering all sectors collectively, the probabilities for fracture trace lengths following power law, exponential, and lognormal distributions stand at 97.83%, 94.98%, and 90.57%, respectively. For fracture segment lengths, these probabilities are 98.00%, 90.05%, and 55.36%, respectively (**Figs. 6.8a and b**; see **Supplementary File_6.1, Sheet-4** for details of MLE calculations). These results clearly demonstrate the dominance of power law scaling over other statistical distributions of fracture lengths within the granites of the study area, suggesting an underlying fractal nature of fracture distribution patterns, which are further discussed in section 6.3.4.

6.3.3 Topological characters

a. Evaluation of topological parameters

Correct identification of different connectivity node types and thereby node count forms the fundamental basis for topological characterization of fracture networks from 2D surface data. Analyses conducted on all 48 outcrop images reveals the proportions of I, Y and X nodes in fracture networks captured from different sectors of the granites. Across the range of observational scales, in the CHn sector, I nodes occur at an average of 51.05%, Y nodes at 32.43% and X nodes at 16.61%. In the CHc sector, the abundance of I nodes decreases, standing at an average of 45.24% while the average occurrence of X nodes is a bit higher at 19.00% and Y nodes have an average of 35.76%. The abundance of I, Y and X nodes in the CHs sector is comparable to that of the CHn sector, with averages at 52.12%, 31.43% and 16.45% respectively. The JN sector has an average of 53.91% occurrence of I nodes, 30.72% for Y nodes, and 15.37% for X nodes. The numeric counts of these node types are used to calculate the number of lines (N_L) and number of branches (N_B) from each outcrop image following equations (6.1) and (6.2) respectively. It is found that both in terms of N_L and N_B, the CHc sector has the maximum abundance followed by the CHn, JN and CHs sectors in decreasing order of abundance. The N_B/N_L ratio, which is a function of the topology of fracture networks, is also highest in the CHc sector at an average of 2.90, followed by the JN sector with an average of 2.62, the CHn sector having an average of 2.52 and then the CHs sector with an average of 2.47. Numeric node type counts and values of N_L and N_B calculated from them are also utilized to derive quantitative estimates of fracture connectivity within the networks which are denoted by connections per line (C_L) and connections per branch (C_B) following equations (6.8) and (6.9) respectively. Average values of C_L

and C_B calculated from each sector indicate highest connectivity in the CHc sector ($C_L = 2.80$; $C_B = 1.60$) followed by the JN sector ($C_L = 2.42$; $C_B = 1.51$), the CHn sector ($C_L = 2.27$; $C_B = 1.48$) and then the CHs sector ($C_L = 2.23$; $C_B = 1.48$) in decreasing order of network connectivity, which is in accordance with the order of N_B/N_L ratio also. The relative proportions of I, Y and X nodes calculated from each data point are represented as ternary plots sector-wise in **Figure 6.9a**, showing fracture connectivity in terms of N_B/N_L ratio and C_L and in **Figure 6.9b**, showing the same in terms of C_B.

b. Branch statistics

Using the counts of different connectivity node types from each outcrop photo, the probabilities of a branch ending as an isolated node (P_I) or a connected node (P_C) are also calculated using equations (6.3) and (6.4), respectively. The probabilities of different branch types, viz. completely isolated (P_{II}), partly connected (P_{IC}), and completely connected (P_{CC}) branches are hence calculated using the values of P_I and P_C in equations (6.5), (6.6), and (6.7), respectively. For each data point, the relative proportions of P_{II}, P_{IC}, and P_{CC} are plotted in a ternary diagram to generate the branch classification plots which are represented sector-wise in **Figure 6.9c**.

In the CHn sector, the average probability of branches being completely isolated (P_{II}), partially connected (P_{IC}), and completely connected (P_{CC}) are 8.95%, 23.26%, and 67.79%, respectively. In the CHc sector, average P_{II} and P_{IC} are a little lower at 5.22% and 18.51%, respectively, while average P_{CC} increases to 76.27%. The CHs sector exhibits similar branch statistics as that of the CHn sector, with average P_{II}, P_{IC}, and P_{CC} values of 9.18%, 23.31%, and 67.51%, respectively. The JN sector shows a little increase in average P_{CC} value, which stands at 69.94%, while average P_{II} and P_{IC} values here are at 8.26% and 21.79%, respectively. The CHs sector shows the highest probability for completely isolated (P_{II}) and partially connected (P_{IC}) branch types, followed by the CHn, JN, and CHc sectors in descending order. In terms of completely connected branches (P_{CC}), the CHc sector shows the highest probability, followed by the JN, CHn, and CHs sectors in descending order. This order of fracture connectivity defined by P_{CC} branch type is the same as that of C_L, C_B and N_B/N_L, highlighting greater fracture connectivity in the CHc and JN sectors as compared to that of the CHn and CHs sectors of the granites.

It is worth observing that in every sector, the relative proportions of P_{II}, P_{IC}, and P_{CC} vary in such a way that their values plot along the exact same curve representing the abundance of C_B within the branch triangle (from $C_B = 0$ at I-I end to $C_B = 2$ at C-C end) **(Fig. 6.9c)**. This is indicative of the phenomenon that some aspect of the underlying topology of these fracture networks remains consistent throughout the granite plutons. This persistent underlying topological pattern across the entire spatial extent of the granites may point towards the possibility that the fracture networks within the younger granites of the CSB were formed during a protracted phase of deformation under the same tectonic stress state.

c. Quantitative assessment of fracture abundance

The quantitative assessment of fracture abundance across different granite sectors of the study area is carried out using the P_{XY} system developed by Sanderson and Nixon (2015). In this system, the dimension of the sampling region is plotted along the X-axis, while the dimensions of the fracture features are represented along the Y-axis. Since this study characterizes fracture networks from 2D surface outcrops, the X-axis always corresponds to sampling area, while the Y-axis may correspond to fracture frequency, fracture lengths and fracture areas. This framework allows the calculation of fracture density/frequency (P_{20}), fracture intensity (P_{21}), and dimensionless intensity (P_{22}) within the 2D sampling region, following equations (6.10), (6.11), and (6.12), respectively. Considering the discrete values of these fracture abundance parameters as calculated from each data point spanning varying sampling areas, it is found that the CHn sector shows the maximum abundance of fractures. Average fracture density (P_{20}) is the highest in the CHn sector, at 407.31 m^{-2}, followed by 319.19 m^{-2} in the CHs sector, 205.61 m^{-2} in the JN sector, and 123.19 m^{-2} in the CHc sector. Average fracture intensity (P_{21}) is also highest in the CHn sector at 23.41 m_{-1}, followed by 16.39 m^{-1} in the CHs sector, 13.15 m^{-1} in the CHc sector, and 11.32 m^{-1} in the JN sector. Dimensionless intensity (P_{22}) also shows a peak at the CHn sector with a value of 1.61 followed by the CHc, CHs and JN sectors with values of 1.56, 0.99 and 0.80, respectively. Detailed calculations and comparisons related to topological characterization are provided in **Supplementary File_6.1, Sheet-1** and **Sheet-3**, respectively, while the data on branch type classification is provided in **Sheet-5** of the same.

d. Spatial comparison of fracture abundance

Values of C_L, C_B, N_B/N_L ratio, fracture density (P_{20}), fracture intensity (P_{21}), and dimensionless intensity (P_{22}) as calculated from each of the 48 data points spread throughout the granite plutons represent a spectrum of fracture abundance and connectivity quantified across varying sampling areas and thus cannot be compared on a one-to-one basis. Therefore, for their spatial comparison, these parameters calculated across varying outcrop scales have been subjected to Chatterjee’s correlation test (Chatterjee, 2021) with respect to the area of the sampling region. Chatterjee’s Correlation test is a robust measure of general dependency, i.e., not just linear or monotonic dependence between two quantities. Results of the test (see **Supplementary**

File_6.1, Sheet-2) suggest that values of C_L and C_B, representing fracture connectivity, and N_B/N_L ratio have no correlation of any kind with the area of sampling region, as is expected, since connectivity, and N_B/N_L ratio, being topological characters of networks, are independent or invariant to scale. Similarly, values of dimensionless intensity (P_{22}) also do not have any correlation with the area of the sampling region. On the other hand, for fracture density (P_{20}) and intensity (P_{21}), the test results exhibit measurable correlations with sampling area, suggesting some functional dependence. When analyzed, in the present geological scenario, both these factors show a power law scaling with area. While the correlation coefficient for fracture density (P_{20}) stands at a significant 0.51 **(Fig. 6.10a)**, for that of fracture intensity (P_{21}), it is quite low, at 0.25. To suffice for this weak correlation, the total length of fractures measured within a defined sampling area, has been utilized as a proxy for fracture intensity. Upon analysis, this parameter shows a significant power law scaling with the area of sampling region, with a correlation coefficient of 0.55 **(Fig. 6.10b)**. Using these power law relationships, calculated fracture densities (P_{20}) and total fracture lengths measured within sample regions of varying areal dimensions are normalized to unit area (the detailed calculation is provided in **Supplementary File_6.1, Sheets-1 and 2**), which effectively represents the latter as fracture intensity (P_{21}), while enabling consistent comparison of these quantitative estimates across all data points collected from different sampling locations and varying areal dimensions throughout the spatial extent of the granite plutons.

Calculated values of C_L, C_B, N_B/N_L ratio, and P_{22} and the normalized values of P_{20} and P_{21} are used to create coloured contour maps of the granite plutons corresponding to each of these parameters. The procedure followed for the preparation of these contour maps is provided in **Supplementary File_6.3**. These maps aid in visual comparison of these spatially varying fracture abundance and connectivity attributes within the study area **(Fig. 6.11)**. The comparative analysis reveals that regions within the CHn sector, particularly those proximal to the CSZ, and parts of the CHc sector, exhibit greater fracture density and intensity **(Figs. 6.11a, b and c)**. However, in terms of fracture connectivity, it is the CHc sector and the south-western portion of the JN sector that show greater connectivity **(Figs. 6.11d, e and f)**, while, despite the high fracture density in parts of the CHn sector, these areas lack significant connectivity.

6.3.4 Fractal attributes

Considering the high self-similarity of the rock materials, the fractal attributes of the fracture networks extracted from the Chitradurga granite (CH) and J. N. Kote granite (JN) have been analyzed using the 2D box-counting method. The application of the box-counting method to different parts of the CH (i.e., CHn, CHc, and CHs) and JN yields different box-counting dimensions (*D*), or fractal dimension values across different scales of observation (see **Supplementary File_6.4**). The analysis reveals varying fractal dimensions, indicating different scaling behaviours at different size ranges. The box-counting plots in this study yielded both single-slope and double-slope regression lines over more than one order of magnitude, potentially corresponding to distinct fracture patterns or scaling regimes.

The fracture networks of the CHn sector show a single, distinct power-law relationship (D_1) over more than one order of magnitude across all scales of observation **(Figs. 6.12a, e, i, m)**. The fractal dimension values (D_1) range from 1.66-1.74. Although a second power-law relationship (D_2) was observed at larger box sizes and smaller outcrop scales (4.62-18.50 m^2), the extent of the slope is less than one order of magnitude and, therefore, cannot be considered as a true self-similar pattern. Overall, the 2D fracture networks of the CHn sector are characterized dominantly by a single fractal dimension.

This is further reflected through the distinctly observable uniformity in the distribution of fracture lengths relative to their orientations **(Figs. 6.12b, f, j, n)**, as well as in the individual frequency distributions of both fracture orientations **(Figs. 6.12c, g, k, o)** and lengths **(Figs. 6.12d, h, l, p)** across incremental scales of observation. South of CHn, the fractal analysis of the fracture networks in the CHc sector shows two distinct power-law relationships (D_1 *and* D_2) over more than one order of magnitude across all scales of observation **(Figs. 6.13a, e, i, m)**. The D_1 and D_2 values range from 1.27-1.70 and 1.29-1.95, respectively. The fracture networks of the CHc sector, characterized by two distinct fractal dimensions, which may have caused distinct scaling behaviours. Despite the apparent uniformity across scales, this is reflected through greater variations in the distribution of fracture lengths relative to their orientations **(Figs. 6.13b, f, j, n)**, and in the frequency distributions of both fracture orientations **(Figs. 6.13c, g, k, o)** and lengths **(Figs. 6.13d, h, l, p)**, particularly visible at smaller outcrop scales.

At the southern Chitradurga granite (CHs), the fractal analysis of the fracture networks shows only a single, distinct power-law relationship (D_1) across all scales of observation, extending over more than one order of magnitude **(Figs. 6.14a, e, i, m)**. Depending on the scale of observations, the fractal dimension values (D_1) vary from 1.61 to 1.74. Although a second power-law relationship (D_2) was observed only at a smaller outcrop scale (7.72 m^2), the extent of the slope is far less than one order of magnitude and, therefore, cannot be considered a separate self-similar pattern. Hence, the fracture network of the CHs sector is characterized by a single fractal dimension. Similar to the CHn sector, this is further demonstrated by the marked uniformity in how fracture lengths are distributed relative to their orientations **(Figs. 6.14b, f, j, n)**, along with the consistent patterns observed in the frequency distributions of both fracture orientations **(Figs. 6.14c, g, k, o)** and lengths **(Figs. 6.14d, h, l, p)** across progressively larger scales of observation. In contrast, the fracture networks of the JN sector show two discrete power-law relationships (*D_1 and D_2*) over more than one order of magnitude across all scales of observation **(Figs. 6.15a, e, i, m)**. With variation in observation scales (4.81-51.21 m^2), the D_1 and D_2 values range from 1.39-1.70 and 1.27-2.09, respectively. Therefore, the fracture networks of the JN sector are characterized by distinct scaling behaviours, represented by two distinct fractal dimensions. Similar to the CHc sector, here, this is manifested by greater variation in the distribution of fracture lengths with respect to their orientations **(Figs. 6.15b, f, j, n)**, as well as in the frequency distributions of both fracture orientations **(Figs. 6.15c, g, k, o)** and lengths **(Figs. 6.15d, h, l, p)** across varying scales of observation.

6.3.5 Discussion

a. Spatial variations in fracture network patterns

Individual fracture characteristics, including length, orientation, and their network attributes like fracture density, intensity, and connectivity, vary significantly across the different sectors of the Chitradurga and J.N. Kote granites. The CHn sector exhibits moderate fracture lengths, dominated by a strong unimodal fracture orientation trending NW to NNW. Despite high fracture density and intensity, this sector displays moderate fracture connectivity. In contrast, the CHc sector features the longest fractures with a bimodal orientation distribution and the highest connectivity, evidenced by a maximum proportion of connected nodes, despite lower fracture density and intensity than in CHn. The CHs sector displays the shortest fracture lengths, primarily a unimodal orientation of fractures trending ~ NE with localized bimodality at the southern end of the granite, moderate fracture density and intensity, but the lowest connectivity among the sectors. Finally, the JN sector shows considerably high fracture lengths and a multimodal orientation distribution, accompanied by moderate fracture density and intensity and relatively higher connectivity (see **Supplementary File_6.1, Sheet-3**). These variations underscore the influence of localized structural controls and associated geological factors on fracture network development within the younger granite plutons of the CSB. Although fracture network attributes are observed to vary spatially within the younger granites of the CSB in terms of their geometry and topology (connectivity), they remain consistent across different incremental field (mesoscopic) scales of observation, reflecting their self-similar nature, as demonstrated by fractal analysis and MLE analysis of fracture length distribution, which dominantly shows a power-law scaling across sectors. The self-similar nature of shear fracturing in strike-slip fault zones displaying Riedel shear geometries has also been previously reported from field based studies on natural exposures and analogue experimental modelling (Tchalenko, 1970; Davis et al., 2000; Kim and Sanderson, 2004; Swanson, 2006). A stress regime index indicative of a trans-tensional to pure strike-slip regime in the Chitradurga region has been reported earlier by Bhowmick and Mondal (2020), attributed to sinistral shearing along the CSZ induced by ESE-WNW directed D_3 compression.

Considering the spatial variations in fracture geometry and their network attributes, along with the ambient stress conditions and regional deformation patterns, the genesis and evolution of fracture networks within the younger granites of the CSB can be effectively interpreted.

b. Genesis of the fracture networks

The fracture networks observed across the entire spatial extent of the granite plutons consist predominantly of steeply dipping shear fractures exhibiting variable strike orientations, characterized by both dextral and sinistral oblique-slip movement along them, as is evidenced by the systematic sense of displacements of earlier quartzo-feldspathic veins by these later developed faults **(Figs. 6.16a, b, c and d)** in all the sectors of the granites. It is important to note, that the sense of displacements of these pre-existing markers along faults of specific orientations show a systematic pattern which remain spatially consistent across the granite plutons, indicating a tectonic control on their origin **(see Fig. 6.16a)**. In addition to shear fractures, development of some later-formed tensile fractures is also observed within the granites. These fractures are predominantly vertical to sub-vertical, appearing black in outcrops and are identifiable by tapered tips at both exposed ends. They exhibit a consistent E-W to ESE-WNW orientation, cross-cutting earlier quartz veins within the granite **(Figs. 6.16e and f)**. Similar to that of the shear fractures, microscopic analysis reveals chlorite as the black vein-filling mineral, displaying undisturbed and undeformed growth **(Figs. 6.16g, h, i and j)**.

Despite the apparent variability in fracture orientations, fault slip analysis conducted on these granites by Mondal et al. (2020) revealed a spatially consistent NNE-SSW to NE-SW directed maximum extension in the region. Minor inconsistencies in raw fault orientation data have been significantly reduced post-analysis, producing consistent maxima and sub-maxima in stress orientation across all the sectors of the granites. This uniformity strongly suggests that all faults within the granites were generated during the same deformational event. Furthermore, branch classification data of fracture networks analyzed across all the granite sectors show that the relative proportions of P_{II}, P_{IC}, and P_{CC} branch types consistently plot along the same curve reflecting abundance of C_B within the branch triangle **(Fig. 6.9c)**. This can be indicative of a persistent underlying topological structure within the fracture networks throughout the plutons. Taken together, the structural coherence in both geometry and topology points strongly toward the development of these fracture networks during a single, spatially extensive deformation phase that affected the younger granites of the CSB. Since the faults and fractures cross-cut all earlier brittle structures observed within the granites and no evidence of deformation post D_3 has been recorded from field investigations, as is evinced by the undisturbed growth of chlorite flakes within both the shear and tensile fractures cutting across pre-existing quartz veins within the granites **(Figs. 6.16e to j)**, it is most likely that the fracture networks developed during late phases of the D_3 deformation, which probably continued up to the late stage of craton evolution, culminating in the stabilization of the area.

In light of the present field observations, coupled with the self-similar nature of the fracture networks within a dominantly strike-slip system, the respective orientations of different faults and tensile fractures comprising the fracture networks within the granites can therefore be interpreted as the different components (R, P, R', P', Y, and T shears) of a regional scale Riedel shear system **(Figs. 6.16a and e, insets)** activated by sinistral shearing along the CSZ during late D_3 deformation of the region. It may be noted that strike variations reflected from individually collected fault slip data has also been previously interpreted as products of Riedel shearing, where the CSZ, coeval with the D_3 deformation, acted as the master shear boundary (Mondal et al., 2020).

c. Factors influencing the development of Riedel fractures

i. Role of ambient stress-state vis-à-vis pluton margin orientation

Although the overall trend of the CSZ in the study area is ~ 330° (Mondal, 2018; Mondal et al., 2020), it is important to consider the spatially changing orientation of the granite pluton margins which may have an important bearing on the generation of a regional scale Riedel shear system. The eastern margin of the Chitradurga granite, which is proximal to the adjacent CSZ, is oriented NNW-SSE in the north, to more NW-SE at the central part, while it turns and changes to NE-SW in the southern part. The eastern margin of the J.N. Kote granite shows an overall NNW-SSE trend, however, there are considerable portions of it oriented NE-SW **(Fig. 6.17a)**. It will be imperative to assume that the stark rheological contrast imparted by the boundary between the granite plutons and adjacent schist belt rocks will result in shear being partitioned along the lithological contact.

Therefore, in the CHn sector, the pluton margin, oriented at ~ 345°-350°, will effectively act as the main boundary shear. Considering the ESE-WNW to SE-NW oriented principal compressive stress axis in this region (Mondal et al., 2020), sinistral shear will be induced along the ~ 345°-350° trending pluton margin. Assuming the angle of internal friction (Φ) of the granites to be ~ 35° (Hoek and Brown, 1980; Jaeger et al., 2009) at the time of brittle fracturing, when the granites were relatively dry (Mondal and Acharyya, 2018), low angle synthetic R shear will be oriented at ~ 330° and antithetic R’ shear at ~ 280° (see **Supplementary File_6.5**). Synthetic P shear component and its conjugate P’ shear will be resolved at ~ 10° and 240°, respectively. Y shears may also develop at ~ 345°-350°, since these are synthetic faults oriented parallel to subparallel to the main boundary shear. Tensile fracture (T) component of the Riedel shear system will be oriented parallel to the principal compression direction **(Fig. 6.17b)**.

Fracture strike orientations, fault-slip data collected from the CHn sector (Mondal et al., 2020) **(Fig. 6.17e)** and field evidence showing systematic sense of offsets of earlier quartzo-feldspathic veins by the later developed faults **(Fig. 6.16b)** conform well to the proposed Riedel shear model **(Fig. 6.17b)**. All synthetic sinistral Riedel shear components range broadly between ~ 330° and 10°, while the antithetic dextral components range between ~ 50° and 100° **(Fig. 6.17e)**, with chlorite filled tensile fractures (T) trending ESE-WNW **(Figs. 6.16e and f)**, broadly aligning with the far-field compressive stress in this sector of the granite.

The CHc sector presents a broadly similar picture with the only difference being the orientation of the pluton margin, which along considerable stretches trends ~ 320° here. The principal compressive stress is oriented more E-W in central and southern regions of the granite (Mondal et al., 2020). Accordingly, sinistral shear is induced along the ~ 320° trending pluton margin and the resulting disposition of all Riedel shear components are shown in **Figure 6.17c**. Here also, fault-slip data conforms to the Riedel shear model, with synthetic sinistral faults, oriented NE-SW and antithetic dextral faults, oriented NE-SW to ENE-WSW **(Fig. 6.17f)**.

In accordance with the change in pluton margin orientation from NNW-SSE/NW-SE to NE-SW, the fault-slip data collected from the CHs and JN sectors exhibit compliance with the proposed Riedel shear model for these two sectors of the granites. Here, the E-W configuration of principal compressive stress axis (Mondal et al., 2020) results in dextral shear being induced along the broadly ~ 45°-50° trending pluton margins. Therefore, low angled synthetic components of the Riedel shear system (R, P, Y) should be oriented ~ NE-SW while the high angled antithetic components (R’ and P’) should be oriented ~ NW-SE **(Fig. 6. 17d)** as is also reflected in fault-slip data collected from these two sectors of the granites **(Fig. 6. 17g)**.

ii. Control of pre-existing structural anisotropy

In granular materials, the formation of Riedel shear fractures is influenced by the grain constituents, which govern their rheology and mechanical behaviour. Rheological transition from brittle to ductile regimes, and the presence of penetrative shape fabrics formed by preferred alignment of flaky mineral grains, are key factors affecting the relative development of low and high angle Riedel fractures (Misra, 2009; Gomez-Rivas and Griera, 2012). Both fracture sets tend to form equally when the material is predominantly brittle and lacks any shape fabric. In isotropic materials, R and R' components of a Riedel shear system generally develop at approximately 15° and 75° to the bulk shear direction, respectively (Dresen, 1991). However, as the material becomes more ductile and develops a flaky grain fabric, fracture formation becomes more localized, typically forming a single set at a low angle to the bulk shear direction. The shape fabric of flaky grains introduces mechanical anisotropy that strongly influences Riedel shear formation. As anisotropy increases, stress concentrates along a single orientation within the 0-90° range, favouring the development of low-angle Riedel shears. In such anisotropic media, these low-angle shears exhibit greater strain softening and tend to propagate at comparatively higher rates (Misra, 2009). This explains the strong unimodal distribution of fracture orientation in the CHn sector, where the development of low angle Riedel shears has been favoured due to the presence of well-developed field foliation defined by preferred alignment of phyllosilicates (dominantly biotite) at ~ 330°-340° within the granite. This is also observed in parts of the CHs and JN sectors, which are closer to the pluton margin and the adjacent CSZ, although the development of a strong field foliation in them are not as conspicuous as is observed in the CHn sector. On the other hand, the CHc sector, which is comparatively finer grained and do no apparently exhibit the development of field foliation, favours the growth of both high and low angle components of the regional Riedel shear system.

iii. Control of grain size

Although the initiation threshold of fractures depends primarily on the strength of the constituent minerals of a rock, grain size plays a significant role in fracture propagation behavior (Eberhardt et al., 1999). Larger grain size increases the fracture toughness of a rock body and enhances the surface roughness of fractures (Aghababaei et al., 2024), making crack propagation more difficult. This is because greater stress is required at the crack tips to drive the fracture forward, effectively limiting fracture growth and reducing overall fracture length. The presence of larger grains in rocks also often leads to fractures getting deflected, branched, or even bridged by individual grains or mineral boundaries, making the fracture path more tortuous, thereby slowing down or halting propagation (Gao et al., 2019). This explains the consistently low abundance and shorter fracture lengths encountered in the CHs sector, which is the coarsest grained sector of the granites, and also, conversely, the greater abundance of fractures with larger lengths in the comparatively finer grained CHc sector. The ease of propagation might have also facilitated the formation of more X nodes within the finer grained portions of the granite bodies, leading to higher connectivity.

iv. Control of structural position (proximity to master shear zone, CSZ)

The intricate interplay of all the aforementioned factors played a key role in the formation and evolution of the fracture networks within the younger granites of the CSB. As is mentioned earlier, the northern part of the Chitradurga granite and the J. N. Kote granite, proximal to the CSZ, experienced dominant simple shear ($W_k = 0.8$), whereas the southern part of the Chitradurga granite, located farther away from the CSZ, was mainly affected by pure shear ($W_k = 0.06$) (Mondal, 2018). This variation in tectonic regime might have played a crucial role in shaping the fracture networks which developed during late D_3 deformation of the region. The fractal dimension estimates from the box-counting methods reflect that greater fracture network complexity corresponds to higher box-counting dimension values (*D*) (Huang et al., 2024), which is observed in the CHc and JN sectors. The variations in space-filling patterns of the fracture networks across different sectors of the granites can also be attributed to the complex interaction of tectonic influence and inherent rock properties, coupled with the spatial disposition of the granites with respect to the CSZ, which dictated the overall deformation style.

The CHn sector, though simple shear dominated due to its proximity to the CSZ, exhibits a strongly unimodal fracture orientation. This results from the influence of pre-existing foliation, defined by preferred alignment of phyllosilicates within the granite, which heavily guided the propagation of slip planes, conveniently accommodating bulk strain in the process. This impeded the unrestricted development of multiple Riedel shear components, leading to a network architecture defined by closely spaced, parallel to sub-parallel fractures, forming a single space-filling pattern in 2D space characterized dominantly by one fractal dimension.

Although the CHc sector lies farther from the CSZ compared to the CHn sector, its finer grain size compensates for this reduced proximity by promoting the development of the key components of the Riedel shear system. Unlike the CHn sector, however, fracture networks in CHc sector do not exhibit a uniform space-filling pattern. Instead, clusters of fractures formed within localized damage zones generated by the pervasive parallel oriented major Riedel shear components (R, R’, P, and Y), which propagated linearly across the width of granite body in this sector **(Fig. 6.7b)**. This spatial heterogeneity resulted in two distinct fractal dimension values, reflecting a more complex and segmented fracture network architecture, which is also visible in the analysis of fracture spacing patterns conducted in this sector **(Fig. 6.7f)**.

The CHs sector, characterized by its coarse grain size and distal position from the CSZ, is predominantly governed by pure shear deformation rather than simple shear. This suppresses the development of the full spectrum of Riedel shear components, with strain instead being localized along favourably oriented planes lying at low angles to the regional shear boundary. Additionally, presence of larger grain size considerably impedes fracture propagation here. Consequently, the fracture networks in this sector are characterized by lower density, intensity, and connectivity, with strike orientation of fractures mostly exhibiting a unimodal distribution, predominantly aligned NE to ENE, parallel to the pluton margin. This structural simplicity is reflected in the fractal analysis, which yields a single fractal dimension value, indicative of a relatively uniform, less complex space-filling pattern compared to other sectors.

The medium grained JN sector, located in close proximity to the CSZ, exhibits a wide variation in fracture strike orientations, reflecting a more complex deformational regime. The dominance of simple shear in this zone likely enabled the sequential development of multiple Riedel shear components. The progressive formation of R, R', P, and Y shears may have led to the superimposition of fracture sets, producing a densely fractured and structurally overprinted network. Here also, localized clusters of fractures form in damage zones developed along parallel propagating, closely-spaced major Riedel shear components, as is observed in spacing analysis of this sector **(Figs. 6.7d and h)**, similar to that of the CHn sector. As a consequence, the fracture architecture in the JN sector is highly heterogeneous and well connected, with clusters of fractures oriented in multiple directions. This intricate spatial pattern is captured by the presence of two distinct fractal dimension values, indicative of a segmented and multifaceted space-filling fracture network.

Fractal dimension values also reflect the connectivity of the fracture networks. Higher *D*-values, as well as the presence of multiple fractal dimension values (i.e., multiple self-similarity slopes), imply greater connectivity, which in turn reflects an increased propensity for flow and transport through fractures (Berkowitz et al., 2000; Doughty and Karasaki, 2002), which is evident in the CHc and JN sectors of the granites. However, it is important to note that small differences in *D*-values may correspond to substantial changes in fracture connectivity and flow processes. Therefore, it is critical to estimate this parameter using robust datasets and with the highest possible accuracy. Any discrepancy in the *D*-value may be related to differences in the resolution of the extracted fracture patterns from the images and/or the scaling factor that determines the number of box-counting points. In particular, low-resolution images may yield inaccurate box counts, especially for smaller box sizes (Roy et al., 2007).

6.4 Fracture network characterization in the metavolcanic rocks

The metavolcanic rocks of the study area are characterized by the widespread development of fracture networks. These networks have predominantly evolved through the interaction and cross-cutting relationships of multiple fracture sets. Unlike the younger granites, that exhibit significant spatial variability in terms of texture and development of fractures networks, as has been discussed above, the metavolcanic rocks display a relatively uniform fabric and composition throughout the study area. Although they appear apparently massive in outcrops, a consistent NW-SE to NNW-SSE magnetic foliation has been recorded in these rocks by Bhowmick and Mondal (2020) through AMS analysis. This lithological homogeneity is mirrored in the architecture of the fracture networks, which display broadly consistent characters throughout the exposures. The systematic nature of these fracture patterns suggests that the processes responsible for their development operated uniformly over large areas. Consequently, the metavolcanic rocks provide an excellent framework for examining regionally persistent brittle deformation patterns, as the fracture networks offer insights into both the mechanical behavior of the host rock and the tectonic forces that governed their formation. However, a robust characterization of these fracture networks along with a comprehensive understanding of their genesis and controlling factors requires further investigation and additional field data. The present contribution therefore summarizes the outcomes of the preliminary analyses carried out on these rocks.

Fracture networks within the metavolcanic rocks of the study area are predominantly exposed on sub-vertical outcrop surfaces. A total of 19 outcrop photographs capturing such networks have been collected for analysis, encompassing surface areas ranging from ~ 0.5 sq. m to ~ 45 sq. m (see **Fig. 6.18a** for the locations of data points). Corresponding details for each data point are provided in **Supplementary File_6.6, Sheet-1**. Representative examples of fracture networks documented from sub-vertical exposures, together with their traced counterparts, are shown in **Figures 6.18b-e**. Sub-horizontal exposures of metavolcanic rocks are rare; one such three-dimensionally exposed view of fracture networks is illustrated in **Figure 6.18f**. The development of triangular and diamond-shaped blocks of rocks produced by the systematic intersection of multiple variably oriented fracture sets, as is evident in this outcrop view, constitutes the characteristic expression of fracture interaction within the metavolcanic rocks. Individual fracture planes forming the networks appear as cross cutting and abutting joint sets with minimal apertures mostly devoid of mineral infill. However, some of these fracture can be identified as fault planes by the presence of slickenside lineations and congruous steps on their exposed surfaces, which also help in identifying the sense of movement along them (Petit, 1987) **(Fig. 6.18g)**.

6.4.1 Geometrical characters

a. Fracture trace lengths and segment lengths

For the fractures constituting the networks within the metavolcanic rocks, dimensional attribute of fracture geometry is presently restricted to the linear extent of fracture traces and their constituting segments as observed on digitized 2D outcrop surfaces. Fracture width (aperture) has not been incorporated in the analysis since the majority of fractures, lacking any mineral infilling, have negligible opening, and thus are beyond the resolution of field-based measurement or image analysis. Analyses of digitized outcrop photographs in FracPaQ reveal that on average, each fracture network comprises about 653 individual traces, with an average trace length of ~ 0.26 m. The average total trace length recorded across all sample locations is about 120 m, highlighting the significant cumulative extent of fracturing within these rocks. When analysed in terms of fracture segments, the networks are further resolved into an average of about 2,026 individual segments. The average segment length is ~ 0.09 m, with the average total segment length being approximately 119 m. Detailed of calculations are provided in **Supplementary File_6.6, Sheet-1.** These values demonstrate that while individual segments are shorter than the traces they constitute; their abundance ensures that the total segmented length is nearly equivalent to the total trace length. Collectively, these results indicate that the fracture networks in the metavolcanic rocks are both extensive and systematically segmented, reflecting a consistent pattern of fracture propagation and interaction across the study area.

b. Fracture orientation and sets

As the analyses were based on sub-vertical outcrop images, extraction of fracture orientation data using FracPaQ was not feasible. Therefore, attitude data of fracture planes constituting the networks within the metavolcanic rocks have been collected manually from the field. It is observed that fracture strike orientation patterns remain broadly consistent across the areal extent of the studied metavolcanic rocks. Four dominant strike orientations are recognized in the metavolcanic rocks, namely NNW, NNE, ENE, and ESE. The rose diagram in **Figure 6.19a** illustrates these preferred orientations, while the strike vs. dip cross-plot of the fracture planes depicted in **Figure 6.19b** shows that the fractures generally exhibit high dip angles, although a few sub-horizontal attitudes are also recorded. However, the multi-modal distribution of fracture orientations, rather than a single dominant trend, across virtually all metavolcanic rock outcrops, restricts the applicability of spacing analyses that rely on placing scanlines along the principal fracture orientation, as was feasible in certain outcrops of the younger granites. This limitation calls for the need of alternative methods, providing scope for further investigation.

6.4.2 Statistical distribution of fracture lengths

Maximum Likelihood Estimation (MLE) analyses, carried out on fracture traces digitized from metavolcanic rock outcrops, reveal that the statistical distribution of fracture lengths, in terms of both traces and segments, is dominated by power law scaling. This scaling relationship is observed consistently across all sample locations, irrespective of the size of the sampling area, underscoring the scale-invariant character of fracture growth and distribution in the metavolcanic rocks.

For fracture trace lengths, the average probability of conforming to a power law distribution is 98%, compared to 74.88% for an exponential distribution and 93.79% for a lognormal distribution. Similarly, for fracture segment lengths, the average probability of following a power law distribution is 94.83%, while exponential and lognormal distributions yield lower probabilities of 88.01% and 85.10%, respectively **(Figs. 6.20a and b; Supplementary File_6.6, Sheet-3)**. These results clearly demonstrate that, although alternative statistical distributions provide acceptable fits in certain instances, the dominance of power law scaling is evident for both fracture traces and segments across the metavolcanic rocks. The prevalence of power law distributions might indicate that fracture nucleation, propagation, and linkage are governed by self-similar processes, consistent with the fractal nature of brittle deformation, as also observed in the granites. Occasional deviations toward exponential or lognormal fits can be interpreted as reflecting localized factors such as lithological heterogeneity or stress perturbations that may have temporarily arrested fracture growth. Overall, the scaling properties confirm the systematic and scale-invariant behavior of fracture networks throughout the metavolcanic sequence. However, detailed fractal analysis using box-counting methods has yet to be performed on the metavolcanic rocks, which may substantiate these observations in a more rigorous manner and therefore provide avenues for future research.

6.4.3 Topological characters

a. Evaluation of topological parameters

Topological analyses conducted on all outcrop images of fracture networks from the metavolcanic rocks reveal that the proportions of I, Y, and X nodes are broadly consistent across the study area. On average, I nodes constitute 26.25%, Y nodes account for 56.46%, and X nodes make up 17.29% of the total node population.

The numeric counts of these node types are used to calculate the number of lines (N_L) and number of branches (N_B) from each outcrop image following the standard topological equation nos. (6.1) and (6.2) respectively. The ratio N_B/N_L, which reflects the network topology, has an average value of 3.48, indicating considerable degree of branching within the fracture networks.

These topological attributes are further used to derive quantitative estimates of fracture connectivity within the metavolcanic networks, denoted by connections per line (C_L) and connections per branch (C_B). The average values of C_L and C_B are found to be 3.88 and 1.81, respectively. Notably, the average C_L value exceeds the universal percolation threshold of C_L=3.57 (Sanderson and Nixon, 2015), indicating that fracture connectivity is considerably high in the metavolcanic rocks, and that the networks might act as fully interconnected systems at the scale of observation.

The relative proportions of I, Y, and X nodes calculated from each outcrop are represented as ternary plots **(Figs. 6.21a and b)**, which demonstrate the internal consistency of fracture topology across the metavolcanic units. These ternary representations, along with plots of C_L, C_B, and N_B/N_L values, collectively underscore the uniformity of topological architecture in the metavolcanic fracture networks, in contrast to the sectoral variations observed in the granites.

b. Branch statistics

Using the counts of different connectivity node types from each outcrop image, the probabilities of a branch ending as an isolated node (P_I) or a connected node (P_C) were calculated using equations (6.3) and (6.4), respectively. From these, the probabilities of different branch types, viz. completely isolated (P_{II}), partly connected (P_{IC}), and completely connected (P_{CC}), were derived using equations (6.5), (6.6), and (6.7) respectively. For each outcrop, the relative proportions of P_{II}, P_{IC}, and P_{CC} are plotted in a ternary diagram to generate the branch classification plots **(Fig. 6.21c)**.

For the metavolcanic fracture networks, the average probability of branches being completely isolated (P_{II}) is 1.39%, partly connected (P_{IC}) is 9.14%, and completely connected (P_{CC}) is 89.47%. The absolute dominance of completely connected branches (P_{CC}) indicates that most branches form robust linkages rather than terminating in isolation. Conversely, completely isolated (P_{II}) and partly connected (P_{IC}) branches are comparatively rare, reflecting the significantly high degree of connectivity within the metavolcanic fracture networks.

Notably, the relative proportions of P_{II}, P_{IC}, and P_{CC} from all outcrops plot along a consistent curve within the branch ternary diagram (from $C_B = 0$ at the I-I end to $C_B = 2$ at the C-C end; **Fig. 6.21c**). This pattern highlights that, despite minor variations between outcrops, the underlying topological characteristics of fracture connectivity remain uniform across the metavolcanic units. The alignment of branch probabilities with the C_B continuum also corroborates the high connectivity indicated by C_L, C_B, and N_B/N_L metrics, emphasizing a coherent topological architecture within the metavolcanic fracture networks.

c. Quantitative assessment of fracture abundance

The quantitative assessment of fracture abundance in the metavolcanic rocks is carried out using the P_{XY} system of Sanderson and Nixon (2015), as applied previously for the granites. For the metavolcanic networks, the average fracture density (P_{20}) is 732.84 m^{-2}, fracture intensity (P_{21}) is 25.57 m^{-1}, and dimensionless intensity (P_{22}) is 1.45. These values indicate a high abundance of fractures across the metavolcanic units, with average P_{20} and P_{21} values notably exceeding the corresponding values observed in the granite sectors. Detailed calculations and comparisons for topological characterization in the metavolcanic rocks are provided in **Supplementary File_6.6, Sheet-1**, while branch type classification data are given in **Sheet-2** of the same file.

d. Spatial comparison of fracture abundance and connectivity

Values of C_L, C_B, N_B/N_L ratio, fracture density (P_{20}), fracture intensity (P_{21}), and dimensionless intensity (P_{22}) calculated from each outcrop of the metavolcanic rocks represent fracture abundance and connectivity across varying sampling areas. For meaningful spatial comparison, these parameters were analysed using Chatterjee's correlation test (Chatterjee, 2021) with respect to the area of the sampling region.

Results indicate that C_L, C_B, and N_B/N_L ratio, being topological network characteristics, and the dimensionless intensity (P_{22}) are invariant to sampling area and show no correlation, as is expected. In contrast, fracture density (P_{20}) and fracture intensity (P_{21}) exhibit very strong power law scaling with sampling area, with correlation co-efficient values of 0.9106 and 0.8023, respectively **(Figs. 6.22a and b)**. However, considering the limited number and sparse density of data points, and their non-uniform spatial distribution within the metavolcanic rocks, area-dependent parameters (P_{20} and P_{21}) are excluded from contour map analyses to prevent potentially biased or misleading spatial interpretations. Therefore, only the scale-invariant parameters, i.e., dimensionless intensity (P_{22}) for fracture abundance and C_L, C_B, and N_B/N_L ratio for fracture connectivity, are employed for spatial comparison using coloured contour maps **(Fig. 6.23;** procedure in **Supplementary File_6.3)**. These maps reveal the spatial consistency in fracture abundance and connectivity within the metavolcanic rocks.

6.4.4 Discussion

The fracture networks in the metavolcanic rocks broadly display spatial uniformity in both their geometrical and topological attributes reflecting the lithological homogeneity of the metavolcanic sequence of the study area. The enhanced connectivity of the metavolcanic fracture networks, primarily resulting from higher fracture density and thereby increased fracture interactions, is likely promoted by the favourable rheological properties of these rocks that render them more susceptible to brittle deformation. The scale-invariant characteristics, with trace and segment lengths following predominantly power-law distributions, indicating self-similar growth and linkage processes operating across multiple scales, which, however, needs to be investigated further.

The metavolcanic rocks of the study area record the imprint of multiple deformation phases and provide critical insights into the genesis of the fracture networks. As mentioned earlier, although no distinct foliation is visible in the field, anisotropy of magnetic susceptibility (AMS) analysis revealed a well-defined NW-SE to NNW-SSE oriented magnetic fabric in these rocks (Bhowmick and Mondal, 2020). This fabric is parallel to both the regional trend of the Chitradurga Shear Zone (CSZ) and the foliation developed in the adjacent metasedimentary rocks. Such correspondence suggests that the magnetic fabric in the metabasalts originated during D_1/D_2 coaxial deformation under NE–SW directed shortening**,** establishing a pre-existing anisotropy that could have subsequently influenced later brittle structures. The later D_3 deformation phase was marked by the development of the CSZ as a major sinistral strike-slip shear zone**,** associated with NW-SE to E-W directed compression (Mondal et al., 2020). It is highly plausible that under this stress regime, both the granites and metavolcanics responded coherently, developing brittle fracture networks that formed syn-tectonically with the activation of the CSZ. Paleostress analysis conducted by Bhowmick and Mondal (2020) with fault-slip measurements from the metavolcanic rocks of this region further constrains this interpretation. In this study, the resultant best-fit reduced stress tensor, obtained using the Right Dihedron method, yields an NNE-SSW extension direction consistent with regional D_3 kinematics under NW-SE directed compression **(Fig. 6.24a)**. The calculated stress ratio (R = 0.72) and regime index (R′ = 1.25) point to a transtensional to pure strike-slip stress regime, in agreement with sinistral shearing along the CSZ. The dominant fracture orientations recorded in the metavolcanic fracture networks encompass NNW, NNE, ENE, and ESE trends. While the NNW-SSE orientations can be attributed to the reactivation of pre-existing magnetic fabrics, the consistent occurrence of variably oriented sets indicates that all are coeval products of D_3 deformation. In addition, WNW-ESE to NW-SE trending Mode I (tensile) cracks with well-defined tips are observed, many of which are quartz-filled. Their collective disposition is best explained within the framework of a regional scale Riedel shear system, where the NNE-SSW, NNW-SSE to NW-SE fractures correspond to P, Y, and R shears, while the NE-SW to ENE-WSW and ESE-WNW sets represent P′ and R′ shears respectively, while the ESE to SE trending quartz filled tensile fractures correspond to the T component **(Figs. 6.24b and c)**. These shear components developed in response to the internal frictional properties of the metabasalts (φ ≈ 30°) (Bhowmick and Mondal, 2020) and were activated under the same sinistral shear kinematics of the CSZ during D_3 deformation, similar to those observed in the younger granites.

These fractures not only define the brittle structural framework of the metavolcanic rock suites but also served as conduits for fluid migration. In particular, the favourably oriented NNW-SSE fabrics inherited from D_1/D_2 deformation were reactivated during late D_3, generating prominent fracture sets aligned with the regional shear framework. These reactivated fractures localized significant quartz vein emplacement during the late stages of D_3 deformation, when brittle failure occurred at shallow crustal levels (as discussed previously in Chapter-4). The close correspondence in fracture style, paleostress results, and kinematic attributes between the metabasalts and adjacent granites underscores their shared tectonic evolution under the regional D_3 stress field. Nevertheless, origin of the sub-horizontal fracture sets developed within the metavolcanic rocks needs to be elucidated and further detailed microstructural and mechanical analyses will be required to fully resolve the relative contributions of inherited anisotropy versus contemporaneous stress reorganization in controlling fracture propagation and networking within the metavolcanic rocks of the region.

6.5 Summary

Structural analysis and characterization of the fracture networks developed within the younger granites and metavolcanic rocks of the study area provide significant insights into their geometric and genetic attributes. Across both lithologies, analyses reveal the self-similar nature of these networks, evident from their consistent fractal organization and dominant power law distributions across multiple scales of observation. Such self-similarity and underlying consistencies in topological attributes reflect a systematic fracturing process governed by scale-invariant mechanisms rather than random brittle failure.

The fracture networks are interpreted to have formed primarily through Riedel shearing mechanisms associated with the activation of the Chitradurga Shear Zone (CSZ) during the late D_3 deformation phase of the terrain. This brittle tectonic influence, triggered by sinistral shearing along the CSZ, is pronounced throughout the metavolcanic rocks and the granites, particularly evident in its sectors proximal to the CSZ, where fracture patterns display strong geometric, fractal, and topological coherence indicative of shear-induced fracturing.

However, detailed spatial analysis reveals contrasting characteristics in terms of network topology and connectivity within the granites and metavolcanic rocks. While the metavolcanic networks exhibit spatially uniform topology and network attributes, significant heterogeneity in the fracture network patterns is observed across the granite plutons. Variations in fracture network geometry, topology, and connectivity properties are not uniformly distributed, but collectively underscore the complex interplay of tectonic forces, deformation patterns, textural heterogeneity, and inherited structural features in controlling fracture development within the granite plutons.

The fracture networks within the granites and metavolcanic rocks of the study area exhibit notable differences in their topological and connectivity attributes. In the granites, node-type distributions vary between sectors, with I nodes ranging from 45-54%, Y nodes from 30-36%, and X nodes from 15-19%. This sectoral variability is reflected in the number of branches per line (N_B/N_L), which spans 2.47-2.90, indicating moderate branching within the networks. Correspondingly, connections per line (C_L) and connections per branch (C_B) are relatively modest (2.23-2.80 and 1.48-1.60, respectively), suggesting that while the granite networks are interconnected, they generally remain below the universal percolation threshold ($C_L = 3.57$). Branch type analysis reveals a mixture of isolated, partially connected, and fully connected branches (P_{II} = 5-9%; P_{IC} = 18-23% and P_{CC} = 67-76%), further highlighting sector-dependent variability in network connectivity.

In contrast, the metavolcanic rocks host fracture networks that are more highly connected and topologically uniform across the study area. Node-type proportions are dominated by Y nodes (56.46%), with fewer I nodes (26.25%) and X nodes (17.29%), reflecting extensive branching. The N_B/N_L ratio averages 3.48, demonstrating a greater degree of branching than observed in the granites. Connectivity metrics are markedly higher, with $C_L = 3.88$ and $C_B = 1.81$; notably, the C_L exceeds the percolation threshold, indicating that the metavolcanic networks are effectively fully interconnected at the scale of observation. Branch statistics reinforce this conclusion, with completely connected branches (P_{CC}) dominating at 89.47%, while isolated (P_{II} = 1.39%) and partly connected (P_{IC} = 9.14%) branches are comparatively much rare. These contrasting topological attributes of the fracture networks observed within the granites and metavolcanic rocks of the study area have been summarized in **Table. 6.1**.

Collectively, these results indicate that fracture networks in metavolcanic rocks are both more branched and more interconnected than those in granites. Furthermore, whereas granite networks exhibit significant sectoral variation in topological attributes and connectivity, metavolcanic networks maintain a consistent topological architecture across all outcrops. Taken together, these observations emphasize that metavolcanic rocks host highly connected, uniform fracture networks, whereas granite networks are moderately connected and sectorally variable. These structural differences have direct implications for fluid flow and mineralization; while the metavolcanic rocks provide consistent pathways for hydrothermal fluids, granite sectors with well-connected fractures, particularly those proximal to the shear zone, may serve as efficient conduits for mineralizing fluids, including gold, silver, and base metals.

The Chitradurga Schist Belt is quite well-known for its mineral potential. It hosts significant base metal mineralization, notably copper and zinc sulphide mineralization reported from Kalyadi and Ingaldhal regions, which are associated with the metavolcanic rocks of the schist belt (Naqvi et al., 1977; Subba Rao and Naqvi, 1997; Antony, 1999). Vein-hosted gold deposits have also been previously identified in the metavolcanic and metasedimentary host rocks of the Gadag and Ajjanahalli regions in its northern and southern parts, respectively (Sarangi et al., 2013; Mondal and Mamtani, 2014; Swain et al., 2018) and shear-controlled gold mineralization has been reported in the Chitradurga region (Gopalakrishna et al., 2018). The detailed characterization and quantification of fracture networks developed within the younger (~ 2.61 Ga) granites and metavolcanic rocks of the CSB therefore present new opportunities for understanding the broader mineral potential of the region. Fracture networks within granitic bodies in particular, which have garnered limited attention, play a critical role in controlling the migration and concentration of hydrothermal fluids, which are often rich in economically valuable minerals such as gold, silver, and other trace elements (Hu et al., 2020). Understanding the geometry, connectivity, and spatial variability of these fracture networks not only aids in reconstructing the tectonic and fluid-flow history of the region but also holds direct economic significance. The connectivity of these fracture systems directly influences the permeability of the rock, thereby governing the extent, direction, and efficiency of fluid flow through the granite. Highly connected fracture networks can serve as efficient pathways for mineralizing fluids, potentially leading to the formation of vein-hosted or disseminated deposits within the granites themselves (Buchholz et al., 1998; Mustard, 2001; Hongrui et al., 2003; Vallance et al., 2004; Li et al., 2013). Given the established gold mineralization in adjacent metavolcanic and metasedimentary rock suites, the younger granites, previously less explored for their resource potential, could also act as viable hosts for similar mineralizing events, particularly in regions where fractures are well connected and spatially associated with known shear zones or pluton margins. While the present work is based on data extracted from 2D surface exposures and is limited in the third dimension, it is cost-effective and provides a crucial foundation for identifying exploration targets. Permeability tensor analysis (Oda et al., 1987; Suzuki et al., 1997; Brown and Bruhn, 1998) based on documented fracture patterns and associated data offer valuable insight into fluid migration pathways within the granites, and integrating subsurface data with it can enhance the assessment of mineralization potential.

Additionally, microscopic observations of fracture apertures and filling materials, supported by geochemical analysis, can further clarify fluid-rock interaction processes. These aspects present significant opportunities for future research. Such insights can guide targeted exploration efforts, especially for structurally controlled mineralization, thereby expanding the scope of resource development in the CSB beyond its traditionally known gold-bearing zones.

The integrated approach adopted in this study therefore provides new insights into the development of fracture networks within the younger granites and metavolcanic rock suites of the Chitradurga Schist Belt (CSB), Western Dharwar Craton (WDC), India. The observed consistencies and spatial variations in fracture network architecture within respective lithologies, reflect a combination of tectonic overprinting and intrinsic rock properties, with implications for regional fluid flow, mineralization potential, waste management, and the mechanical behaviour of Neo-Archean crustal blocks during late phases of craton evolution and stabilization.

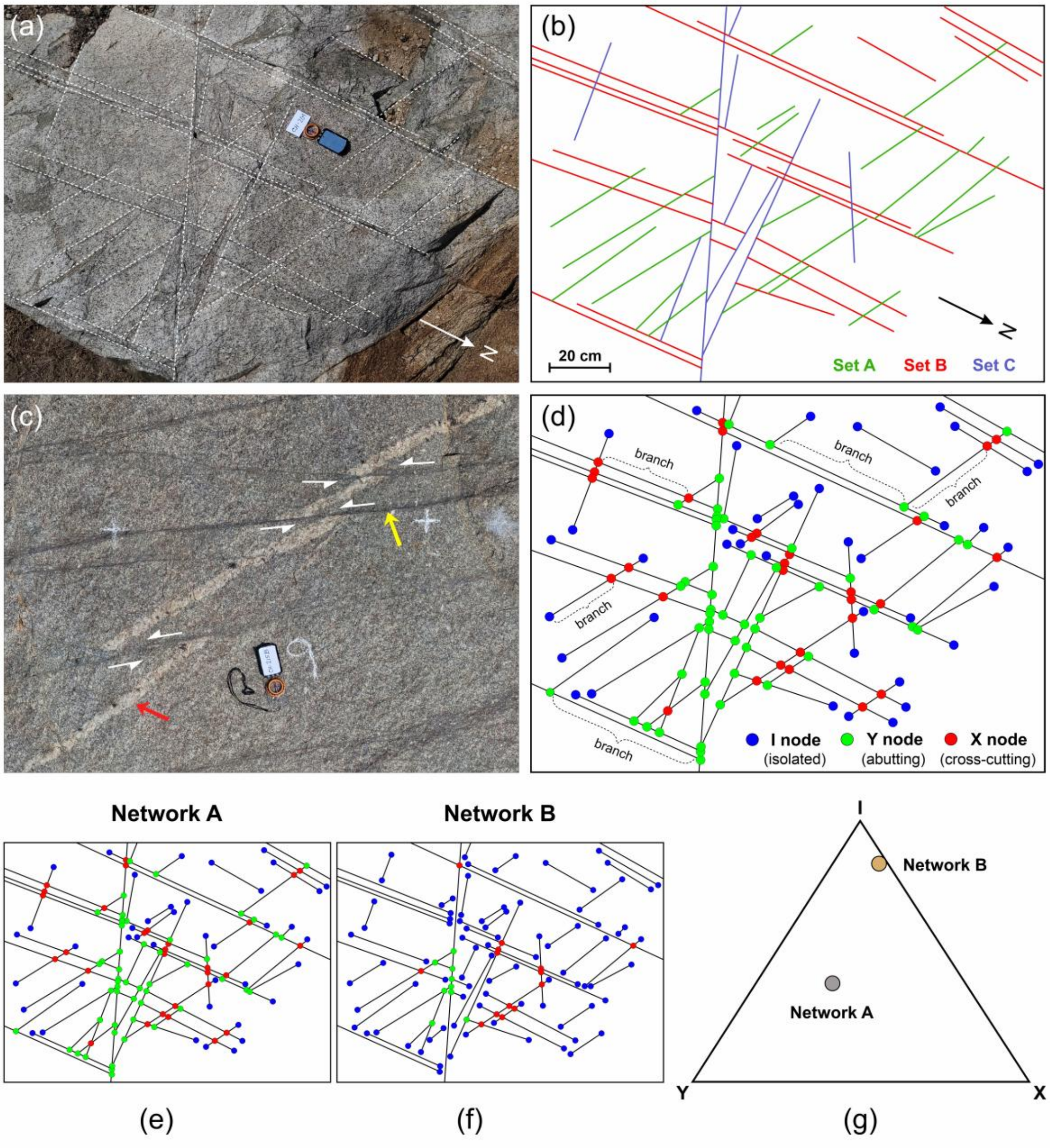

Fig. 6.1 (a) Field photograph of a natural fracture network observed in granite. Fracture traces exposed on the outcrop surface are marked by faint white dashed lines for clarity. The compass is 20 cm in length. **(b)** Simplified traced image of the same fracture network as observed in (a). Different fracture sets based on orientation are marked in different colours. **(c)** A network of fractures with diverse origins or formation mechanisms. The quartz vein (red arrow in the figure) represents a dilatational fracture, likely formed by the intrusion of vein fluid. In contrast, the thin black fractures (yellow arrow) consistently offset the quartz vein with a sinistral sense of displacement, indicating their formation as shear fractures. Contd.

Fig. 6.1 Contd. **(d)** Inter-relations of different elements of the fracture network shown in (a) and (b), expressed in terms of node and branch topology. **(e)** and **(f)** show two fracture networks, networks A & B respectively, which have similar geometry in terms of fracture trace, orientation, length, and spacing but differ in how individual fractures interact and relate. **(g)** shows the difference in topology of the two networks shown in (e) and (f) in an I-Y-X ternary plot elucidating that two fracture networks having apparently similar geometries can have drastically different topologies (after Sanderson and Nixon, 2015).

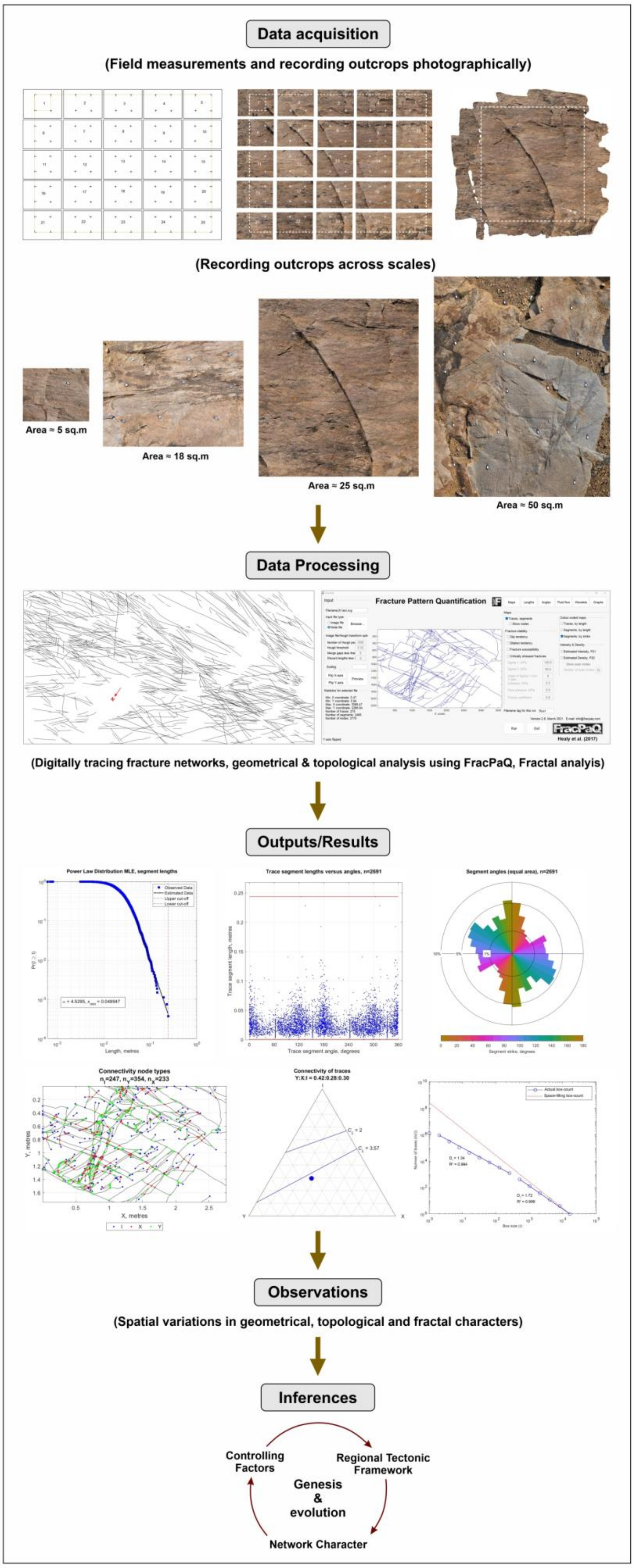
Data acquisition
(Field measurements and recording outcrops photographically)
(Recording outcrops across scales)
Area ≈ 5 sq.m
Area ≈ 18 sq.m
Area ≈ 25 sq.m
Area ≈ 50 sq.m
Data Processing
Fracture Pattern Quantification
FracPaQ
Healy et al. (2017)
(Digitally tracing fracture networks, geometrical & topological analysis using FracPaQ, Fractal analyis)
Outputs/Results
Power Law Distribution MLE, segment lengths
Length, metres
Trace segment lengths versus angles, n=2691
Trace segment length, metres
Trace segment angle, degrees
Segment angles (equal area), n=2691
Segment strike, degrees
Connectivity node types
X, metres
Y, metres
Connectivity of traces
Y:X:I = 0.42:0.28:0.30
Observations
(Spatial variations in geometrical, topological and fractal characters)
Inferences
Controlling Factors
Regional Tectonic Framework
Genesis & evolution
Network Character

Fig. 6.2 Flowchart summarizing the methodology of the work undertaken. Step-1 (data acquisition) incorporates direct field measurements of fractures and photographically recording outcrops. Outcrops have been recorded across scales. Larger areas photographed in an overlapping grid pattern has been ortho-rectified and stitched to produce a 2D orthomosaic using Agisoft Metashape Pro. In Step-2 (data processing) the acquired photographs have been traced manually using Corel Graphics academic perpetual Suite 2021 and subsequently the binary traced image files have been processed in FracPaQ Version 2.8 for geometrical and topological analyses and for 2D box counting in Benoit Version 1.3 for fractal analysis. Step-3 (outputs/results) compiles the results generated from the analyses in terms of fracture length and orientation, fracture length distribution, connectivity node types and corresponding I-Y-X ternary plot and fractal dimension values from 2D box counting amongst others. Consistent observations from all the acquired results are compiled in Step-4 (observations) which finally leads to Step-5 (inferences) whereby, a holistic characterization of the fracture networks helps in understanding the controls on their genesis and evolution within the established regional tectonic framework.

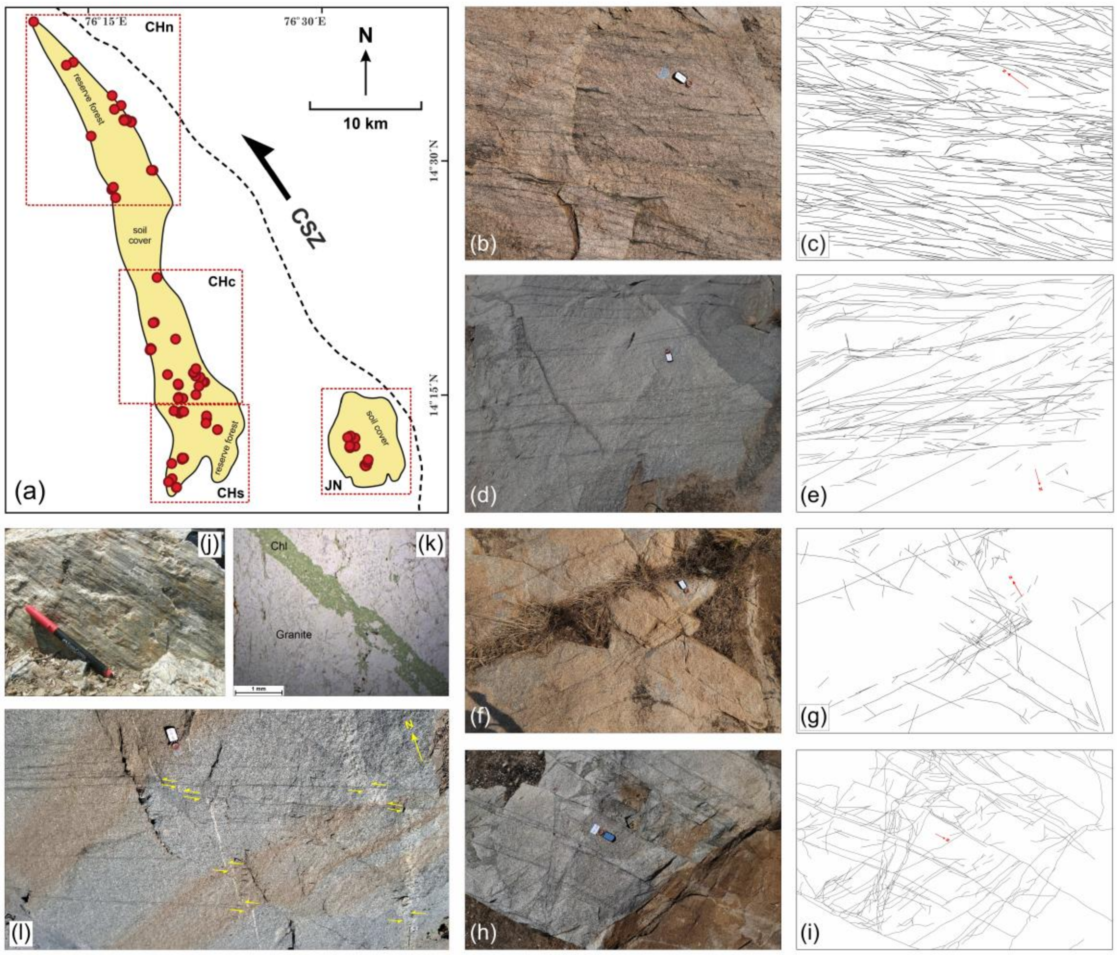

Fig. 6.3 (a) Outline map of the two younger granite bodies, the Chitradurga granite (CH) and the J.N. Kote granite (JN) showing the disposition of the study locations marked by red dots. Field photographs of fracture networks and their traced counterparts are shown respectively in **(b)** and **(c)** from the northern part (CHn), in **(d)** and **(e)** from the central part (CHc), in **(f)** and **(g)** from the southern part (CHs) of the Chitradurga granite and in **(h)** and **(i)** from the J.N. Kote granite (JN). The compass seen in all the photographs is 20 cm in length and the photographs are all ~ 5 sq. m in area. The mirror of the compass points towards the north in every photograph. Genetically, almost all of these fractures are small-scale oblique-slip fault planes originating as shear fractures within the granites as is evidenced by slip along them delineated by oblique slicken lines as seen in **(j)** with chlorite (Chl) filling in their apertures as seen in the PPL photomicrograph in **(k).** In absence of exposed fault planes, the sense of movement can be deciphered based on the offsets of pre-existing markers. Such systematic sinistrally offset quartz veins along traces of ESE-WNW trending fractures within the granite can be seen in **(l)**.

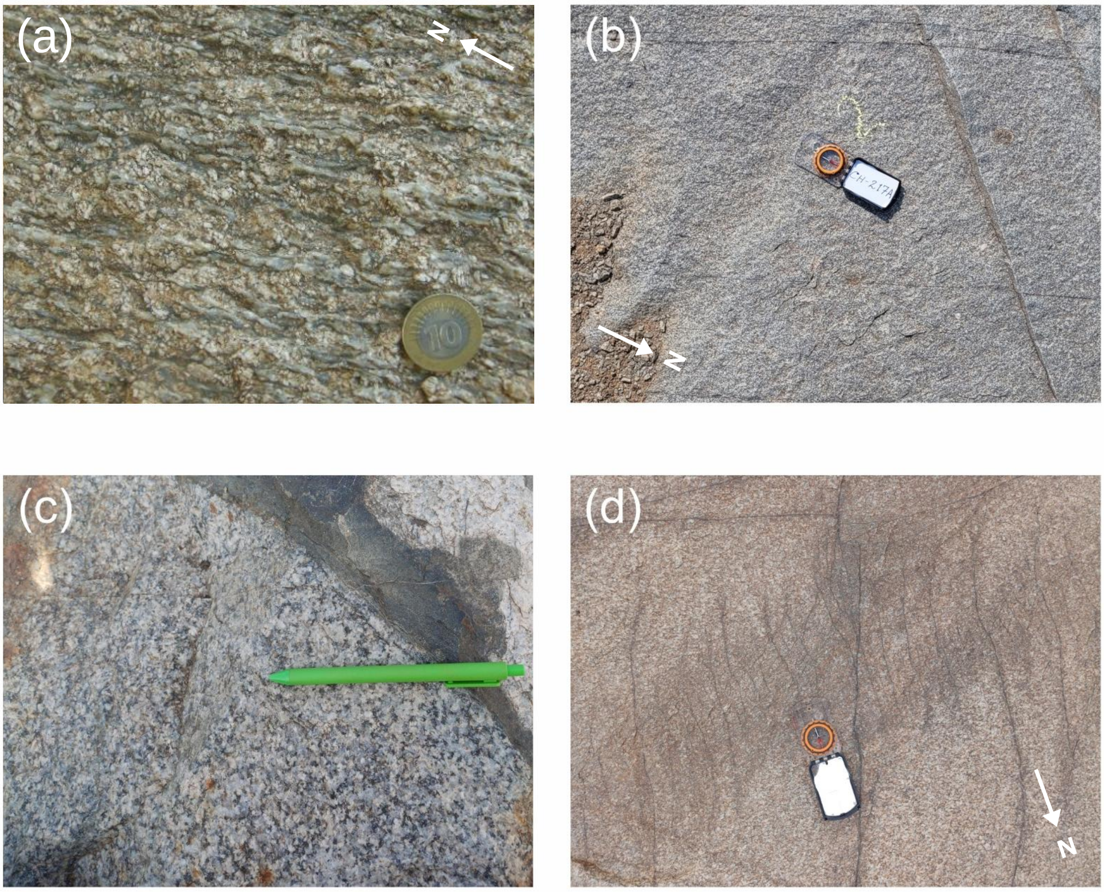

Fig. 6.4 Close-up view of field photographs showing the general appearance, texture and grain size in the different sectors of the Chitradurga and J.N. Kote granites as observed in macroscopic scale. **(a)** the CHn sector, which is generally coarse grained and shows conspicuous development of a NW-SE to NNW-SSE oriented field foliation. Development of field foliation is not as prominent in any other sector of the granites; **(b)** the fine grained CHc sector; **(c)** the coarse to very-coarse grained CHs sector of the Chitradurga granite; tip of pen points north; and **(d)** the medium grained JN sector, a separate pluton, exhibiting a grain size range in between that of the CHc and CHs sectors. The compass and the pen used as scales are 20 cm and 14.5 cm in length respectively and the coin is 2.6 cm in diameter.

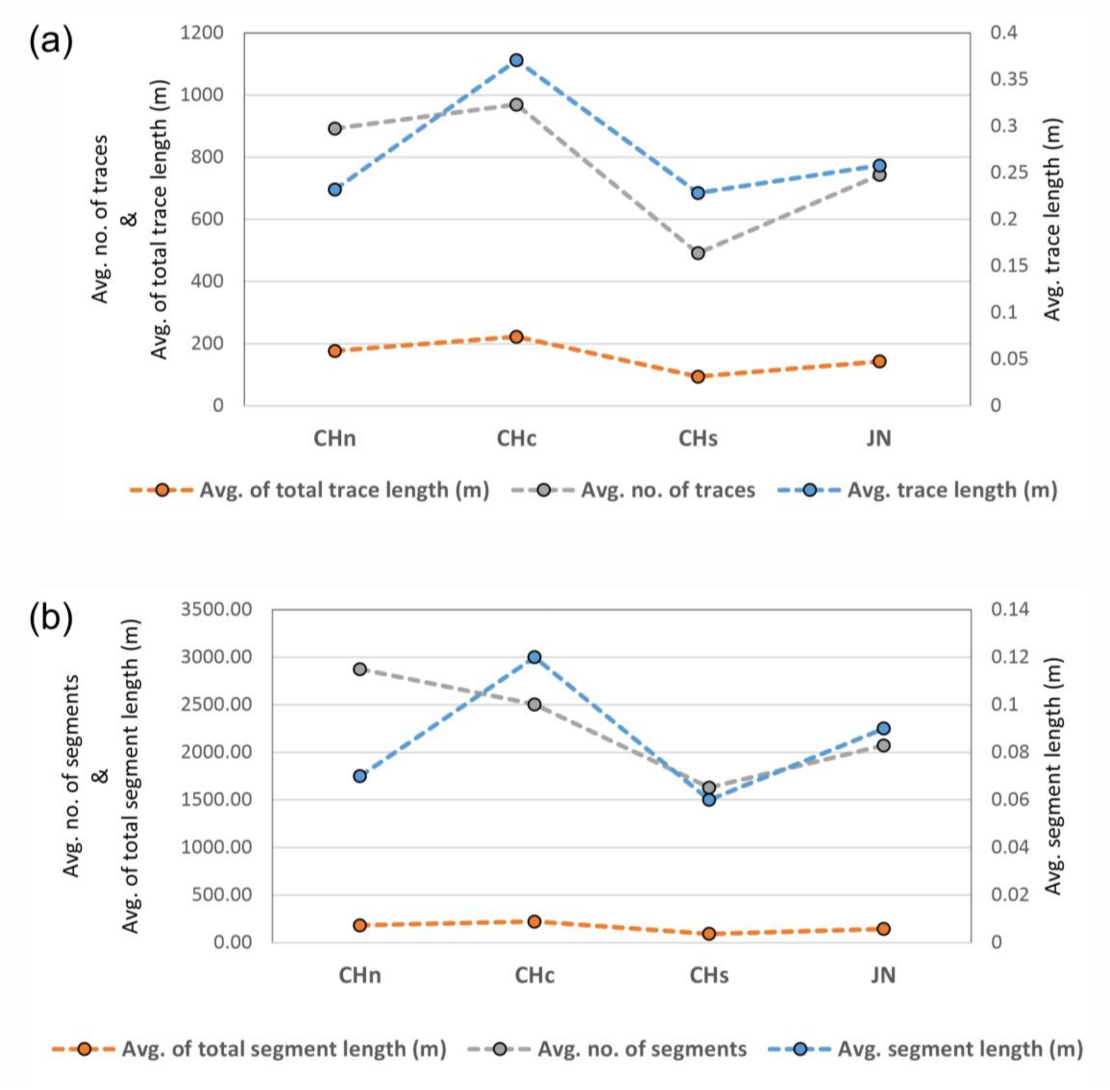

Fig. 6.5 Graphs showing the values for average number of fractures, average fracture length and average of total fracture length encountered in each sector of the granites both in terms of **(a)** fracture traces and **(b)** fracture segments.

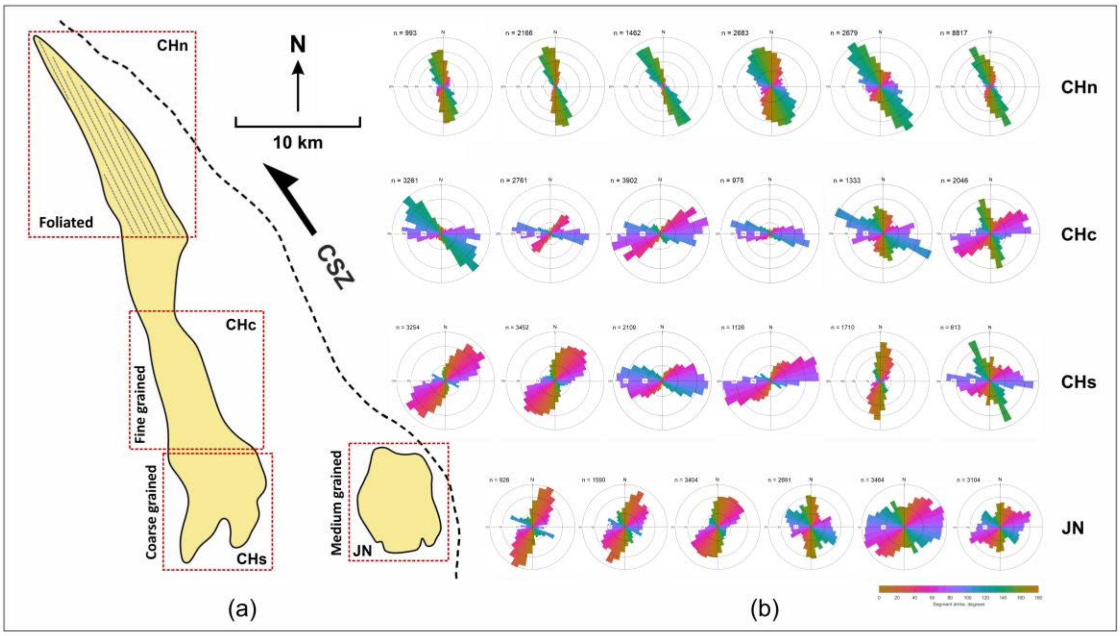

Fig. 6.6 (a) Outline maps of the two younger granites subdivided into sectors based on their texture and the orientations of fractures observed in them. **(b)** Rose diagrams showing orientations of fractures from each granite sector. Multiple rose plots from each sector are representative of outcrop photographs captured and analyzed across varying scales of observation. 'n' corresponds to the total number of fracture segments recorded from an analyzed outcrop image.

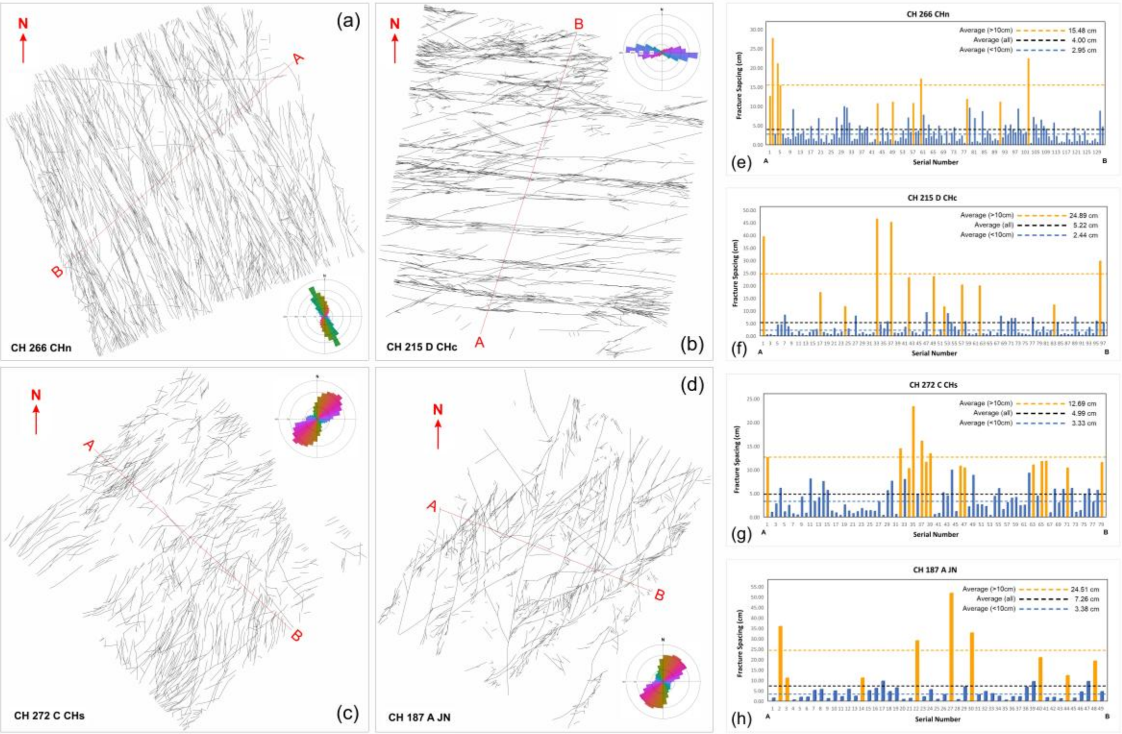

Fig. 6.7 (a), **(b)**, **(c)** and **(d)** show traced images of fracture networks observed in four granite outcrops in the CHn, CHc, CHs and JN sectors respectively. The traced fracture networks in (a) and (b) cover an area of ~ 25 sq. m each while those in (c) and (d) cover ~ 15 sq. m each. Fracture orientation is mostly unimodal in these outcrops which aids in placing a single scanline (red lines marked A-B) across the dominant trend of fractures to assess their spacing. **(e)**, **(f)**, **(g)** and **(h)** show the graphical results for fracture spacing measured from (a), (b), (c) and (d) respectively. Note that spacing in between fractures is not uniform. Rather, spacing pattern in every case comprises of at least two distinct phases as suggested in the graphs by separating the peaks in orange and blue colours taking 10 cm spacing as the threshold value. While the overall average spacing is much closer to the average of spacing < 10 cm, the average for spacing > 10 cm stands far from it in every case. The difference in between overall average spacing and average of spacing > 10 cm is still larger in case of CH 215 D CHc (f) and CH 187 JN (h) than that of CH 266 CHn (e) and CH 272 C CHs (g).

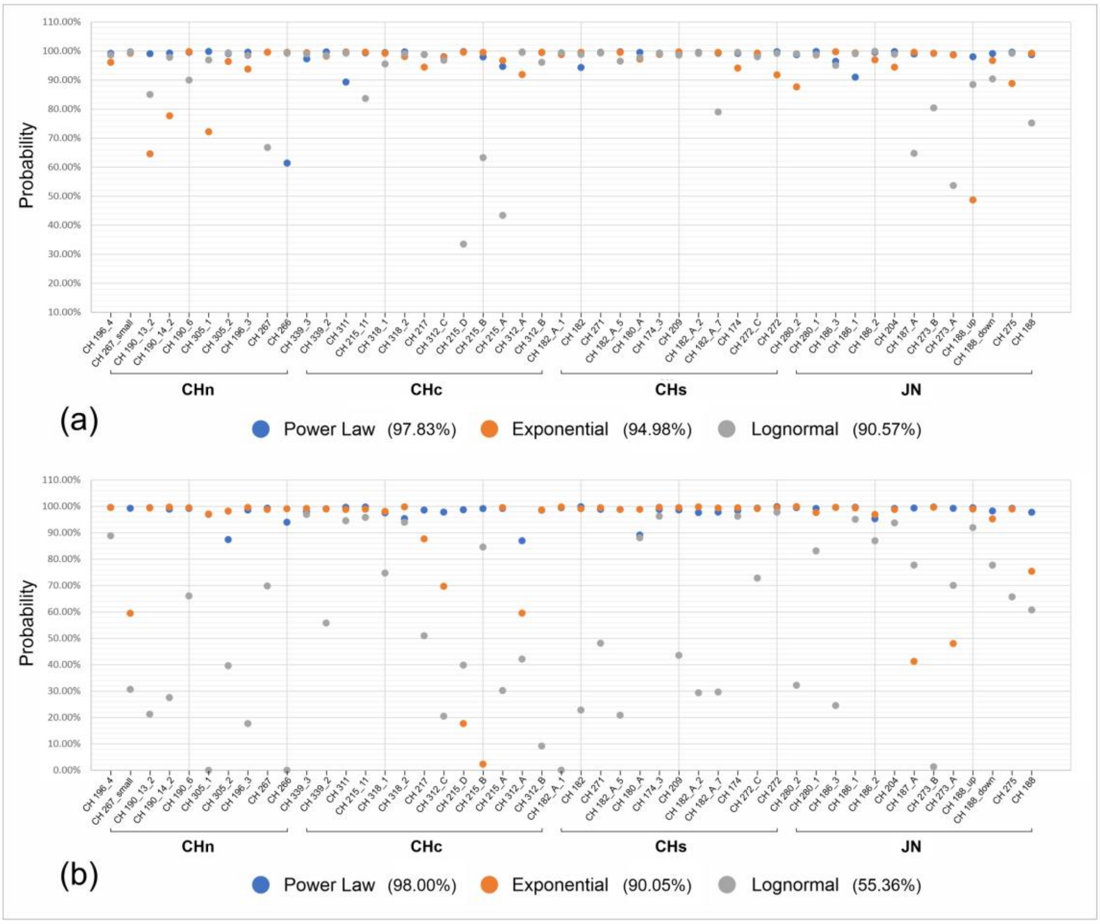

Fig. 6.8 Graphs showing the probability of fracture lengths being power law, exponentially or log-normally distributed as determined from Maximum Likelihood Estimate (MLE) analysis conducted in FracPaQ version 2.8. **(a)** shows the results for fracture trace lengths and **(b)** shows the same for fracture segment lengths. In both graphs, the sample location numbers across the entire range of observed scales have been plotted along the abscissa and corresponding values for probability of fracture length distribution are plotted along the ordinate. Sample location numbers are sub-divided into respective sectors. Note that in both cases probability for fracture lengths being power law distributed is the highest across every sector.

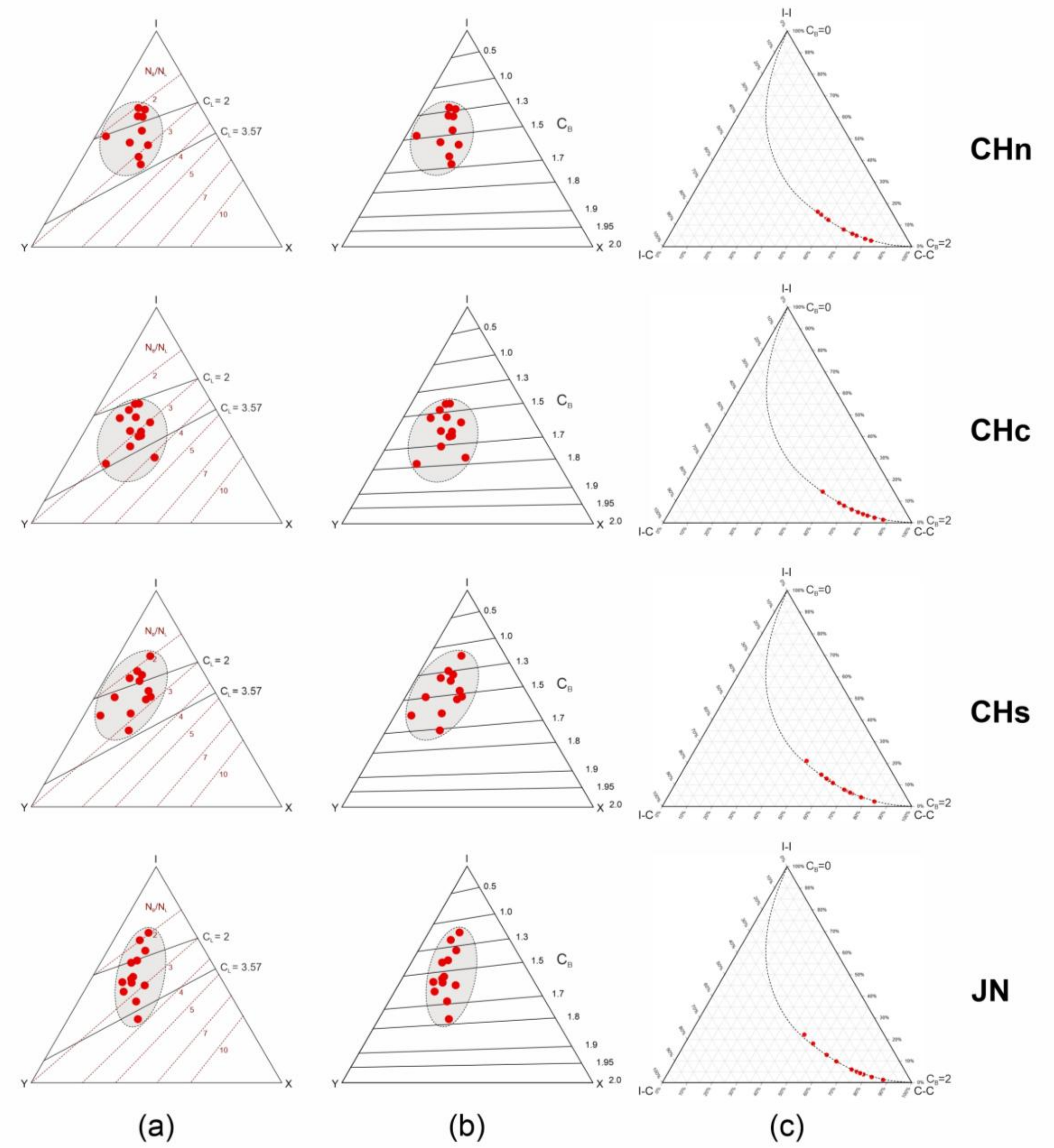

Fig. 6.9 Triangular plots for assessing fracture connectivity, shown sector-wise. **(a)** shows fracture connectivity in terms of Connections per Line (C_L) and the ratio of Number of Branches (N_B) to Number of Lines (N_L) (N_B/N_L) within an I-Y-X ternary plot while **(b)** shows the same in terms of Connections per Branch (C_B). **(c)** shows branch classification plot representing proportions of different branch types (I-I, I-C, C-C) with numbers from 0 to 2 indicating the value for connections per branch (C_B). Note that values of C_B plot along the same curve in each of the sectors of the granite bodies.

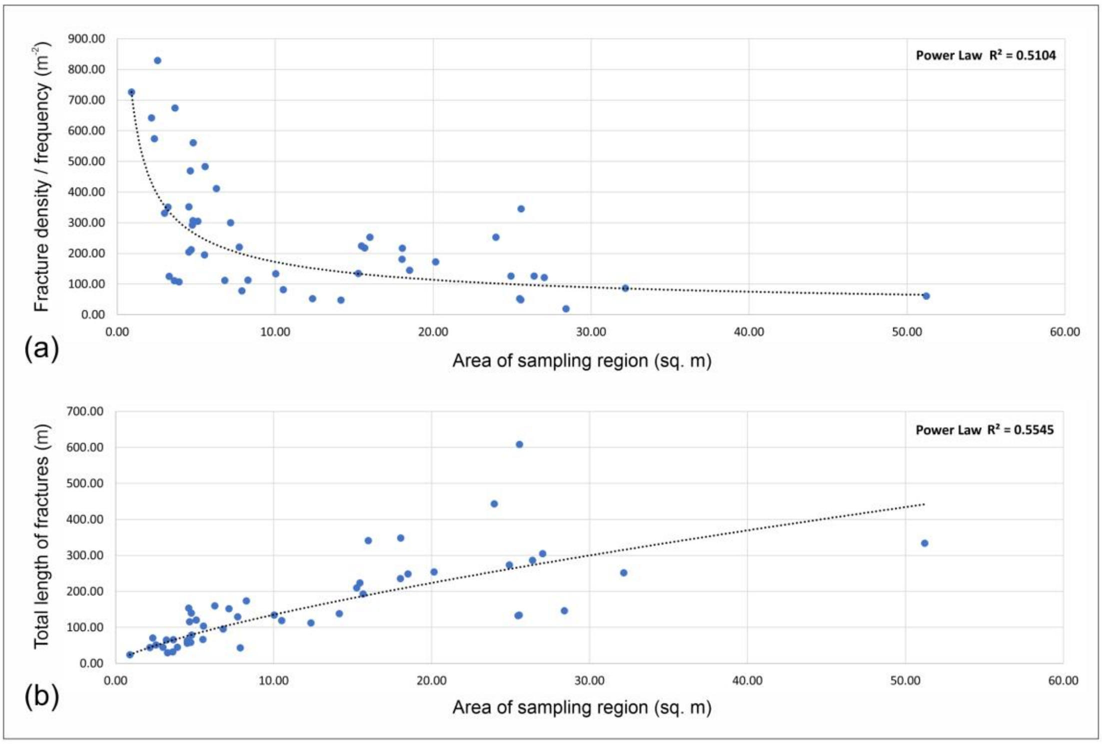

Fig. 6.10 Graphs showing **(a)** trend of fracture frequency/density across the entire areal extent of sampling region and **(b)** shows the same for total length of fractures measured within a designated sampling area. While fracture frequency/density shows a decreasing trend with increasing sampling area and vice-versa for total length of fractures, note, that in both cases, the highest R^2 value is recorded for a power law scaling with area of sampling region.

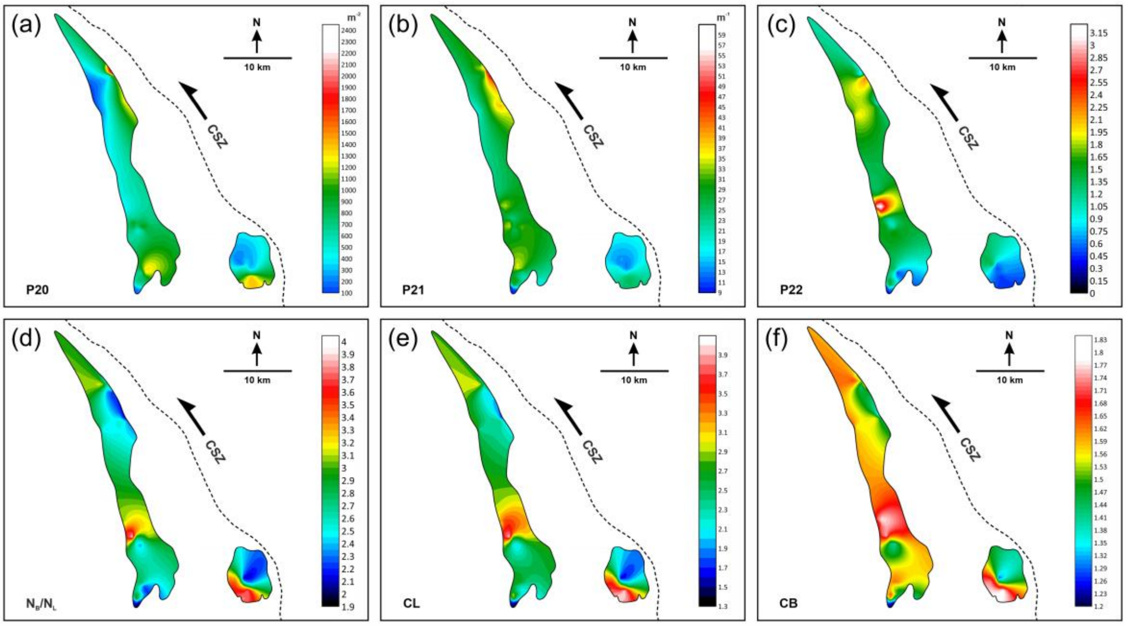

Fig. 6.11 Coloured contour maps of Chitradurga and J.N. Kote granites showing comparative spatial variations in fracture abundance and connectivity within the study area: **(a)** fracture density/frequency (P_{20}), **(b)** fracture intensity (P_{21}), **(c)** dimensionless intensity (P_{22}), **(d)** Number of branches (N_B)/Number of lines (N_L) ratio and fracture connectivity defined by **(e)** Connections per Line (C_L) and **(f)** Connections per Branch (C_B) across the areal extent of the granite plutons.

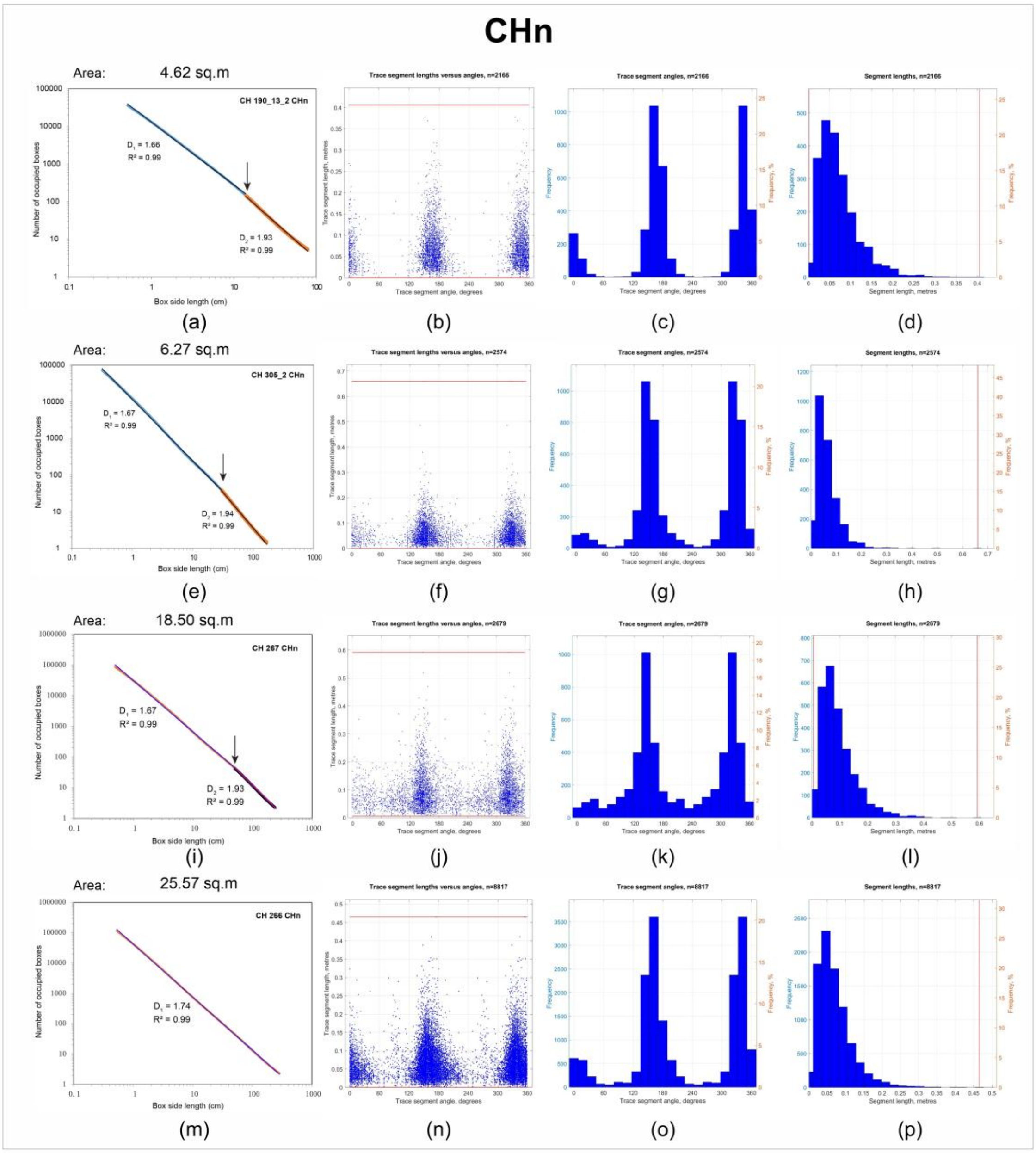

Fig. 6.12 Detection of the number of fracture-forming processes based on fractal analysis (2D box counting) for the CHn sector. The analysis has been conducted across scales on traced images of fracture networks captured photographically from 2D outcrop surfaces of granite. The first column **(a)**, **(e)**, **(i)**, **(m)** shows 2D box counting results for fracture networks conducted in increasing order of sampling area. Similarly, the second column **(b)**, **(f)**, **(j)**, **(n)** shows corresponding graphical results for fracture segment length vs. segment angle while the third **(c)**, **(g)**, **(k)**, **(o)** and fourth **(d)**, **(h)**, **(l)**, **(p)** columns show frequency plots of fracture segment angles and lengths, respectively. Note the similarity of fracture patterns recorded across different scales of observation in every sector which is also suggestive of their fractal nature.

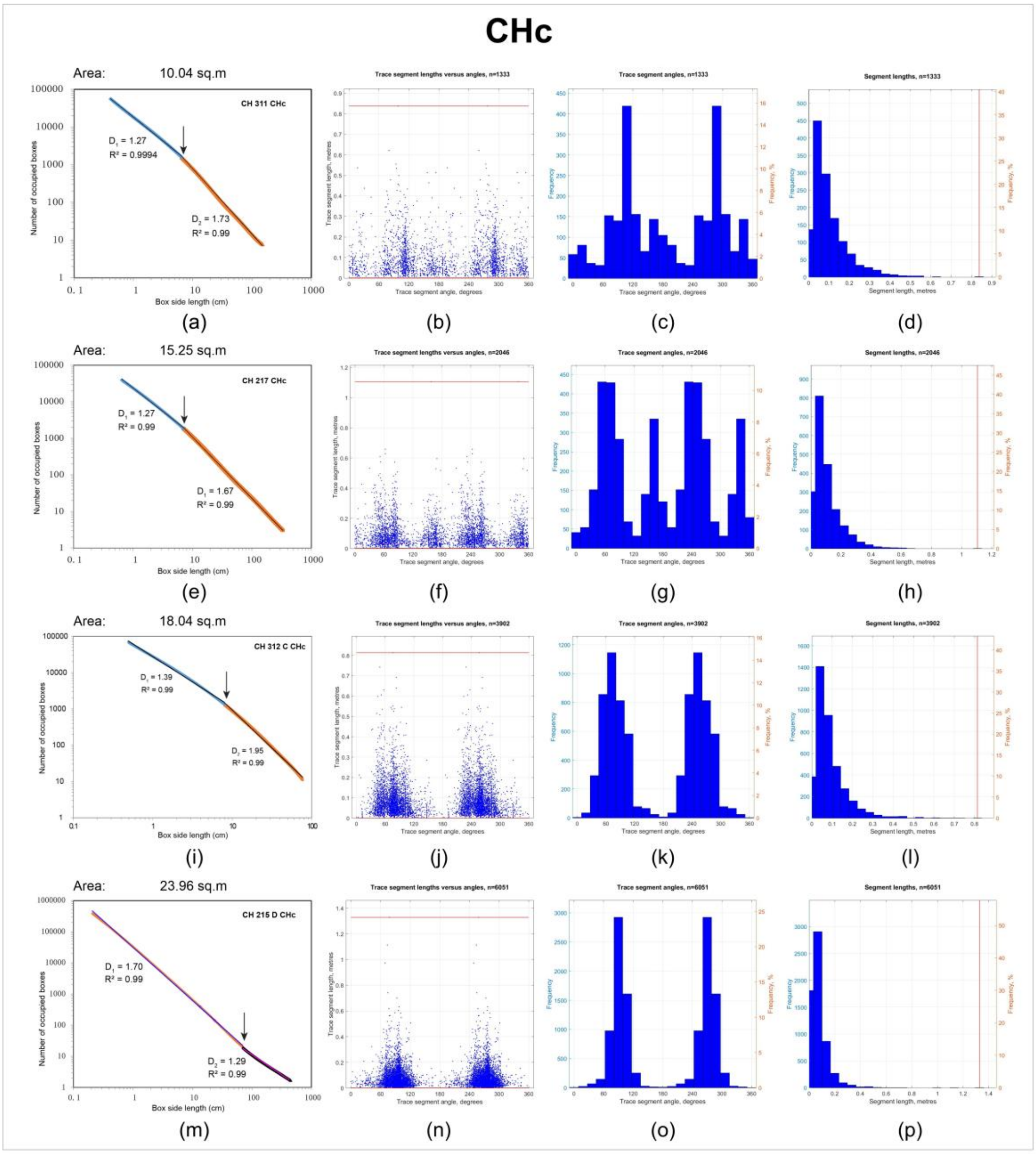

Fig. 6.13 Detection of the number of fracture-forming processes based on fractal analysis (2D box counting) for the CHc sector. The analysis has been conducted across scales on traced images of fracture networks captured photographically from 2D outcrop surfaces of granite. The first column **(a)**, **(e)**, **(i)**, **(m)** shows 2D box counting results for fracture networks conducted in increasing order of sampling area. Similarly, the second column **(b)**, **(f)**, **(j)**, **(n)** shows corresponding graphical results for fracture segment length vs. segment angle while the third **(c)**, **(g)**, **(k)**, **(o)** and fourth **(d)**, **(h)**, **(l)**, **(p)** columns show frequency plots of fracture segment angles and lengths, respectively. Note the similarity of fracture patterns recorded across different scales of observation in every sector which is also suggestive of their fractal nature.

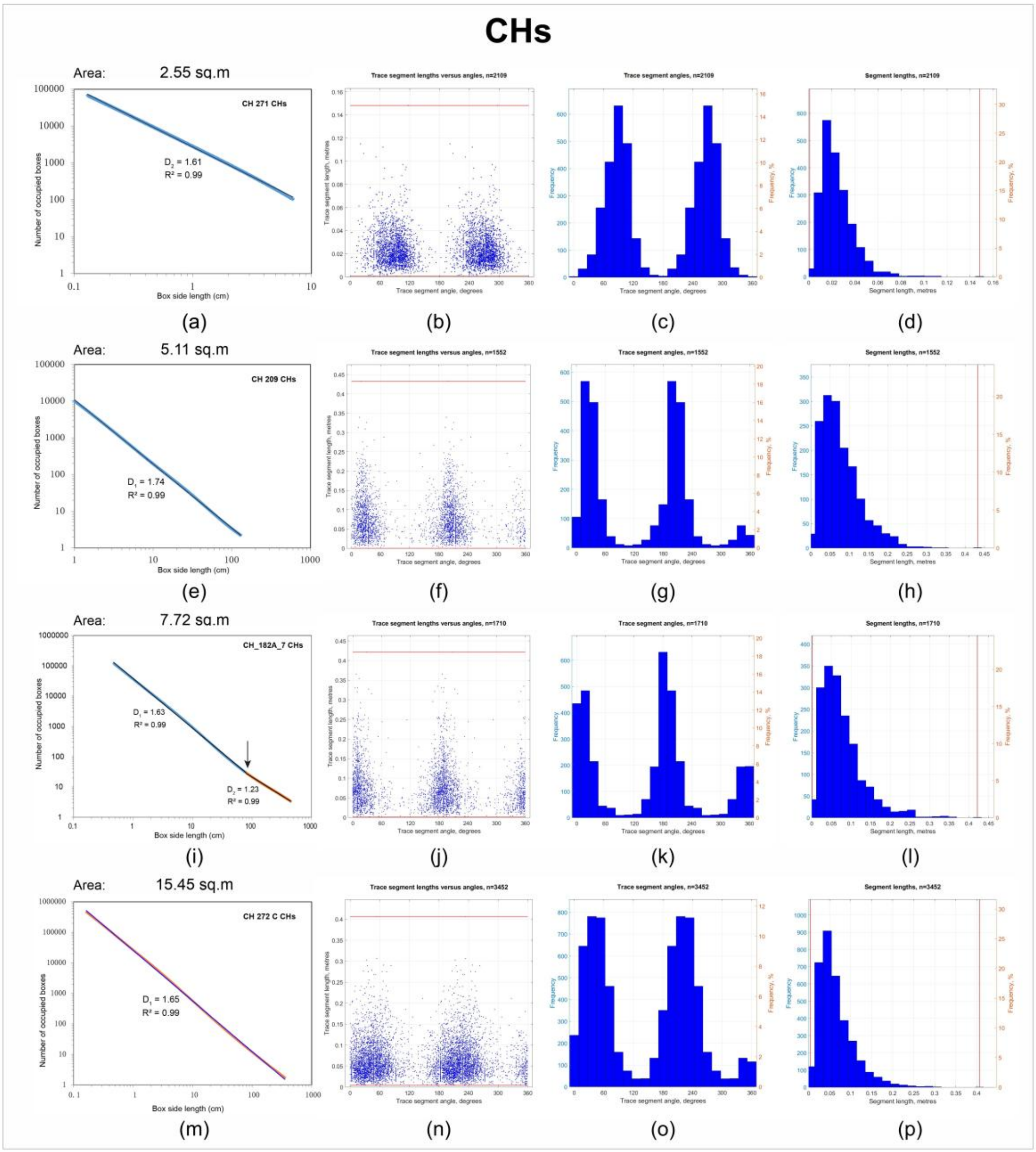

Fig. 6.14 Detection of the number of fracture-forming processes based on fractal analysis (2D box counting) for the CHs sector. The analysis has been conducted across scales on traced images of fracture networks captured photographically from 2D outcrop surfaces of granite. The first column **(a)**, **(e)**, **(i)**, **(m)** shows 2D box counting results for fracture networks conducted in increasing order of sampling area. Similarly, the second column **(b)**, **(f)**, **(j)**, **(n)** shows corresponding graphical results for fracture segment length vs. segment angle while the third **(c)**, **(g)**, **(k)**, **(o)** and fourth **(d)**, **(h)**, **(l)**, **(p)** columns show frequency plots of fracture segment angles and lengths, respectively. Note the similarity of fracture patterns recorded across different scales of observation in every sector which is also suggestive of their fractal nature.

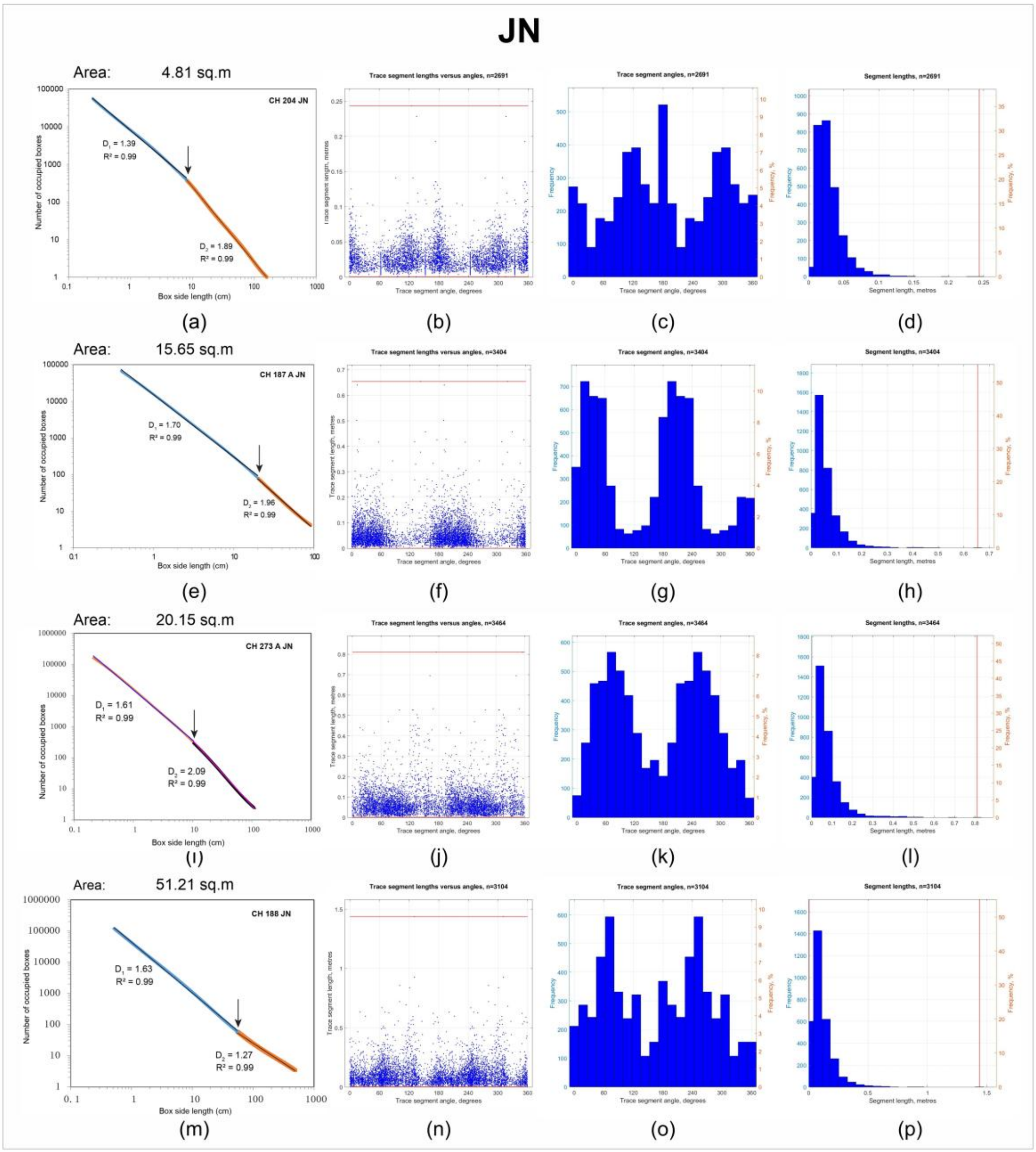

Fig. 6.15 Detection of the number of fracture-forming processes based on fractal analysis (2D box counting) for the JN sector. The analysis has been conducted across scales on traced images of fracture networks captured photographically from 2D outcrop surfaces of granite. The first column **(a)**, **(e)**, **(i)**, **(m)** shows 2D box counting results for fracture networks conducted in increasing order of sampling area. Similarly, the second column **(b)**, **(f)**, **(j)**, **(n)** shows corresponding graphical results for fracture segment length vs. segment angle while the third **(c)**, **(g)**, **(k)**, **(o)** and fourth **(d)**, **(h)**, **(l)**, **(p)** columns show frequency plots of fracture segment angles and lengths, respectively. Note the similarity of fracture patterns recorded across different scales of observation in every sector which is also suggestive of their fractal nature.

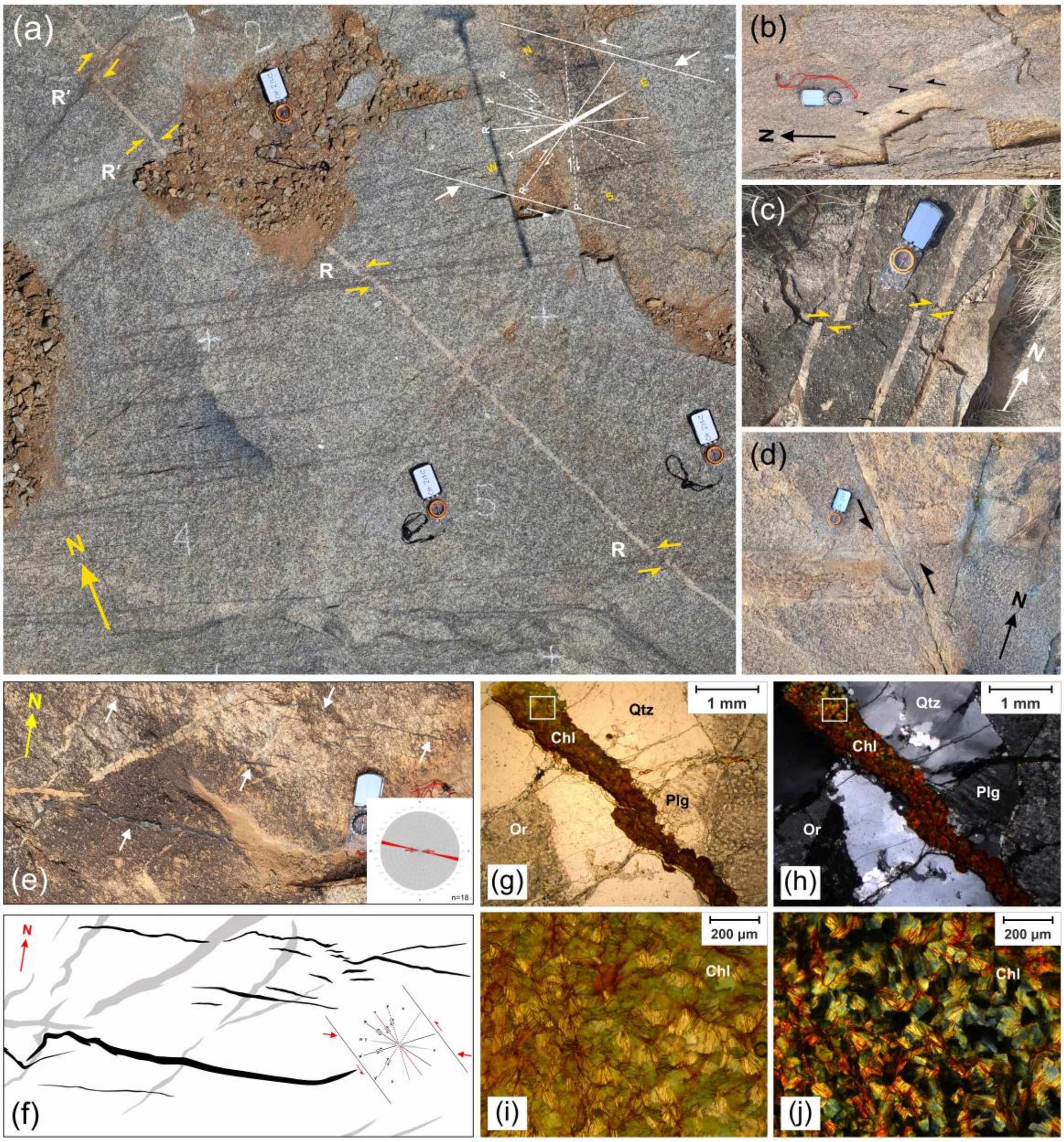

Fig. 6.16 Field and microscopic evidences in support of the proposed Riedel shear model. **(a)** shows a granite outcrop from the CHc sector where a pre-existing quartzo-feldspathic vein has been systematically offset by the later developed fractures. Note that the sense of displacements of the vein along differently oriented fractures, as indicated by yellow half-arrows, are in agreement with the proposed Riedel shear model for the sector which is shown in the inset diagram. **(b)**, **(c)** and **(d)** show field photographs of similarly displaced pre-existing quartzo-feldspathic veins by later developed fractures from the CHn, CHs and JN sectors respectively. Contd.

Fig. 6.16 Contd. **(e)** shows development of tensile fractures, identified by presence of tips at both ends, within a granite outcrop from the CHn sector, representing T (tensile, Mode-I) component of the Riedel shear model. The fractures are filled in by black-coloured veins (marked by white arrows) which cross-cut the earlier quartzo-feldspathic veins present within the granite. Inset figure presents orientation data of such black vein filled tensile fractures collected from the granite outcrop shown in the image. **(f)** shows traced counterpart of (e) with the earlier quartzo-feldspathic veins marked in grey colour and the later developed cross-cutting tensile fractures marked in black colour for clarity. The Riedel shear model for CHn sector is shown in the inset. **(g)** and **(h)** show photomicrographs in PPL and XPL respectively, revealing chlorite (Chl) as the black coloured vein mineral filling the tensile fractures within granite which is primarily composed of quartz (Qtz), orthoclase (Or) and plagioclase (Plg). **(i)** and **(j)** zoomed-in view in PPL and XPL respectively, of a portion of the chlorite vein marked by solid white boxes in (g) and (h) exhibiting undisturbed growth of spectacular chlorite flakes within the tensile fractures.

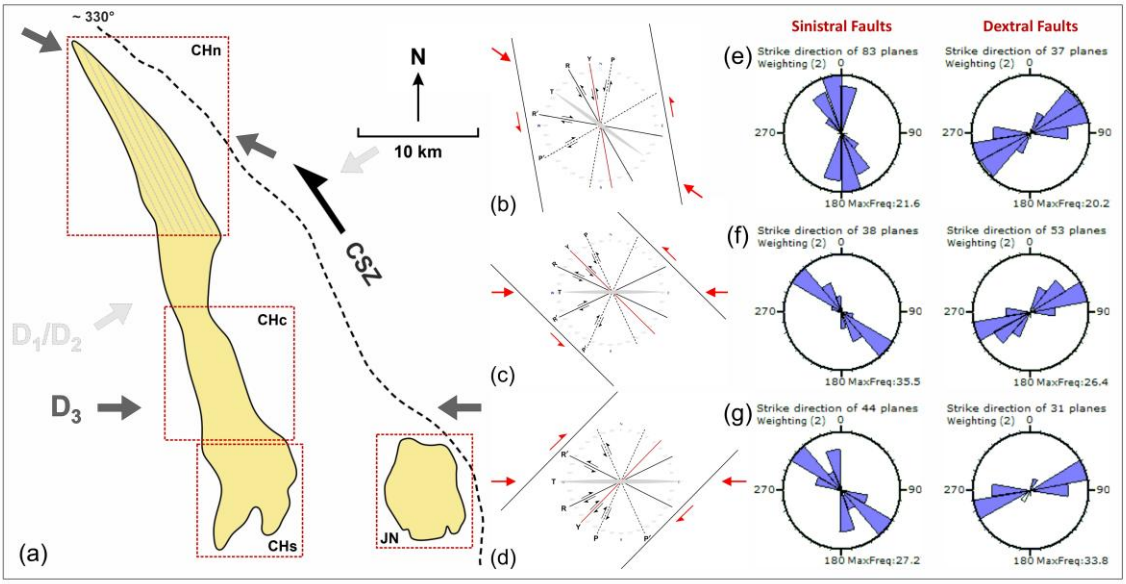

Fig. 6.17 Outline maps of the two younger granite plutons showing established paleostress orientations across the granite sectors. The earlier NE-SW oriented co-axial D_1/D_2 compression is shown in light grey colour whereas, the later D_3 compression, oriented ESE-WNW in the northern part to E-W in the southern part of the granite is shown in dark grey colour. **(b)**, **(c)** and **(d)** show the genetic Riedel shear models considering CSZ as the master shear boundary for CHn, CHc, CHS and JN sectors respectively. Bold red arrows mark the compression direction. Note the change in orientation of the boundary shear in the models in accordance with change in pluton margin orientation along which shear will be partitioned. **(e)** and **(f)** show fault-slip data collected from the CHn and CHc sectors and **(g)** shows the same for the CHs and JN sectors of the granite bodies (from Mondal et al., 2020).

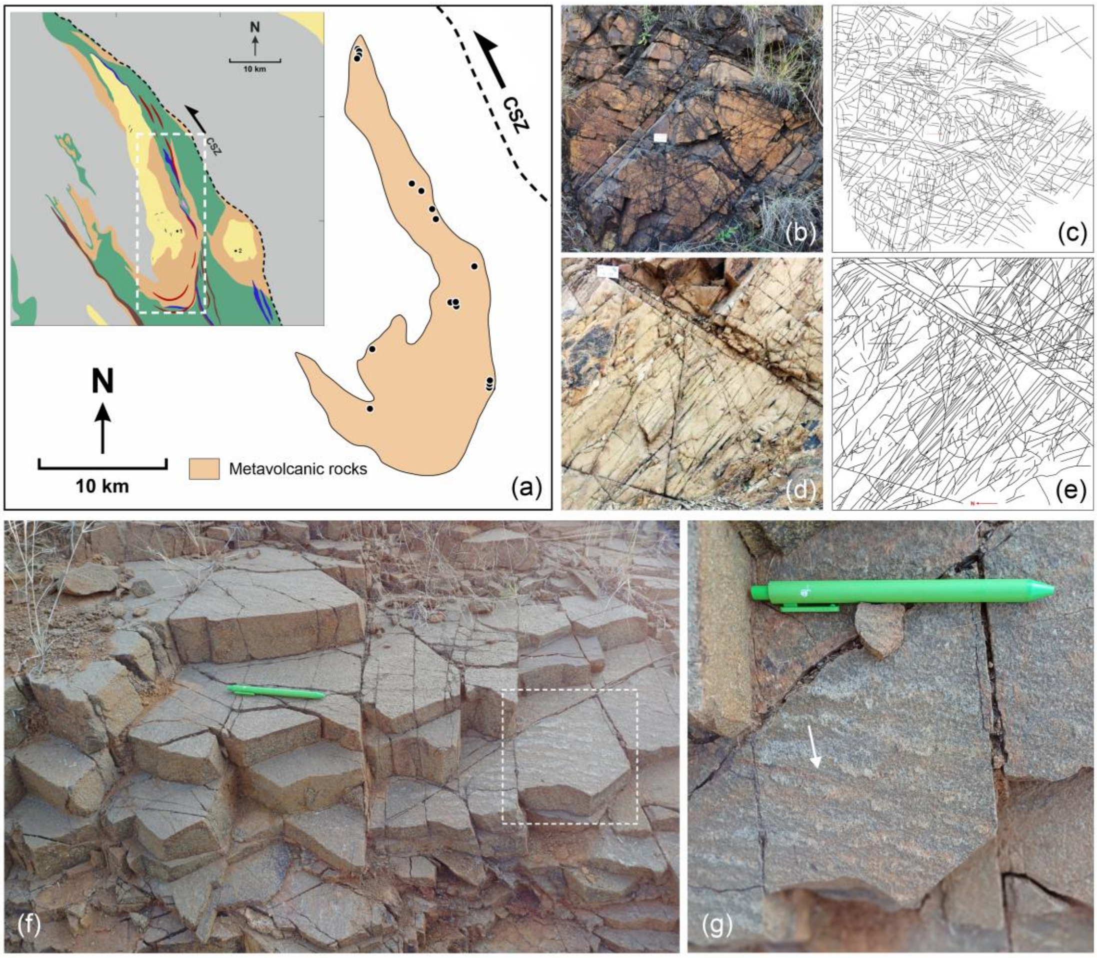

Fig. 6.18 (a) Outline map of the metavolcanic rock domain adjoining the younger granites of the CSB, in the Chitradurga region, showing the disposition of the study locations marked by black dots. Geological map of the study area, the central portion of the Chitradurga Schist Belt (CSB), is shown in the inset with the studied metavolcanic rock domain marked within white dashed box. Representative field photographs of fracture networks observed on sub-vertical outcrop sections of the metavolcanic rocks are shown respectively in **(b)** and **(d)** and their traced counterparts are shown in **(c)** and **(e)** respectively. The white card used as scale is 8.9 cm in length. **(f)** 3D outcrop view of the fracture networks developed within the metavolcanic rocks. The observed triangular and diamond-shaped rock blocks formed by systematic intersections of variably oriented fracture sets represent the characteristic fracture interaction within the metavolcanic rocks. **(g)** Close view of a sub-horizontal fracture surface (marked by white dashed box in f), showing evidence of slip along them delineated by the presence of oblique slicken lines and slickenfibres marked by solid white arrow. The pen used as scale is 14 cm in length.

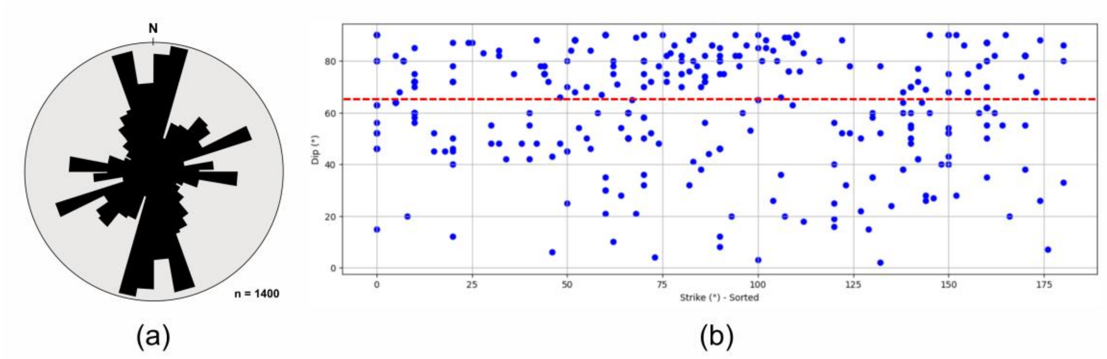

Fig. 6.19 (a) Rose diagram illustrating the dominant strike orientations of fracture planes in the metavolcanic rocks. **(b)** Plot of fault plane strike versus dip, showing a mean dip of ~ 65°, indicating that the faults are predominantly steeply dipping, with a minor proportion of low-angle faults.

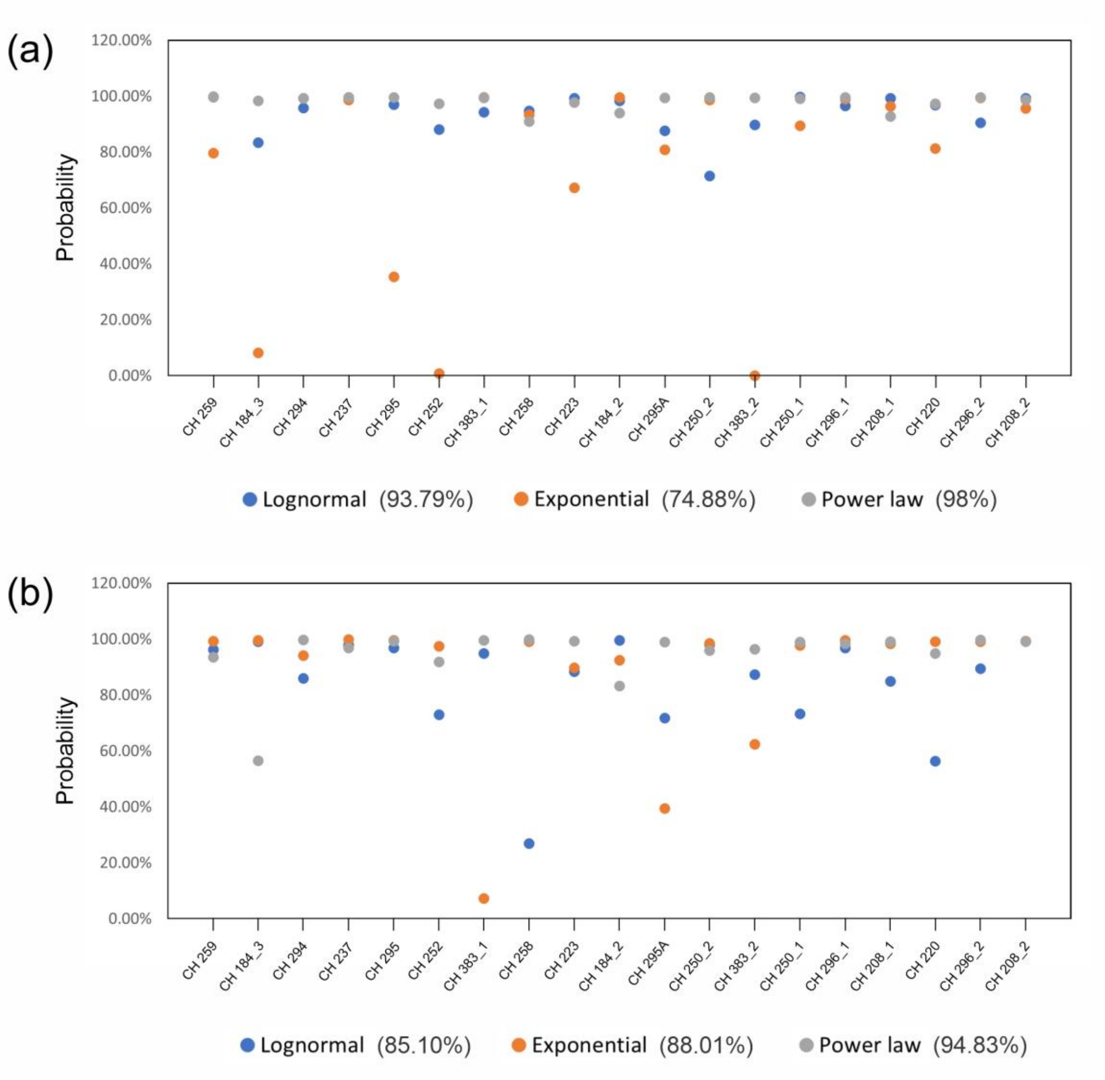

Fig. 6.20 Graphs showing the probability of fracture lengths being power law, exponentially or log-normally distributed as determined from Maximum Likelihood Estimate (MLE) analysis conducted in FracPaQ version 2.8. **(a)** shows the results for fracture trace lengths and **(b)** shows the same for fracture segment lengths. In both graphs, the sample location numbers across the entire range of observed scales have been plotted along the abscissa and corresponding values for probability of fracture length distribution are plotted along the ordinate. Note that in both cases probability for fracture lengths being power law distributed is the highest across every sector.

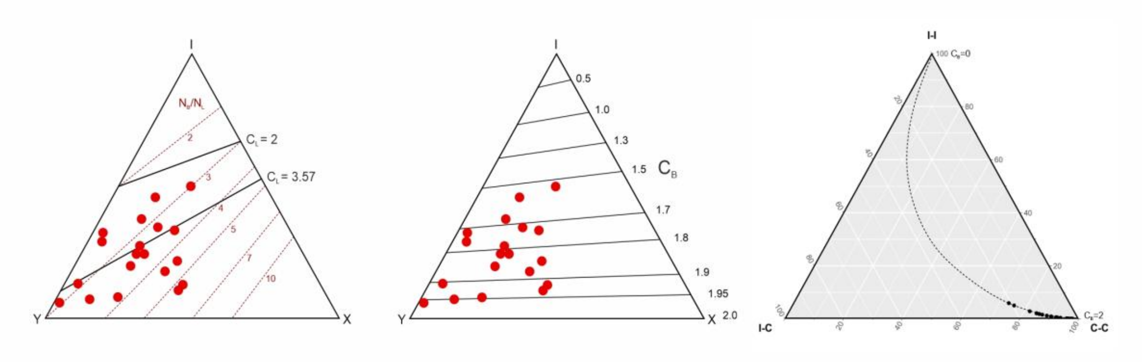

(a) (b) (c)

Fig. 6.21 Triangular plots for assessing fracture connectivity in the metavolcanic rocks. **(a)** shows fracture connectivity in terms of Connections per Line (C_L) and the ratio of Number of Branches (N_B) to Number of Lines (N_L) (N_B/N_L) within an I-Y-X ternary plot while **(b)** shows the same in terms of Connections per Branch (C_B). **(c)** shows branch classification plot representing proportions of different branch types (I-I, I-C, C-C) with numbers from 0 to 2 indicating the value for connections per branch (C_B). Note the dominance of Y nodes across all data points in (a) and (b) and, high C_B values consistently approaching 2 in (c). This indicates greater connectivity and therefore corresponding values of C_L exceeds the percolation threshold of $C_L = 3.57$ making the metavolcanic fracture networks fully connected, effectively allowing for regional-scale fluid migration or hydrothermal circulation.

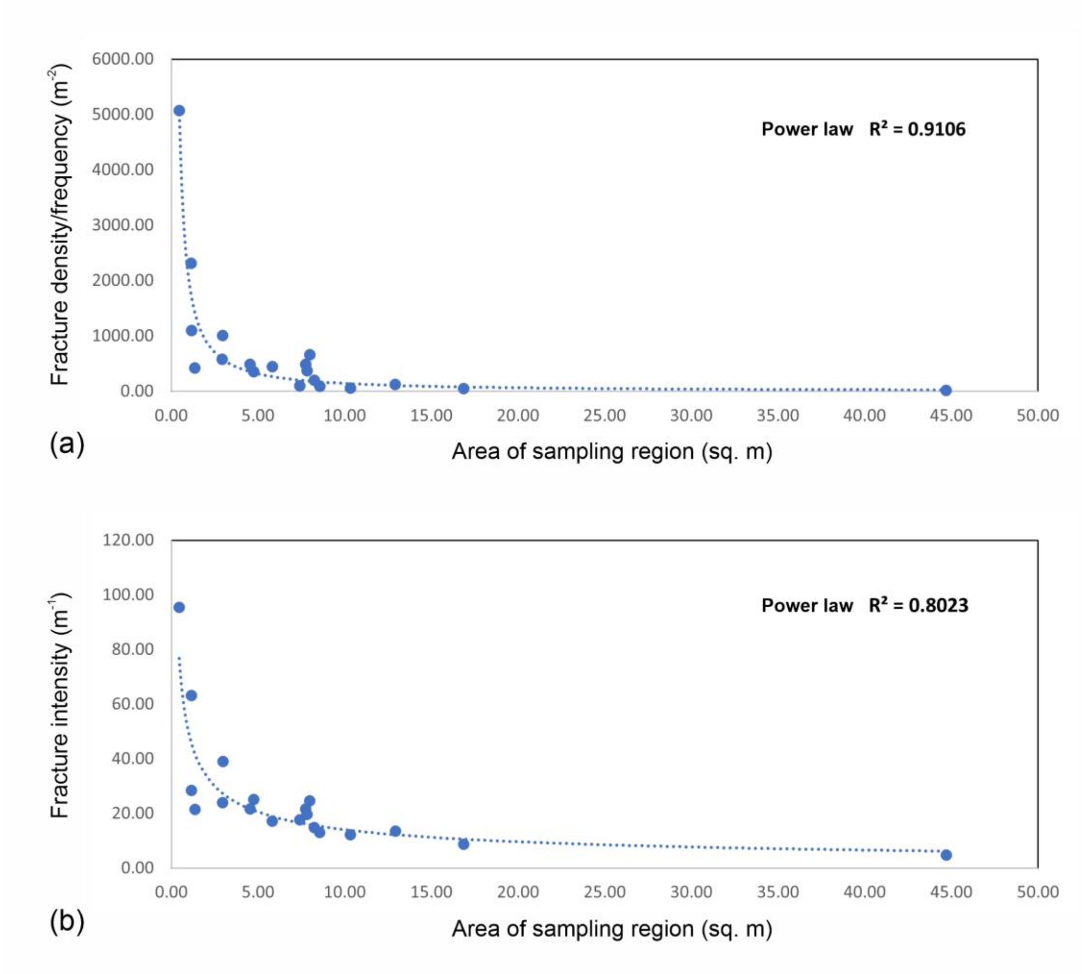

Fig. 6.22 Graphs showing **(a)** trend of fracture frequency/density (P_{20}) across the entire areal extent of sampling region and **(b)** shows the same for fractures intensity (P_{21}) in the metavolcanic rocks. Both fracture frequency/density and intensity show a decreasing trend with increasing sampling area with a very strong power law scaling. R^2 represents the correlation co-efficient.

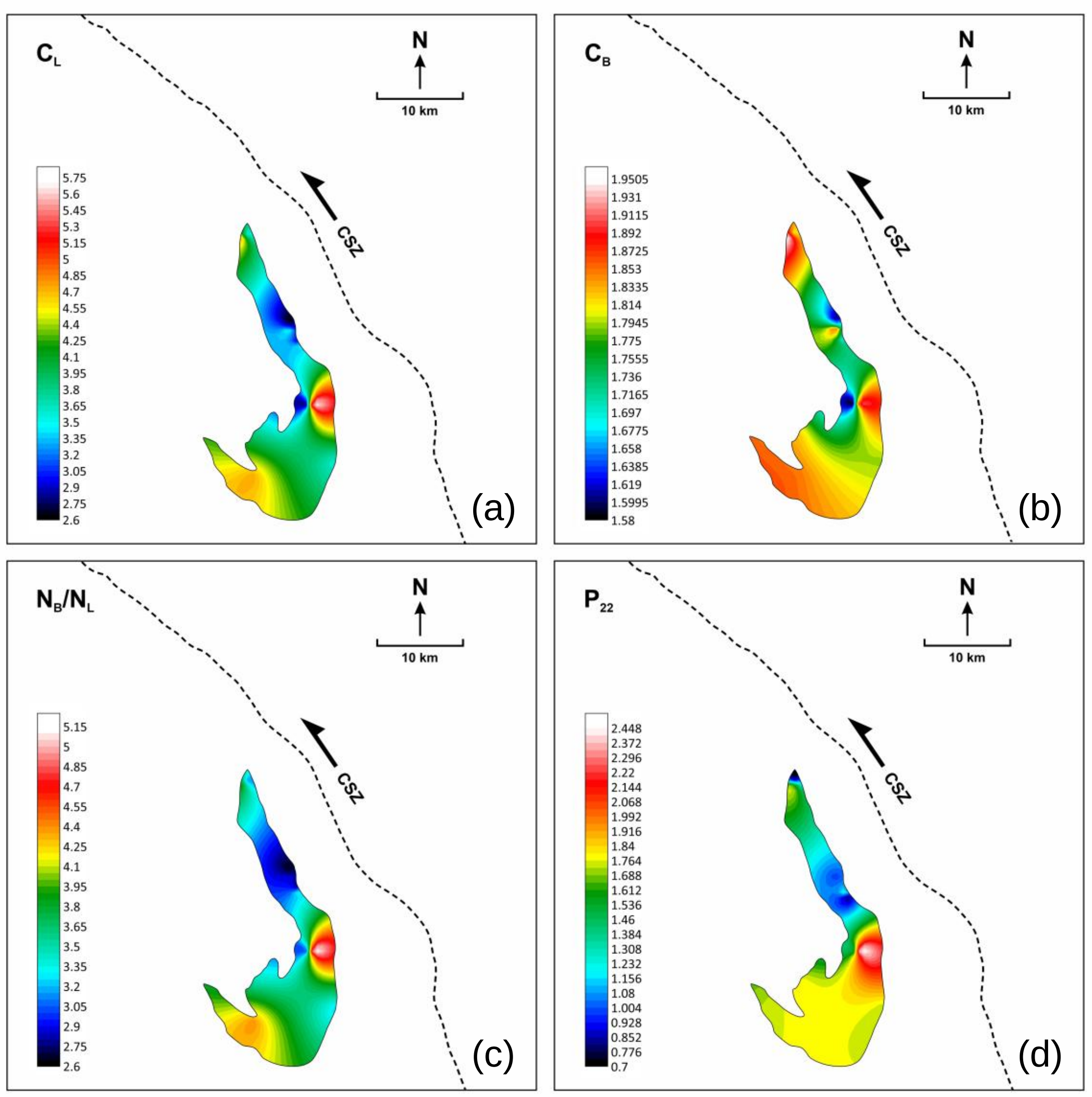

Fig. 6.23 Coloured contour maps of the metavolcanic rock domain adjacent to the younger granites of the CSB showing comparative spatial variations in fracture abundance and connectivity within the study area. Fracture connectivity defined by **(a)** Connections per Line (C_L) and **(b)** Connections per Branch (C_B) across the areal extent of the metavolcanic rocks. **(c)** shows the ratio of number of branches (N_B)/number of lines (N_L), which is an expression of the topology of the networks. **(d)** shows fracture abundance in terms of dimensionless intensity (P_{22}). Note the spatial consistency amongst all the four parameters showing greater fracture abundance and connectivity within the metavolcanic rocks marked in bright red colour.

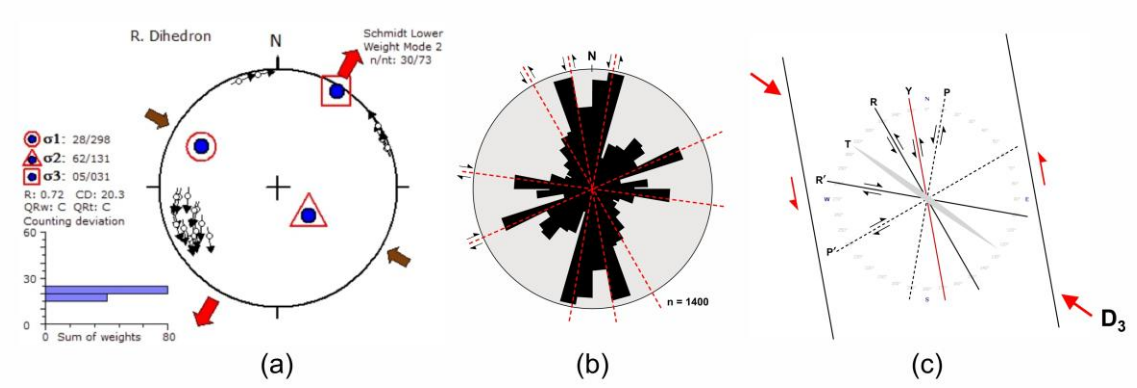

Fig. 6.24 (a) Paleostress analysis (using right dihedron method) of faults recorded in the metavolcanic rocks of the study area; for both left lateral and right lateral normal faults. Red arrow marks the extension direction and brown arrow marks the principal compression direction. Note that the NW-SE compression inferred from fault-slip analysis is consistent with the regional D_3 compression direction. The histogram shows the minimum values for counting deviation. *n* and *nt* are the number of data accepted for tensor calculation and total number of data respectively. R (stress ratio) = $(\sigma_2-\sigma_3) / (\sigma_1-\sigma_3)$ (from Bhowmick and Mondal, 2020). **(b)** The varied orientations of fractures planes can be interpreted as the development of Y, P, R, P′, R′, and T shears within a Riedel shear system, formed in response to NW-SE directed shortening associated with the late D_3 deformation of the region. n = number of data. **(c)** shows the corresponding genetic sinistral Riedel shear model considering CSZ as the master shear boundary activated during regional D_3 deformation. Bold red arrow marks the NW-SE oriented D_3 compression direction.

Attribute	Granites	Metavolcanics	Observations
Node proportions	**I**: 45 - 54%, **Y**: 30 - 36%, **X**: 15 - 19% (sector dependent)	**I**: 26.25%, **Y**: 56.46%, **X**: 17.29%	Granites show higher proportion of I nodes, metavolcanics are dominated by Y nodes, indicating more branching.
N_B/N_L ratio	2.47 - 2.90 (sector dependent)	3.48	Metavolcanics have higher branching per line than granites, indicating more complex network topology.
Connections per line (C_L)	2.23 - 2.80 (sector dependent)	3.88	Metavolcanics exceed the percolation threshold (CL = 3.57), suggesting more interconnected networks than granites.
Connections per branch (C_B)	1.48 - 1.60 (sector dependent)	1.81	Metavolcanics exhibit higher connectivity at the branch level.
Branch types (P_{II}, P_{IC}, P_{CC})	**P_{II}** - 5 to 9% **P_{IC}** - 18 to 23% **P_{CC}** - 67 to 76% (sector dependent)	**P_{II}** - 1.39% **P_{IC}** - 9.14% **P_{CC}** - 89.47%	Metavolcanic networks are dominated by completely connected branches, while granites have a mix of isolated, partially, and fully connected branches.
Fracture abundance (P_{20}, P_{21}, P_{22})	**P_{20}** - 123 to 407 m^{-2} **P_{21}** - 11 to 23 m^{-1} **P_{22}** - 0.80 to 1.61 (sector dependent)	**P_{20}** - 733 m^{-2} **P_{21}** - 25.57 m^{-1} **P_{22}** - 1.45	Metavolcanics are characterized by significantly higher fracture density (P_{20}), while their fracture intensity (P_{21}) and dimensionless intensity (P_{22}) are comparable with those of the granites.
Spatial consistency	Sectoral variations in topology and connectivity	Uniform topology and connectivity across all outcrops	Metavolcanic networks show more uniform, coherent connectivity compared to sectorally variable granite networks.

Table. 6.1 Summary table for the comparison of key topological and thereby connectivity attributes of the fracture networks observed in the younger granites and metavolcanic rocks of the study area.

Chapter 7: Discussion and Conclusions

CHAPTER 7

Discussion and Conclusions

7.1 Introduction

From the detailed observations, investigations, analyses and discussions elaborated in the preceding chapters, it is evident that the studied terrain in the Chitradurga Schist Belt (CSB), Western Dharwar Craton (WDC), southern India, records a distinct and pervasive brittle deformation phase in its tectonic evolution, which is manifested through the development of characteristic brittle structures in different lithologies of the region. As outlined, these brittle structures are primarily represented by quartz veins, mafic dykes, and the development of fracture networks that are intimately linked to fault activity and their strong mutual interactions. The structures are most prominently developed in the younger granites and metavolcanic rocks of the CSB, where they constitute the dominant suite of brittle features. In contrast, the metasedimentary sequences of the region exhibit a conspicuous absence of such pervasively developed brittle structures, except for sporadically developed joint planes. This contrasting behavior highlights the critical role of inherent rock rheology in governing the response of different lithologies to externally imposed stresses during late stages of deformation. The variation in structural development thus provides important insights into the concept of mechanical stratigraphy within the terrain.

Among the various vein systems observed in the rocks of the region, the quartz veins, developed extensively and consistently within the metavolcanic sequences, are particularly diagnostic. These veins have been interpreted as products of *fault-valve* mechanism, whereby pre-existing anisotropies such as foliations, faults, and fractures were episodically reactivated under variable fluid pressure conditions, during the late stages of D_3 deformation, enabling cyclic fluid flow and vein emplacement (Bhowmick and Mondal, 2020; 2021). The present study quantifies the minimum number of such fluid pressure events from statistical analysis of heterogeneous vein data distribution patterns and also quantifies the magnitude of those pulses. These veins represent the dominant brittle structure in the metavolcanic rocks and preserve a robust record of fluid-assisted deformation. However, as discussed earlier (Chapter 3), other vein types are also present, most notably the quartzo-feldspathic veins, quartz veins and the chlorite veins observed within the younger granites. Although these granite-hosted veins are relatively less pervasive compared to the quartz veins in the metavolcanics, their occurrence is consistent and therefore remain of significant tectonic importance, providing critical constraints on the broader brittle tectonic history of the terrain.

Mafic dykes intruding the younger granites of the CSB also record a complex history of emplacement and subsequent deformation. Structural and microscopic evidence indicates two generations of dolerite dykes, both belonging to the newer dyke swarm that intruded the ~ 2.61 Ga younger granites at the upper stratigraphic levels of the CSB. Magma overpressure estimates further reveal two distinct depth ranges of dyke emplacement; a deeper level at ~ 20-25 km and a shallower level at ~ 9-13 km corroborating the interpretation of episodic dyke injection within the younger granites of the schist belt. As interpreted from the study of outcrop attributes, the initial intrusion of these dykes occurred as NNE-SSW to NE-SW oriented magma-driven extension fractures under the broadly NE-SW directed D_1/D_2 far-field compression. Subsequently, with the onset of E-W to ESE-WNW directed D_3 compression, the dykes were subjected to sinistral shearing, as reflected in their NNW-SSE oriented continuous to discontinuous en echelon outcrop patterns, testifying to their structural modification under mixed loading condition in response to the evolving stress field of the terrain.

The fracture networks observed within the granites and metavolcanic rocks of the CSB similarly highlight the regional tectonic control on brittle deformation. These are interpreted as the product of intense fault activity associated with a regional-scale Riedel shear system, which developed through the activation of sinistral shear along the NW-SE oriented Chitradurga Shear Zone (CSZ) during D_3 deformation, under the same E-W to ESE-WNW compressional stress regime that modified the dykes. These fractures networks not only define the brittle structural architecture of the terrain but also reflect the kinematic coherence of the brittle features across the different lithologies of the schist belt, all developed under the same regional shear system.

Taken together, the evidence from veins, dykes, and fracture networks converges to a consistent picture; the study area within the CSB underwent a well-defined brittle deformation phase during the protracted D_3 deformation event. This brittle phase, variably manifested in the younger granites, metavolcanic, and metasedimentary rocks, depending on immanent lithological rheology, is central to reconstructing the tectonic evolution of the study area. A comprehensive understanding of brittle deformation in the CSB therefore requires that these structures: all veins, dykes, and fracture networks, be examined in concert. Their spatial distribution, mutual cross-cutting relations, and relative temporal development together form the basis for deciphering the sequential evolution of brittle deformation in the region. Such an integrated approach is essential for constructing a coherent brittle tectonic evolution model for the study area.

7.2 Spatial interrelations and temporal evolution of brittle structures

The brittle structures preserved within the younger granites and metavolcanic rocks of the CSB exhibit a clear spatial distribution and relative temporal succession, reflecting the progressive evolution of brittle structures under changing stress regimes of the region. Based on mutual cross-cutting relationships observed in the field, the earliest brittle structures recognized within the younger granites are the quartzo-feldspathic veins. These veins which are meter scale in length and centimeter scale in thickness, dominantly trend NW to NNW, occurring particularly along the pluton margins **(Fig. 7.1a; Fig. 3.1e** of Chapter 3**)**. Microscopic examination reveals that these veins are dominantly aplitic in composition (fine-grained granite) **(Figs. 7.1b and c)**. Their spatial association with the contacts between the younger granites and the older TTG gneisses provides important insights into their origin. The ~ 2.61 Ga younger granites of the CSB are widely regarded as products of crustal reworking of the earlier TTG gneisses (Naqvi and Rogers, 1987; Meert et al., 2010) which, in the study area, have syn-tectonically intruded the greenstone sequences during the D_2 deformation phase (Jayananda, 2006). The concentration of aplitic veins near granite-TTG contacts suggests that they might represent residual melts expelled during the final stages of granite crystallization from the TTGs (Kumar, 2014; Glazner et al., 2020). Such residual melts, being highly mobile and fluid-saturated, tend to accumulate at the margins or upper levels of the crystallizing pluton (John and Stünitz, 1997; Vanderhaeghe, 2001; Weinberg, 2006). Eventually, they can be injected into the contact zones or through favourably oriented pre-existing structural anisotropies as aplitic dykes and veins. Their fine grain size reflects rapid cooling within these narrow conduits, while their composition remains broadly similar to the parent granite.

Field relationships further corroborate this model. Patches and enclaves of older TTG gneisses are observed to be preserved within the granites at sites where aplitic dykes occur, particularly near the pluton margins **(Figs. 7.2a and b)**, implying that the emplacement of these late-stage melts exploited weaknesses at granite-TTG contacts. Additionally, the dominant and systematic NW-SE to NNW-SSE orientation of these steeply dipping aplitic veins **(Fig. 7.1a)** is consistent with the foliation imparted to the granites during NE-SW directed D_1/D_2 compression, indicating that the emplacement of the aplites was strongly controlled by pre-existing structural anisotropy. A minor subset of aplite veins, emplaced in NNE-SSW to NE-SW orientations sub-parallel to the D_1/D_2 far-field compression, are now preserved in folded geometries with NW-SE trending axial planes **(Fig. 7.3)**. This observation further substantiates that their intrusion took place during the progressive D_2 phase, exploiting pre-existing planes of anisotropy within the granitic host. On the basis of present field relationships, the aplitic veins within the younger granites can therefore be best interpreted as late-stage residual melts segregated from the granites during their crystallization, with their emplacement preferentially localized along structural anisotropies and at contacts with the older TTG crust. Nevertheless, definitive confirmation of this interpretation requires further petrological and geochemical characterization.

Contemporaneous with this D_1/D_2 stress regime, by the time the granites have solidified to a considerable extent, mafic dykes were initially emplaced within the younger granites as NNE-SSW to NE-SW trending magma-driven extension fractures, representing the earliest phase of dyke emplacement in the granites. Field relationships further demonstrate that these mafic dykes cross-cut the aplitic veins **(Fig. 7.5c)**.

The aplitic veins are cross-cut by quartz veins, which are generally smaller in dimension (cm scale) and display a consistent ENE-WSW orientation across the plutons **(Fig. 7.4)**.

Their systematic distribution and termination at well-defined tips indicate their formation as dilatational fractures. These quartz veins themselves are subsequently cross-cut by chlorite veins, which have been interpreted as the tensile (T) component of the regional Riedel shear system **(see Figs. 6.16 e and f;** Chapter 6**)** developed through sinistral shearing along the Chitradurga Shear Zone (CSZ) during D_3 deformation of the terrain, under an E-W to ESE-WNW directed far-field compression (as discussed in Chapter 6). The systematic displacement of both quartz and aplite veins by individual fault planes constituting the fracture networks further corroborates the Riedel shear model **(Figs. 7.5a and b)**. Although pervasive fracture networks are not well-developed within the granites in the vicinity of the mafic dykes, discrete fracture planes are observed transecting the dykes, thereby constraining their relative temporal sequence **(Fig. 7.5d)**. The timing of chlorite vein emplacement is significant, as such tensile fractures may typically form in the later stages of Riedel shear system evolution, when slip along existing fault planes is impeded and strain accommodation necessitates the opening of tensile mode fractures. As discussed earlier (Chapter 6), this is also evidenced by the pristine, undeformed growth of chlorite flakes within the fracture filling veins, as observed under microscope, indicating the terminal phases of brittle tectonism in the terrain. **(see Figs. 6.16 g, h, i, j;** Chapter 6**)**.

The same regional-scale Riedel shear system is also reflected in the fracture networks developed within the metavolcanic rocks (as discussed in Chapter 6), underscoring the regional control and kinematic consistency of brittle features across lithologies.

Contemporaneous to this phase, as D_3 deformation progressed, the mafic dykes that were initially emplaced during D_1/D_2 phase, were subjected to sinistral shearing, producing segmented or continuous en echelon geometries trending broadly NNW.

Their present disposition reflects mixed mode I-III loading under the reoriented regional stress field (as discussed in Chapter 5).

During the late stages of D_3 deformation, pre-existing anisotropies, including foliation, faults, and fractures, were repeatedly reactivated in the metavolcanic sequences under fluctuating fluid pressure conditions, facilitating the emplacement of extensive quartz vein systems. Although the source of the silica-enriched fluids remains uncertain; however, it is plausible that residual magmatic fluids from the adjacent granitic plutons were mobilized and channelized along pre-existing fractures. Episodic pulses of elevated fluid pressure exploited these weaknesses, producing mesh-like networks of quartz veins that constitute the most pervasive brittle structure in the metavolcanic rocks of the CSB (as discussed in Chapter 4). Therefore, taken together, the sequential evolution brittle structures within the studied area of the CSB can be summarized into the following stages **(Fig. 7.6)**:

Stage 1: Development of NW to NNW trending pervasive fabric (regional trend of foliation) within the greenstone sequences of the CSB on account of early NE-SW directed D_1/D_2 co-axial far-field compression.

Stage 2: Syn-tectonic granite emplacement during D_2 deformation. Intrusion of aplitic veins in the younger granites guided by NW to NNW trending foliation planes (pre-existing anisotropy in the granites, induced by NE-SW directed D_1/D_2 co-axial compression), with folded NE-NNE subsets confirming structural control **(Fig. 7.6a)**.

Stage 3: Intrusion of mafic dykes within the granites as NNE-SSW to NE-SW trending magma-driven extension fractures during ongoing D_2 deformation phase **(Fig. 7.6b)**.

Stage 4: Development of ENE-WSW oriented quartz veins that cross-cut the aplitic veins, formed as dilatational fractures, during late D_2 phase **(Fig. 7.6c)**.

Stage 5: Initiation of systematic fault networks as part of the D_3 regional Riedel shear system under E-W to ESE-WNW compression in both the granites and metavolcanic rocks **(Fig. 7.6e)**. Contemporaneous sinistral shearing and segmentation of the mafic dykes in the granites, producing systematic en echelon outcrop geometries under mixed Mode I-III loading **(Fig. 7.6d)**.

Stage 6: Intensification of the fracture networks and development of chlorite veins as the tensile (T) components of the regional Riedel shear system **(Fig. 7.6f)**. Late-stage (late D_3) fluid-assisted reactivation of pre-existing anisotropies and fractures in the metavolcanic sequences, generating the pervasive quartz vein system in the metavolcanic rocks **(Fig. 7.6g)**.

This succession illustrates the protracted sequence of brittle tectonics associated with evolving stress fields under different deformation phases of the CSB within the study area, and highlights the interplay between pre-existing anisotropies, magmatic processes, fluid-assisted reactivation and regional stress regimes in controlling the brittle tectonic architecture of the terrain.

7.3 Conclusions

The present study focuses on the conspicuous development of brittle structures across diverse lithologies in the Chitradurga region of the Chitradurga Schist Belt (CSB), Western Dharwar Craton (WDC), southern India. It aims to investigate the genesis, evolution, and structural characterization of these brittle features within the broader tectonic framework of the region. The CSB represents a classic Archean granite-greenstone terrain, and the lithologies examined in the study area are broadly categorized into three groups: the ~ 2.61 Ga younger granites, and the older metavolcanic sequences, and metasedimentary successions of the schist belt. Distinct suites of brittle structures identified across these lithologies offer key insights into the late-stage structural evolution of the cratonic block. The methodology employed to investigate the brittle structures integrates detailed field observations, structural analyses, statistical modeling, and innovative mathematical approaches. Together, these methods constrain the episodicity and magnitudes of fluid-pressure pulses from vein data distributions, estimate magma overpressure, depth of origin and emplacement mechanisms from dyke outcrop dimensions and attributes, and unravel the genetic architecture and connectivity of brittle fault-fracture systems developed extensively in the rocks of the region. Collectively, these findings provide a robust framework for understanding the brittle tectonic evolution of the studied terrain and how magmatism, fluid flow, and brittle faulting interacted to shape the mechanical architecture of the CSB, offering critical insights into the dynamics of late-stage craton stabilization processes. The principal outcomes of the study are summarized as follows:

1. The study area in the CSB preserves a distinct brittle deformation phase within its tectonic history. The plethora of brittle structures observed in the area has been broadly classified into three categories: (i) the development of various vein systems, most notably the pervasive quartz veins emplaced within the metavolcanic rocks of the region; (ii) mafic dykes intruding the younger granites; and, (iii) interconnected fracture networks strongly associated with fault activity that affected both the granites and metavolcanic sequences. These structural features are most extensively developed within the younger granites and metavolcanic rocks, where they collectively constitute the dominant brittle architecture of the terrain.

2. In contrast, the metasedimentary sequences of the CSB exhibit only sporadically developed joint sets and lack the pervasive development of brittle structures observed in the two other rock types. This contrast highlights the crucial role of inherent rock

rheology in modulating the response of different lithologies to external stresses, thereby emphasizing the significance of mechanical stratigraphy in controlling the structural evolution of a terrain during the late stages of deformation.

3. Statistical methods involving fuzzy clustering of vein orientation data, supported by deterministic approach of scaled 3D Mohr circle analysis, identified discrete fluid pressure (P_f) events and their representative magnitudes from heterogeneous quartz vein data distribution patterns recorded from the metavolcanic sequences of the CSB. Two P_f events of higher fluid pressure magnitudes are recognized in the Gadag region, in the northern part of CSB (maximum P_f variation, $\Delta P_f \sim 36.25$ MPa), suggesting near-lithostatic P_f conditions, favourable for thick vein development with prospects for gold mineralization, whereas, three relatively lower magnitude fluid pressure events are identified in the Chitradurga region ($\Delta P_f \sim 11.67$ MPa), reflecting multiple fluid pulses generating intense mesh-like networks of relatively thinner veins.

4. Two novel mathematical methods have been formulated to retrieve complete dyke dimensions (full length and maximum opening displacement or width) from their partial exposures, thereby significantly improving the recovery of near-true dyke parameters from limited exposures. The first method applies to partial dyke outcrops featuring at least one exposed tip, while the second method addresses dyke outcrops with no visible tips. Both methods, validated against field and published datasets, provided robust estimates of magma overpressure (~ 27-72 MPa), and emplacement depths (~ 9-25 km), when applied to partially exposed mafic dykes observed within the younger granites of the CSB along with stress intensity factors for the host granite (~ 132-689 MPa/m^2).

5. Structural analysis of outcrop attributes revealed that mafic dykes intruding the younger granites of the Dharwar Craton often record hybrid Mode I-III emplacement

rather than pure opening-mode intrusion. A comprehensive model for the progressive spatio-temporal evolution of dykes under mixed Mode I-III loading is developed, wherein incremental orders of dyke horn formation, continuous curved geometries, and bridged dyke segments are effectively explained. Based on field and microscopic investigations, two dyke generations are recognized within the ~ 2.61 Ga younger granites of the Chitradurga Schist Belt, reflecting episodic magmatism corroborating the variation in emplacement depth estimates.

6. A geological model for dyke emplacement and evolution within the younger granites of the CSB has been proposed, in which, the dykes were initially emplaced as NNE-SSW to NE-SW extension fractures during NE-SW directed D_1/D_2 co-axial compression and were later sinistrally sheared into NNW trending characteristic en echelon geometries suggestive of mixed mode I-III loading conditions, under the influence of the adjacent NW-SE trending Chitradurga Shear Zone, (CSZ), which activated during D_3 deformation of the region, on account of an E-W to ESE-WNW directed compressive stress field.

7. Fracture networks in both granites and metavolcanic rocks display fractal organization and power-law scaling, indicating self-similar and scale-invariant processes governing their formation. The fracture networks are interpreted as products of fault interaction developed primarily through a regional scale sinistral Riedel shear system associated with the activation of the Chitradurga Shear Zone (CSZ) during D_3 deformation of the terrain under E-W to ESE-WNW directed far-field compression. The granites exhibit spatial variations in fracture network geometry, topology, and connectivity, reflecting the complex interplay of tectonic forces, deformation patterns, textural heterogeneity, and inherited structures in governing their fracture development, with connectivity generally below the percolation threshold (C_L = 3.57), with some

sectors showing greater connectivity. In contrast, metavolcanic rocks preserve uniformly well-connected networks throughout the study area ($C_L = 3.88$ > percolation threshold), dominated by fully connected branches (P_{CC} ~ 89%), representing effectively interconnected fluid pathways at the scale of observation. These contrasting fracture attributes between the respective lithologies exerts a first-order control on fluid flow and mineralization. Metavolcanic rocks form consistently permeable conduits for hydrothermal circulation, whereas the granites provided locally efficient pathways, particularly along shear zone-proximal sectors. Such structural controls align with known gold and base metal sulphide mineralization in the CSB and highlight the potential of the younger granites as prospective hosts where fracture connectivity is high and spatially associated with shear zones.

8. The spatial interrelations of brittle structures in the study area has been integrated into a coherent brittle tectonic evolution model for the CSB, reconstructed from mutual field cross-cutting relationships and following is the sequence: intrusion of NW-SE to NNW-SSE oriented aplitic veins along granite-TTG contacts guided by pre-existing structural anisotropy (foliation) of the granites; emplacement of mafic dykes in the granites as NNE-SSW to NE-SW oriented extension fractures during D_1/D_2 compression; development of cross-cutting ENE-WSW oriented quartz veins in the granites during late D_2 phase; initiation of regional fracture networks in the granites and metavolcanic rocks under D_3 sinistral Riedel shear system; contemporaneous dyke segmentation into sinistral en echelon patterns under mixed Mode I-III loading; intensification of the fracture networks and development of chlorite veins as tensile elements of the Riedel shear system; and final reactivation of pre-existing anisotropies in the metavolcanic rocks under elevated fluid pressure conditions during late D_3 generating the pervasive quartz vein systems within the metavolcanic rocks.

This temporal progression underscores the combined influence of pre-existing anisotropy, magmatism, fluid overpressure, and evolving stress regimes in constructing the brittle tectonic architecture of the terrain, with implications extending beyond tectonic reconstructions to mineral exploration, management of waste repositories, permeability assessment, and Archean crustal mechanics.

7.4 Scope for future work

This comprehensive study examined the brittle structures, represented by veins, dykes, and fracture networks within the major lithologies of the Chitradurga Schist Belt (CSB), in the Chitradurga region of Western Dharwar Craton (WDC), southern India, constraining fluid pressure episodes and magnitudes from veins, estimates of magma overpressure and emplacement depths from dykes, and the origin, evolution, and characterization of fracture networks in the granites and metavolcanic rocks of the region. From their collective synthesis, the present study has established a structural and temporal framework for brittle tectonic evolution of the studied area in the CSB. However, certain petrological and geochemical aspects remain unresolved which can significantly augment the structural investigations. Addressing these aspects through targeted future investigations would not only refine the current structural interpretation but also shed light on the petrogenetic and tectonic processes that governed the brittle evolution of the terrain. Future work may be directed along the following lines:

a. Petrological and geochemical study of the aplitic veins in relation to the host granites and adjacent TTGs

Such investigations could confirm whether the aplites represent residual melts expelled during late-stage granite crystallization or whether their compositions record significant assimilation from the older TTG crust. This will refine models of melt segregation, differentiation, and host-pluton interaction during syn-tectonic granite emplacement.

b. Geochemistry and high resolution microscopy of the fracture-filling minerals (quartz, chlorite etc.)

Detailed mineral chemistry and geochemical analyses of fracture-filling quartz and chlorite veins can elucidate the physicochemical conditions of vein formation and the nature of the associated fluid sources. High-resolution microscopy can further resolve crystal growth orientations. Together, these approaches will refine constraints on the timing of mineral precipitation relative to deformation, thereby clarifying the temporal relationship between fluid flow and tectonic processes.

c. Fracture network characterization in the BIFs and tuffs observed in the CSB

Quantitative network analysis in these lithologies, which have not been addressed in the present study, can determine whether fracture propagation followed the same stress field responsible for brittle deformation in the granites and metavolcanics or whether they preserve distinct, lithology-controlled signatures. This will advance understanding of how mechanical heterogeneity governs fracture evolution across the belt.

d. Origin of the discrete joint sets developed within the metasedimentary sequences of the CSB

By integrating structural analysis, microstructures, and paleostress reconstructions, the genesis of these joint systems can be assessed. Clarifying whether they are products of far-field regional stress, exhumation related stress relaxation, or localized deformation during basin inversion, will offer insights into the tectonic regime prevailing during and after sedimentation.

e. Petrological, geochemical, geochronological, and magnetic studies of the mafic dykes intruding the younger granites of the CSB

Comprehensive investigation of the mafic dykes can constrain deeper crustal or mantle source characteristics, magma differentiation, and crustal interaction processes. Magnetic fabric studies may further clarify emplacement dynamics and kinematic regimes. Together, these investigations can refine the temporal framework of dyke activity and link it to regional tectono-magmatic pulses in the evolution of the Dharwar Craton with relation to global correlation of Archean cratonic blocks.

By integrating these future investigations, it will be possible to develop a more robust, multi-scale understanding of how brittle deformation, fluid activity, and magmatism interacted to shape the crustal architecture of the Chitradurga Schist Belt. Such studies would not only enhance the interpretations made in this work but also contribute significantly to broader models of craton stabilization and Late-Archaean tectonics.

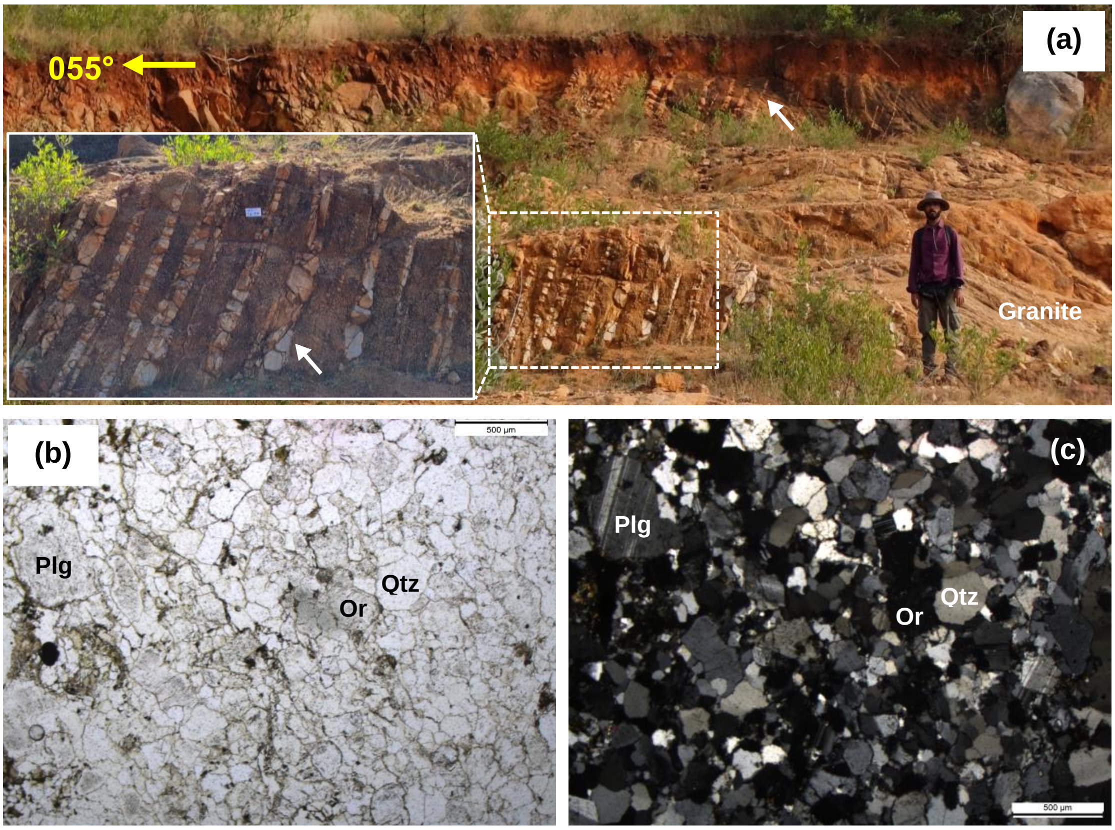

Fig. 7.1 (a) Field photograph showing the disposition of aplitic veins intruding the younger granites. The veins strike NW and dip steeply (~ 78-80°) towards NE. The inset highlights the closely-spaced, parallel, and systematic nature of the intrusions. White arrows indicate the aplitic veins. **(b)** and **(c)** show photomicrographs of the aplite veins under PPL and XPL, respectively. Note the fine-grained granitic texture, with quartz (Qtz), orthoclase (Or), and plagioclase (Plg) as the dominant mineral constituents. The scale bar in both the images is 500 μm in length.

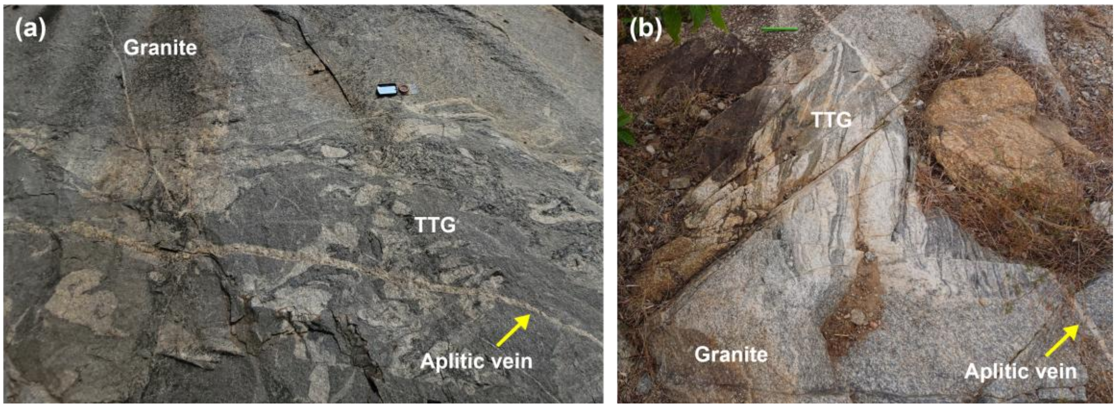

Fig. 7.2 (a) and **(b)** show enclaves of older TTG gneisses within the younger granites. Such enclaves are most commonly found near the pluton margins, where aplite vein intrusions are also more abundant.

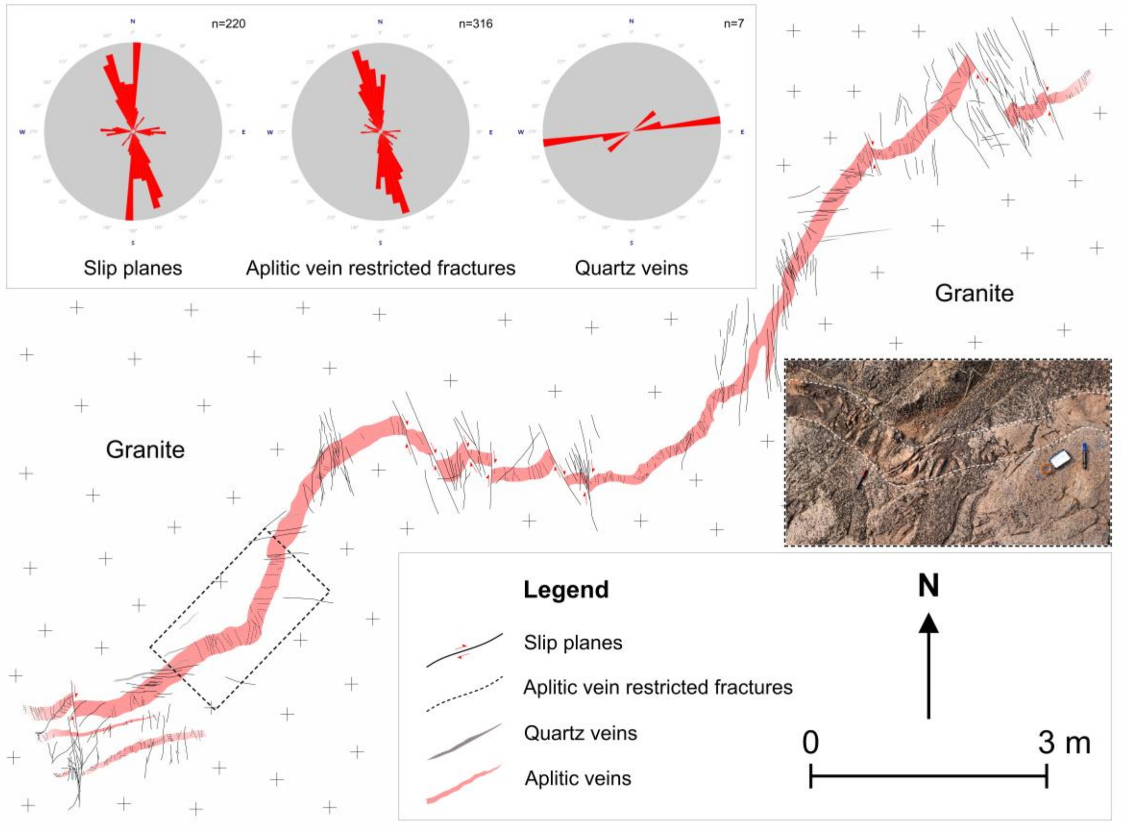

Fig. 7.3 Detailed map showing a folded aplite vein that initially intruded the granite in a NE-SW orientation, parallel to the far-field compression of the D$_1$/D$_2$ coaxial deformation phase of the CSB. The axial planes of the folded vein trend broadly NW-SE. The portion of the aplite vein featuring a prominent fold hinge (dashed black box) is shown in the inset field photograph, where the vein outline is traced with faint white dashed lines for clarity. The compass is 20 cm in length. The aplite vein is systematically offset by numerous small-scale faults (slip planes) which have a dominant NNW to NNE trend, as shown in the inset rose diagram. These slip planes are the components of the regional Riedel shear system, developed through sinistral shear along the Chitradurga Shear Zone (CSZ), acting as the master shear boundary during D$_3$ deformation under E-W to ESE-WNW directed compression. The vein-restricted fractures display a strong NNW oriented maximum, as shown in the inset rose diagram, which lies at a high angle to the overall orientation of the aplite vein. This consistent high-angle relationship to the vein margin and their restriction to the vein are suggestive of their origin as thermal fractures. A few small ENE-WSW oriented quartz veins also cross-cut the aplite vein (inset rose diagram). Their dilatational nature, indicated by tipped terminations, suggests emplacement during the late D$_2$ deformation phase under ENE-WSW directed compression. n = number of data.

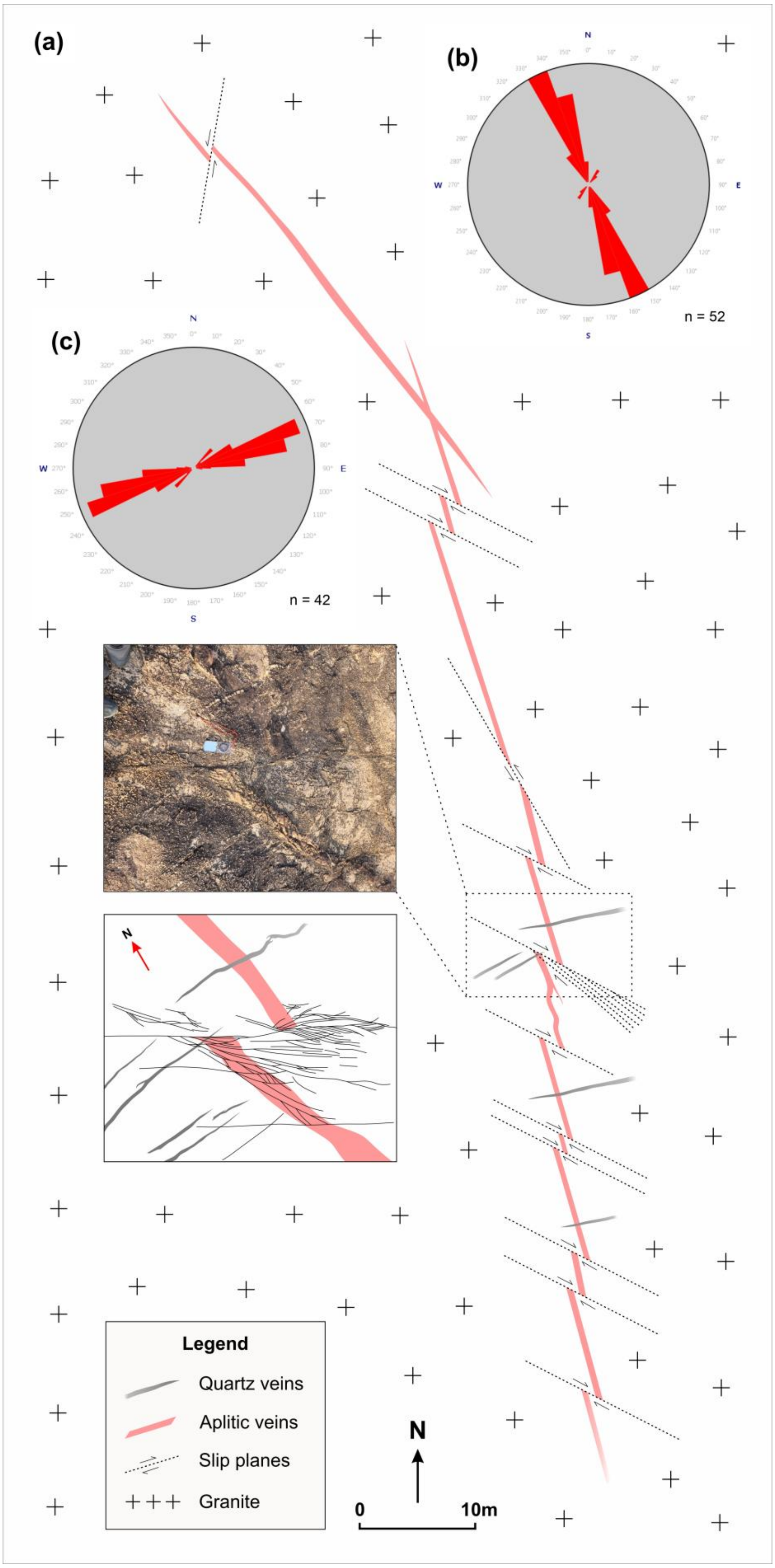
(a)
(b)
N
W
E
S
n = 52
(c)
N
W
E
S
n = 42
N
Legend
Quartz veins
Aplitic veins
Slip planes
+++ Granite
N
0
10m

Fig. 7.4 (a) Sketch map showing two NNW oriented aplite veins within the granite. These veins remain unfolded, unlike those with an initial NE-SW orientation, but are systematically offset by the Riedel shear slip planes. The inset field photograph (dashed black box) highlights cross-cutting E-W quartz veins, which themselves are also truncated by the slip planes, indicating their mutual temporal relationships. **(b)** Rose diagram showing the dominant NW to NNW trend of the aplite veins observed across the granite plutons. **(c)** Rose diagram of cross-cutting quartz veins showing a dominant ENE-WSW trend. n = number of data.

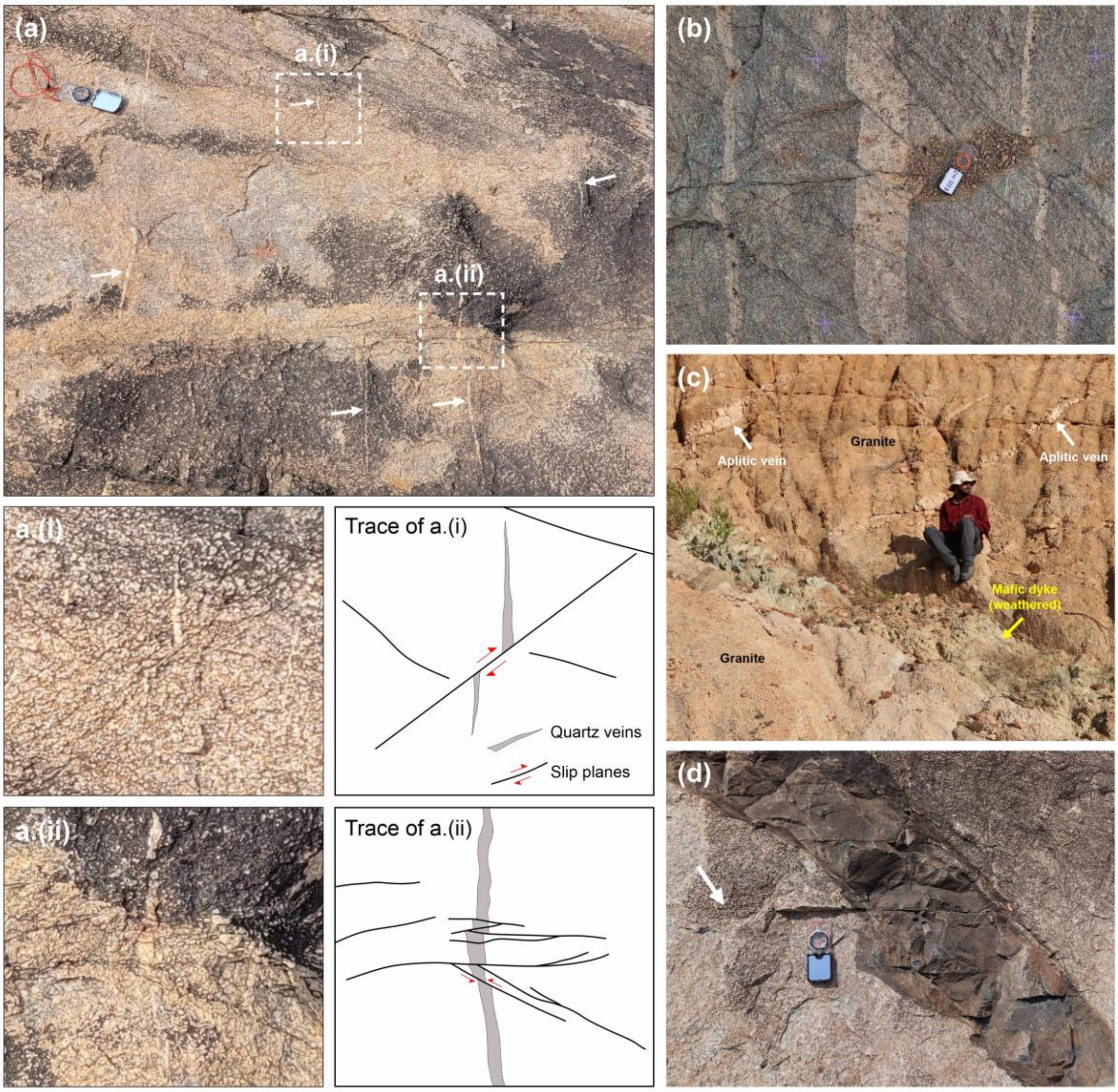

Fig. 7.5 Field photographs illustrating mutual cross-cutting relationships among brittle structures in the younger granites. Contd.

Fig. 7.5 Contd. **(a)** Outcrop showing ENE-WSW oriented quartz veins cut by the Riedel faults, with inset figures **a(i)** and **a(ii)** (marked in dashed white boxes) displaying zoomed views and their traced counterparts. **(b)** Systematic displacement of parallel aplite veins by a network of Riedel faults. **(c)** Field photo showing a NNE trending mafic dyke truncating earlier NW-SE oriented aplite veins. **(d)** Discrete fracture planes (white arrow) of the Riedel shear system cross-cutting a mafic dyke.

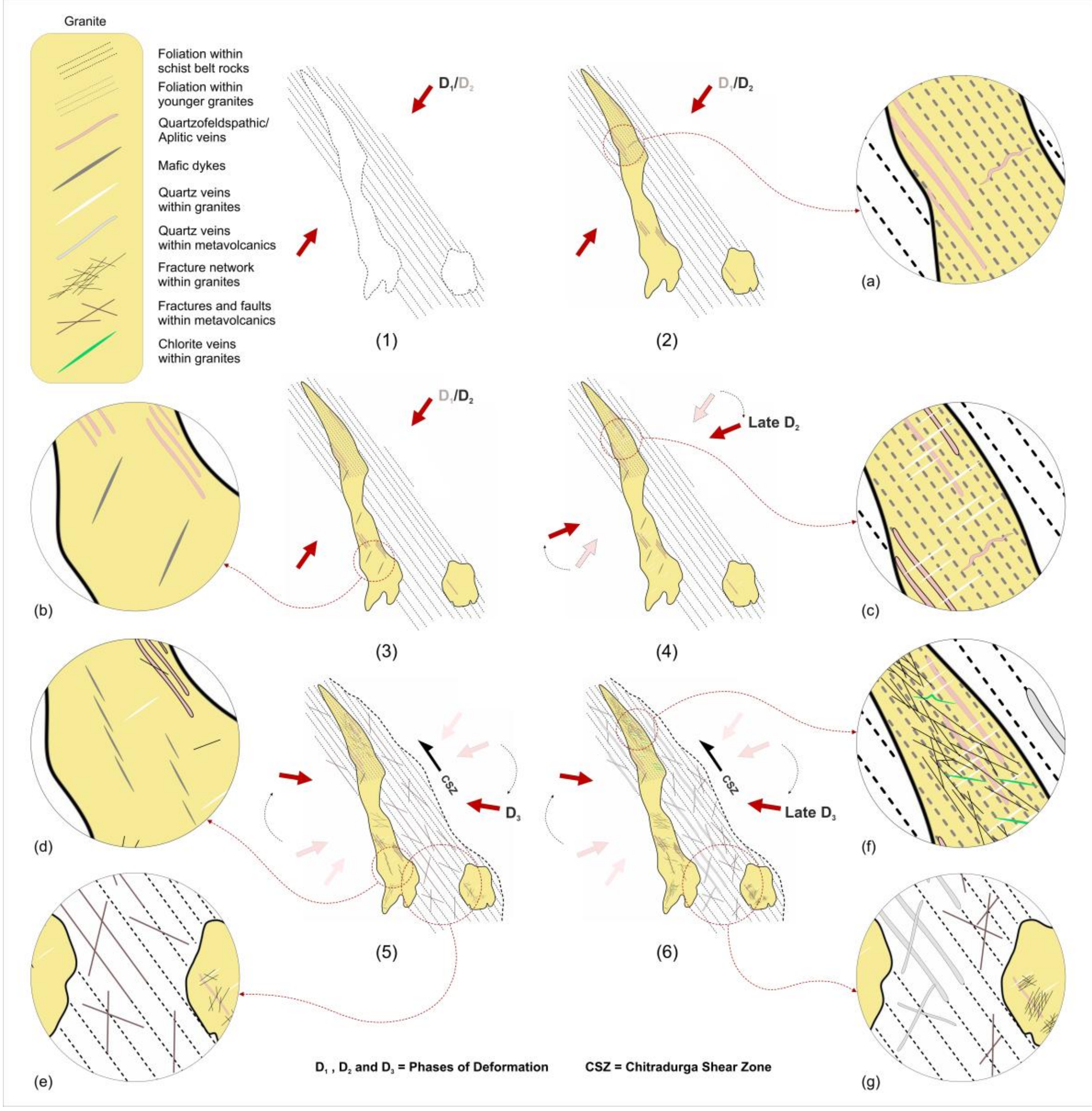

Fig. 7.6 The brittle tectonic evolution model of the study area in the Chitradurga region of the Chitradurga Schist Belt (CSB), Western Dharwar Craton (WDC), southern India.

Appendix

The appendix provides a comprehensive list of all supplementary materials referenced in the main text, along with their corresponding Google Drive links, which are also hyperlinked within respective chapters of the main document.

Supplementary sheet – 5.1

Geological map of the Saltora-Bero sector of Chotanagpur Granite Gneiss Complex (CGGC), showing the location of the studied felsic dykes and their field photographs.

https://drive.google.com/file/d/12M3kNcigUXIg2EKuo_rOCVIkG2yAThtk/view?usp=sharing

Supplementary sheet – 5.2

Details of measurements, calculations, comparison and error analyses of the dyke test data set used for the first method of complete dyke dimension estimation involving partial dyke outcrops having at least one exposed tip.

https://docs.google.com/spreadsheets/d/1b-Y9Dod1ZLFI4Qwvx14kkvHVBFFqtmzy/edit?usp=sharing&ouid=111390733534597761714&rtpof=true&sd=true

Supplementary sheet – 5.3

Details of comparison and error analyses for the first method of complete dyke dimension estimation involving partial dyke outcrops having at least one exposed tip against the published dyke data set of Miyake-jima, Japan, from Kusumoto et al. (2013).

https://docs.google.com/spreadsheets/d/18pUzxPhCRUm-sBtcAdQTnSy2X-KW5eBd/edit?usp=sharing&ouid=111390733534597761714&rtpof=true&sd=true

Supplementary sheet – 5.4

Table summarizing all calculated results, generated on application of the first method of complete dyke dimension estimation involving partial dyke outcrops having at least one exposed tip, for the mafic dykes emplaced within the ~ 2.61 Ga Chitradurga granite of CSB, WDC, India.

https://drive.google.com/file/d/1mQ-ygOs5Jmwl72P_5WyKSQ3tV_gDyleP/view?usp=sharing

Supplementary sheet – 5.5

Python code developed for the estimation of complete dyke dimensions by Ellipse DE method, for partial dyke outcrops having no exposed tips, by Biswas et al. (2025).

https://drive.google.com/file/d/19aGob_K_DL7hYLGvwgTxzRpl6sO3Ye9o/view?usp=sharing

Supplementary sheet – 5.6

Field photographs of felsic dykes emplaced within porphyritic granite of CGGC, near Bero hills, Purulia, India.

https://drive.google.com/file/d/1WzP9BhppkLjKFq4unsKLXzpLRqGNtWjE/view?usp=sharing

Supplementary sheet – 5.7

Details of measurements, used data portions, calculations and comparison of the dyke test data set used for the second method of complete dyke dimension estimation involving partial dyke outcrops devoid of exposed tips.

https://docs.google.com/spreadsheets/d/1fCeapXIxtqEIzms9FLqdxz5WBZEVDPmr/edit?usp=sharing&ouid=111390733534597761714&rtpof=true&sd=true

Supplementary sheet – 5.8

Error analyses with the test dyke data set for the second method of complete dyke dimension estimation involving partial dyke outcrops devoid of exposed tips.

https://docs.google.com/spreadsheets/d/1wV0JXecmKBPwgjeiah855x9atUStYM7F/edit?usp=sharing&ouid=111390733534597761714&rtpof=true&sd=true

Supplementary sheet – 5.9

Field data and results generated for the partially exposed mafic dykes having no exposed tip emplaced within the Chitradurga (CH) granite and Closepet granite of Pavagada (PV) region, of the WDC and EDC respectively.

https://docs.google.com/spreadsheets/d/1nd4ot5Luan4AD565Pfq6vYAQhyLZ57Pi/edit?usp=sharing&ouid=111390733534597761714&rtpof=true&sd=true

Supplementary sheet – 5.10

Table summarizing all results generated for the Chitradurga (CH) and Pavagada (PV) dykes of WDC and EDC respectively, on application of the second method of complete dyke dimension estimation involving partial dyke outcrops devoid of exposed tips.

https://docs.google.com/spreadsheets/d/180w8EweVsyWW7CxC-J0DuGAoP4-L3YWd/edit?usp=sharing&ouid=111390733534597761714&rtpof=true&sd=true

Supplementary File – 6.1

Details of location, collected data, analyses and comparison of the fracture networks recorded from the ~ 2.61 Ga younger granites of the CSB, WDC, India.

https://docs.google.com/spreadsheets/d/1Cc53jV4jChkAQfatM3nuYh_0UHzbLhV3/edit?usp=sharing&ouid=111390733534597761714&rtpof=true&sd=true

Supplementary File – 6.2

Details of spacing analysis conducted on the fracture networks recorded from the ~ 2.61 Ga younger granites of the CSB, WDC, India.

https://docs.google.com/spreadsheets/d/1tX41LxO6fi7DIbA7R32cmmrEGu1pS2-b/edit?usp=sharing&ouid=111390733534597761714&rtpof=true&sd=true

Supplementary File – 6.3

Procedure followed for the preparation of coloured contour maps for the spatial comparison of fracture abundance and connectivity for the fracture networks observed in the younger granites and metavolcanic rocks of the CSB, WDC, India.

https://drive.google.com/file/d/1vzzsVGV2HclmjMhPSB13EU4f2UMR6AVi/view?usp=sharing

Supplementary File – 6.4

Graphical representation of all the results generated through fractal analyses (2D box-counting) of the fracture networks observed within the younger granites of the CSB, WDC, India.

https://drive.google.com/file/d/1iKxgqsfT45CE4whwQ-g7b3UbFFRJKbuA/view?usp=sharing

Supplementary File – 6.5

Schematic illustration of a sinistral Riedel shear system.

https://drive.google.com/file/d/14owv-SoZzfYiGYik6MQuZDTAZP2044dD/view?usp=sharing

Supplementary File – 6.6

Details of location, collected data, analyses and comparison of the fracture networks recorded from the metavolcanic rocks of the CSB, WDC, India.

https://docs.google.com/spreadsheets/d/12Pom_mEM1Eibv13-jeGQLqBuw-OUMdEP/edit?usp=sharing&ouid=111390733534597761714&rtpof=true&sd=true

- **Link to the entire google drive folder containing all supplementary materials:**

https://drive.google.com/drive/folders/1m61-1GPRwczlaACOqMloyWi8WzX3_R_r?usp=sharing

References

Abdullahi, A. I., Umar, N. D., Igwe, O., Ikenna, A. O., 2022. Fracture network characterization applied to mineralization in Lower Benue Trough, Nigeria. Arabian Journal of Geosciences, 15(16), 1406.

Acharyya, S. S., Mondal T. K., 2019. Stress enhanced tensile fractures in elliptical clast in conglomerate. Journal of Structural Geology 122, 81–88.

Aghababaei, M., Behnia, M., Aliha, M. R. M., 2024. Experimental investigation on the effect of grain size of granitic rocks on the fracture roughness and toughness. Geomechanics for Energy and the Environment, 38, 100535.

Agnon, A., Lyakhovsky, V., Baer, G., Heimann, A., 1995. Damage distribution and localization during dyke intrusion. The Physics and Chemistry of Dykes, 65-78.

Anand, P., Chakraverty, S., Mukherjee, S., 2021. Fuzzy set concept in structural geology: Example of ductile simple shear. Journal of Earth System Science 130, 193.

Anderson, E. M., 1937. IX.—The dynamics of the formation of cone-sheets, ring-dykes, and caldron-subsidences. Proceedings of the Royal Society of Edinburgh, 56, 128-157.

Anderson, T. L., 2005. Fracture Mechanics: Fundamentals and Applications, 3rd ed. Taylor and Francis, London.

André, A. S., Sausse, J., Lespinasse, M., 2001. New approach for the quantification of paleostress magnitudes: application to the Soultz vein system (Rhine graben, France). Tectonophysics, 336(1-4), 215-231.

Antony, J. P., 1999. Ore Group Classification-A Case Study from Ingaldhal Sulphide Deposit, Karnataka Craton, India. Gondwana Research, 2(1), 67-77.

Babar, M. D., Kaplay, R. D., Mukherjee, S., Kulkarni, P. S., 2017. Evidence of the deformation of dykes from the Central Deccan Volcanic Province, Aurangabad, Maharashtra, India. Geological Society, London, Special Publications, 445(1), 337-353.

Baer, G., Beyth, M., Reches, Z., 1994. Dikes emplaced into fractured basement, Timna Igneous Complex, Israel. Journal of Geophysical Research 99, 24039–51. Bhatt, S., Rana, V., Mamtani, M.A., 2017. Deciphering relative timing of fabric development in granitoids with similar absolute ages based on AMS study (Dharwar Craton, South India). Journal of Structural Geology 94, 32–46.

Bajgain, S., Ghosh, D. B., Karki, B. B., 2015. Structure and density of basaltic melts at mantle conditions from first-principles simulations. Nature communications, 6(1), 1-7.

Balakrishnan, S., Hanson, G. N., Rajamani, V., 1999. U–Pb ages for zircon and titanite from the Ramagiri area, southern India: evidence for accretionary origin of the Eastern Dharwar Craton during the late Archean. Journal of Geology 107, 69–86.

Ball, E., 1980. An example of very consistent brittle deformation over a wide intracontinental area: the late Pan-African fracture system of the Tuareg and Nigerian shield. Tectonophysics, 61(4), 363-379.

Banerji, A. K. 1991. Presidential address. Geology of the Chotanagpur region. Indian Journal of Geology, 63, 275–282.

Basu, A., Mishra, D. A., Roychowdhury, K., 2013. Rock failure modes under uniaxial compression, Brazilian, and point load tests. Bulletin of Engineering Geology and the environment, 72(3), 457-475.

Becerril, L., Galindo, I., Gudmundsson, A., Morales, J. M., 2013. Depth of origin of magma in eruptions. Scientific reports, 3(1), 1-6.

Beckinsale, R.D., Drury, S.A., Holt, R.W., 1980. 3,360-Myr old gneisses from the South Indian Craton. Nature, 283(5746).

Begg, G., Burg, J. P., Wilson, C. J. L., 1987. Ductile and brittle deformation in the Cann Valley granitoids, Victoria. Australian Journal of Earth Sciences, 34(1), 95-110.

Berkowitz, B., 2002. Characterizing flow and transport in fractured geological media: A review. Advances in water resources, 25(8-12), 861-884.

Berkowitz, B., 2002. Characterizing flow and transport in fractured geological media: A review. Advances in water resources, 25(8-12), 861-884.

Berkowitz, B., Bour, O., Davy, P., Odling, N., 2000. Scaling of fracture connectivity in geological formations. Geophysical Research Letters, 27(14), 2061-2064.

Bhatt, et al., 2017. Deciphering relative timing of fabric development in granitoids with similar absolute ages based on AMS study (Dharwar Craton, South India). Journal of Structural Geology 94, 32–46.

Bhowmick, S., Mondal, T. K., 2020. Control of pre-existing fabric in fracture formation, reactivation and vein emplacement under variable fluid pressure conditions: an example from Archean Greenstone belt, India. Solid Earth, 11, 1227–46.

Bhowmick, S., Mondal, T. K., 2021. Influence of fluid pressure changes on the reactivation potential of pre-existing fractures: a case study in the Archaean metavolcanics of the Chitradurga region, India. Geol. Mag. 1–15.

Biswas, S. K., Mondal, T. K., 2024. Dyke emplacement under mixed loading conditions: Insights from the Dharwar Craton, India. Journal of Asian Earth Sciences, 276, 106359.

Biswas, S. K., Mondal, T. K., Saha, A., Mukhopadhyay, A. K., Mukherjee, A., 2025. Estimating Complete Dyke Dimensions from Partial Exposures. Journal of Structural Geology, 105350.

Biswas, S. K., Saha, K., Das, G., Mondal, T. K., 2023. Estimation of magma overpressure from partially exposed dykes-A new approach. Journal of Structural Geology, 168, 104822.

Blenkinsop, T.G., 1991. Cataclasis and processes of particle size reduction. Pure and Applied Geophysics, 136(1), 59–86.

Bonnet, E., Bour, O., Odling, N. E., Davy, P., Main, I., Cowie, P., Berkowitz, B., 2001. Scaling of fracture systems in geological media. Reviews of geophysics, 39(3), 347-383.

Bonnet, E., Bour, O., Odling, N. E., Davy, P., Main, I., Cowie, P., Berkowitz, B., 2001. Scaling of fracture systems in geological media. Reviews of geophysics, 39(3), 347-383.

Bons, P. D., Elburg, M. A., Gomez-Rivas, E., 2012. A review of the formation of tectonic veins and their microstructures. Journal of structural geology, 43, 33-62.

Bouhallier, H., Chardon, D., Choukroune, P., 1995. Strain patterns in Archaean dome-and-basin structures: the Dharwar craton (Karnataka, South India). Earth and Planetary Science Letters 135, 57–75.

Brown, E. T., Hoek, E., 1980. Underground excavations in rock. CRC Press.

Brown, S. R., Bruhn, R. L., 1998. Fluid permeability of deformable fracture networks. Journal of Geophysical Research: Solid Earth, 103(B2), 2489-2500.

Brown, S.R., Bruhn, R.L., 1998. Fluid permeability of deformable fracture networks. Journal of Geophysical Research Solid Earth 103 (B2), 2489e2500.

Bruce, P. M., Huppert, H. E., 1989. Thermal control of basaltic fissure eruptions. Nature, 342(6250), 665-667.

Buchholz, P., Herzig, P., Friedrich, G., Frei, R., 1998. Granite-hosted gold mineralization in the Midlands greenstone belt: a new type of low-grade gold deposit in Zimbabwe. Mineralium Deposita, 33, 437-460.

Burchardt, S., 2018. Volcanic and Igneous Plumbing Systems: Understanding Magma Transport, Storage, and Evolution in the Earth's Crust. Elsevier.

Burg, J. P., 1999. Ductile structures and instabilities: their implication for Variscan tectonics in the Ardennes. Tectonophysics, 309(1-4), 1-25.

Bussell, M. A., 1989. A simple method for the determination of the dilation direction of intrusive sheets. Journal of Structural Geology, 11(6), 679-687.

Caputo, R., 2005. Stress variability and brittle tectonic structures. Earth-Science Reviews, 70(1-2), 103-127.

Castaing, C., Halawani, M.A., Gervais, F., Chilès, J.P., Genter, A., Bourgine, B., Ouillon, G., Brosse, J.M., Martin, P., Genna, A., Janjou, D., 1996. Scaling relationships in intraplate fracture systems related to Red Sea rifting. Tectonophysics, 261(4), 291–314.

Cathles, L. M., Adams, J. J., 2005. Fluid flow and petroleum and mineral resources in the upper (< 20-km) continental crust.

Chadwick, B., 1994. The Dharwar Supergroup in western Karnataka: A reviewbased on the Bababudan and Ranibennur tract. In: GeoKarnataka (MGD century volume), Karnataka Asst. Geol. Assoc., Department of Mines and Geology, Govt. of Karnataka, Bangalore, 81–94.

Chadwick, B., Ramakrishnan, M., Vasudev, V.N., Viswanatha, M. N., 1989. Facies distributions and structure of a Dharwar volcano sedimentary basin: evidence for late Archaean transpression in Southern India? Journal of the Geological Society of London 146, 825–34.

Chadwick, B., Ramakrishnan, M., Viswanatha, M. N., & Srinivasa Murthy, V., 1978. Structural studies in the Archaean Sargur and Dharwar supracrustal rocks of the Karnataka craton. Journal Geological Society of India, 19(12), 531-549.

Chadwick, B., Ramakrishnan, M., Viswanatha, M. N., 1981. The stratigraphy and structure of the Chitradurga region: an illustration of cover-basement interaction in the late Archaean evolution of the Karnataka craton, southern India. Precambrian Research, 16(1-2), 31-54.

Chadwick, B., Vasudev, V. N., Ahmed, N., 1996. The Sandur schist belt and itsadjacent plutonic rocks: implications for late Archaean crustal evolution in Karnataka. Journal of the Geological Society of India 47, 37–57.

Chadwick, B., Vasudev, V. N., Hedge, G. V., 2003. The Chitradurga schist belt and its adjacent plutonic rocks NW of Tungabhadra, Karnataka: a duplex in the late Archean convergent setting of the Dharwar craton. Journal of the Geological Society of India 61, 611–613.

Chadwick, B., Vasudev, V. N., Hedge, G. V., Nutman, A. P., 2007. Structure and SHRIMP U/Pb zircon ages of granites adjacent to the Chitradurga schist belt: implications for Neoarchaean convergence in the Dharwar craton, southern India. Journal of the Geological Society of India 69, 5–24.

Chadwick, B., Vasudev, V. N., Hegde, G. V., 1999. Magmatism, structure, emplacement and plate tectonic setting of late Archaean Dharwar batholith, south India. Department of Mines and Geology, Government of Karnataka, Geological Studies 316, 67.

Chadwick, B., Vasudev, V. N., Hegde, G. V., 2000. The Dharwar Craton, southern India, interpreted as the result of Late Archaean oblique convergence. Precambrian Research 99, 91–111.

Chadwick, B., Vasudev, V.N., Hedge, G.V., 2003. The Chitradurga schist belt and its adjacent plutonic rocks NW of Tungabhadra, Karnataka: a duplex in the late Archean convergent setting of the Dharwar craton. Journal of Geological Society of India 61, 611–613.

Chakrabarti, C., Mallick, B.S., Pyne, T.K., Guha, D., 2006. A manual of the Geology of India. Geological Survey of India, Kolkata.

Chardon, D., Choukroune, P., Jayananda, M., 1998. Sinking of the Dharwar basin (South India): implications for Archaean tectonics. *Precambrian Research*, *91*(1-2), 15-39.

Chardon, D., Peucat, J. J., Jayananda, M., Choukroune, P., Fanning, C. M., 2002. Archaean granite–greenstone tectonics at Kolar (south India): interplay of diapirism and bulk inhomogeneous contraction during juvenile magmatic accretion. Tectonics 21, 1–17.

Chatterjee, S., 2021. A new coefficient of correlation. Journal of the American Statistical Association, 116(536), 2009-2022.

Clemente, C. S., Amorós, E. B., Crespo, M. G., 2007. Dike intrusion under shear stress: effects on magnetic and vesicle fabrics in dikes from rift zones of Tenerife (Canary Islands). Journal of Structural Geology, 29(12), 1931-1942.

Condie, K. C., 1981. Archean greenstone belts (Vol. 3). Elsevier.

Correa-Gomes, L. C., Souza Filho, C. R., Martins, C. J. F. N., Oliveira, E. P., 2001. Development of symmetrical and asymmetrical fabrics in sheet-like igneous bodies: the role of magma flow and wall-rock displacements in theoretical and natural cases. Journal of Structural Geology, 23(9), 1415-1428.

Cox, S. F., 1987. Antitaxial crack-seal vein microstructures and their relationship to displacement paths. Journal of Structural Geology, 9(7), 779-787.

Cox, S. F., 2005. Coupling between deformation, fluid pressures, and fluid flow in ore-producing hydrothermal systems at depth in the crust.

Currie, K. L., Ferguson, J., 1970. The mechanism of intrusion of lamprophyre dikes indicated by “offsetting” of dikes. Tectonophysics, 9(6), 525-535. https://doi.org/10.1016/0040-1951(70)90003-X

Currie, K. L., Ferguson, J., 1970. The mechanism of intrusion of lamprophyre dikes indicated by “offsetting” of dikes. Tectonophysics, 9(6), 525-535.

Daniels, K. A., Kavanagh, J. L., Menand, T., R. Stephen, J. S., 2012. The shapes of dikes: Evidence for the influence of cooling and inelastic deformation. Bulletin, 124(7-8), 1102-1112.

Das, D., Mondal, T.K., Hossain, M.S., 2019. Quantification of Quartz Reefs and Mafic Dykes of Bundelkhand, Craton, Central India: A Study Based on Spatial and Fractal Analysis. J. Geol. Soc. India, 94, 227–237.

Das, G., Biswas, S. K., Mondal, T. K., Mondal, S., 2024. Evolution of tensile fractures in feldspar porphyroclast and its implication in paleostress estimation. Journal of Structural Geology, 179, 105039.

Davis, G. H., Bump, A. P., García, P. E., Ahlgren, S. G., 2000. Conjugate Riedel deformation band shear zones. Journal of Structural Geology, 22(2), 169-190.

Davis, G. H., Reynolds, S. J., Kluth, C. F., 2011. Structural geology of rocks and regions. John Wiley & Sons.

Deb, T., Bhattacharyya, T., 2022. The evolution of the fracture systems under progressive sinistral shear in the Bundelkhand Craton, Central India: A review and new insights. Earth-Science Reviews, 235, p.104238.

Deciphering relative timing of fabric development in granitoids with similar absolute ages based on AMS study (Dharwar Craton, South India). J. Struct. Geol., 94, 32–46.

Delaney, P. T., Pollard, D. D., 1981. Deformation of host rocks and flow of magma during growth of minette dikes and breccia-bearing intrusions near Ship Rock, New Mexico (No. 1202). USGPO.

Delaney, P. T., Pollard, D. D., Zioney, J. I., McKee, E. H., 1986. Field relations between dikes and joints: emplacement processes and palaeostress analysis. Journal of Geophysical Research 91, 4920–38.

Dershowitz, W. S., Einstein, H. H., 1988. Characterizing rock joint geometry with joint system models. Rock mechanics and rock engineering, 21(1), 21-51.

Dey, S., Nandy, J., Choudhary, A.K., Liu, Y., Zong, K., 2015. Neoarchaean crustal growth by combined arc–plume action: evidence from the Kadiri Greenstone Belt, eastern Dharwar craton, India. Geological Society, London, Special Publications, 389(1), pp.135-163.

Dimri, V., 2005. Fractal behaviour of the earth system (Vol. 208). Berlin: Springer.

Doughty, C., Karasaki K., 2002. Flow and transport in hierarchically fractured rock. Journal of Hydrology, 263, 1–22.

Dresen, G., 1991. Stress distribution and the orientation of Riedel shears. Tectonophysics, 188(3-4), 239-247.

Drury, S. A., Harris, N. B. W., Holt, R. W., Reeves-Smith, G. J., Wightman, R. T., 1984. Precambrian tectonics and crustal evolution in South India. The Journal of Geology, 92(1), 3-20.

Drymoni, K., Browning, J., Gudmundsson, A., 2021. Volcanotectonic interactions between inclined sheets, dykes, and faults at the Santorini Volcano, Greece. Journal of Volcanology and Geothermal Research, 416, 107294. https://doi.org/10.1016/j.jvolgeores.2021.107294

Eberhardt, E., Stimpson, B., Stead, D., 1999. Effects of grain size on the initiation and propagation thresholds of stress-induced brittle fractures. Rock mechanics and rock engineering, 32, 81-99.

Ernst, R.E., Head, J.W., Parfitt, E., Grosfils, E., Wilson, L., 1995. Giant radiating dyke swarms on Earth and Venus. Earth Science Reviews, 39, 1–58.

Evans, D. A. D., Halls, H. C., 2010. Restoring Proterozoic deformation within the Superior craton. Precambrian Research, 183(3), 474-489. https://doi.org/10.1016/j.precamres.2010.02.007

Evans, D. A. D., Halls, H. C., 2010. Restoring Proterozoic deformation within the Superior craton. Precambrian Research, 183(3), 474-489.

Faye, G. D., Yamaji, A., Yonezu, K., Tindell, T., Watanabe, K., 2018. Paleostress and fluid-pressure regimes inferred from the orientations of Hishikari low sulfidation epithermal gold veins in southern Japan. Journal of Structural Geology, 110, 131-141.

Ferrill, D. A., Smart, K. J., Morris, A. P., 2019. Fault failure modes, deformation mechanisms, dilation tendency, slip tendency, and conduits v. seals. In Integrated Fault Seal Analysis (eds SR Ogilvie, SJ Dee, RW Wilson and WRBailey). Geological Society of London, Special Publication no. 496, 75–98.

Ferrill, D. A., Winterle, J., Wittmeyer, G., Sims, D., Colton, S., Armstrong, A., Morris, A. P., 1999. Stressed rock strains groundwater at Yucca Mountain, Nevada. GSA Today 9, 1–8.

Fialko, Y.A., Rubin, A.M., 1999. Thermal and mechanical aspects of magma emplacement in giant dike swarms. Journal of Geophysical Research, 104, 23033–23049.

Foley, S. F., 1989. Emplacement features of lamprophyre and carbonatitic lamprophyre dykes at Aillik Bay, Labrador. Geological Magazine, 126(1), 29-42.

Forstner, S. R., Laubach, S. E., 2022. Scale-dependent fracture networks. Journal of Structural Geology, 165, 104748.

Fossen, H., 2016. Structural geology. Cambridge university press.

Fossen, H., Cavalcante, G. C. G., Pinheiro, R. V. L., Archanjo, C. J., 2019. Deformation–progressive or multiphase?. Journal of Structural Geology, 125, 82-99.

Gao, W., Iqbal, J., Xu, D., Sui, H., Hu, R., 2019. Effect of brittle mineral size on hydraulic fracture propagation in shale gas reservoir. Geofluids, 2019(1), 9147048.

Geshi, N., Browning, J., & Kusumoto, S., 2020. Magmatic overpressures, volatile exsolution and potential explosivity of fissure eruptions inferred via dike aspect ratios. Scientific reports, 10(1), 9406. https://doi.org/10.1038/s41598-020-66226-z

Geshi, N., Kusumoto, S., Gudmundsson, A., 2010. The geometric difference between non feeders and feeder dikes. Geology, 38, 195–198.

Ghodke, S. S., Rathna, K., Kokandakar, G. J., Nagaraju, B., More, L. B., Bhosle, M. V., Kumar, K. V., 2018. Emplacement and growth of alkaline dikes: insights from the shonkinite dikes (Elchuru alkaline complex, SE India). Journal of Structural Geology, 117, 219-236.

Ghose, N.C., 1983. Geology, tectonics and evolution of the Chhotanagpur granite-gneiss complex, Eastern India. In Structure and tectonics of Precambrian rocks of India (pp. 211-247).

Glazner, A. F., Bartley, J. M., Coleman, D. S., Lindgren, K., 2020. Aplite diking and infiltration: A differentiation mechanism restricted to plutonic rocks. Contributions to Mineralogy and Petrology, 175(4), 37.

Glazner, A.F., Bartley, J.M., Carl, B.S. 1999. Oblique opening and noncoaxial emplacement of the Jurassic independence dike swarm, California. Journal of Structural Geology, 21, 1275–1283.

Gomez-Rivas, E., Griera, A., 2012. Shear fractures in anisotropic ductile materials: an experimental approach. Journal of Structural Geology, 34, 61-76.

Gopalakrishna, G., Shareef, M., Nagesh, P. C., 2018. Shear-Controlled Gold Mineralization of GR Halli Area of Chitradurga Schist Belt, Dharwar Craton: Insights from Fluid Inclusion Study. Open Journal of Geology, 8(7), 662-673.

Gudmundsson, A., 1983a. Form and dimensions of dykes in eastern Iceland. Tectonophysics, 95(3-4), 295-307.

Gudmundsson, A., 1983b. Stress estimates from the length/width ratios of fractures. Journal of Structural Geology, 5(6), 623-626. https://doi.org/10.1016/0191-8141(83)90075-5

Gudmundsson, A., 1988. Effect of tensile stress concentration around magma chambers on intrusion and extrusion frequencies. Journal of Volcanology and Geothermal Research, 35(3), pp.179-194. https://doi.org/10.1016/0377-0273(88)90015-7

Gudmundsson, A., 2009. Toughness and failure of volcanic edifices. Tectonophysics, 471(1-2), 27-35. https://doi.org/10.1016/j.tecto.2009.03.001

Gudmundsson, A., 2011. Rock fractures in geological processes. Cambridge University Press. https://doi.org/10.1017/CBO9780511975684

Gudmundsson, A., 2020. Volcanotectonics: Understanding the structure, deformation and dynamics of volcanoes. Cambridge University Press.

Gudmundsson, A., 2022. The propagation paths of fluid-driven fractures in layered and faulted rocks. Geol. Mag. 1–24.

Gudmundsson, A., 2022a. The propagation paths of fluid-driven fractures in layered and faulted rocks. Geological Magazine, pp.1-24. https://doi.org/10.1017/S0016756822000826

Gudmundsson, A., 2022b. Transport of Geothermal Fluids along Dikes and Fault Zones. Energies, 15(19), p.7106. https://doi.org/10.3390/en15197106

Gudmundsson, A., Drymoni, K., Browning, J., Acocella, V., Amelung, F., Bonali, F.L., Elshaafi, A., Galindo, I., Geshi, N., Geyer, A. and Heap, M.J., 2022. Volcanotectonics: the tectonics and physics of volcanoes and their eruption mechanics. Bulletin of volcanology, 84(8), p.72.

Gupta, S., Rai, S. S., Prakasam, K. S., Sriganesh, D., Chadha, R. K., Priestly, K. and Gaur, V. K., 2003. First evidence for anomalous thick crust beneath mid-Archean Dharwar craton. Current Science 14(9,10), 1219–1226.

Halls, H.C., Fahrig, W.F., 1987. Mafic Dyke Swarms. Special Paper 34. Geological Association of Canada, pp. 503.

Healy, D., 2017. FracTend MATLAB code, GitHub. https://github.com/DaveHealy-Aberdeen/FracTend.

Healy, D., Rizzo, R. E., Cornwell, D. G., Farrell, N. J., Watkins, H., Timms, N. E., ... Smith, M., 2017. FracPaQ: A MATLAB™ toolbox for the quantification of fracture patterns. Journal of Structural Geology, 95, 1-16.

Hoek. E., Brown, E. T., 1980. Empirical strength criterion for rock masses. Journal of the geotechnical engineering division, 106(9), 1013-1035.

Hongrui, F., Mingguo, Z., Yihan, X., & Jin-Hui, Y., 2003. Ore-forming fluids associated with granite-hosted gold mineralization at the Sanshandao deposit, Jiaodong gold province. China, 38(6), 739-750.

Honório, G. B., Nogueira, F. C. C., Nicchio, M. A., Vasconcelos, D. L., Souza, J. A. B., Freitas, R. B. R. M., ... Ferreira, H. A. S., 2025. Topological and petrophysical analyses across a fault zone containing deformation bands. Journal of Structural Geology, 190, 105295.

Hossain, M.S., Kruhl, J.H., 2015. Fractal Geometry-Based Quantification of Shock-Induced Rock Fragmentation in and around an Impact Crater. Pure and Applied Geophysics, 172(7), 2009-2023.

Hu, H., Liu, S., Fan, H. R., Yang, K., Zuo, Y., Cai, Y., 2020. Structural networks constraints on alteration and mineralization processes in the Jiaojia gold deposit, Jiaodong Peninsula, China. Journal of Earth Science, 31, 500-513.

Huang, J., Wei, X., Zheng, Z., Su, X., Zuo, J., 2024. Linear fractal evolution characteristics of rock crack distributions during loading process. Scientific Reports, 14, 18303.

Irwin, G.R., 1960. Plastic zone near a crack and fracture toughness. Proceedings of the seventh Sagamore Ordnance materials conference, vol. IV. New York: Syracuse University; p. 63–78.

Irwin, G.R., 1968. Linear fracture mechanics, fracture transition, and fracture control. Engineering fracture mechanics, 1(2), pp.241-257.

ISRM, 2007. The complete ISRM suggested methods for rock characterization, testing and monitoring: 1974–2006. In: Ulusay R, Hudson JA (eds) Suggested methods prepared by the commission of testing methods. ISRM, compilation arranged by the ISRM Turkish national group, Kozan Ofset, Ankara.

Jaeger, C., 1979. Rock mechanics and engineering. Cambridge University Press.

Jaeger, J. C., Cook, N. G., 1969. Fundamentals of rock mechanics, Methuen & Co. Ltd., London, 513.

Jaeger, J. C., Cook, N. G., Zimmerman, R., 2009. Fundamentals of rock mechanics. John Wiley & Sons.

Janoušek, V., Bonin, B., Collins, W. J., Farina, F., Bowden, P., 2020. Post-Archean granitic rocks: contrasting petrogenetic processes and tectonic environments. Geological Society, London, Special Publications, 491(1), 1-8.

Jayananda, M., Chardon, D., Peucat, J.-J., Capdevila, R., 2006. 2.61 Ga potassic granites and crustal reworking in the western Dharwar craton, southern India: tectonic, geochronologic and geochemical constraints. Precambrian Research, 150, 1–26.

Jayananda, M., Kano, T., Peucat, J. J., Channabasappa, S., 2008. 3.35 Ga komatiite volcanism in the western Dharwar craton, southern India: coanstraints from Nd isotopes and whole–rock geochemistry. Precambrian Research 162, 160–179.

Jayananda, M., Kano, T., Peucat, J. J., Channabasappa, S., 2008. 3.35 Ga komatiite volcanism in the western Dharwar craton, southern India: constraints from Nd isotopes and whole-rock geochemistry. Precambrian Research, 162(1-2), 160-179.

Jayananda, M., Mahabaleswar, B., 1991. Relationship between shear zones and igneous activity: the Closepet Granite of southern India. Proceedings of the Indian Academy of Sciences-Earth and Planetary Sciences, 100(1), 31-36.

Jayananda, M., Martin, H., Peucat, J. J., Mahabaleswar, B., 1995. Late Archaean crust-mantle interactions: geochemistry of LREE-enriched mantle derived magmas. Example of the Closepet batholith, southern India. Contributions to Mineralogy and Petrology, 119(2), 314-329.

Jayananda, M., Miyazaki, T., Gireesh, R. V., Mahesha, N., Kano, T., 2009. Synplutonic mafic dykes from late Archaean granitoids in the Eastern Dharwar Craton, Southern India. Journal of the Geological Society of India, 73, 117-130.

Jayananda, M., Moyen, J. F., Martin, H., Peucat, J. J., Auvray, b., Mahabaleswar, B., 2000. Late Archaean (2500–2500Ma) juvenile magmatism in the Eastern Dharwar craton, southern India: constraints from geochronology, Nd–Sr isotopes and whole rock geochemistry. Precambrian Research 99, 225–254.

Jayananda, M., Peucat, J. J., Chardon, D., Krishna Rao, B., Fanning, M. C., Corfu, F., 2013. Neoarchean greenstone volcanism and continental growth, Dharwar craton, south India: constraints from SIMS U–Pb zircon geochronology and Nd isotopes. Precambrian Research 227, 55–76.

Jing, L., Stephansson, O., 1997. Network topology and homogenization of fractured rocks. In Fluid flow and transport in rocks: Mechanisms and effects (pp. 191-202). Dordrecht: Springer Netherlands.

John, B. E., Stünitz, H., 1997. Magmatic fracturing and small-scale melt segregation during pluton emplacement: evidence from the Adamello massif (Italy). In Granite: from segregation of melt to emplacement fabrics (pp. 55-74). Dordrecht: Springer Netherlands.

Jolly, R. J. H., Sanderson, D. J., 1995. Variation in the form and distribution of dykes in the Mull swarm, Scotland. Journal of Structural Geology, 17(11), 1543-1557.

Jolly, R. J. H., Sanderson, D. J., 1997. A Mohr circle reconstruction for the opening of a pre-existing fracture. Journal of Structural Geology, 19, 887–892.

Kattenhorn, S. A., Watkeys, M. K., 1995. Blunt-ended dyke segments. Journal of Structural Geology, 17(11), 1535-1542.

Kavanagh, J. L., Burns, A. J., Hazim, S. H., Wood, E. P., Martin, S. A., Hignett, S., Dennis, D. J., 2018. Challenging dyke ascent models using novel laboratory experiments: Implications for reinterpreting evidence of magma ascent and volcanism. Journal of Volcanology and Geothermal Research, 354, 87-101.

Kaye, B.H., 1989. A random walk through fractal dimensions. Weinheim, VCH Publishers, p. 421.

Kaye, B.H., 1993. Chaos and Complexity. VCH Publishers, Weinheim, p. 593.

Kim, Y. S., Sanderson, D. J., 2004. Similarities between strike-slip faults at different scales and a simple age determining method for active faults. Island Arc, 13(1), 128-143.

Kolb, J., Rogers, A., & Meyer, F. M., 2005. Relative timing of deformation and two-stage gold mineralization at the Hutti Mine, Dharwar Craton, India. Mineralium Deposita, 40(2), 156-174.

Kruhl, J.H., 2013. Fractal-geometry techniques in the quantification of complex rock structures: A special view on scaling regimes, inhomogeneity and anisotropy. Journal of Structural Geology, 46, 2–21.

Kumar, S., 2014. Magmatic processes: review of some concepts and models. Modelling of magmatic and allied processes, 1-22.

Kusumoto, S., Geshi, N., Gudmundsson, A., 2013. Aspect ratios and magma overpressures of non-feeder dikes observed in the Miyake-jima volcano (Japan), and fracture toughness of its upper part. Geophysical Research Letters, 40(6), 1065-1068.

Lahiri, S., Mamtani, M. A., 2016. Scaling the 3-D Mohr circle and quantification of paleostress during fluid pressure fluctuation–Application to understand gold mineralization in quartz veins of Gadag (southern India). Journal of Structural Geology, 88, 63-72.

Lan, M., He, Y., Wang, C. et al., 2024. Fractal evolution characteristics of fracture meso-damage in uniaxial compression rock masses using bonded block model. Scientific Report, 14, 17979.

Laubach, S. E., Hundley, T. H., Hooker, J. N., Marrett, R. A., 2018b. Spatial arrangement and size distribution of normal faults, Buckskin Detachment upper plate, Western Arizona. Journal of Structural Geology, 108, 230-242.

Laubach, S. E., Lamarche, J., Gauthier, B. D., Dunne, W. M., Sanderson, D. J., 2018a. Spatial arrangement of faults and opening-mode fractures. Journal of Structural Geology, 108, 2-15.

Lawn, B., Wilshaw, R., 1975. Indentation fracture: principles and applications. Journal of Materials Science, 10, 1049-1081.

Li, X. C., Fan, H. R., Santosh, M., Hu, F. F., Yang, K. F., Lan, T. G., 2013. Hydrothermal alteration associated with Mesozoic granite-hosted gold mineralization at the Sanshandao deposit, Jiaodong Gold Province, China. Ore Geology Reviews, 53, 403-421.

Li, Y., Chen, J., Shang, Y., 2017. Connectivity of three-dimensional fracture networks: A case study from a dam site in Southwest China. Rock Mechanics and Rock Engineering, 50(1), 241–249.

Liu, X., Zhang, C., Liu, Q., Birkholzer, J., 2009. Multiple-point statistical prediction on fracture networks at Yucca Mountain. Environmental Geology, 57, 1361–1370.

Lonergan, L., Wilkinson, J., McCaffrey, K. E. N., 1999. Fractures, fluid flow and mineralization: an introduction. Geological Society, London, Special Publications, 155(1), 1-6.

Lucca, A., Balsamo, F., De Risio, C. A., Ogata, K., Porta, F., Tavani, S., Storti, F., 2025. Facies and mechanical stratigraphy control fracture intensity, topology and fractal dimension in folded turbidite sandstones, Northern Apennines, Italy. Journal of Structural Geology, 191, 105307.

Luo, Y., Zhu, Y., Huang, F., Xia, B., 2024. Fractal permeability model of fracture network based on topological graph theory. Journal of China Coal Society, 49(8), 3561-3570.

Lyakhovsky, V., Ben-Zion, Y., Agnon, A., 1997b. Distributed damage, faulting, and friction. Journal of Geophysical Research: Solid Earth, 102(B12), 27635-27649.

Lyakhovsky, V., Reches, Z. E., Weinberger, R., Scott, T. E., 1997a. Non-linear elastic behaviour of damaged rocks. Geophysical Journal International, 130(1), 157-166.

Ma, S. M., Kellett, D. A., Godin, L., Jercinovic, M. J., 2020. Localisation of the brittle Bathurst fault on pre-existing fabrics: a case for structural inheritance in the northeastern Slave craton, western Nunavut, Canada. Canadian Journal of Earth Sciences, 57(6), 725-746.

Maccaferri, F., Bonafede, M., Rivalta, E., 2010. A numerical model of dyke propagation in layered elastic media. Geophysical Journal International, 180(3), 1107-1123. https://doi.org/10.1111/j.1365-246X.2009.04495.x

Mandelbrot, B.B., 1977. Fractals: Form, Chance, & Dimension. W.H. Freeman & Company, San Francisco, CA, p. 365.

Mandelbrot, B.B., 1982. The Fractal Geometry of Nature. W.H. Freeman & Company, New York, p. 468.

Mandl, G., 2005. Rock joints. Springer-Verlag Berlin Heidelberg.

Mandl, G., 2013. Faulting in brittle rocks: an introduction to the mechanics of tectonic faults. Springer Science & Business Media.

Manikyamba, C., Naqvi, S. M., Subba Rao, D. V., Ram Mohan, M., Khanna, T. C., Rao, T. G., Reddy, G. L. N., 2005. Boninites from the Neoarchean Gadwal greenstone belt, Eastern Dharwar craton, India: Implications for Archaean subduction processes. Earth and Planetary Science Letter 230, 355–384.

Manzocchi, T., 2002. The connectivity of two-dimensional networks of spatially correlated fractures. Water Resources Research, 38(9), 1-1.

Marrett, R., Gale, J. F., Gómez, L. A., Laubach, S. E., 2018. Correlation analysis of fracture arrangement in space. Journal of Structural Geology, 108, 16-33.

Martinez-Poza, A. I., Druguet, E., 2016. Structure and tectonic setting of the SE Sardinia mafic dyke swarm. Insights for the stress state during magma emplacement in the upper crust. Journal of Geodynamics, 101, 170-185. https://doi.org/10.1016/j.jog.2016.05.012

Martinez-Poza, A.I., Druguet, E., Castano, L.M., Carreras, J. 2014. Dyke intrusion into a pre-existing joint network: the Aiguablava lamprophyre dyke swarm (Catalan Coastal Ranges). Tectonophysics, 630, 75–90.

Matin, A., Banerjee, S., Gupta, C. D., Banerjee, N., 2012. Progressive deformation across a ductile shear zone: an example from the Singhbhum Shear Zone, eastern India. International Geology Review, 54(3), 290-301.

Mauldon, M., Dunne, W.M., Rohrbaugh, M.B., 2001. Circular scanlines and circular windows: new tools for characterizing the geometry of fracture traces. Journal of Structural Geology 23 (2), 247e258.

Mazumdar, S.K., 1988. Crustal evolution of the Chhotanagpur gneissic complex and the mica belt of Bihar. Memoir-Geological Society of India, (8), pp.49-83.

Mazzarini, F., Isola, I., 2007. Hydraulic connection and fluid overpressure in upper crustal rocks: Evidence from the geometry and spatial distribution of veins at Botrona quarry, southern Tuscany, Italy. Journal of Structural Geology, 29(8), 1386-1399.

Mazzarini, F., Musumeci, G., 2008. Hydrofracturing-related sill and dyke emplacement at shallow crustal levels: the Eastern Elba Dyke Complex, Italy. Geological Society, London, Special Publications, 302(1), 121-129.

Mazzarini, F., Musumeci, G., Viola, G., Garofalo, P. S., Mattila, J., 2019. Structural and lithological control on fluid circulation, dilation and ore mineralization (Rio Albano mine, Island of Elba, Italy). Journal of Structural Geology, 126, 210-230.

McGarr, A., 1980. Some constraints on levels of shear stress in the crust from observations and theory. Journal of Geophysical Research: Solid Earth, 85(B11), 6231-6238.

McKeagney, C. J., Boulter, C. A., Jolly, R. J. H., Foster, R. P., 2004. 3-D Mohr Circle analysis of vein opening, Indarama lode-gold deposit, Zimbabwe: implications for exploration, Journal of Structural Geology,26, 12751291.

Meert, J. G., 2014. Strange attractors, spiritual interlopers and lonely wanderers: the search for pre-Pangean supercontinents. Geoscience Frontiers, 5(2), 155-166.

Meert, J. G., Pandit, M. K., 2015. The Archaean and Proterozoic history of Peninsular India: tectonic framework for Precambrian sedimentary basins in India.

Meert, J. G., Pandit, M. K., Pivarunas, A., Katusin, K., Sinha, A. K., 2017. India and Antarctica in the Precambrian: a brief analysis. Geological Society, London, Special Publications, 457(1), 339-351.

Meert, J. G., Pandit, M. K., Pradhan, V. R., Banks, J., Sirianni, R., Stroud, M., Newstead, B., Gifford, J., 2010. Precambrian crustal evolution of Peninsular India: A 3.0-billion-year odyssey. Journal of Asian Earth Sciences 39, 483–515.

Mendes, L. D. C., Correia, U. M., Cunha, O. R., Oliveira, F. M., Vidal, A. C., 2022. Topological analysis of fault network in naturally fractured reservoirs: A case study from the pre-salt section of the Santos Basin, Brazil. Journal of Structural Geology, 159, 104597.

Mériaux, C., Lister, J. R., Lyakhovsky, V., Agnon, A., 1999. Dyke propagation with distributed damage of the host rock. Earth and Planetary Science Letters, 165(2), 177-185. https://doi.org/10.1016/S0012-821X(98)00264-7

Mildren, S. D., Hillis, R.R., Kaldi, J., 2002. Calibrating predictions of fault seal reactivation in the Timor Sea. The APPEA Journal 42, 187–202.

Mishra, D. C., 2011. A unified model of Neoarchean–Proterozoic convergence and rifting of Indian cratons: Geophysical constraints, 2, 610–630.

Misra, A. A., Mukherjee, S., 2017. Dyke–brittle shear relationships in the western Deccan strike-slip zone around Mumbai (Maharashtra, India). In: Mukherjee, S., Misra, A. A., Calvès, G., Nemčok, M. (Eds) Tectonics of the Deccan Large Igneous Province. Geological Society, London, Special Publications, 445(1), 269-295.

Misra, S., Mandal, N., Chakraborty, C., 2009. Formation of Riedel shear fractures in granular materials: Findings from analogue shear experiments and theoretical analyses. Tectonophysics, 471(3-4), 253-259.

Moisy, F., 2008. Computing a fractal dimension with Matlab: 1D, 2D and 3D Box-counting. Fluids, Automation and Thermal Systems (FAST), University Paris Sud.

Mondal, T. K., Acharyya, S. S., 2018. Fractured micro-granitoid enclaves: a stress marker, Journal of Structural Geology, 113, 33–41.

Mondal, T. K., Bhowmick, S., Das, S., Patsa, A., 2020. Paleostress field reconstruction in the western Dharwar craton, south India: evidence from brittle faults and associated structures of younger granites. Journal of Structural Geology, 135, 104040.

Mondal, T. K., Mamtani, M. A., 2013. 3-D Mohr circle construction using vein orientation data from Gadag (southern India) e implications to recognize fluid pressure fluctuation. J. Struct. Geol., 56, 45–56.

Mondal, T. K., Mamtani, M. A., 2014. Fabric analysis in rocks of the Gadag region (southern India)—implications for time relationship between regional deformation and gold mineralization. Tectonophysics, 629, 238-249.

Mondal, T. K., Mamtani, M. A., 2016. Palaeostress analysis of normal faults in granite–implications for interpreting Riedel shearing related to regional deformation. J. Geol. Soc, 2014–2136.

Mondal, T.K., 2018. Evolution of fabric in Chitradurga granite (south India)-A study based on microstructure, anisotropy of magnetic susceptibility (AMS) and vorticity analysis. Tectonophysics 723, 149–161.

Mondal, T.K., Acharyya, S.S., 2018. Fractured micro-granitoid enclaves: a stress marker. Journal of Structural Geology 113, 33–41.

Mondal, T.K., Bhowmick, S., Das, S., Patsa, A., 2020. Paleostress field reconstruction in the western Dharwar Craton, south India: Evidences from brittle faults and associated structures of younger granites. Journal of Structural Geology, Vol. 135, 104040.

Morris, A., Ferrill, D. A., Henderson, D. B., 1996. Slip-tendency analysis and fault reactivation. Geology, 24(3), 275-278.

Moyen, J. F., Nédélec, A., Martin, H., Jayananda, M., 2003. Syntectonic granite emplacement at different structural levels: The Closepet granite, South India. Journal of Structural Geology, 25(4), 611-631.

Mukherjee, S., 2018. Locating center of gravity in geological contexts. International Journal of Earth Sciences 107, 1935-1939.

Mukhopadhyay, D. and Matin, A., 1993. The structural anatomy of the Sandur schist belt—a greenstone belt in the Dharwar craton of South India. Journal of Structural Geology, 15(3-5), pp.309-322.

Mukhopadhyay, D., 1986. Structural pattern in the Dharwar craton. The Journal of Geology, 94(2), 167-186.

Mukhopadhyay, D., 2001. The Archaean nucleus of Singhbhum: the present state of knowledge. Gondwana Research, 4(3), 307-318.

Mukhopadhyay, D., Baral, M. C., 1985. Structural geometry of the Dharwar rocks near Chitradurga. Journal Geological Society of India, 26(8), 547-566.

Mukhopadhyay, D., Baral, M. C., Ghosh, D., 1981. A tectono-stratigraphic model of the Chitradurga schist belt, Karnataka, India. Journal Geological Society of India, 22(1), 22-31.

Mukhopadhyay, D., Ghosh, D., 1983. Superposed Deformation in the Dharwar Rocks of the Southern Part of the Chitradurga Schist Belt Near Dodguni, Karnataka. In: Naqvi, S. M. and Rogers, J. J. W. (Eds.), Precambrian of South India. Geological Society of India, Memoir No.4, 275–292.

Mustard, R., 2001. Granite-hosted gold mineralization at Timbarra, northern New South Wales, Australia. Mineralium Deposita, 36, 542-562.

Naha, K., Mukhopadhyay, D., Dastidar, S., Mukhopadhyay, R. P., 1995. Basement – cover relations between a granite gneiss body and its meta–sedimentary envelop: a structural study from the early Precambrian Dharwar province, southern India. Precambrian Research 72, 283–299.

Naha, K., Srinivasan, R., Gopalan, K., Pantulu, G. V. C., Subba rao, M. V., Vrevsky, A. B., Bogomolov, Y. S., 1993. The nature of basement in the Archaean Dharwar craton of southern India and the age of the Peninsular Gneiss. Proceeding of Indian Academy of Science (Earth and planet Sci) 102 (4), 547–565.

Naha, K., Srinivasan, R., Jayaram, S., 1991. Sedimentological, structural and migmatitic history of the Archaean Dharwar tectonic province, southern India. Proceedings of the Indian Academy of Science (Earth Planetary Science) 100, 413–433.

Naqvi, S. M., 1981. The oldest supracrustals of the Dharwar craton, India. Journal of the Geological Society of India 22, 458–469.

Naqvi, S. M., Rao, T. H., Natrajan, R., Satyanarayana, K., Rao, V. D., Hussain, S. M., 1977. Mineralogy, geochemistry and genesis of the massive base metal sulfide deposits of Chitradurga (Ingaldhal), Karnataka, India. Precambrian Research, 4(4), 361-386.

Naqvi, S. M., Rogers, J. J. W. (Eds.) 1983. Precambrian of South India. The Geological Society of India, Memoir No. 4.

Naqvi, S. M., Rogers, J. J. W., 1987. Precambrian Geology of India. Oxford University press.

Naqvi, S. M., Rogers, J. J. W., 1987. Precambrian Geology of India. Oxford Monographs on Geology and Geophysics no. 6. New York: Oxford University Press.

Narayanaswami, S., Ziauddin, M., Ramachandra, A. V., 1960. Structural control and localization of gold-bearing lodes, Kolar gold field, India. Economic Geology, 55(7), 1429-1459.

Neuman, S. P., 2005. Trends, prospects and challenges in quantifying flow and transport through fractured rocks. Hydrogeology Journal, 13, 124-147.

Nicholson, R., Pollard, D. D., 1985. Dilation and linkage of echelon cracks. Journal of Structural Geology, 7(5), 583-590.

Nordbäck, N., Ovaskainen, N., Markovaara-Koivisto, M., Skyttä, P., Ojala, A., Engström, J., Nixon, C., 2023. Multiscale mapping and scaling analysis of the censored brittle structural framework within the crystalline bedrock of southern Finland. Bulletin of the Geological Society of Finland, 95(1).

Nutman, A. P., Chadwick, B., Krishna Rao, B., Vasudev, V. N., 1996. SHRIMP U/Pb zircon ages of acid volcanic rocks in the Chitradurga and Sandur groups, and granites adjacent to the Sandur schist belt, Karnataka. Journal of the Geological Society of India, 47.

Oda, M., 1983. A method for evaluating the effect of crack geometry on the mechanical behavior of cracked rock masses. Mechanics of Materials, 2(2), 163-171.

Odling, N. E., Gillespie, P., Bourgine, B., Castaing, C., Chiles, J. P., Christensen, N. P., ... Watterson, J., 1999. Variations in fracture system geometry and their implications for fluid flow in fractures hydrocarbon reservoirs. Petroleum Geoscience, 5(4), 373-384.

Osagiede, E. E., Nixon, C. W., Gawthorpe, R., Rotevatn, A., Fossen, H., Jackson, C. A. L., Tillmans, F., 2023. Topological characterization of a fault network along the northern North Sea rift margin. Tectonics, 42(8), e2023TC007841.

Otsubo, M., Miyakawa, A., Kawasaki, R., Sato, K., Yamaguchi, A., Kimura, G., 2016. Variations in stress and driving pore fluid pressure ratio using vein orientations along megasplay faults: Example from the Nobeoka Thrust, Southwest Japan. Island Arc, 25(6), 421-432.

Panara, Y., Chandra, V., Finkbeiner, T., Petrovic, A., Zühlke, R., Khanna, P., Vahrenkamp, V., 2023. Fracture intensity and associated variability: A new methodology for 3D digital outcrop model analysis of carbonate reservoirs. Marine and Petroleum Geology, 158, 106532.

Papanastasiou, P., 1997. The influence of plasticity in hydraulic fracturing. International Journal of Fracture, 84(1), pp.61-79. https://doi.org/10.1023/A:1007336003057

Paranthaman, S., 2005. Geology and geochemistry of Archaean Ghattihosahalli mafic–ultramafic complex, Chitradurga, Karnataka. Journal of the Geological Society of India 66, 653–657.

Park, S.-I., Kim, Y.-S., Ryoo, C.-R., Sanderson, D.J., 2010. Fractal analysis of the evolution of a fracture network in a granite outcrop, SE Korea. Geosciences Journal, 14(2), 201–215.

Parker, A. P., 1981. The mechanics of fracture and fatigue. E & F N Spon, London.

Pascal, C., 2021. Paleostress Inversion Techniques: Methods and Applications for Tectonics. Elsevier.

Passchier, C. W., Trouw, R. A., 2005. Microtectonics. Berlin, Heidelberg: Springer Berlin Heidelberg.

Paulatto, M., Moorkamp, M., Hautmann, S., Hooft, E., Morgan, J. V., Sparks, R. S. J., 2019. Vertically extensive magma reservoir revealed from joint inversion and quantitative interpretation of seismic and gravity data. Journal of Geophysical Research: Solid Earth, 124(11), 11170-11191.

Peacock, D. C. P., Sanderson, D. J., 2018. Structural analyses and fracture network characterisation: Seven pillars of wisdom. Earth-Science Reviews, 184, 13-28.

Perugini, D., Poli, G., Christofides, G., Eleftheriadis, G., 2003. Magma mixing in the Sithonia Plutonic Complex, Greece: evidence from mafic microgranular enclaves. Mineralogy and Petrology, 78(3), 173-200.

Petit, J.-P., 1987. Criteria for the sense of movement on fault surfaces in brittle rocks. Journal of Structural Geology 9, 597–608.

Peucat, J. J., Bouhallier, H., Fanning, C. M., Jayananda, M., 1995. Age of the Holenarsipur greenstone belt, relationships with the surrounding gneisses (Karnataka, South India). The Journal of Geology, 103(6), 701-710.

Phillips, W. J., 1974. The dynamic emplacement of cone sheets. Tectonophysics, 24(1-2), 69-84.

Poland, M. P., Fink, J. H., Tauxe, L., 2004. Patterns of magma flow in segmented silicic dikes at Summer Coon volcano, Colorado: AMS and thin section analysis. Earth and Planetary Science Letters, 219(1-2), 155-169.

Pollard, D. D., & Aydin, A., 1988. Progress in understanding jointing over the past century. Geological Society of America Bulletin, 100(8), 1181-1204.

Pollard, D. D., 1973. Equations for stress and displacement fields around pressurized elliptical holes in elastic solids. Journal of the International Association for Mathematical Geology, 5(1), 11-25.

Pollard, D. D., 1987. Elementary fracture mechanics applied to the structural interpretation of dykes. In Mafic dyke swarms (Vol. 34, pp. 5-24).

Pollard, D. D., Aydin, A., 1988. Progress in understanding jointing over the past century. Geological Society of America Bulletin, 100(8), 1181-1204.

Pollard, D. D., Delaney, P. T., Duffield, W. A., Endo, E. T., Okamura, A. T., 1983. Surface deformation in volcanic rift zones. In Developments in Geotectonics (Vol. 19, pp. 541-584). Elsevier.

Pollard, D. D., Fletcher, R. C., 2005. Fundamentals of structural geology. Cambridge University Press.

Pollard, D. D., Martel, S. J., 2020. Quantitative Structural Geology. Cambridge University Press.

Pollard, D. D., Segall, P. A. U. L., Delaney, P. T., 1982. Formation and interpretation of dilatant echelon cracks. Geological Society of America Bulletin, 93(12), 1291-1303.

Pollard, D. D., Segall, P., 1987. Theoretical displacement and stresses near fractures in rocks: With application to faults, points, veins, dykes, and solution surfaces, in Fracture Mechanics of Rock, edited by B. K., Atkinson, pp. 277–349, Academic Press, London.

Priest, S. D., 1993. Discontinuity analysis for rock engineering. Springer Science & Business Media.

Quinta, A., Tavani, S., Roca, E., 2012. Fracture pattern analysis as a tool for constraining the interaction between regional and diapir-related stress fields: Poza de la Sal Diapir (Basque Pyrenees, Spain). Geological Society, London, Special Publications, 363(1), 521–532.

Rama Rao, J.V., Balakrishna, B., Murty, N.V.S., Ajaykumar, P., Ramakrishna Rao, M.V., Acharya, R.S., Sankaram, S.P., 2015. A comprehensive view from geophysical signatures over Chitradurga Schist Belt, Karnataka. Journal of Geological Society of India 86, 489–499.

Rama Rao, J.V., Balakrishna, B., Murty, N.V.S., Ajaykumar, P., Ramakrishna Rao, M.V., Acharya, R.S., Sankaram, S.P., 2015. A comprehensive view from geophysical signatures over Chitradurga Schist Belt, Karnataka. Journal of Geological Society of India 86, 489–499.

Ramakrishnan, M., 1994. Stratigraphic evolution of Dharwar Craton. Geo Karnataka (MGD Centenary Volume), Karnataka Asst. Geol. Assoc., Dept. of Mines and Geology, Govt. of Karnataka, Bangalore, 6–35.

Ramakrishnan, M., Vaidyanadhan, R., 2010. Geology of India, vol. 1. Geological Society of India, Bangalore.

Ramakrishnan, M., Viswanatha, M, N., Swami Nath, J., 1976. Basement –cover relationships of Peninsular Gneiss with high–grade schists and greenstone belts of southern Karnataka. Journal of the Geological Society of India 17, 97–111.

Ramsay, J. G., 1980. The crack–seal mechanism of rock deformation. Nature, 284(5752), 135-139.

Ramsay, J. G., 1986. The techniques of modern structural geology. The Techniques of Modern Structural Geology, Folds and Fractures, 2, 309-700.

Rao, D. S., Naqvi, S. M., 1997. Geological setting, mineralogy, geochemistry and genesis of the Middle Archaean Kalyadi copper deposit, western Dharwar craton, southern India. Mineralium Deposita, 32, 230-242.

Rao, Y. B., Naha, K., Srinivasan, R., Gopalan, K., 1991. Geology, geochemistry and geochronology of the Archaean Peninsular gneiss around Gorur, Hassan district, Karnataka, India. Proceedings of the Indian Academy of Sciences-Earth and Planetary Sciences, 100(4), 399-412.

Rivalta, E., Dahm, T., 2006. Acceleration of buoyancy-driven fractures and magmatic dikes beneath the free surface. Geophysical Journal International, 166(3), 1424-1439.

Rivalta, E., Taisne, B., Bunger, A. P., Katz, R. F., 2015. A review of mechanical models of dike propagation: Schools of thought, results and future directions. Tectonophysics, 638, 1-42. https://doi.org/10.1016/j.tecto.2014.10.003

Rogers, J. J. W., 1986. Dharwar craton and the assembly of Peninsular India, Journal of Geology 94, 129-143.

Rogers, J. J., 1996. A history of continents in the past three billion years. The Journal of Geology, 104(1), 91-107.

Rogers. J. J., Santosh, M., 2002. Configuration of Columbia, a Mesoproterozoic supercontinent. Gondwana Research, 5(1), 5-22.

Roy, A., Perfect, E., Dunne, W.M., McKay, L.D., 2007. Fractal characterization of fracture networks: An improved box-counting technique. Journal of Geophysical Research, 112(B12201), 1–9.

Ruz, J., Browning, J., Cembrano, J., Iturrieta, P., Gerbault, M., Sielfeld, G., 2020. Field observations and numerical models of a Pleistocene-Holocene feeder dyke swarm associated with a fissure complex to the east of the Tatara-San Pedro-Pellado complex, Southern Volcanic Zone, Chile. Journal of Volcanology and Geothermal Research, 404, 107033. https://doi.org/10.1016/j.jvolgeores.2020.107033

Sanderson, D. J., Nixon, C. W., 2015. The use of topology in fracture network characterization. Journal of Structural Geology, 72, 55-66.

Sanderson, D. J., Nixon, C. W., 2018. Topology, connectivity and percolation in fracture networks. Journal of Structural Geology, 115, 167-177.

Sanyal, S., Sengupta, P., 2012. Metamorphic evolution of the Chotanagpur granite gneiss complex of the east Indian shield: current status. Geological Society, London, Special Publications, 365(1), pp.117-145.

Sarangi, S., Srinivasan, R., Balaram, V., 2013. REE geochemistry of auriferous quartz carbonate veins of Neoarchean Ajjanahalli gold deposit, Chitradurga schist belt, Dharwar Craton, India. Geoscience Frontiers, 4(2), 231-239.

Sarkar, A., Mallik, A. K., 1994. Geochronology and geochemistry of Precambrian mafic dykes from Kolar gold field, Karnataka. MEMOIRS-GEOLOGICAL SOCIETY OF INDIA, 111-132.

Sarma, D. S., Fletcher, I. R., Rasmussen, B., McNaughton, N. J., Mohan, M. R., Groves, D. I., 2011. Archean gold mineralization synchronous with late cratonization of the Western Dharwar Craton, India: 2.52 Ga U-Pb ages of hydrothermal monazite and xenotime in gold deposits. Miner. Depos. 46, 273-288.

Sarma, D. S., McNaughton, N. J., Fletcher, I. R., Groves, D. I., Mohan, M. R., Balaram, V., 2008. Timing of gold mineralization in the Hutti gold deposit, Dharwar Craton, South India. Economic Geology, 103(8), 1715-1727.

Sarma, D.S., Fletcher, I.R., Rasmussen, B., McNaughton, N.J., Mohan, M.R., Groves, D.I., 2011. Archean gold mineralization synchronous with late cratonization of the Western Dharwar Craton, India: 2.52 Ga U-Pb ages of hydrothermal monazite and xenotime in gold deposits. Mineralium Deposita, 46, 273–288.

Sarma, D.S., McNaughton, N.J., Belusova, E., Mohan, M.R., Fletcher, I.R., 2012. Detrital zircon U–Pb ages and Hf-isotope systematics from the gadag greenstone belt: archean crustal growth in the western Dharwar craton, India. Gondwana Res. 22 (3), 843–854. https://doi.org/10.1016/j.gr.2012.04.001

Seetharam, S. C., Perko, J., Jacques, D., Mallants, D., 2014. Influence of fracture networks on radionuclide transport from solidified waste forms. Nuclear Engineering and Design, 270, 162–172.

Seffens, W., 1999. Order from Chaos. Science magazine, 285(5431), 1228.

Segall, P., 1984. Formation and growth of extensional fracture sets. Geological Society of America Bulletin, 95(4), 454-462.

Sengupta, S., Roy, A., 2012. Tectonic Amalgamation of Crustal Blocks along Gadag Mandya Shear Zone in Dharwar Craton of Southern India. Journal of the Geological Society of India 80, 75–88.

Seshadri, T.S., Chaudhuri, A., Harinadha Babu, P., Chayapathi, N., 1981. Chitradurga belt. In: Swaminanath, J., Ramakrishnan, M. (Eds.), Early Precambrian Supracurstals of Southern Karnataka. Geological Survey of India Memoir 112, 163–198.

Shakiba, M., Lake, L. W., Gale, J. F., Laubach, S. E., Pyrcz, M. J., 2023. Multiscale spatial analysis of fracture nodes in two dimensions. Marine and Petroleum Geology, 149, 106093.

Shakiba, M., Lake, L. W., Gale, J. F., Laubach, S. E., Pyrcz, M. J., 2024. Stochastic reconstruction of fracture network pattern using spatial point processes. Geoenergy Science and Engineering, 236, 212741.

Sibson, R. H., 1992. Implications of fault-valve behaviour for rupture nucleation and recurrence. Tectonophysics, 211, 283–93.

Sibson, R. H., 1996. Structural permeability of fluid-driven fault-fracture meshes. Journal of Structural geology, 18(8), 1031-1042.

Sibson, R. H., 1996. Structural permeability of fluid-driven fault-fracture meshes. Journal of Structural Geology, 18, 1031–43.

Sibson, R. H., 2000. A brittle failure mode plot defining conditions for high flux–flow. Economic Geology, 95, 41–8.

Sibson, R. H., 2020. Preparation zones for large crustal earthquakes consequent on fault-valve action. Earth, Planets and Space, 72:31, 1-20.

Sibson, R. H., Scott, J., 1998. Stress/fault controls on the containment and release of over pressured fluids: examples from gold-quartz vein systems in Juneau, Alaska, Victoria, Australia, and Otago, New Zealand. Ore Geol. Rev. 13, 293e306.

Simmons, S. F., White, N. C., John, D. A., 2005. Geological characteristics of epithermal precious and base metal deposits.

Sneddon, I. N., Lowengrub M., 1969. Crack Problems in the Classical Theory of Elasticity, Wiley, New York.

Söderlund, U., Bleeker, W., Demirer, K., Srivastava, R.K., Hamilton, M., Nilsson, M., Pesonen, L.J., Samal, A.K., Jayananda, M., Ernst, R.E. Srinivas, M., 2019. Emplacement ages of Paleoproterozoic mafic dyke swarms in eastern Dharwar craton, India: Implications for paleoreconstructions and support for a∼ 30° change in dyke trends from south to north. Precambrian Research, 329, pp.26-43.

Spence, G. H., Redfern, J., Aguilera, R., Bevan, T. G., Cosgrove, J. W., Couples, G. D., Daniel, J. M. (Eds.)., 2014, August. Advances in the study of fractured reservoirs. Geological Society of London.

Sreehari, L. and Toyoshima, T., 2020. Structural architecture and geological relationships in the southern part of Chitradurga Schist Belt, Dharwar craton, South India. Journal of Mineralogical and Petrological Sciences, 115(2), pp.102-117.

Srikantia, S. V., Bose, S. S., 1985. Archaean Komatiites from Banasandra area of Kibbanahalli arm of Chitradurga supracrustal belt in Karnataka. Journal of the Geological Society of India 26, 407–417.

Srikantia, S. V., Rao, M. S., 1990. Unusual concentric structure in komatiite of Kibbanahalli arm of Chitradurga supracrustal belt near Banasandra, Karnataka. Journal of the Geological Society of India 36, 424–429.

Srikantia, S. V., Venkataramana, P., 1989. The Archaean komatiites of Nagamangala supracrustal belt, Karnataka. Journal of the Geological Society of India 33, 210–214.

Srivastava, D. C., Pradhan, A., 1995. Late brittle tectonics in a Precambrian ductile belt: evidence from brittle structures in the Singhbhum Shear Zone, eastern India. Journal of Structural Geology, 17(3), 385-396.

Stephens, T. L., Walker, R. J., Healy, D., Bubeck, A., England, R. W., 2018. Mechanical models to estimate the paleostress state from igneous intrusions. Solid Earth 9, 847–58.

Stephens, T. L., Walker, R. J., Healy, D., Bubeck, A., England, R. W., McCaffrey, K. J., 2017. Igneous sills record far-field and near-field stress interactions during volcano construction: Isle of Mull, Scotland. Earth and Planetary Science Letters 478, 159–74.

Suzuki, K., Oda, M., Yamazaki, M., Kuwahara, T., 1998. Permeability changes in granite with crack growth during immersion in hot water. International Journal of Rock Mechanics and Mining Sciences, 35(7), 907-921.

Swain, S. K., Sarangi, S., Srinivasan, R., Sarkar, A., Kesarwani, M., Mazumdar, A., Satyanarayanan, M., 2018. Stable isotope (COS) and geochemical studies of auriferous quartz carbonate veins, Neoarchaean orogenic Ajjanahalli and Gadag Gold Field, Chitradurga schist belt, Dharwar Craton, southern India: Implication for the source of gold mineralizing fluids. Ore Geology Reviews, 95, 456-479.

Swami Nath, J. Ramakrishnan, M. (Eds.), 1981. Early Precambrian Supracrustals of southern Karnataka. Geological Survey of India, Memoir 112.

Swami Nath, J., Ramakrishnan, M., Viswanatha, M. N., 1976. Dharwar Stratigraphic model and Karnataka craton evolution. Rec. Geological Survey of India 107 (2), 149–175.

Swanson, M. T., 2006. Late Paleozoic strike-slip faults and related vein arrays of Cape Elizabeth, Maine. Journal of Structural Geology, 28(3), 456-473.

Taylor, P. N., Chadwick, B., Moorbath, S., Ramakrishnan, M., Viswanatha, M. N., 1984. Petrography, chemistry and isotopic ages of Peninsular Gneiss, Dharwar acid volcanic rocks and the Chitradurga Granite with special reference to the late Archean evolution of the Karnataka Craton, southern India. Precambrian Research, 23(3-4), 349-375.

Tchalenko, J. S., 1970. Similarities between shear zones of different magnitudes. Geological Society of America Bulletin, 81(6), 1625-1640.

Terzaghi, R. D., 1965. Sources of error in joint surveys. Geotechnique, 15(3), 287-304.

Thyng, K. M., Greene, C. A, Hetland, R. D., Zimmerle, H. M., DiMarco, S. F., 2016. True Colors of Oceanography Guidelines for Effective and Accurate Colormap Selection. Oceanography 29, 9–13.

Torvela, T., Ehlers, C., 2010. From ductile to brittle deformation: structural development and strain distribution along a crustal-scale shear zone in SW Finland. International Journal of Earth Sciences, 99(5), 1133-1152.

Townsend, M. R., Pollard, D. D., Smith, R. P., 2017. Mechanical models for dikes: A third school of thought. Tectonophysics, 703, 98-118.

Tsang, C. F., 2015. *Hydrologic issues associated with nuclear waste repositories*. Water Resources Research, 51(10), 8042–8059.

Turcotte, D.L., 1989. Fractals in Geology and Geophysics. Pure and Applied Geophysics, 131(1–2), 171–196.

Twiss, R. J., Moores, E. M., 1992. Structural geology. Macmillan.

Uday Raj, B., Naqvi, S. M., 1995. Relicts of sedimentary precursors in Archaean gneisses: Melkote parageneiss–An example from Dharwar craton. Journal of the Geological Society of India 46, 497–520.

Valdiya, K. S. 2010. The making of India-Geodynamic evolution. Macmillan Pub. India. Ltd.

Vallance, J., Boiron, M. C., Cathelineau, M., Fourcade, S., Varlet, M., Marignac, C., 2004. The granite hosted gold deposit of Moulin de Cheni (Saint-Yrieix district, Massif Central, France): petrographic, structural, fluid inclusion and oxygen isotope constraints. Mineralium Deposita, 39, 265-281.

Vanderhaeghe, O., 2001. Melt segragation, pervasive melt migration and magma mobility in the continental crust: the structural record from pores to orogens. Physics and Chemistry of the Earth, Part A: Solid Earth and Geodesy, 26(4-5), 213-223.

Velde, B., Dubois, J., Moore, D., Touchard, G., 1991. Fractal patterns of fractures in granites. Earth and Planetary Science Letters, 104(1), 25-35.

Velde, B., Dubois, J., Touchard, G., Badri, A., 1990. Fractal analysis of fractures in rocks: the Cantor's Dust method. Tectonophysics, 179(3–4), 345–352.

Venkatadasu, S. P., Ramakrishnan, M., Mahabaleshwar, B., 1991. Sargur-Dharwar relationship around komatiite-rich Jayachamarajapura greenstone belt in Karnataka. Journal of Geological Society of India 38, 577–592.

Warren, J. M., Hansen, L. N., 2023. Ductile deformation of the lithospheric mantle. Annual Review of Earth and Planetary Sciences, 51, 581-609.

Watterson, J., 1968. Plutonic development of the Ilordleq area, South Greenland. Part II: Late-kinematic basic dykes. Bulletin Grønlands Geologiske Undersøgelse, 70, 1-104.

Węglińska, E., Leśniak, A., Pasternacki, A., Wandycz, P., 2024. Mapping a fracture network formed by hydraulic fracturing in a shale gas reservoir. Geology, Geophysics and Environment, 50(3), 213-230.

Weinberg, R. F., 2006. Melt segregation structures in granitic plutons. Geology, 34(4), 305-308.

Weinberger, R., Lyakhovsky, V., Baer, G., Agnon, A., 2000. Damage zones around en echelon dike segments in porous sandstone. Journal of Geophysical Research: Solid Earth, 105(B2), 3115-3133.

Windley, B. F., 1973. A Discussion on the evolution of the Precambrian crust-Crustal development in the Precambrian. Philosophical Transactions of the Royal Society of London. Series A, Mathematical and Physical Sciences, 273(1235), 321-341.

Xu, J., Yang, L., Liu, Z., Ding, Y., Gao, R., Wang, Z., Mo, S., 2021. A new approach to embed complex fracture network in tight oil reservoir and well productivity analysis. Natural Resources Research, 30, 2575-2586.

Xu, S.S., Nieto-Samaniego, A.F., Alaniz-Alvarez, S.A. 2013. Emplacement of pyroclastic dykes in Riedel shear fractures: an example from the Sierra de San Miguelito, central Mexico. Journal of Volcanology and Geothermal Research, 250, 1–8.

Yamaji, A., 2016. Genetic algorithm for fitting a mixed Bingham distribution to 3D orientations: a tool for the statistical and paleostress analyses of fracture orientations. Island Arc, 25(1), 72-83.

Yamaji, A., Sato, K., 2011. Clustering of fracture orientations using a mixed Bingham distribution and its application to paleostress analysis from dike or vein orientations, Journal of Structural Geology,33, 1148–1157.

Yamaji, A., Sato, K., Tonai, S., 2010. Stochastic modelling for the stress inversion of vein orientations: Paleostress analysis of Pliocene epithermal veins in southwestern Kyushu, Japan. Journal of Structural Geology, 32(8), 1137-1146.

Zhang, X., Si, G., Bai, Q., Xiang, Z., Li, X., Oh, J., Zhang, Z., 2023. Effects of discrete fracture networks on simulating hydraulic fracturing, induced seismicity, and trending transition of relative modulus in coal seams. International Journal of Coal Science & Technology, 10(1), 1–15.

Zhao, Y.S., Feng, Z.C., Liang, W.G., Yang, D., Hu, Y.Q., Kang, T.H., 2009. Investigation of fractal distribution law for the trace number of random and grouped fractures in a geological mass. Engineering Geology, 109(3–4), 224–229.

Publications from the present work

Published/Accepted

1. **Biswas, S.K.**, Mondal, T. K., Saha, A., Mukhopadhyay, A.K., and Mukherjee, A. (2025). Estimating Complete Dyke Dimensions from Partial Exposures. *Journal of Structural Geology*, 192, 105350. https://doi.org/10.1016/j.jsg.2025.105350

2. **Biswas, S.K.**, and Mondal, T. K. (2024). Dyke emplacement under mixed loading conditions: insights from the Dharwar Craton, India. *Journal of Asian Earth Sciences*, 276, 106359. https://doi.org/10.1016/j.jseaes.2024.106359

3. Das, G., **Biswas, S. K.**, Mondal, T. K., and Mondal, S. (2024). Evolution of tensile fractures in feldspar porphyroclast and its implication in paleostress estimation. *Journal of Structural Geology*, 179, 105039. https://doi.org/10.1016/j.jsg.2023.105039

4. **Biswas, S. K.**, Saha, K., Das, G., and Mondal, T. K. (2023). Estimation of magma overpressure from partially exposed dykes-A new approach. *Journal of Structural Geology*, 168, 104822. https://doi.org/10.1016/j.jsg.2023.104822

5. Bhowmick, S., **Biswas, S. K.** and Mondal, T. K. (2023). Quantifying fluid pressure events using shallow crustal veins. *International Journal of Earth Sciences*, 1-16. https://doi.org/10.1007/s00531-023-02362-x

6. Mondal, S., Mondal, T. K., **Biswas, S. K.**, and Das, G. (2023). Understanding the 3D spatiotemporal evolution of fractures in pillow basalt. *Geologica Acta*, 21.8, 1-10, I. https://doi.org/10.1344/GeologicaActa2023.21.8

Communicated/Under Review

1. **Biswas, S.K.**, Banik, B., Hossain, M.S., and Mondal, T.K. *Genesis and spatial variations in geometry, topology and fractal attributes of naturally occurring fracture networks in granites.* (submitted to Journal of Structural Geology, under review; as of 29.08.2025).

In preparation

1. **Biswas, S.K.**, and Mondal, T.K. *Temporal evolution and spatial interrelations of brittle structures within Neo-Archean granites: A study on late-stage Precambrian brittle tectonics from the ~ 2.6 Ga granites of the Chitradurga Schist Belt, Western Dharwar Craton, India.*

Conference Abstracts

1. **Biswas, S.K.** & Mondal, T.K. Estimating aspect ratios and magma overpressures from partially exposed dykes. International Association of Volcanology and Chemistry of the Earth's Interior (IAVCEI) LASI VII (Laccoliths, sills and dykes: The physical geology of subvolcanic systems) conference at Hveragerði, Iceland, to be held from 8-11th of September, 2025, pp. 43.

2. Mondal, T.K., **Biswas, S.K.**, Dey, A. The Ellipse Speaks: Reconstructing Dyke Geometry from Single-Tipped Exposures. International Association of Volcanology and Chemistry of the Earth's Interior (IAVCEI) LASI VII (Laccoliths, sills and dykes: The physical geology of subvolcanic systems) conference at Hveragerði, Iceland, to be held from 8-11th of September, 2025, pp. 55.
3. **Biswas, S.K.**, Banik, B., Mondal, T.K., Hossain, M.S. Spatial variations in Geometry, Topology and Fractal attributes of a Riedel shear induced Fracture Network system in Granites. *EGU General Assembly 2025*, *Vienna*, *Austria* (https://doi.org/10.5194/egusphere-egu25-866).
4. **Biswas, S.K.** & Mondal, T.K. Veins, Dykes and Fracture Networks: A saga of brittle tectonics from the Archean Chitradurga Schist Belt, Western Dharwar Craton, India. *National Conference on Dynamic Processes of the Earth (DPE) 2025, Department of Geology, Presidency University, Kolkata*, *India*, pp. 28.
5. **Biswas, S.K.** & Mondal, T.K. Estimating aspect ratios and magma overpressures from partially exposed dykes. *IISER Kolkata, Department of Earth Sciences, Annual Day, Convergence,* 2025.
6. **Biswas, S.K.**, Banik, B., Mondal, T.K., Hossain, M.S. Understanding the development of fracture networks: a study based on network topology. *Rock Deformation and Structures (RDS-VIII), IISER Bhopal, India,* 2024, pp. 7.
7. **Biswas, S. K.**, Mondal T. K., Saha A., Mukhopadhyay A. K., & Mukherjee A. Complete Dyke Dimensions from Incomplete Outcrops. *European Society for Deformation mechanisms, Rheology and Tectonics (DRT-Society), DRT 2024, Barcelona, Spain*, pp. 20.
8. Mondal, T.K., & **Biswas, S.K.** Dykes and their magma overpressure. *EGU General Assembly 2024*, *Vienna*, *Austria* (https://doi.org/10.5194/egusphere-egu24-392).
9. **Biswas, S.K.**, Sultana, J., Mondal, T.K., Hossain, M.S. Spatial variations of fracture network patterns in Neo-Archean granites: implications in understanding late stage Precambrian brittle tectonics. *International Association for Structural Geology and Tectonics (IASGT) IIT Kharagpur (India) Workshop*, 2024, pp. 194-196.
10. **Biswas, S. K.**, Saha, K., Das, G., & Mondal, T. K. Magma overpressure estimates from partially exposed dykes. *Rock Deformation and Structures (RDS-VII), Varanasi, India,* 2022, pp. 19.
11. Mondal, T.K., Bhowmick, S., & **Biswas, S.K.** Determining fluid pressure cycles from vein orientation data. *Rock Deformation and Structures (RDS-VII), Varanasi, India,* 2022, pp. 3.

WEBPAGE DEVELOPED

Web interface developed for calculating complete dyke dimensions and magma overpressure from partially exposed dykes based on Biswas et al. (2023) and (2025). https://isi-structural-geology-group.github.io/Complete-Dyke-Dimensions-and-Magma-Overpressure-Calculator/index.html